ANTENNAS FOR 5G AND 4G/LTE MOBILE DEVICES

by

Khaled Mahbub Morshed

Dissertation submitted in fulfilment of the requirements

for the degree of

DOCTOR OF PHILOSOPHY

Department of Engineering
Faculty of Science and Engineering
Macquarie University
Sydney, Australia

November 2017

ABSTRACT

Increasing demand for high data throughput and reliable service for mobile traffic have motivated the development of 5G mobile communication system, which are currently in the planning stage. Proposed 28 GHz millimeter-wave bands have much potential for forthcoming 5G mobile communication because of the available massive bandwidth and relatively low atmospheric absorption compared with 60 GHz Wi-Gig and other short-range systems. Although the standards for 5G mobile devices have not been finalized as yet, this thesis focuses on the design and development of single-beam antennas and pattern reconfigurable antennas, which are potentially suitable for forthcoming 5G mobile devices.

This thesis initially develops three highly efficient antennas radiating boresight at 28 GHz. Firstly, a narrow-band compact planar inverted-F antenna (PIFA) is developed. Then, a method is presented to convert this narrow-band PIFA to a wideband PIFA while maintaining the same size of the antennas (i.e. 4 mm $\times$ 4 mm). Also, a wideband leaky-wave antenna (LWA) array is presented and investigated. Methods to enhance the efficiency and impedance bandwidth of the antennas are proposed. All the antennas have stable boresight radiation in both the x-z and y-z planes. The impact of the mobile device battery on antenna performance is investigated using one of the PIFAs.

A novel 1-D and 2-D pattern reconfigurable antenna has been developed and investigated for 28 GHz band. Firstly, a basic LWA radiating off-boresight was designed for mobile devices. Then, a wideband LWA radiating boresight was

developed and investigated. This was followed by a novel multi-feed antenna being developed, prototyped and verified experimentally, for 1-D beam switching. The antenna is able to switch beam in three different directions along the antenna axis such as boresight, forward and backward directions using three feeds at three different positions. Because of the wide beamwidth, the antenna radiation patterns can fill 128° of space (3-dB coverage), i.e. θ = -64° to +64° at the azimuth angle of $\phi = 0°$. Then two antennas are placed at right angles to each other to achieve 2-D beam switching. The 2-D beam switching antenna pair was prototyped and tested after integrating them into the ground plane of a mobile device. The antenna is able to point the beam in five different directions, and in fact its beam covers 167° (θ = -89° to 78°) at $\phi = 0°$, and 154° (θ = -72° to 82°) at $\phi = 90°$.

For 5G mobile communications, a new technology of cognitive radio named licensed shared access (LSA) has been demonstrated and two bands (1452-1492 and 2300-2400 MHz) have been allocated by the European Commission. More bands are expected to be allocated for LSA operation from the bands 698-960, 1427-2690 and 3400-3800 MHz. Hence, the future mobile device antenna require to cover all the LSA and LTE bands while having no null in the radiation patterns. To cover these frequency bands, initially a planar antenna was developed for the said LSA bands and the performance of the antenna was investigated with and without a battery of a mobile device. Secondly, another planar antenna was developed to reduce the number of nulls in the radiation patterns. These antennas cover the LSA (1452-1492 and 2300-2400 MHz), mid-LTE (1427-2690 MHz), GSM1800, GSM1900, UMTS and 2.4 GHz WLAN bands. Thirdly, a dual-band antenna loaded with a small vertical plate was developed and investigated. This antenna covers the LSA, mid-LTE and high-LTE (3400-3800 MHz) bands.

In the lower LSA band radiation patterns there is no null but a null is present in the higher LSA band and two nulls are evident in the high-LTE band. Fourthly, a novel wideband antenna having a planar structure, loaded with an L-shaped vertical plate was developed and prototyped; thus the concept was validated experimentally. The antenna radiation patterns have no nulls and cover the above-mentioned bands. All the antennas were designed without requiring an active or passive component for input impedance matching. The dual-band and wideband antennas cover the aforementioned bands even when the size of the substrate and ground plane is varied between 120 mm $\times$ 70 mm and 240 mm $\times$ 170 mm. This makes them suitable for mobile devices of different sizes, for instance smart phones and tablet computers.

The final contribution this thesis makes in the development of a highly efficient inverted-L-feed capacitive-coupled inverted-L antenna for the low-LTE (698-960 MHz) band. Similar to the previous antennas this antenna does not require any lumped components for input impedance matching. The antenna is presented for future mobile devices utilizing LSA/spectrum reallocation within the low-LTE band. The measured reflection coefficient bandwidths are 684-732, 714-774, 748-823, 788-882, and 820-965 MHz for the tuning inductor values of 9, 7, 5, 3, and 1 nH, respectively. Therefore, this antenna concept is suitable for conversion to a frequency reconfigurable antenna, with switchable inductors. The prototype's radiation performance was measured with the 1 nH inductor to verify the concept.

Although some modern commercial mobile phone handsets use very thin antennas with relatively poor performance due to their low cost and high emphasis on handset aesthetics, high-performance antennas such as those developed in this thesis are required for some multiband (4G/5G/LSA) applications. One of them is a defense application where a handset - carried by many military personnel -

detects, intercepts and jams mobile phone signals used by the enemy to trigger explosive devices such as land mines. Such handsets for improvised threat detection and neutralization require high-performance antennas with high efficiency and gain and their thickness and cost are not critical.

STATEMENT OF CANDIDATE

I certify that the work in this thesis has not previously been submitted for a degree nor has it been submitted as part of the requirements for a degree to any other university or institution other than Macquarie University.

I also certify that the thesis is an original piece of research and it has been written by me.

In addition, I certify that all information sources and literature used are indicated in the thesis.

Khaled Mahbub Morshed

ACKNOWLEDGMENTS

First of all, I would like to acknowledge the blessings of Allah, the almighty, who kept me strong and patience throughout my candidature.

I would like to express my heartiest gratitude and thankfulness to my Principal Supervisor Professor Karu Esselle, director of the Centre for Collaboration in Electromagnetic and Antenna Engineering (C4CELANE), Macquarie University, for his sincere guidance, continued encouragement, invaluable support and suggestions throughout my study at Macquarie University, Australia. He has been a great source of motivation for me, continuously providing insightful comments with detailed attention to my arguments and timely advice on my work. He offered comprehensive comments and suggestions in reviewing my writings at the same time respecting my voice. Also, I would like to thank my associate supervisor Professor Michael Heimlich for his kind support, valuable feedback, and inspiration.

I am greatly indebted to Dr. Debabrata K. Karmokar for his valuable time, efforts, sincere advice, support, encouragement, and recommendation throughout this thesis.

I would like to extend my appreciation to all academic, administrative and technical staff at the Department of Engineering, Macquarie University. Special thanks to my fellow PhD colleagues and friends for being supportive and providing courage and inspiration during the study period.

I gratefully acknowledge Department of Electronics and Communication En-

gineering, Khulna University of Engineering and Technology, Khulna, Bangladesh for allowing me with study leave for this PhD study. I equally acknowledge my colleagues at Bangladesh for supporting me throughout this study.

I am also grateful to A/Professor Ladislau Matekovits, Politecnico di Torino University, Italy, for his support for millimeter-wave antenna measurement. My gratitude also goes to A/Professor Ashraf Uz Zaman, Chalmers University of Technology, Gtenborg, Sweden for his great support and guidance during my research visit. Special thanks goes to Dr. Keith Imrie, Honorary Associate, Department of Engineering, Macquarie University in proof-reading my research papers and my thesis from time to time. I am grateful to Mr. Phillip Thomas for also proof-reading my thesis.

Finally, my sincere and heartfelt gratitude to my respected parents for their silent inspiration. I would especially like to thank my passionate life partner, beloved wife Sumyea Sabrin, and sweet daughter Fatima Mehreen Morshed for their continuous unconditional support and sacrifices to make my study smooth.

To

My Parents Abdul Mannan and Halima Khatun

&

My wife Sumyea Sabrin

&

My daughter Fatima Mehreen Morshed

Contents

List of Figures

List of Tables

Acronyms

CF	Center Feed
DCS	Digital Cellular Systems
ETSI	European Telecommunications Standards Institute
FCC	Federal Communications Commission
FDD	Frequency Division Duplex
GSG	Ground-Signal-Ground
GSM	Global System for Mobile Communications
HPBW	Half-Power Beamwidth
HW-MLWA	Half-Width Microstrip Leaky-Wave Antenna
LF	Left Feed
LSA	Licensed Shared Access
LTE	Long Term Evolution
LWA	Leaky-Wave Antenna
MLD	Main Lobe Direction
MLWA	Microstrip Leaky-Wave Antenna
PCS	Personal Communications Service

PIFA	Planar Inverted-F Antenna
PMA	Planar Monopole Antenna
RF	Right Feed
SIW	Substrate Integrated Waveguide
SLL	Side-Lobe Level
SP	Smart Phone
TC	Table Computer
TDD	Time Division Duplex
UMTS	Universal Mobile Telecommunications Service
WWAN	Wireless Wide Area Network

List of Symbols

k_z	Complex Wavenumber
β	Phase Constant
α	Attenuation Constant
f	Frequency
λ	Wavelength
ϵ_r	Relative Permittivity
$tan\delta$	Loss Tangent

Chapter 1

Introduction

1.1 Introduction

The increasing demands that are inherent in mobile traffic and where a reliable service can be enjoyed, have led to the development of 5G mobile communication system. Currently, 4G/long-term evolution (LTE) and 4G/LTE-advanced mobile communication systems are now deployed in many countries. It is expected that they will be deployed in many other countries soon [1–9]. The forthcoming 5G wireless communication system will enable users to experience 20 Gb/s download speed (peak), given that current users have 1 Gb/s (peak) with 4G. Such an improvement in the wireless network will help to enhance other technologies/sectors including but not limited to the following: cloud computing, smart cities, remote health care, automatic vehicles, internet of things (IoT), artificial intelligence, agriculture, education, and virtual reality.

Presently, the 5G mobile communications system are still at the planning stage. There are five important technologies under consideration that will lead to fundamental changes in the development of future 5G mobile communications where the aim is to achieve 100 to 1000 times the date rate of 4G [1, 2, 10, 11]. These five technologies are device-

centric architecture, millimeter-wave, cognitive radio, smart device, and native support for machine to machine (M2M) communications [2, 10–14]. However, of these five 5G mobile communications technologies only two are receiving more priority from the researchers and industry. One is millimeter-wave [15–21] and the other is licensed shared access (LSA), which is a new cognitive radio technology that allows sharing of spectrum among mobile network operators [2, 22–25]. Field trials on these two promising technologies for 5G have already started [23, 26, 27]. A 1.5 GHz (1452-1492 MHz) band and a 2.3 GHz (2300-2400 MHz) band have been allocated for LSA service. The proposed LSA service has been tested in the 2.3 GHz band in Europe and more bands are expected to be allocated in the near future [23, 28, 29].

Moreover, millimeter-wave bands are attractive for future 5G mobile communications because of the massive available bandwidth. The current spectrum which is below 6 GHz is in fact very limited. Several bands above 6 GHz are under consideration for future 5G mobile devices including the proposals from International Telecommunication Union (ITU), Samsung, and HUAWEI [15,30–32]. The following bands 24.25-27.5, 31.8-33.4, 37-43.5, 45.5-50.2, 50.4-52.6, 66-76, and 81-86 GHz are closely examining under the agenda 10 of World Radiocommunication Conference (WRC)-15 and to be finalised in WRC-19 under agenda 1.13. The frequency bands 27.5-28.35, 37-37.6, 37-38.6, 38.6-40, and 64-71 GHz already allocated in United States for future 5G [33] while Korea and Japan closely examining 28 GHz band future 5G mobile devices. An extensive propagation measurement using a steerable beam for 28 GHz millimeter-wave is presented in [34] to assess the effectiveness of this band under line-of-sight and non-line-of-sight conditions. The maximum path loss is only 7 dB/km or 1.4 dB/200m attenuation at the 28 GHz millimeter-wave band when the cell size is in the order of 200 m [1,35,36]. This atmospheric absorption does not create significant path loss compared to the 38 GHz millimeter wave band. Therefore, a directive and highly efficient antenna is sufficient for mobile terminals,

making it possible to mitigate the path loss that occurs in the 28 GHz band. Since the standards for 5G mobile communications have not been finalized, an antenna with a single directed beam or an antenna with pattern reconfigurable capability would be sufficient for 28 GHz millimeter-wave band.

While the 5G mobile communication system is in the planning stage, the 4G/LTE and 4G/LTE-advanced are in the deployment stage. Because of the significantly increasing demand for spectrum below 6 GHz, new bands have been released regularly for LTE and LTE-advanced over the years. For example, according to the European Telecommunications Standards Institute (ETSI) 'release 09' (April 2010) [37], the frequency ranges allocated for LTE mobile communication system are 824-960, 1427-1501, 1710-2170, and 2500-2690 MHz. They have 11-frequency division duplex (FDD) and 6-time division duplex (TDD) LTE bands. More bands allocated in 'release 12' (May 2015) [38] and the extended frequency ranges for 4G/LTE are 698-960, 1427-2690, and 3400-3800 MHz, consisting of 30-FDD and 12-TDD LTE bands. These frequency ranges are titled as low-LTE, mid-LTE, and high-LTE bands, respectively, in this thesis. Moreover, additional 6-FDD and 4-TDD LTE bands added in ETSI 'release 14' (April 2017) and the extended frequency ranges for LTE and LTE-advanced are 452-468, 698-960, 1427-2690, 3400-3800, and 5150-5925 MHz, consisting of 36-FDD and 16-TDD bands [3]. As well, the frequency ranges 452-468 and 5150-5925 MHz are named as very-low-LTE and very-high-LTE bands, respectively, in this thesis. Mobile phone companies in different countries are making available these newly allocated bands to users to meet the market demand. For example, the LTE11 (1427-1496 MHz) and LTE21 (1447-1511 MHz) bands have been recently deployed in Japan by 'au mobile' and 'NTT Docomo', respectively, and the LTE24 (1525-1661 MHz) band in the United States by 'Ligado Networks' [39, 40]. Consequently, future mobile devices require multi-band antennas to cover the aforementioned frequency ranges so that the 4G/LTE and 4G/LTE-advanced standards are met.

1.2 Challenges and Research Objectives

In defense application multiband (4G/5G/LSA) handset antennas with high performance are required where a handset is very useful device to detects, intercepts and jams mobile phone signals used by the enemy to trigger explosive devices such as land mines. Such handsets require to cover all the mobile communication bands (4G/LTE, 5G, and LSA) without null in the radiation patterns for improvised threat detection and neutralization.

The standards are not available for millimeter-wave 5G mobile device antennas because the forthcoming 5G mobile communication system are in the planning and development phases. However, antennas with single directed beam [17,41–51] or pattern reconfigurable operation [15,52–58] are currently being developed for 28 GHz millimeter-wave 5G mobile devices. Most of the beam switching antennas reported for mobile device application are phased array. However, the amount of power required to drive a millimeter-wave phase shifter for the phased array antenna is almost seven times to the power consumed by the display of the mobile phone for video playback lasting five minutes [59,60]. The maximum beam switching ranges achieved using the planar antennas with multiple feeds are θ = +48° to θ = -48° [52]. All the reported antennas - either phased array or planar antenna are able to switch beam along a particular axis, i.e. 1-D beam switching. Also, the area occupied by the antenna is large compared to the space occupied by the LTE/4G antenna. Therefore, a compact antenna with single directed beam as well as 1-D and 2-D pattern reconfigurable antenna having extended beam switching capabilities without using the phase shifter is a suitable candidate for 28 GHz millimeter-wave 5G mobile devices. A brief analysis of the above discussed issues is presented in Section 2.5 of Chapter 2.

The antennas for 4G/LTE mobile devices studied extensively in the literature can be categorized as either planar inverted-F antenna (PIFA) or planar monopole antenna (PMA). Among those, planar antennas, without ground connection but with or without an inductively/capacitively loaded parasitic element, are considered to be a PMA.

Conversely, the planar antennas having at least one grounding point (mainly by using a shorting point called a metallic via) are considered to be a PIFA. These antennas have been proposed either to cover the dual-frequency ranges (698-960, 1710-2690 MHz) [61–71] or to cover the triple-frequency ranges (698-960, 1710-2690, and 3400-3800 MHz) [72, 73] using the single antenna with single feed or dual feeds. Antennas for LTE handset reported in [74, 75] to cover additional very-high (5150-5925 MHz) frequency range together with the three other frequency ranges were mentioned previously. Overall, most of the previously reported LTE/4G mobile device antennas cover low-LTE and high-LTE frequency ranges. However, they are unable to cover the whole 1427-2690 MHz frequency range which includes both the LSA bands and mid-LTE frequency range. These antennas have good omnidirectional radiation patterns without null in the low-LTE band and at the frequency close to 1710 MHz in the frequency range 1710-2690 MHz. On the other hand, all of the reported antennas suffer from nulls in the radiation patterns, especially at the frequency close to the higher frequency limit (2690 MHz) of the mid-LTE frequency range as well as in the high-LTE, and very-high-LTE frequency ranges [61–75]. Therefore, antennas having good omnidirectional radiation patterns without null over the operating bands for 4G/LTE operation are in great demand to cover the frequency ranges 698-960, 1427-2690, and 3400-3800 MHz. A brief study on the above discussed issues is presented in Section 2.4 of Chapter 2.

This thesis focuses on two main issues/problems. The first main aim is to develop compact antennas with a single directed beam, and 1-D and 2-D pattern reconfigurable antennas with wide scanning range for forthcoming 5G mobile devices. The second main aim is to design and develop small-size antennas for both the LSA, low-LTE, mid-LTE, and high-LTE bands by overcoming nulls from the radiation patterns over the operating band. Therefore, the objectives of this thesis are:

- To design and develop compact antennas radiating at boresight for 28 GHz millimeter-

wave 5G mobile devices, investigate the impact of the superstrate, which acts as a dielectric load, and study the influence of the mobile device battery, on antenna performance.

- Designing single element antennas radiating at boresight and off-boresight direction.
- To design and develop 1-D pattern reconfigurable antenna with the combination of boresight and off-boresight radiating antennas. Validation of the concept will be achieved through fabrication and experiment.
- To develop a method to achieve 2-D pattern reconfigurable operating using the 1-D pattern reconfigurable antenna, and to validate the concept through fabrication and experiment.
- To design and develop planar antennas without a vertical plate and input impedance matching circuit for both the LSA bands, and to investigate the suitability of the planar structure to cover the mid-LTE band. Verifying the performance of the planar antennas will be done with and without the presence of the mobile device battery.
- To design and develop a vertical plate loaded dual-band antenna for the LSA, mid-LTE, and high-LTE bands with a minimum number of nulls in the radiation patterns of the antenna. The performance of the dual-band antenna with different-sized mobile device PCBs like smart phone (SP), SP plus, mini tablet computer (TC), and TC will be investigated.
- Design and development of a vertical plate loaded wideband antenna for the LSA, mid-LTE and high-LTE bands by removing nulls in the radiation patterns. Prototyping the model and conducting an experiment will be conducted to verify the

concept. Suitability testing with different-sized mobile devices will also be undertaken.

- To design and develop a highly efficient antenna for low-LTE band without null in the radiation patterns. Testing passive reconfiguration to validate the suitability of the antenna so that it can be converted into a frequency reconfigurable antenna for future spectrum reallocation or LSA operation in 5G mobile communications. Experimenting on the proposed concept will be done for verification purposes.

1.3 Research Contributions

The key contributions of this thesis are overcoming some limitations of 5G antennas, and to improve scanning range of the pattern reconfigurable antenna for 28 GHz millimeter-wave 5G mobile devices. Furthermore this thesis focuses on overcoming some limitations that exist in 4G mobile device antennas. The major contributions of this thesis include:

- Three planar antennas with boresight radiation for 28 GHz millimeter-wave band are proposed. Two of the proposed antennas are categorized as planar inverted-F antenna (PIFA) and the other is a leaky-wave antenna (LWA) array. These antennas are developed for future 5G mobile device applications. In order to enhance the efficiency and achieve a wide impedance bandwidth, a single layer superstrate acting as a dielectric load is applied. One of the designs is investigated with and without the effect of a battery in order to assess the influence of the mobile device battery on antenna performance.

- A basic LWA radiating in the region between boresight and endfire named as off-boresight direction is designed for 28 GHz millimeter-wave 5G mobile devices. Then a boresight radiating LWA is developed. It is a simple but effective method for

achieving boresight radiation from a single element LWA at 28 GHz band.

- A method is proposed to achieve beam switching in backward, boresight, and forward directions from a 1-D LWA. The proposed antenna has three feed points, one at the center and two at the ends of the antenna. By selecting these three feeds it is possible to switch the beam in three different directions along the antenna axis. The 1-D pattern reconfigurable antenna was prototyped and tested in order to validate the proposed method.

- A method is developed to achieve 2-D pattern reconfigurable operation using the two 1-D pattern reconfigurable antennas. The 2-D beam switching antenna with device ground plane was prototyped and measured. The proposed method is validated through experiments.

- Most of the antennas proposed for 4G/LTE/WWAN operation use a lumped component-based circuit for input impedance matching which introduces losses in the antenna system. Two planar antennas are developed to investigate whether the planar structure can sufficiently achieve coverage for both the LSA, mid-LTE (1427-2690 MHz), and high-LTE (3400-3800 MHz) bands without using impedance matching circuit (to match input impedance) or vertical plate (to improve radiation performance). In order to discover the influence of the mobile device battery on antenna performance, one of the designs is investigated with and without the effect of a battery.

- An antenna loaded with a small vertical plate is proposed to cover the LSA, mid-LTE and high-LTE bands. This dual-band antenna is developed by investigating the other two planar antennas mentioned previously. The proposed antenna is modeled without using an input impedance matching circuit as well.

- A novel antenna loaded with an L-shaped vertical plate is proposed which covers

both the LSA, mid-LTE, and high-LTE bands in a single wide operating band. The wideband antenna is developed based on an investigation of the previously mentioned two planar and a dual-band antennas. Similar to the dual-band antenna, no input impedance matching circuit is used to achieve wideband operation. The antenna was prototyped and tested to validate the idea.

- A novel inverted-L feed capacitive-coupled inverted-L antenna with high efficiency has been developed to operate in the low-LTE (698-960 MHz) band. The antenna does not require any input impedance matching circuit. The proposed antenna is suitable for converting into a frequency reconfigurable antenna, which is suitable for future spectrum reallocation in 5G mobile communications. The proposed model was fabricated and tested to validate the method. Also, the passive reconfiguration technique is investigated experimentally, from which a specific frequency range within the low-LTE band can be selected. This aim is to improve the potential of the antenna for emerging spectrum reallocation or LSA operation in forthcoming 5G systems.

1.4 Publications

The following papers including published, under review, and under preparation for peer-reviewed journals and conference proceedings are the outcomes of research conducted during the author's candidature.

Journal Articles

1. K. M. Morshed, D. K. Karmokar, and K. P. Esselle, "1-D and 2-D Pattern Reconfigurable Antenna for 28 GHz Millimeter-Wave 5G Mobile Devices," Intended Journal: *IEEE Transactions on Antennas and Propagation* (In preparation, planned

for submission in December 2017).

2. K. M. Morshed, K. P. Esselle, and D. K. Karmokar, "Antenna without Matching Network for 5G Licensed Shared Access Mobile Devices in LTE Low-Band," *IEEE Antennas and Wireless Propagation Letters* (Submitted).

3. K. M. Morshed, K. P. Esselle, and D. K. Karmokar, "Antennas for Licensed Shared Access in 5G Communications with LTE Mid and LTE High Bands Coverage," *IEEE Transactions on Antennas and Propagation* (under review).

Conference Papers

1. K. M. Morshed, D. K. Karmokar, and K. P. Esselle, "Highly Efficient Leaky-Wave Antenna Array for 28 GHz Millimeter-Wave Terminals," in *Proc. IEEE 85th Vehicular Technology Conference (VTC2017-Spring)*, Sydney, Australia, June 2017.

2. K. M. Morshed, K. P. Esselle, M. Heimlich, D. Habibi, and I. Ahmad, "Wideband Slotted Planar Inverted-F Antenna for Millimeter-Wave 5G Mobile Devices," in *Proc. IEEE Region 10 Symposium (TENSYMP)*, Bali Island, Indonesia, May 2016.

3. K. M. Morshed, K. P. Esselle, and M. Heimlich, "Dielectric Loaded Planar Inverted-F Antenna for Millimeter-Wave 5G Hand Held Devices," in *Proc. European Conference on Antennas and Propagation (EuCAP)*, Davos, Switzerland, April 2016.

4. K. M. Morshed, K. P. Esselle, M. Heimlich, M. D. Mueck, and S. G. Hay, "A Simple Planar Monopole Antenna for Mobile Handset Applications," in *Proc. International Symposium on Antennas and Propagation (ISAP)*, Tasmania, Australia, November 2015.

1.5 Outline of the Thesis

This thesis consists of ten chapters and an outline of the remaining nine chapters is presented below.

Chapter 2 begins with a discussion of the frequency bands allocated, under review, and proposed for 3G, 4G, 4G-advanced and 5G mobile communications. A comprehensive literature review is presented on the topic of 4G/LTE mobile phone antennas, the focus being on frequency range and radiation patterns characteristics. Furthermore, antennas reported for 5G mobile communications focusing on licensed shared access (LSA) and 28 GHz millimeter-wave bands are studied together with pattern reconfigurable antennas. Finally, a summary of what authors' knowledge is lacking is presented in the literature review.

Chapter 3 presents the development of three planar antennas for 28 GHz millimeter wave band radiating at boresight direction. These antennas are developed for future 5G mobile devices. In order to enhance efficiency and achieve a wide impedance bandwidth, a single layer superstrate (acts as a dielectric load) is applied. The aim is to improve gain and directivity of the antennas. Initially, a highly efficient, narrow-band compact PIFA has been developed. The performance of the antenna is evaluated in two different case studies that take into account and otherwise the effect of a mobile phone battery. The antenna indicates a similar level of performance in both cases. Secondly, a wideband LWA array has been investigated for 5G millimeter-wave band where each element of the array is terminated with a rectangular microstrip. Thirdly, a highly efficient compact wideband PIFA is developed. Like the previous two developments, a superstrate that acts as a dielectric load is applied in order to enhance the efficiency and subsequently the gain and directivity of the antenna. Owing to good performance and convenience of fabrication, these proposed antennas are attractive for future 5G mobile devices. A comparison with the reference antennas to date is presented to justify the suitability of

the proposed antennas for future 5G mobile devices.

Chapter 4 presents an examination of a basic leaky-wave antenna (LWA) radiating in the forward direction, a region between boresight and endfire; this is known as the off-boresight direction and it applies to 28 GHz millimeter-wave 5G mobile devices. The antenna was studied thoroughly in order to understand the working modes. Secondly, a single element LWA is developed that radiates towards the boresight. The half-power beamwidth (HPBW) of the antenna increases slightly when the frequency also increases within the antenna operating band. Furthermore the beam does not split into two beams within the band of interest. However, to find the frequency at which the boresight beam splits into two off-boresight beams, a brief investigation is presented based on antenna performance.

Chapter 5 presents a novel LWA for 1-D pattern reconfigurable operation. The antenna is designed using the ideas discussed in the previous chapter. The 1-D beam switching antenna has three feed points, one at the center and two at the sides of the antenna. By selecting these three feeds independently it is possible to switch the beam in three different directions along the antenna axis. The antennas performance is optimized for each feed while the other feeds are inactive. The 1-D pattern reconfigurable antenna was prototyped and the operation was verified through measurements. Secondly, using two 1-D beam switching antennas a 2-D pattern reconfigurable operation is achieved. The performance of the 2-D beam switching antenna is tested after placing the antenna at the corner of the ground plane of a mobile device. A comparison with the reference antennas to date is presented to justify the superiority of the proposed antenna for future 5G mobile device application.

Chapter 6 presents the development of two novel planar antennas for mobile devices. Firstly, an antenna with an O-shaped ground plane is developed. The antennas performance is tested with and without the presence of a mobile-device battery to observe its

effect on antenna performance. Two nulls are observed in the radiation patterns over the operating band of the antenna. Secondly, another planar antenna is developed and this one covers the lower LSA band without null in the radiation patterns. However, a null is exist in the radiation patterns at the frequency close to the higher frequency limit (2690 MHz) of the mid-LTE band. Both planar antennas cover the LSA bands (1452-1492 and 2300-2400 MHz) and mid-LTE band (1427-2690 MHz). However, they are unable to cover the high-LTE band (3400-3800 MHz).

Chapter 7 presents a dual-band antenna using the methods proposed in the previous chapter (Chapter 6). The primary focus here is to develop an antenna which can cover the LSA, mid-LTE, and high-LTE bands. The antenna proposed is modeled using a planar structure loaded with an I-shaped small vertical plate. Most of the proposed antennas uses passive or active lumped component-based input impedance matching circuit to cover the above mentioned bands. The antenna described here does not require any input impedance matching circuit and hence the structure is simple. The antenna covers the lower LSA bands without null in the radiation patterns. However, one of the disadvantages of the antenna is that a null is observed in the radiation patterns at the frequency close to the higher frequency limit of the mid-LTE band, and two nulls in the high-LTE band.

Chapter 8 presents an L-shaped vertical plate loaded wideband antenna covering the LSA, mid-LTE, and high-LTE bands. The antenna is developed using methods discussed in the previous two chapters. In this design approach the objective is to reduce antenna size and to remove the null from the radiation patterns. Similar to the previous antennas, the proposed antenna discussed in this chapter does not require any active or passive lumped component-based input impedance matching circuit. In order to verify the concept the wideband antenna was prototyped and tested.

Chapter 9 presents an inverted-L feed capacitive-coupled inverted-L antenna with high efficiency without using any antenna input matching circuit. The antenna has been de-

signed to operate in the low-LTE band. The proposed antenna is suitable for converting into a frequency reconfigurable antenna. The passive reconfiguration technique is investigated for the antenna structure so that a specific operating band within the greater low-LTE band can be selected. It promises much in the emerging spectrum reallocation or LSA operation in forthcoming 5G systems. The proposed antenna was prototyped and tested to validate the concept.

Chapter 10 presents the conclusions of this thesis and is followed by some recommendations for future research.

Chapter 2

Background Overview and Related Work

2.1 Introduction

This chapter firstly discusses the frequency bands allocated for 3G and 4G mobile communications. Also, the bands under review are looked at, and proposed for 4G advanced, and future 5G mobile communications. Secondly, the chapter reviews developments related to LTE/WWAN antennas focusing on mobile device applications. Thirdly, it reviews up to date progress on the design and development of 5G mobile antennas, focusing on 28 GHz millimeter-wave band since. This thesis unable to review antennas for licensed shared access (LSA) band since there is no antenna has been reported in the literature to date to cover this band. Antennas with fixed beam and beam switching capability, related to 5G mobile devices, are also discussed. Fourthly and finally, it summarizes the limitations of mobile device antennas and suggests a scope for further development.

This chapter is organized as follows. Section 2.2 presents a summary of the frequency bands needed to be covered by future mobile device antennas. Section 2.3 reviews different

types of antenna geometry developed for LTE/WWAN mobile device applications, and Section 2.4 reviews the frequency ranges covered by the developed antennas and their radiation properties for the LTE/WWAN operation. Section 2.5 reviews different types of antennas (fixed beam and beam switching) studied in the literature for 28 GHz millimeter-wave 5G mobile devices. Section 2.6 presents a brief study on power consumed by different components of a smartphone. Section 2.7 briefly studied the antennas uses superstrate as a dielectric load to improve the performance of the antenna. A brief study is presented on leaky-wave antenna (LWA) focusing on half-width microstrip line concept for beam scanning in Section 2.8. The limitations of antennas reported for 4G and 5G mobile devices and scope for the future development are briefly presented in Section 2.9.

2.2 3G, 4G, and 5G Frequency Bands

This section, firstly, presents a summary of the frequency bands that are covered by 3G and 4G mobile communication systems. These bands are broadly named referred to as long-term evolution (LTE), global system for mobile communications (GSM), digital cellular systems (DCS), personal communications service (PCS), and universal mobile telecommunications service (UMTS). Secondly, a list of the frequency bands that are under consideration for future 5G mobile communications is mentioned here.

Table 2.1: GSM, DCS, and PCS frequency bands.

Band	Frequency Range (MHz)
GSM850	824-894
GSM900	880-960
GSM1800/DCS1800	1710-1880
GSM1900/PCS1900	1850-1990

The frequency bands used for GSM, DCS and PCS operation are summarized in Table 2.1 [4, 76–79] and these bands are covered by 1G to 4G mobile devices. In order to cover the listed bands a mobile device antenna with the bandwidths of 136 MHz (824-960) and 280 MHz (1710-1990 MHz) are required.

Table 2.2: FDD-UMTS frequency bands.

Band No.	Frequency Range (MHz)	Band No.	Frequency Range(MHz)
1	1920-2170	2	1850-1990
3	1710-1880	4	1710-2155
5	824-894	6	830-885
7	2500-2690	8	880-960
9	1749-1880	10	1710-2170
11	1427-1496	12	699-746
13	746-787	14	758-798
19	832-888	20	791-862
21	1447-1511	22	3410-3590
25	1850-1995	26	814-894

The UMTS frequency bands are used by the 3G mobile communications. There are two broad categories of UMTS bands based on the type of duplexing used in communications: one is frequency division duplex (FDD)-UMTS and the other is time division duplex (TDD)-UMTS bands. FDD-UMTS contains 26 sub-bands, where bands numbered 15, 16, 17, 18, 23 and 24 were reserved frequency bands, and TDD-UMTS contains 8 sub-bands [80–82]. Table 2.2 and Table 2.3 list the FDD-UMTS and TDD-UMTS bands proposed for 3G mobile communications [80–82]. Therefore, a mobile device antenna with the bandwidths of 261 MHz (699-960 MHZ), 1263 MHz (1427-2690 MHz), and 180

MHz (3410-3590 MHz) are required in order to cover the greater FDD-UMTS and TDD-UMTS bands.

Table 2.3: TDD-UMTS frequency bands.

Band No.	Frequency Range (MHz)
A Lower	1900-1920
A Upper	2010-2025
B Lower	1850-1910
B Upper	1930-1990
C	1910-1930
D	2570-2620
E	2300-2400
F	1880-1920

Table 2.4: FDD-LTE and LTE advanced frequency bands.

LTE/LTE-Advanced Band	Frequency Range (MHz)	LTE/LTE-Advanced Band	Frequency Range (MHz)
1	1920-2170	2	1850-1990
3	1710-1880	4	1710-2155
5	824-894	6	830-885
7	2500-2690	8	880-960
9	1749-1880	10	1710-2170
11	1427-1496	12	699-746
13	746-787	14	758-798
17	704-746	18	815-875
19	830-890	20	791-862
21	1447-1511	22	3410-3590
23	2000-2200	24	1525-1661
25	1850-1995	26	814-894
27	807-869	28	703-803
29	717-728	30	2305-2360
31	452-468	32	1452-1496
65	1920-2200	66	1710-2200
67	738-758	68	698-783
69	2570-2620	70	1695-2020

Similar to the UMTS band, the long-term evolution (LTE)/evolved-universal terrestrial access network (E-UTRAN) and LTE advanced/evolved-universal terrestrial access (E-UTRA) bands are broadly categorized as FDD-LTE and TDD-LTE bands [3, 4, 7, 8]. These FDD-LTE and TDD-LTE bands contain 38 FDD-LTE and 16 TDD-LTE sub-bands,

respectively, and they are listed in Table 2.4 and Table 2.5, respectively. These bands are used in 4G mobile communications and beyond.

Table 2.5: TDD-LTE and LTE advanced frequency bands.

LTE/LTE-Advanced Band	Frequency Range (MHz)	LTE/LTE-Advanced Band	Frequency Range (MHz)
33	1900-1920	34	2010-2025
35	1850-1910	36	1930-1990
37	1910-1930	38	2570-2620
39	1880-1920	40	2300-2400
41	2496-2690	42	3400-3600
43	3600-3800	44	703-803
45	1447-1467	46	5150-5925
47	5855-5925	48	3550-3700

This section study the frequency bands under consideration for future 5G mobile communications. In Europe, a 1.5 GHz (1452-1492 MHz) band and a 2.3 GHz (2300-2400 MHz) band have been allocated for licensed shared access (LSA) services by the European Commission [28, 29, 83]. It should be noted that LSA is a new cognitive radio technology reported for 5G mobile communications. These are the bands allocated below 6 GHz for future 5G. However, a 1.5 GHz (28 - 29.5 GHz) of bandwidth is available at around 28 GHz for 5G communication [1, 15]. Also, in the United States, the Federal Communications Commission (FCC), which was created by statute to regulate interstate communications by radio, television, wire, satellite, and cable, allocated 11 GHz of spectrum for future 5G networks and technologies where 3.85 GHz spectrum for licensed use and 7 GHz for unlicensed used [33]. The allocated bands are listed below:

- Licensed use: 27.5-28.35, 37-38.6 and 38.6-40 GHz,
- Unlicensed use: 64-71 GHz,
- Shared access: 37-37.6 GHz.

In addition, in world radiocommunication conference (WRC)-15 several regional organisations established a new agenda item for WRC-19 to consider the identification of frequency bands for international mobile telecommunications in the frequency range 6 to 100 GHz [30]. The spectrum above 6 GHz will be agreed at WRC-19 under agenda item 1.13 which is considering following provisional bands 24.25-27.5, 31.8-33.4, 37-43.5, 45.5-50.2, 50.4-52.6, 66-76, and 81-86 GHz for future 5G. However, 28 GHz band is of particular interest of United States and has been approved for 5G use while Japan and Korea are closely examining this frequency band for 5G [31, 32]. This 28 GHz band will be the complement of 24 GHz band which is being studied at WRC-19. Since, the 28 GHz band already allocated in one country for 5G mobile communications, couple of other countries are studying this band while Samsung, Huawei and several research group around the world already started developing prototype for this 28 GHz band [15, 31–33], this thesis consider all 28 GHz bands for developing antennas for future 5G mobile devices.

The standardisation of 5G is an on-going effort and significant industry research is devoted to find out a good set of requirements in order to ensure a balance between implementation complexity, system performance and flexibility [84, 85]. The major high level requirements for 5G are given below:

- Bandwidth: 100 MHz (minimum) and 1000 MHz (maximum)
- Data rate: 1-10 Gbps,
- Latency: under 1 ms,
- Capacity expansion: by a factor of 1000.

Table 2.6: Frequency ranges required to be covered by future mobile device antennas and their title/name called in the rest of this thesis.

Frequency Range	Title in this Thesis
452-468 MHz	Very-low-LTE
698-960 MHz	Low-LTE
1427-2690 MHz	Mid-LTE
3400-3800 MHz	High-LTE
5150-5925 MHz	Very-high-LTE
1452-1492 MHz	1.5 GHz LSA
2300-2400 MHz	2.3 GHz LSA
28-29.5 GHz*	28 GHz millimeter-wave
27.5-28.35 GHz*	28 GHz millimeter-wave

*All frequency ranges that are proposed for 28 GHz millimeter-wave band for forthcoming 5G mobile communications are considered.

Overall, future mobile device's antennas will need to cover the frequency ranges listed in Table 2.6 in order to have coverage for all allocated and proposed bands (LSA, millimeter-wave, GSM, UMTS, and LTE/LTE-advanced). In other words they have to on a mobile device suitable for 3G, 4G, 4G-advanced, and 5G operations.

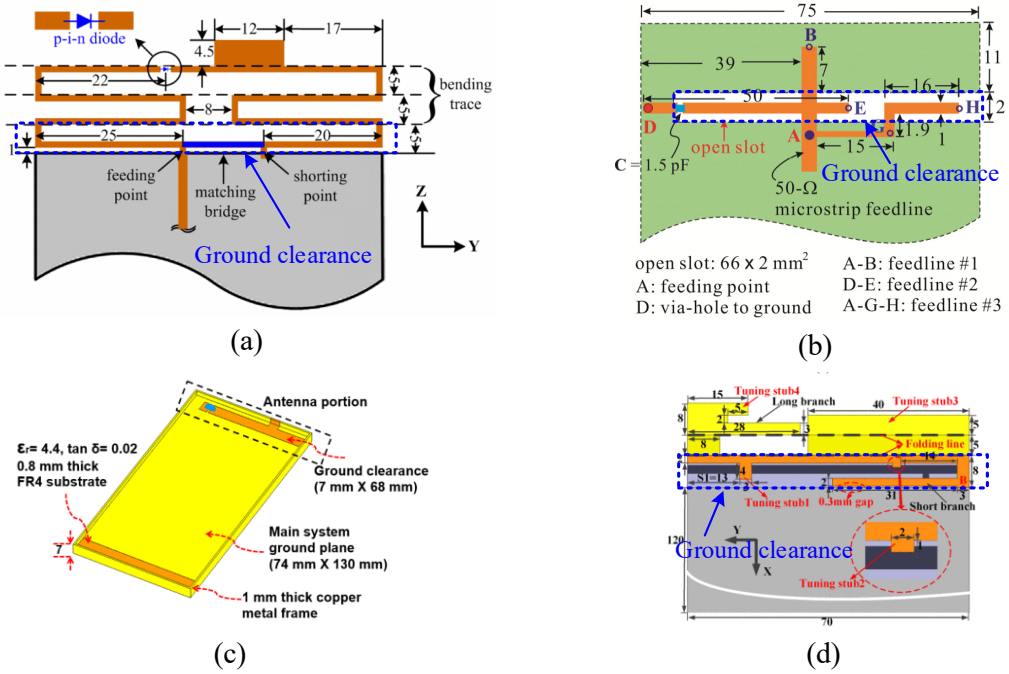

Figure 2.1: Different shapes of ground clearance used in LTE/WWAN mobile device antenna (a) presented in [86], (b) presented in [87], (c) presented in [88], and (d) presented in [89].

2.3 Configuration of Antennas for LTE/WWAN Mobile Devices

In recent mobile devices two types of antennas have been used: one is the planar inverted-F antenna (PIFA) and the other is the planar monopole antenna (PMA) [77,90,91]. In this thesis, a planar microstrip antenna with at least one ground connection is considered to be a PIFA. A planar microstrip antenna without ground connection together with or without an inductive/capacitive parasitic element (with or without ground connection) loaded to the antenna is considered to be a PMA. The following two sub-sections briefly present the above mentioned PIFA and PMA. All of the reported antennas have a ground clearance

beneath the antenna structure that helps to achieve the omnidirectional radiation from the antenna. An example of such ground clearance is shown in Fig. 2.1

This section firstly discussed about the fundamental equations related to the design of PIFA and PMA, secondly, discussed different types of PIFA and PMA reported in the literature. The configuration of the shorted patch antenna is shown in Fig. 2.2 (a). When the shorting pin is absent the microstrip patch antenna usually operate in the half-wavelength mode. The fundamental first resonance frequency of the rectangular patch based on cavity-model approximation can be calculated as [77, 91, 92]

$$f_{10} = \frac{c}{2L\sqrt{\epsilon_r}} \tag{2.1}$$

where f_{10} resonant frequency of the TM_{10} mode and c speed of light. Fig. 2.2 (b) shows the geometry of a planar inverted-L patch with a inserted slit of length l. The first resonant frequency of the planar inverted-L patch is calculated as

$$f_1 = \frac{c}{4(L+h)} \tag{2.2}$$

which is operating in the quarter-wavelength mode. The reduction of the length can be achieved by meandering the line or creating different shaped slots within the patch while having at least one shorting pin.

The impedance matching of a PIFA can be controlled by controlling the distance D between the shorting pin and feed point, shown in Fig. 2.3. The resonant length of this PIFA can be approximated as

$$L_1 + L_2 - W = \frac{\lambda}{4} \tag{2.3}$$

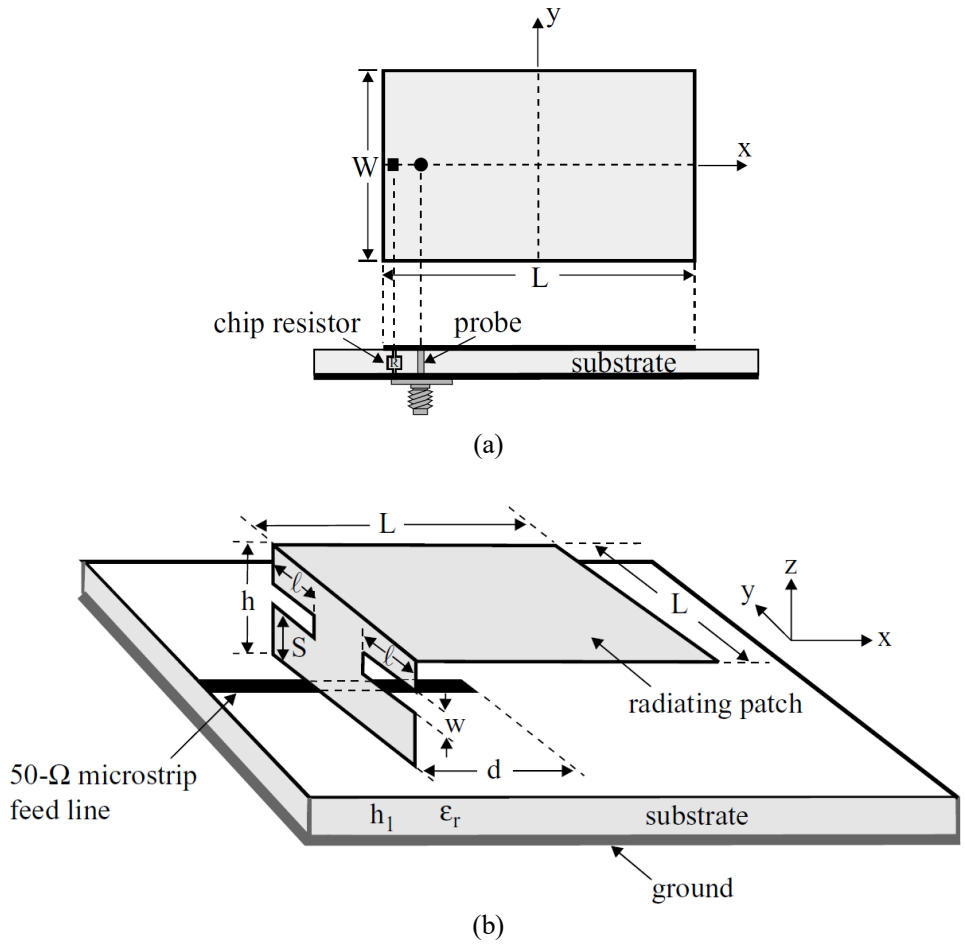

Figure 2.2: Geometry of a (a) compact microstrip antenna with a shorting pin, and (b) planar inverted-L patch antenna [91].

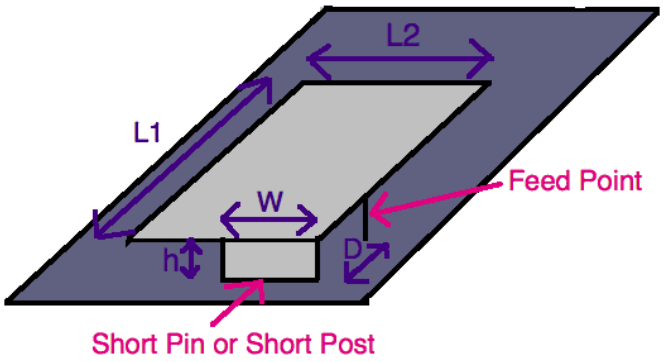

Figure 2.3: Geometry of a PIFA with shorting plane [93].

2.3.1 Planar Inverted-F Antenna (PIFA)

PIFA is widely used in mobile device applications because of its compact size and omnidirectional radiation [77, 91]. A PIFA consists of a planar structure with at least one ground connection.

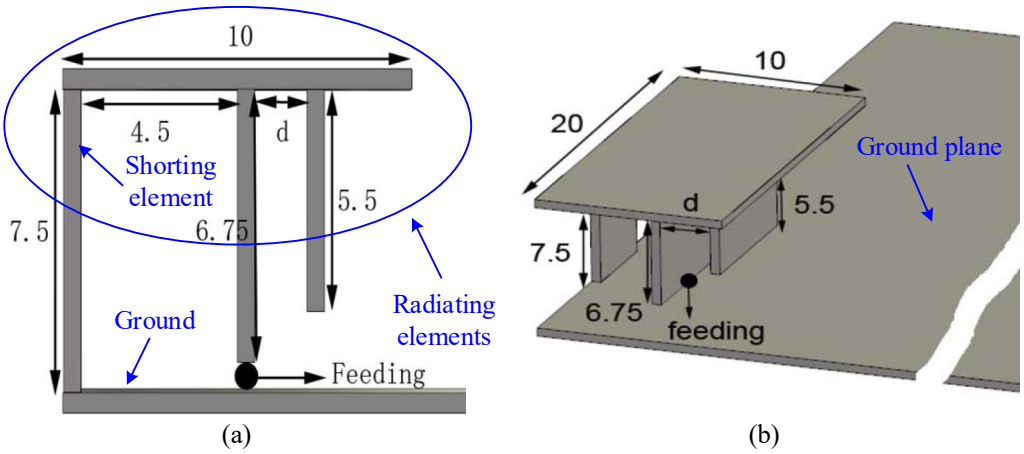

Figure 2.4: Geometry of an ultra-wideband PIFA for wireless applications (a) side view, and (b) perspective view [94].

Firstly, the study of a basic geometry of the PIFA for wireless communication application having a radiator of planar inverted-F shape loaded with a non-grounded rectangular element (parallel to the feed strip or shorting strip) is presented. An example is shown in Fig. 2.4. The simulated and measured reflection coefficient together with the simulated current distributions are shown in Fig. 2.5 of the antenna (see Fig. 2.4). The antenna resonating in the $\lambda/4$ modes at four frequencies (3.4, 6.6, 9 and 12.5 GHz) were verified through current distributions and from the length of the electrical path followed by the current distributions.

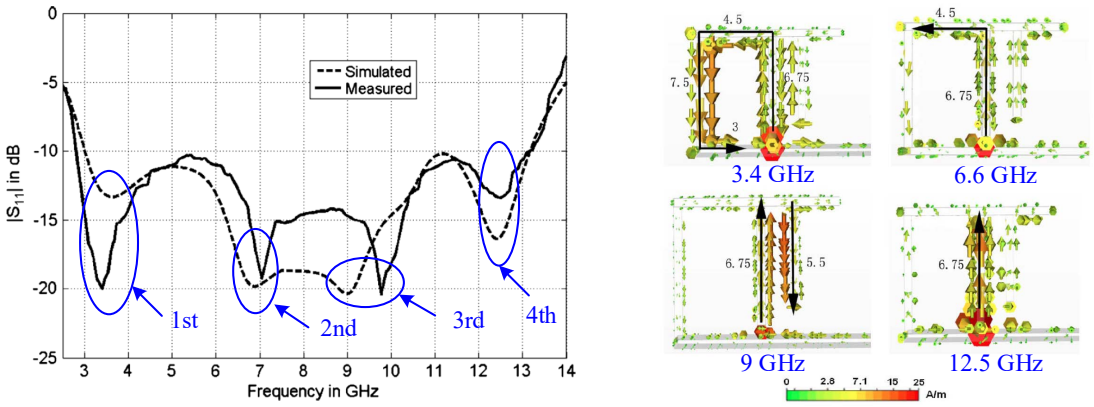

(a) (b)

Figure 2.5: Reflection coefficient and current distributions of the ultra-wideband PIFA for wireless applications (a) reflection coefficient, and (b) current distribution [94].

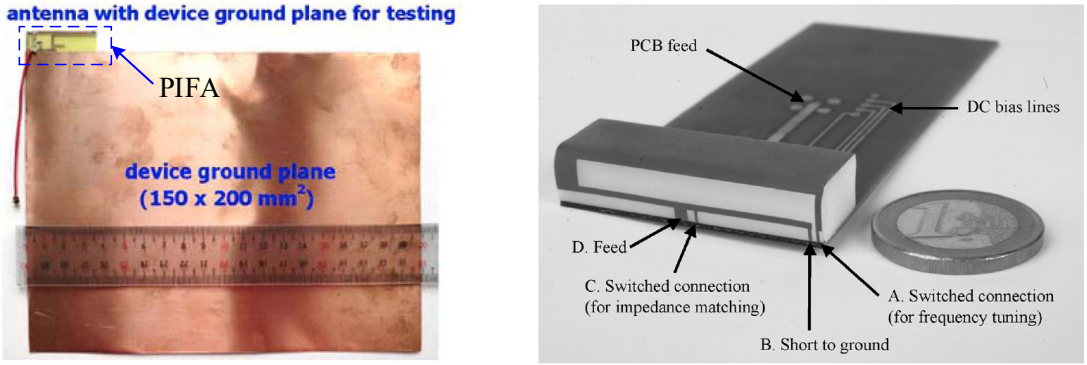

(a) (b)

Figure 2.6: The placement of the PIFA with respect to the ground plane of the mobile devices reported for mobile device applications where the PIFA and the ground plane are on the (a) same side of the substrate [73], and (b) the opposite side of the substrate [95].

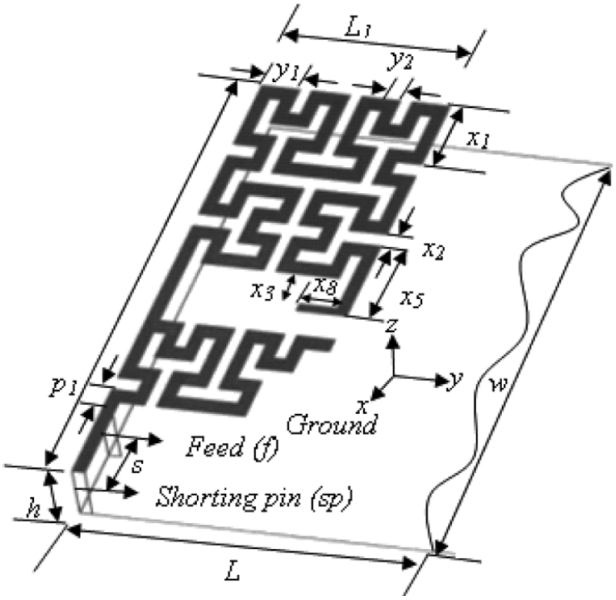

Figure 2.7: Geometry of the Hilbert PIFA for dual-band mobile devices [96].

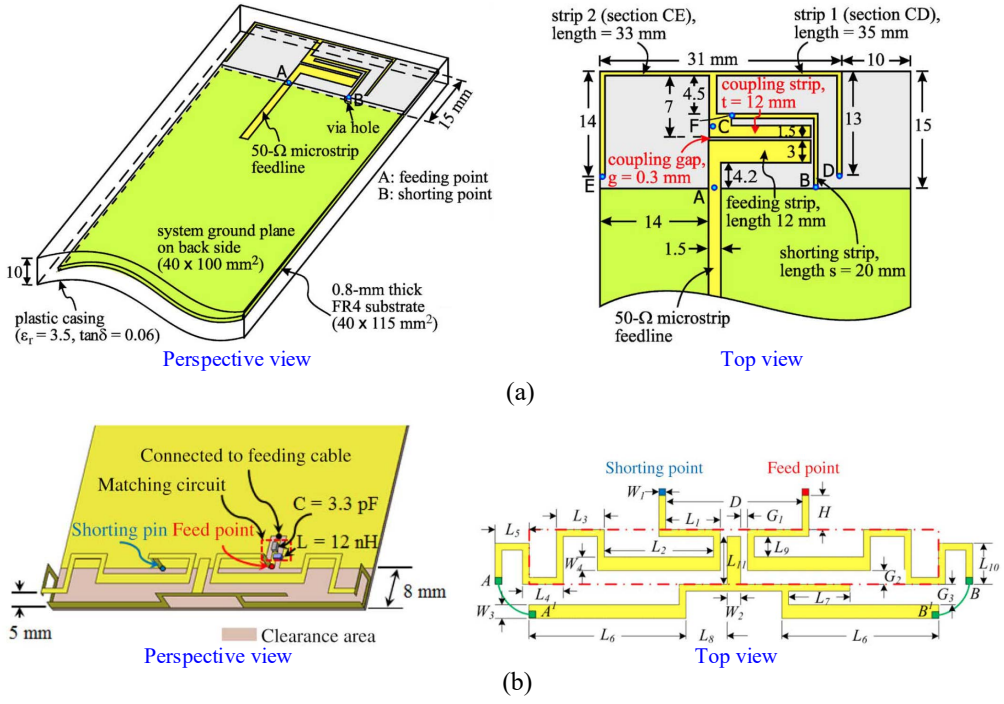

Figure 2.8: Geometry of the dual-band PIFA for mobile handset with single grounding point: (a) without vertical plate [97], and (b) with vertical plate [61].

The PIFA and the ground plane of the mobile device are placed either on the same side of the substrate [61, 73] or the opposite side [63, 95] as shown in Fig 2.6. Now, different types of geometry of the PIFA reported for mobile device applications are discussed. In early 2005, a dual-band Hilbert PIFA for mobile devices applications was reported as covering the GSM900 and GSM1900 bands [96]. Using the Hilbert profile the length of the current flow path decreases effectively, thus resulting in a compact antenna. The geometry of the Hilbert PIFA is shown in Fig. 2.7.

The PIFA with or without vertical plate and having one shorting point either operating in the single resonant mode [98] or multi-resonant mode [61], has been reported in the literature. The geometry of a dual-band PIFA with one shorting point is shown in Fig.2.8. It is also possible to design dual-band and triple-band PIFA with two shorting points [62, 63, 73, 99]. Of these, the geometry presented in [62, 63, 73] has a vertical plate while the antenna presented in [99] does not have any vertical plate. The geometry of a dual-band and a triple-band PIFA with two shorting points is illustrated in Fig. 2.9.

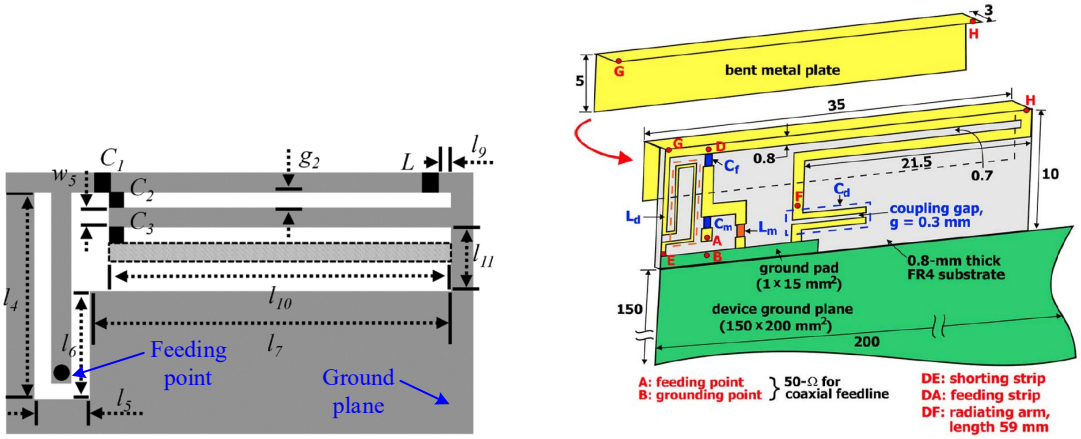

Figure 2.9: Geometry of the PIFA for mobile handset with two grounding points (a) dual-band antenna without vertical plate [99], and (b) triple-band antenna with vertical plate [73].

2.3.2 Planar Monopole Antenna (PMA)

A PIFA without a ground connection or shorting point is known as PMA. This section presents the configuration of different types of PMA reported for mobile device applications. A planar microstrip as a radiating element loaded with an inductively/capacitively coupled parasitic element is also considered as a PMA in this thesis.

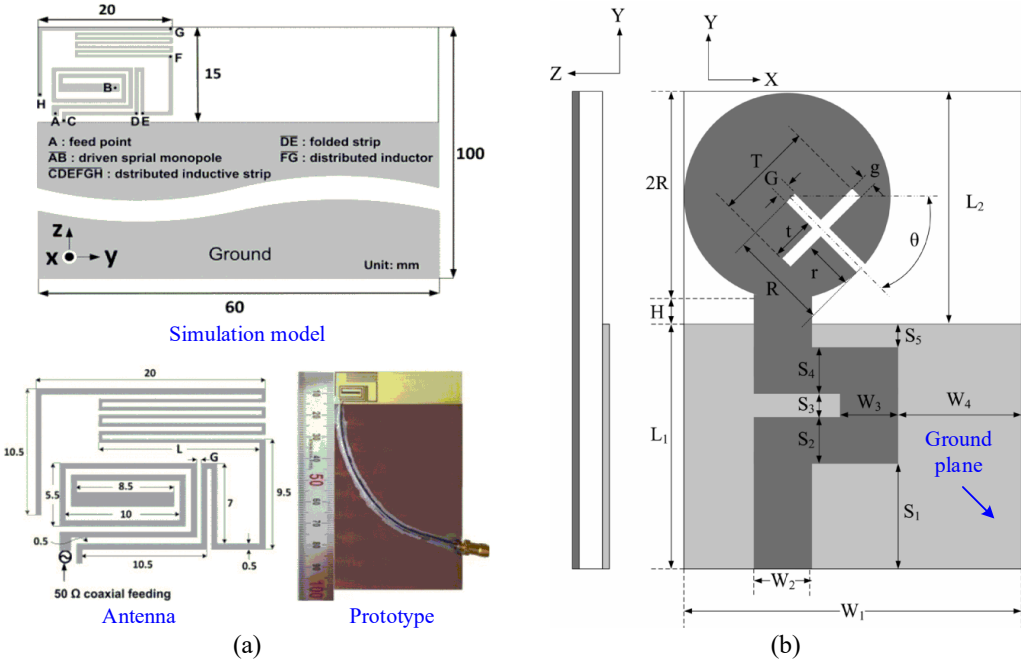

Figure 2.10: The placement of the PMA with respect to the ground plane of the mobile device reported for mobile device applications where the PMA and the ground plane are on the (a) same side of the substrate [100], and (b) the opposite side of the substrate [101].

Considering the placement of the antenna element with respect to the ground plane there are two types of PMA reported for mobile devices. One is the antenna element and the ground plane is on the same side of the substrate [100] while the other is the antenna element. The ground plane is on opposite sides of the substrate [101]. The configurations of these two types of antennas are depicted in Fig. 2.10.

PMAs with a ground cooperative structure have been reported in the literature and

it has been reported they achieve dual-band and triple-band operation; they are suitable for LTE/WWAN mobile devices [68, 74, 102]. These types of PMAs have two geometry components: one component is slotted monopole printed on the front side of the substrate where feeding is provided; and the other component comprises slotted strips connected to the ground on the back side of the substrate. One of the reported antenna's configuration of this type is shown in Fig. 2.11 (a).

Also, dual-band and triple-band PMAs with a vertical plate have been proposed for LTE/WWAN mobile devices [67, 72]. These types of PMAs have a planar microstrip element loaded with a vertical plate of a different shape and do not have parasitic element connected to the ground plane. A PMA loaded with an L-shaped vertical plate reported for octa-band LTE/WWAN mobile devices is shown in Fig. 2.11 (b).

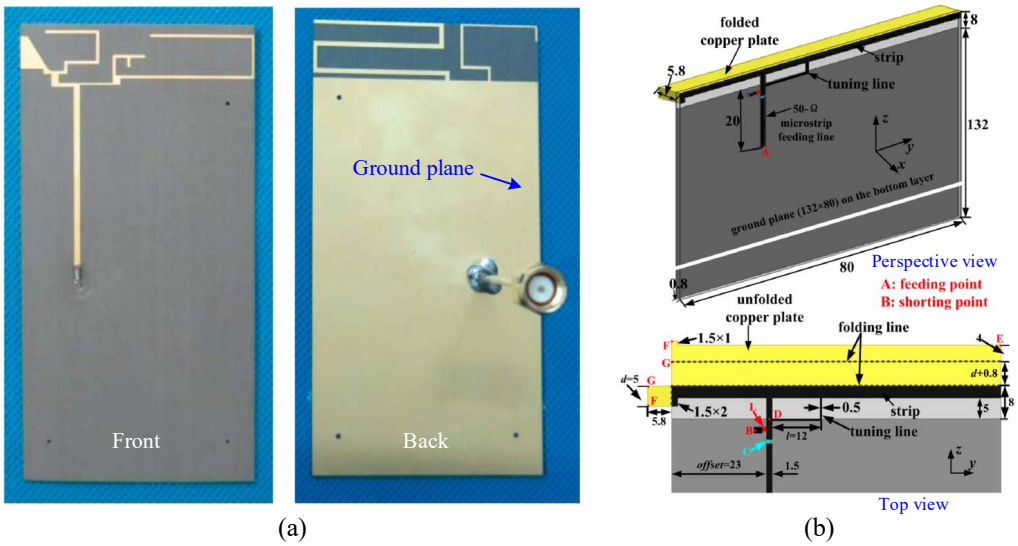

Figure 2.11: The PMA with (a) ground cooperative structure [101], and (b) vertical plate [67].

Another type of PMA has been studied in the literature where a PMA is loaded with an inductive/capacitively coupled parasitic element which is connected to the ground plane [64–66, 103]. In this type of design the PMA composed of a planar microstrip

antenna is connected to the feed. A parasitic element connected to the ground is placed on the same side of the substrate as shown in Fig 2.12.

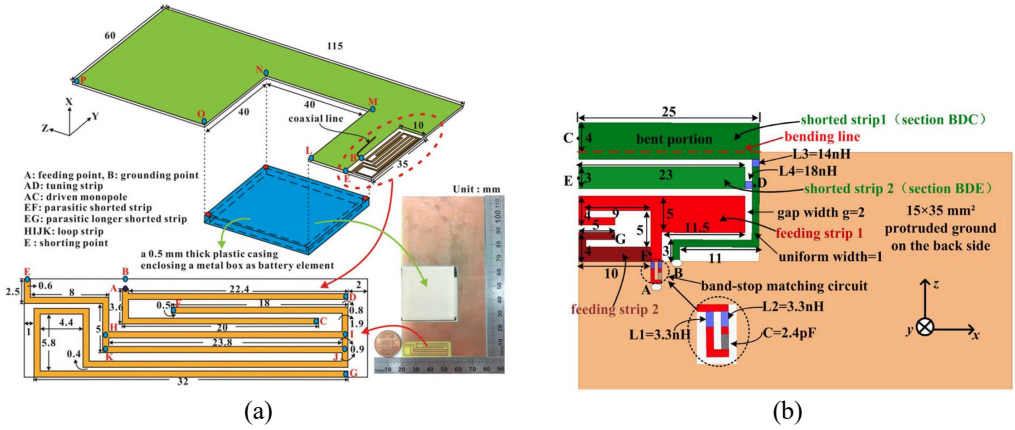

Figure 2.12: Inductive/capacitively loaded PMA's for LTE/WWAN mobile device applications (a) reported in [64], and (b) reported in [66].

The above mentioned PMA's for LTE/WWAN mobile devices employ single port feeding to excite the antenna. Also, two-port PMA has been studied for mobile device applications [69,71]. Here, the antenna presented in [69] is embedded in the ground plane on the back surface of the substrate and the antenna presented in [71] has a direct feed matching network and a gap coupled feed matching network (both feed together called hybrid feed network), as shown in Fig. 2.13.

For LTE/WWAN mobile devices, the performance of a PMA with a dielectric resonator antenna has been analyzed using either dielectric as a part of the feed network [104] or the microstrip printed on a magneto-dielectric material [70]. PMAs with dielectric material for mobile devices are shown in Fig. 2.14.

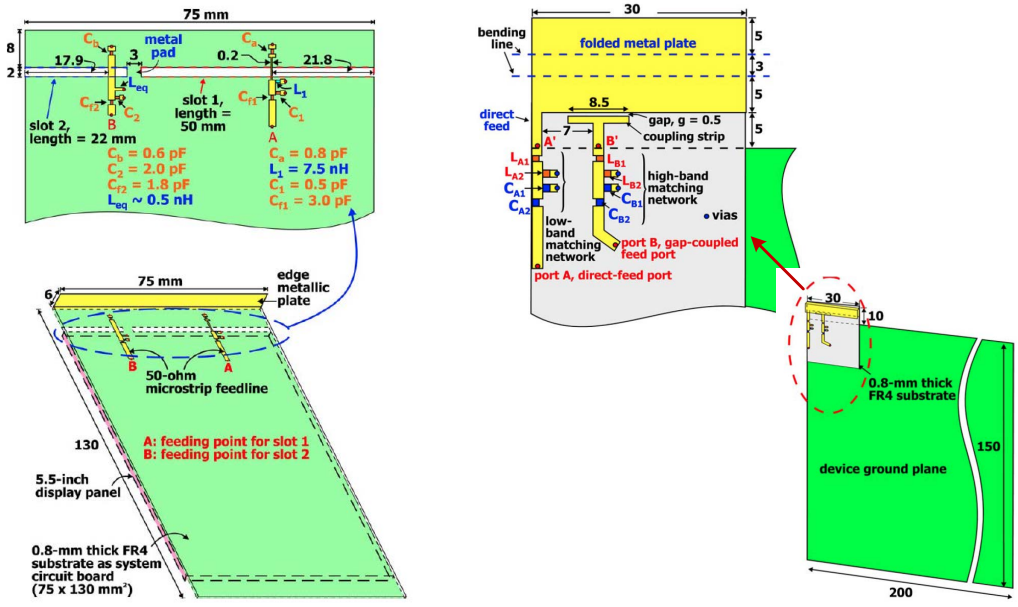

Figure 2.13: Dual-port PMA's for LTE/WWAN mobile device applications (a) ground cooperative antenna [69], and (b) hybrid feed antenna [71].

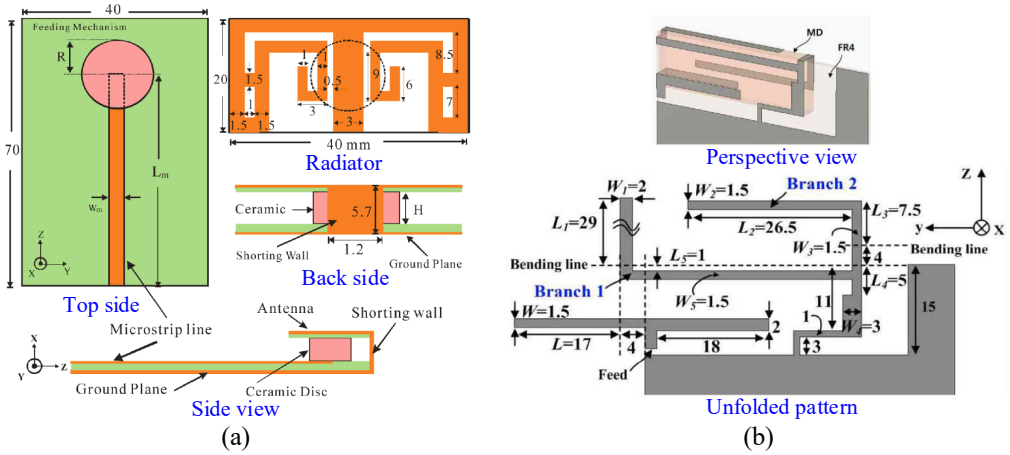

Figure 2.14: The dielectric PMA's where (a) the dielectric material is part of the feed network [104], and (b) the PMA printed on a magneto-dielectric material [70].

2.4 Operating Bands and Radiation Patterns of the LTE/WWAN Mobile Device Antennas

This section presents a brief analysis of antennas reported for LTE/WWAN mobile device applications, focusing on achieved operating bands and their radiation pattern characteristics. The dual band PIFA's proposed for mobile device application operating in the $\lambda/8$ [97], $\lambda/4$ [98], or multi-resonant ($\lambda/2$, λ, $3\lambda/2$) [61] modes cover two frequency ranges: firstly, 770-1080 MHz (maximum coverage achieved at the first operating band by the design presented in [61]); and secondly, 1710-2700 MHz (maximum coverage achieved at the second operating band from according to the design presented in [98]). The radiation patterns achieved from these designs reveal good omnidirectional patterns in the first operating band and nearly omnidirectional at the frequency close to the lower frequency limit of the second operating band. However, a null in the radiation pattern is observed at the frequency close to the upper frequency limit of the second operating band, as shown in Fig. 2.15.

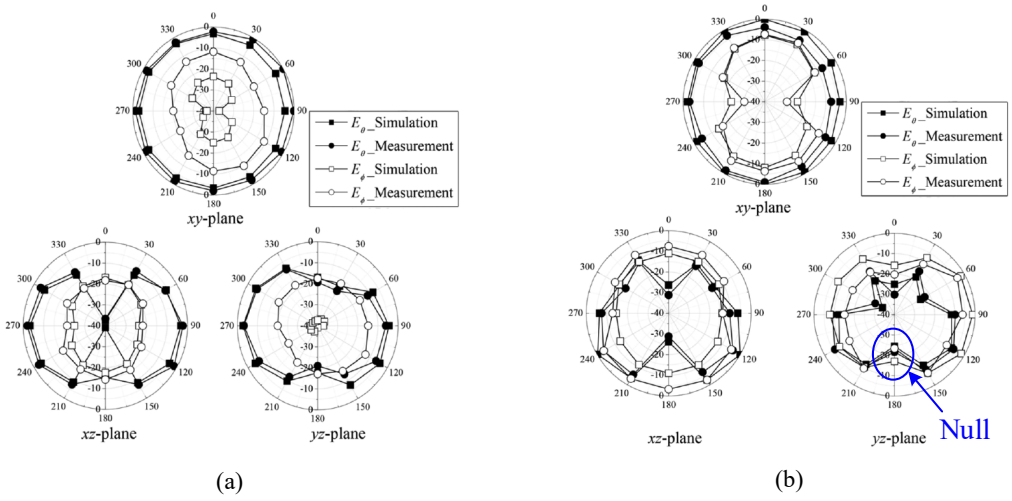

Figure 2.15: Radiation patterns of a heptaband PIFA with independent resonance control for mobile handset applications at (a) 872, and (b) 2120 MHz [98].

A multi-resonance feed structure (input impedance matching circuit) used with PIFA to achieve dual and wide operating bands for LTE/WWAN mobile devices covers 694-1003/1656-2772 MHz from the design presented in [62] and covers 698-960/1710-2690 MHz from the design presented in [63]. These antennas provide omnidirectional radiation in the first frequency range but in the second frequency range the antennas have nearly omnidirectional radiation patterns close to the frequency 1710 MHz. As well as, they have almost directed radiation with nulls at the frequency close to the 2690 MHz, as depicted in Fig. 2.16. It is evident that nulls in the radiation patterns can be observed at a frequency close to the upper frequency limit of the second frequency range while frequency reconfigurable design has been studied [105] (page 474, Fig. 7), [99] (page 515, Fig. 18).

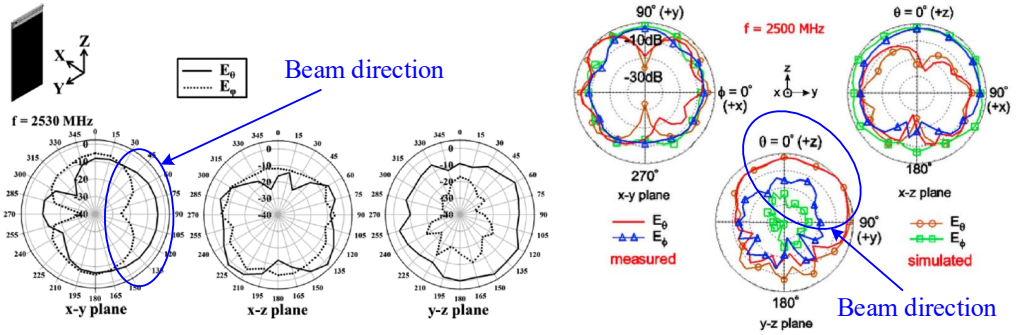

Figure 2.16: Nearly directed radiation patterns from the reported PIFA antennas at the frequency (a) 2530 MHz [62], and (b) 2500 MHz [63].

The above mentioned different types of PIFA are able to cover two frequency bands, i.e. low-LTE band and part of the mid-LTE band. Triple band PIFA has been proposed for mobile device applications [73] and the antennas cover low, part of mid, and high-LTE bands. Similar to the previous antennas, the antenna has nearly omnidirectional radiation at the low-LTE band, and one and two nulls are observed in the mid and high-LTE bands, respectively, as indicated in Fig. 2.17. Therefore, either PIFA with input

impedance matching circuit or PIFA with multiple elements reported to cover dual-band or triple-band has null in the radiation patterns at the frequency close to the upper frequency limit of the mid-LTE band and in the whole high-LTE band.

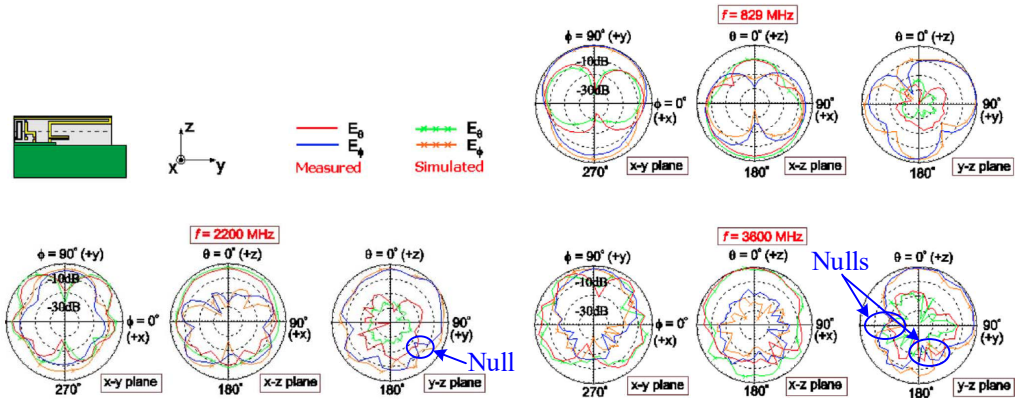

Figure 2.17: Radiation patterns of a triple-wideband antenna to cover low, part of mid, and high-LTE bands [73].

Now the PMA has been reported in the literature for mobile device applications are investigated. Using ground cooperative structure with PMA it is possible to achieve a dual-operating band that covers low-LTE and part of the mid-LTE bands [68, 102], while the triple band can cover low, part of mid, and high-LTE bands [74]. The maximum coverage achieved by the antenna is reported in [74] and the achieved frequency ranges are 790-1061, 1650-2775, and 3132-6382 MHz. These reported antennas have nearly omnidirectional radiation at low-LTE band and at a frequency close to 1650 MHz. Yet nulls in the radiation patterns are observed at the frequency close to the upper frequency limit of the mid-LTE band and at whole high-LTE band, as shown in Fig. 2.18. As well, a PMA with a ground cooperative structure has been shown in one study to widen the low frequency range, while the antenna covers TV white spaces and digital television bands with an operating bandwidth of 470-860 MHz [106]. However, two nulls in the radiation patterns are observed at 850 MHz, shown in [106] (page 4005).

The PMA with a vertical plate has been investigated for mobile phone applications where antenna in [67] has two operating bands (690-980, 1630-2740 MHz) and antenna in [72] has three operating bands (700-960, 1710-2690, and 3400-3600 MHz). These antennas do not completely cover the mid and high-LTE bands.

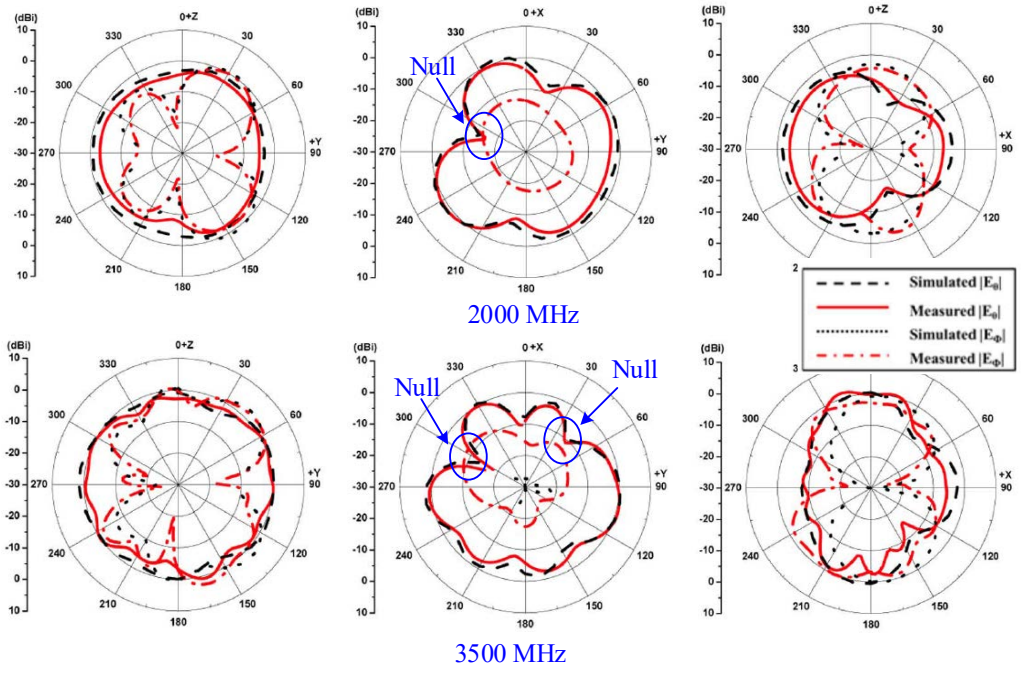

Figure 2.18: Radiation patterns of a triple-band monopole antenna with ground cooperative structure to cover low, part of mid, and high-LTE bands [74].

Using a capacitively/inductively coupled loading element to the PMA has been the subject of studies on mobile devices [64–66,103]. These antennas have dual-band and cover the low-LTE band completely except the antenna reported in [103]. However, all the reported PMAs with loading elements are unable to cover the mid-LTE band completely. The maximum coverage achieved by the design is presented in [64] and the achieved bandwidths are 691-968 and 1554-2730 MHz. Similar to the other reported PMAs, nulls in the radiation patterns are observed at the mid-LTE band for these capacitively/inductively loaded PMAs, as illustrated in Fig. 2.19 (a).

Dual-wideband PMAs have been studied where hybrid feed antenna [71] and ground cooperative antenna [69] are presented. However, these antennas are able to cover low and part of mid-LTE bands and unable to cover completely the high-LTE band. Also, nulls in the radiation patterns are observed at 2600 MHz, as shown in Fig. 2.19 (b).

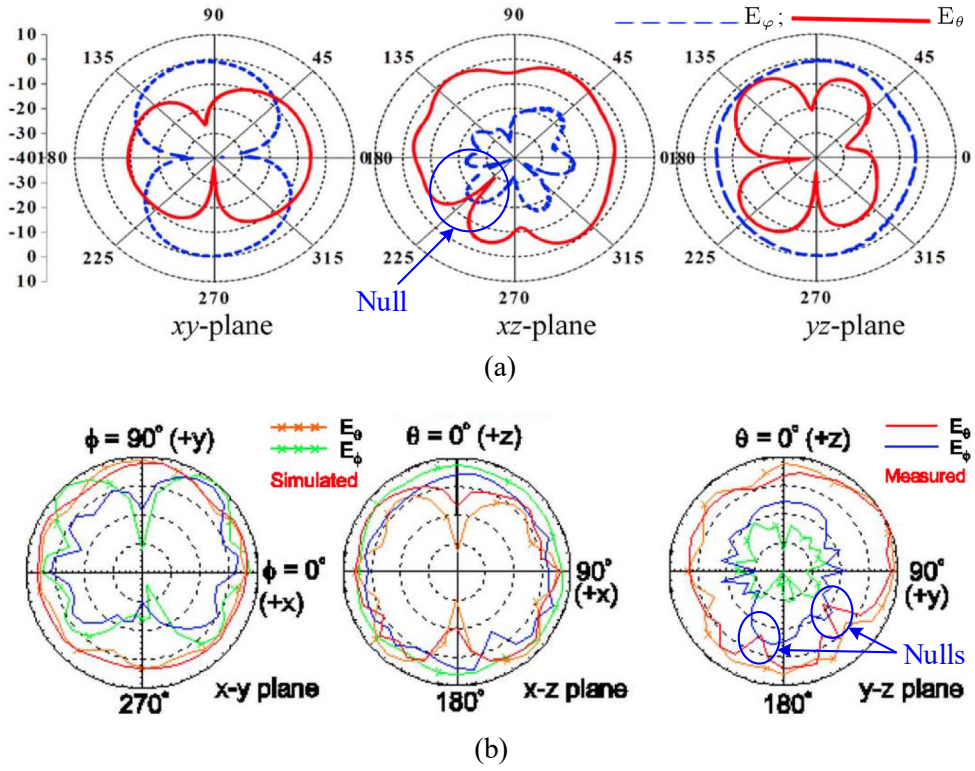

Figure 2.19: Radiation patterns of a (a) capacitively/inductively loaded monopole antenna at 2650 MHz [64], and (b) dual-port PMA at 2600 MHz [71].

Antenna researchers are trying to achieve triple band operation from a LTE/WWAN mobile antenna to cover the low, part of the mid, and high-LTE bands. They are also attempting to widen the operating bandwidth of the antenna in order to cover newly allocated frequency ranges for 4G and 4G advanced mobile communication. Recently, a tunable handset antenna reported in [107] to cover the TV white space has greater bandwidths of 578-831, 1756-2312, and 2501-2586 MHz. A loop antenna with six resonant

modes investigated for LTE smartphone in [75] has four wide operating bandwidths of 660-1100, 1710-3020, 3370-3900, and 5150-5850 MHz. However, nulls in the radiation patterns are observed at 2560, 3640, and 5345 MHz, as reported in [75] (page 3748).

Therefore, all the antennas reported for LTE mobile devices are unable to completely cover the low, mid and high-LTE bands (listed in Table 2.6). All the reported antennas utilize a single antenna with single feed or single antenna with dual feed to cover low, part of mid and high-LTE bands. These above discussed reported antennas have good omnidirectional radiation in the low-LTE band, and nearly omnidirectional radiation patterns at a frequency close to 1700 MHz in the mid-LTE band. However, in those designs there are nulls in the radiation patterns which have been observed at the frequency close to 2600 MHz in the mid-LTE band, and also in the entire high-LTE band.

2.5 Antennas for Millimeter-Wave 5G Mobile Devices

This section discusses different types of antennas reported for 28 GHz millimeter-wave 5G mobile devices. It is obvious that a wideband, highly directive antenna with high efficiency is required for mobile devices to mitigate the path loss. Since the 5G standards for mobile device antenna have not as yet been finalized, there are different topologies that have been developed by antenna researchers for the mobile devices. These include, for example, an antenna with single directed beam [51] or an antenna with pattern reconfigurable capability [15].

2.5.1 Fixed Beam Antenna

Different types of antennas with a single directed beam have been studied for 28 GHz millimeter-wave communications, for instance patch antenna [41], printed slot antenna [42],

and printed slot array [43–45], and geometry of three antennas are shown in Fig. 2.20. The slot array reported in [43] has wide beamwidth of 180° but the size of the antenna is big enough to hold 10% space of a 120 mm × 70 mm mobile phone. In addition, Huygens source antenna investigated in [46] was undertaken to verify its suitability for future 5G mobile communications. The achieved peak gain is 4 dBi.

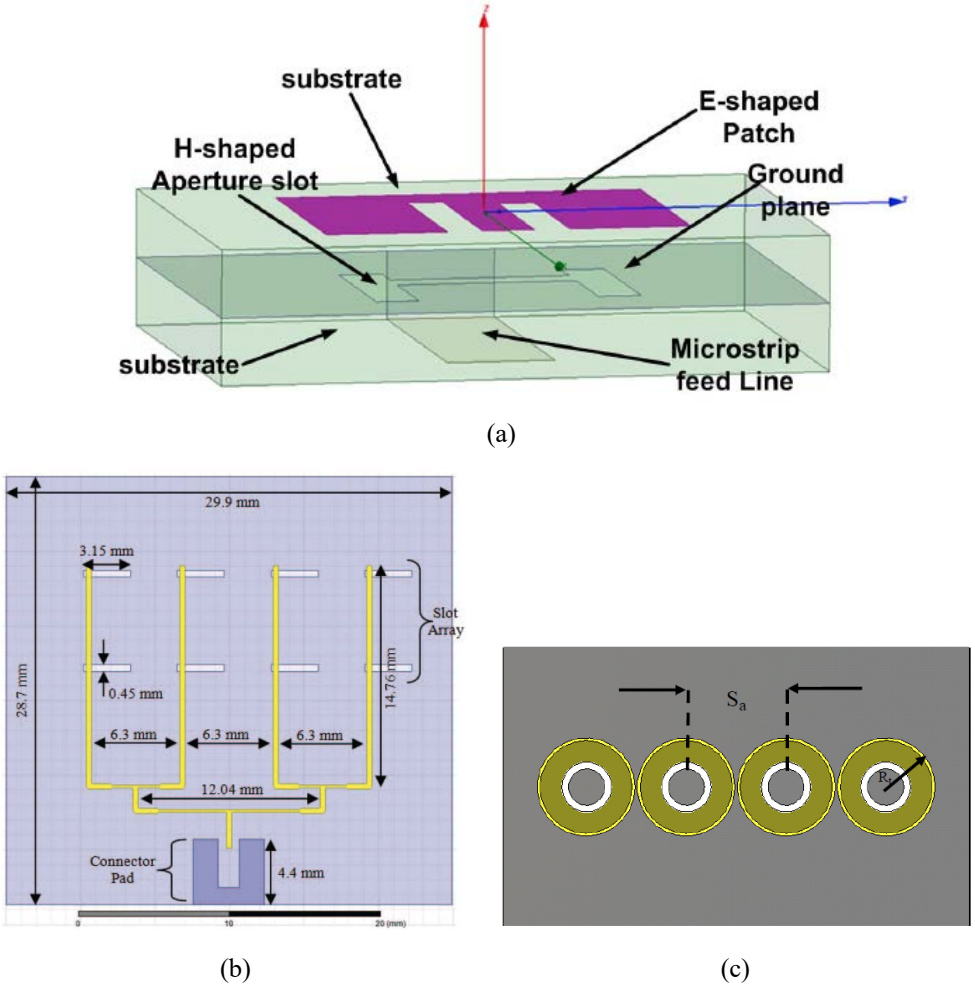

Figure 2.20: Geometry of (a) E-shaped patch antenna [41], (b) slot array [43], and (c) 4-elements array [45].

Planar grid array, a kind of 2-D array, antenna has been studied for 28 GHz millimeter-wave band to achieve boresight radiation [47]. Another 2-D array based on Franklin

antenna has been investigated for the same applications [17]. The geometry of these two types of 2-D array are shown in Fig. 2.21.

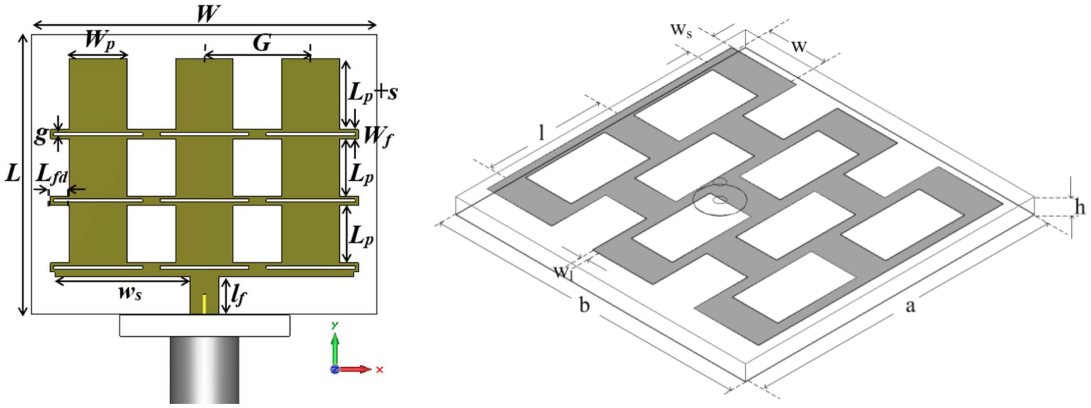

Figure 2.21: Geometry of the 2-D antenna array reported for 28 GHz millimeter-wave band: (a) enhanced Franklin antenna array [17], and (b) grid array [47].

It is possible to achieve high gain using antenna array as discussed above. It is also possible to design high gain antenna based on substrate integrated waveguide (SIW) technology. The SIW antenna has been investigated for 28 GHz millimeter-wave 5G mobile device applications [48–51]. The configuration of a SIW antenna is shown in Fig. 2.22 where multi-layered cavity is used to achieve high gain. Similar antenna configuration are demonstrated in Fig 2.23 (a) and Fig. 2.24. This type of antenna exudes very good radiation performance but the size of the antennas limits their suitability for mobile device applications. Most of these SIW based array antenna produces fan-shaped beam not pencil beam. On the other hand, small-sized multi-layered Huygens source can be use to achieve the boresight radiation but the gain of the antenna is below 4.5 dBi. The geometry of such antenna is shown in Fig. 2.23 (b).

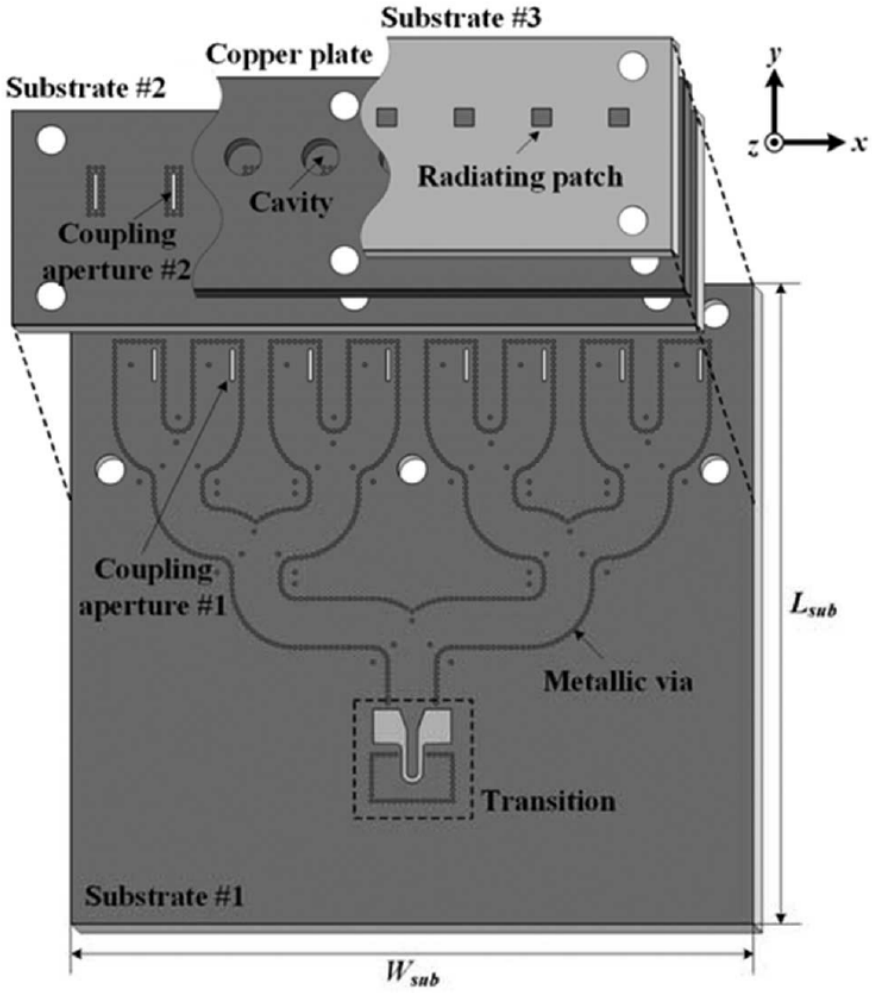

Figure 2.22: Geometry of the SIW antenna proposed for 28 GHz millimeter-wave band [51].

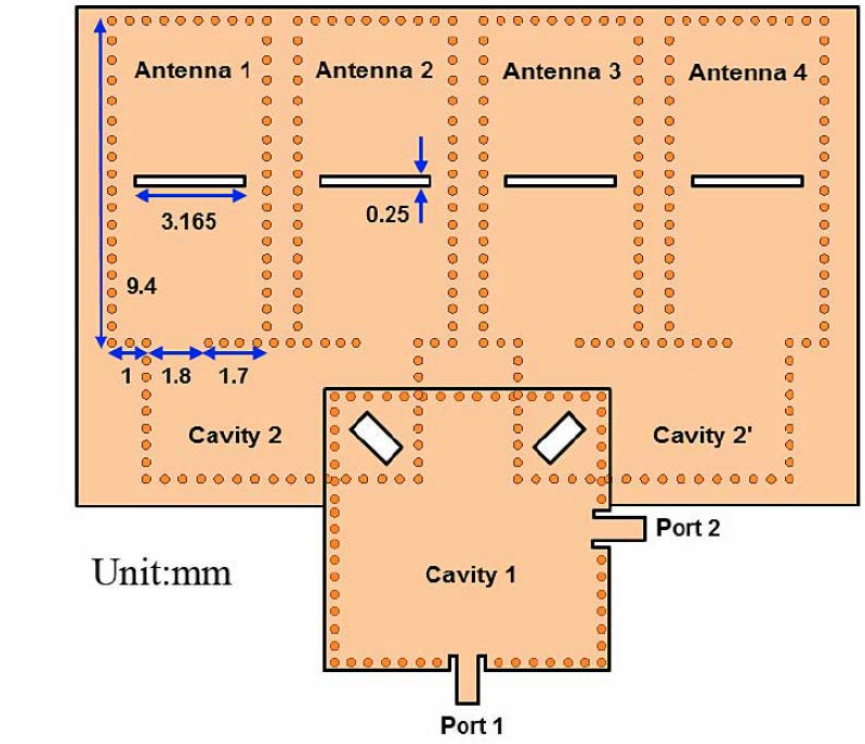

(a)

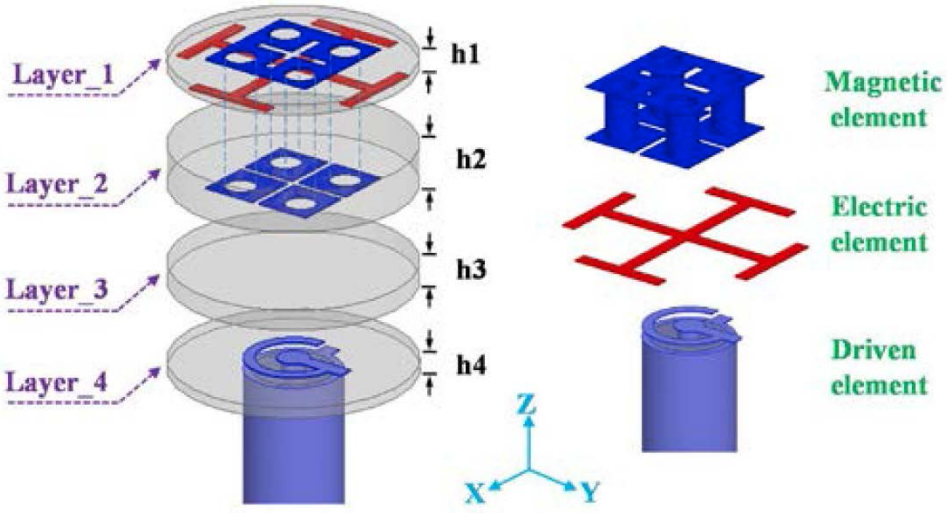

(b)

Figure 2.23: Geometry of (a) monopulse array [48], and (b) multi-layer huygens source antenna [108] with boresight radiation.

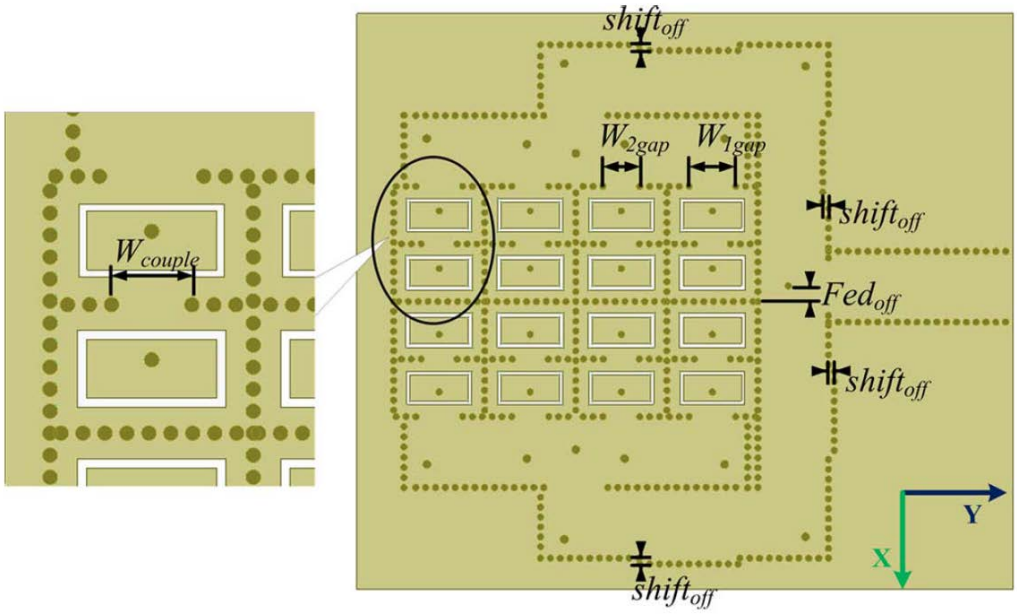

(a)

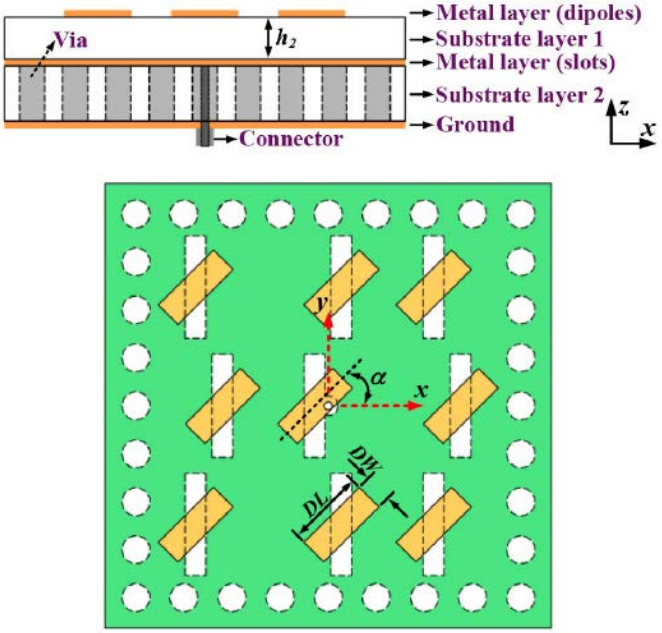

(b)

Figure 2.24: Geometry of (a) SIW cavity-backed patch antenna [50], and (b) slotted cavity antenna [49] with boresight radiation.

A size comparison between the reported SIW antennas and 4G antennas is shown in Table 2.7. The percentage of space occupied by the antenna is calculated with respect to the standard size of 120 mm × 70 mm of a mobile device substrate. Only the antenna reported in [49] occupied 1% less space than the spaced required for 4G antenna reported in [73]. Otherwise, the SIW antenna reported for 5G mobile devices requires equal or more space compared to the 4G antenna.

Table 2.7: A comparison of the area occupied by the 4G and 28 GHz millimeter-wave 5G antennas.

Ref.	Application	Area (mm^2)	% Space Occupied*
[73]	4G	350	4
[51]	5G	4445	53
[48]	5G	340	4
[49]	5G	256	3
[50]	5G	924	11

* The percentage of space occupied by the antennas is calculated with reference to the standard size of the substrate 120 mm × 70 mm.

2.5.2 Pattern Reconfigurable Antenna

Antennas with pattern reconfigurable capability have been studied in recent years for millimeter-wave communications focusing on 28 GHz band [15,52,53]. In order to achieve beam switching from an antenna, phased array antenna has received much attention from millimeter-wave antenna design researchers. Samsung mobile demonstrated 32 element phased array with testing for future 5G mobile devices, geometry shown in Fig. 2.25 (a). The phased array antenna with 4 elements [54] [shown in Fig. 2.26 (a)], 8 elements [55]

[shown in Fig. 2.25 (b)], 10 elements [56] [shown in Fig. 2.26 (b)], and 32 elements [57] has been investigated for 28 GHz millimeter-wave applications. The four elements phased array is able to switch beam θ = +35° to θ = -35° and achieved 3-dB coverage angle is 90° [54]. The eight elements phased array reported in [55] is designed to scan beam along the endfire direction (θ = +90°) from ϕ = -70° to ϕ = +70°. The ten elements phased array antenna is able to scans beam from boresight to endfire [56]. The antenna is able to produce two simultaneous beam scan between ϕ = 0° and ϕ = ±45°. The 32 elements phased array is also able to scan beam along the endfire direction.

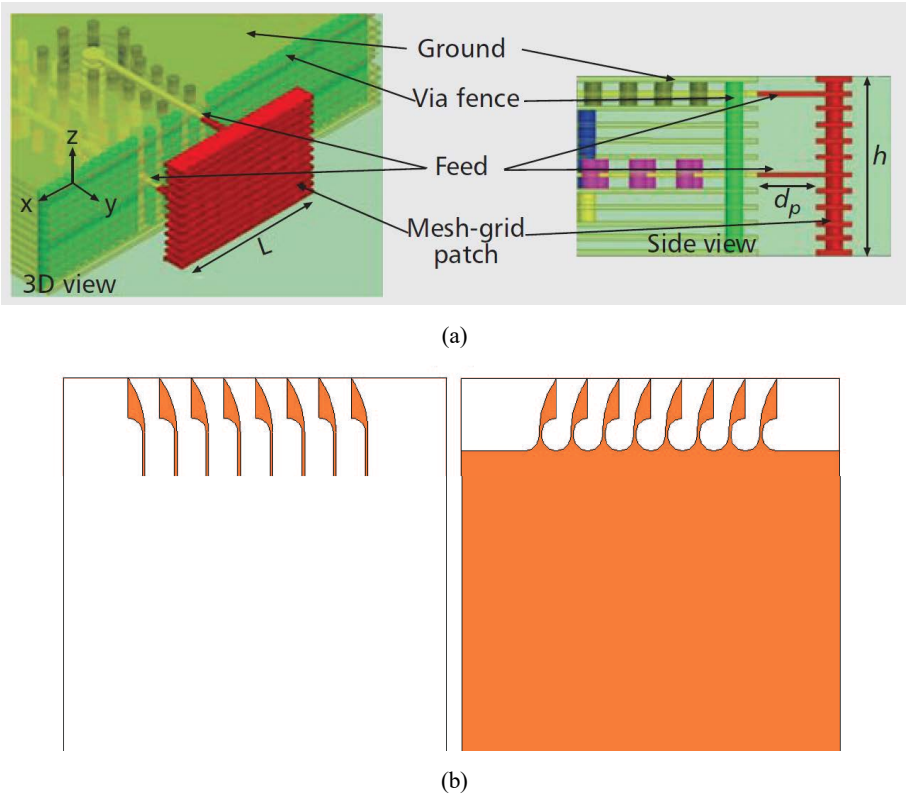

Figure 2.25: Geometry of the (a) 32 elements [15], and (b) 8 elements [55] phased array antennas.

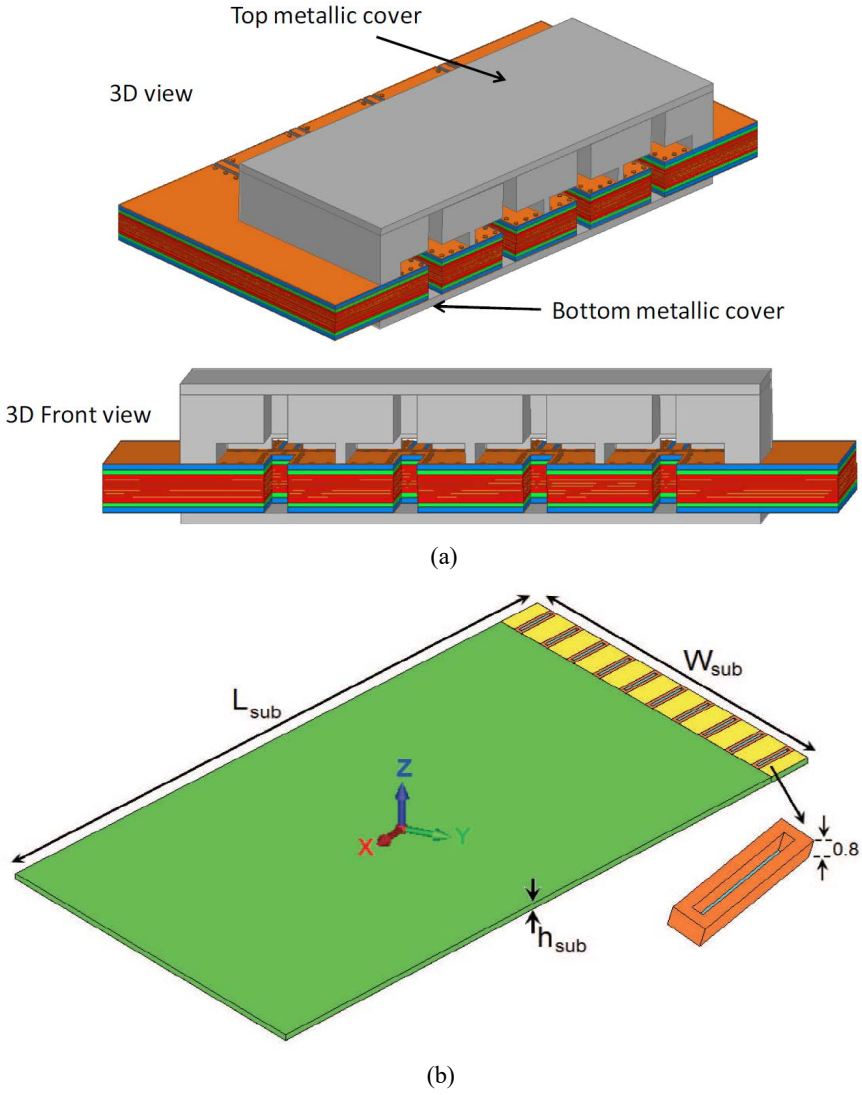

Figure 2.26: Geometry of the (a) 4 elements [54], and (b) 10 elements [56] phased array antennas.

The antenna reported in [57] scans beam from ϕ = -60° to ϕ = +60° while the antenna in [15] scans beam from ϕ = -70° to ϕ = +70°. Overall, the achieved maximum coverage from the few phased array antennas are: θ = +35° to θ = -35° in the boresight (ϕ = 0°) direction; and most of the cases beam scans in the endfire (θ = 90°) with a coverage from ϕ = -70° to ϕ = +70°.

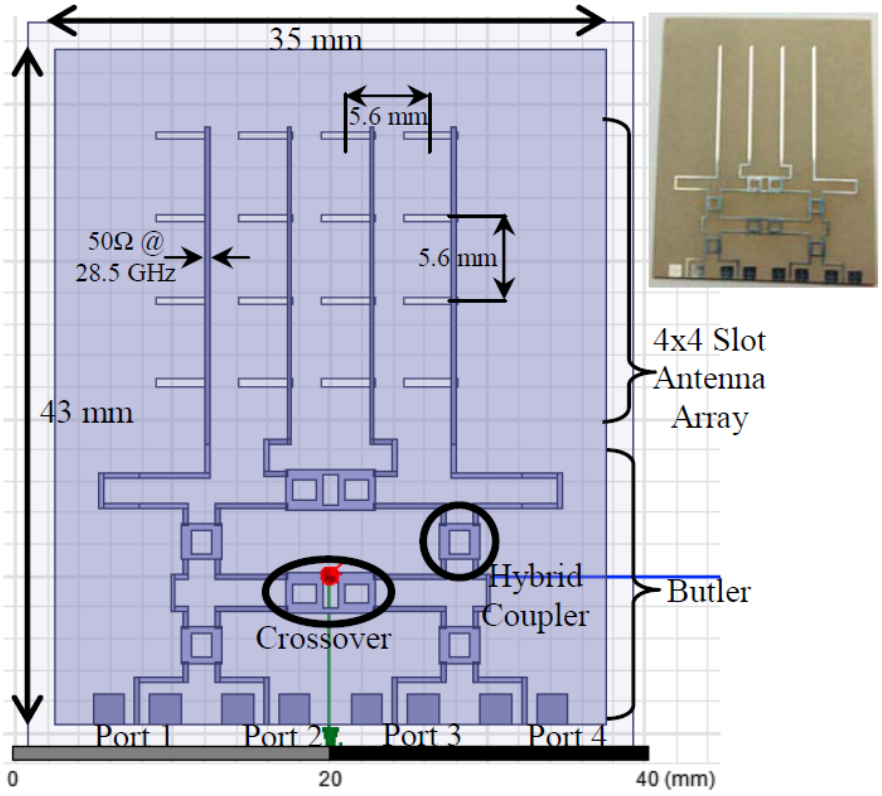

(a)

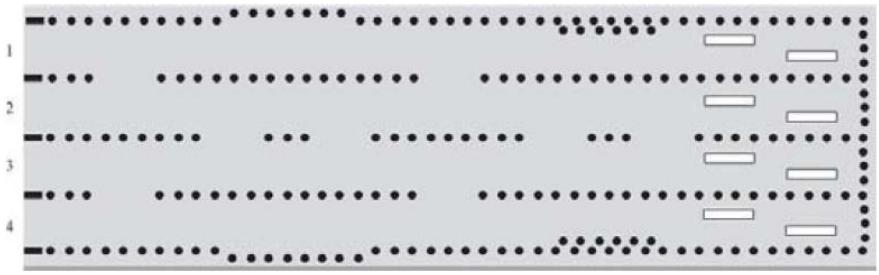

(b)

Figure 2.27: Geometry of the (a) switched beam planar array [58], and (b) slot array [52] fed by Butler matrix.

On the other hand, planar antennas were also studied for beam switching at millimeter-wave band [43, 52, 53, 58]. Using Butler matrix a 4 ports antenna demonstrates beam switching at two different directions ($\theta = +20°$, and $\theta = +45°$). Because of the dual beam the antenna is able to scan angles at $\theta = \pm 20°$, and $\theta = \pm 45°$. The geometry of the

antenna is shown in Fig. 2.27 (a). In addition, Butler matrix-based 8 ports slot array has been presented to scan beam around the boresight direction [52]. The geometry of the antenna is shown in Fig. 2.27 (b). The antenna is able to scan beam from $\theta = +48^{\circ}$ to $\theta = -48^{\circ}$. Consequently, it is generally possible to have a 1-D beam switching using either the phased array or other geometry where phase shifter or integrated power divider is required. All the reported antennas have been designed with more than one port (4 to 32 ports). Furthermore these reported antennas are unable to provide 2-D beam switching.

Considering the study presented in this section, most of the antennas developed and illustrated by either researchers or industrial organizations for mobile device application have fan-shaped beam or radiation pattern with wide beamwidth. Depending on the antenna configuration, these antennas can be used either to switch beam in different directions or to point beam in a fixed radiation. However, pencil-shaped beam is preferred for the base station antenna to support communication with mobile communication while targeting to shift all complexity to the base station antenna and keeping the mobile device antenna as simple as possible in order to avoid excessive power consumption by the antenna driving circuitry [2, 15].

2.6 Power Consumption in a Smartphone

The power consumed by the different components of a mobile phone have been studied in-depth in [59]. Maximum power was consumed by the display features on the mobile device. The power consumed by different components of the mobile phone vary according to what is being accessed, like audio playback, browsing, video playback, etc.

Fig. 2.28 depicts the power consumed by the display for varying levels of brightness and the power consumed by different components of the mobile device under video playback conditions. The results make clear that with the increase in brightness levels the power

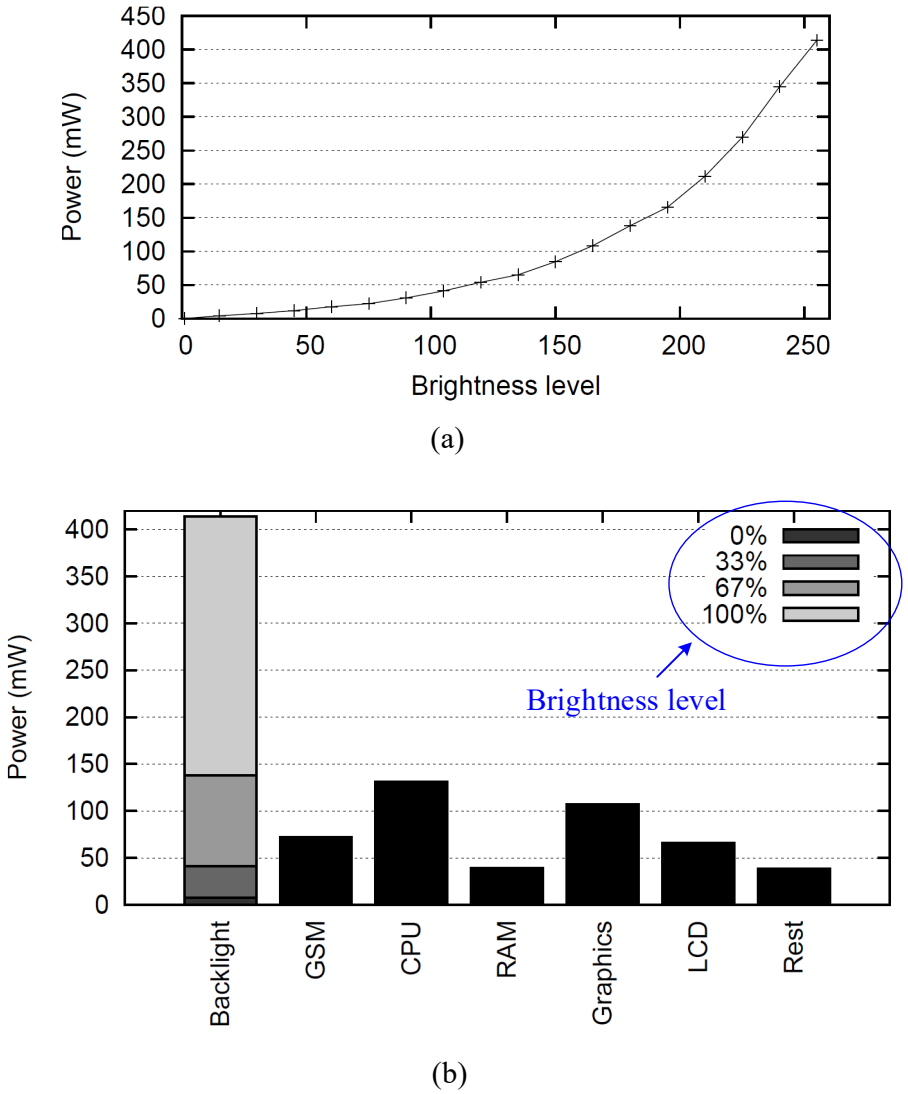

Figure 2.28: Power consumption in a smartphone (a) display backlight power for varying brightness levels, and (b) video playback power for different components [59].

consumed by the display increases rapidly. The display's consumption of minimum and maximum power is 8.4 and 414 mW, respectively, as shown in Fig. 2.28 (a). Also, the average power consumed by the display is 410 mW for a 5 minute video playback when the brightness is 100% (brightness level 255), shown in Fig. 2.28 (b). However, the power consumed in one second by an 8-bit programmable phase shifter at 32-37 GHz is 10 mW,

resulting in 600 mW power being consumed in one minute [60]. Therefore, use of the phase shifter in order to run the phased array antenna for beam switching in a mobile device will cause a significant reduction in battery life. This is a great disadvantage of a mobile phone.

2.7 Antenna with Dielectric Superstrate/Load

A dielectric layer as a superstrate/load can be applied to increases the gain and efficiency and bandwidth of the antenna. In addition, dielectric superstrate can be used to improve the impedance matching of the antenna. When a patch antenna is covered by a single dielectric layer it shifts the resonant frequency of the antenna [109]. This resonant frequency shift depends on the thickness of the dielectric superstrate, and has a liner relationship between them. It is also demonstrated that the dielectric superstrate increases the gain of the microstrip patch antenna [110].

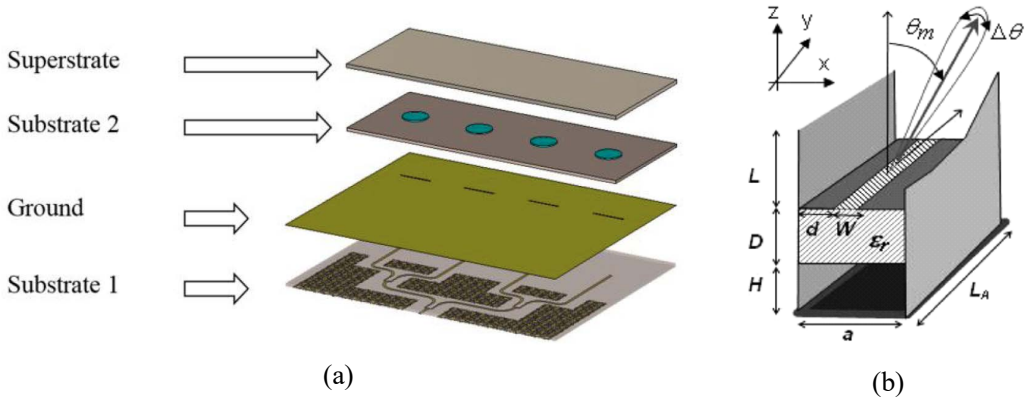

Figure 2.29: Geometry of antenna with dielectric superstrate: (a) patch array [111], and (b) leaky-wave antenna [112].

The gain of a patch array antenna is enhanced by applying a dielectric superstrate [111] and the geometry of the antenna is shown in Fig. 2.29 (a). A substrate-superstrate

configuration for designing leaky-wave antenna is presented in [112] in order to increase the gain of the antenna; geometry of the antenna is shown in Fig. 2.29 (b).

All the aforementioned antennas with dielectric superstrate does not have a cavity between the superstrate and the antenna. However, using a air filled cavity the directivity of the slot array is increased by approximately 15 dBi which is illustrated in [113]. Such antenna geometry is shown in Fig. 2.30 (b) and the antenna uses unprinted superstrate. On the other hand, the gain of the slot antenna improved by 8 dBi with the use of printed dielectric superstrate [114], and the geometry of the antenna is shown in Fig. 2.30 (a).

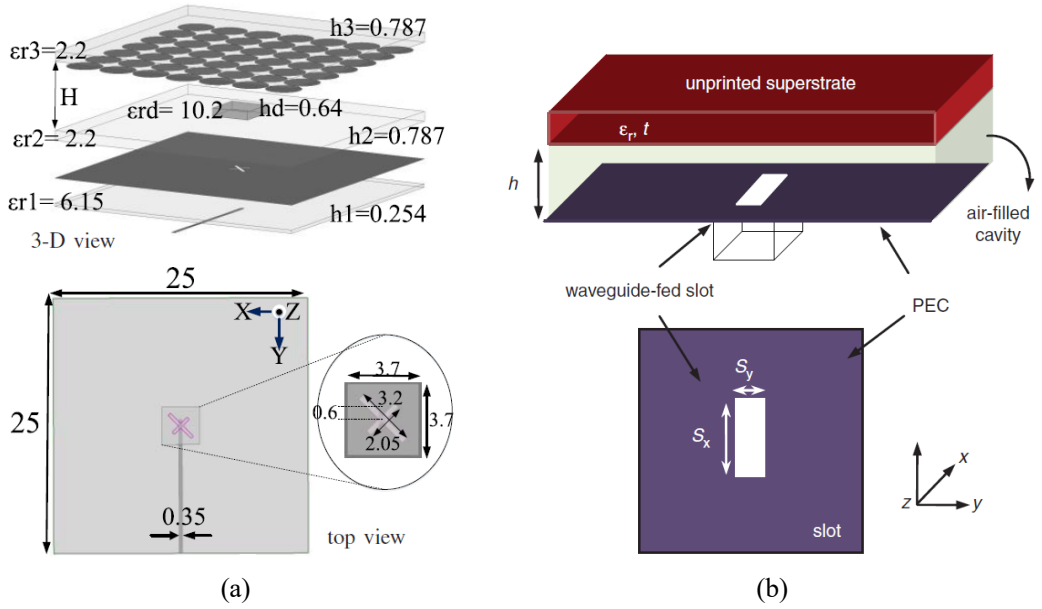

Figure 2.30: Geometry of slot antenna with resonator cavity and with: (a) printed dielectric superstrate [114], and (b) unprinted dielectric superstrate [113].

The antennas studied in this section uses superstrate as a dielectric load either to increase gain or to improve impedance matching. It is also demonstrated that the dielectric superstrate can be used to improve both the gain and bandwidth of the antenna [115,116]. Such antennas geometry are shown in Fig. 2.31.

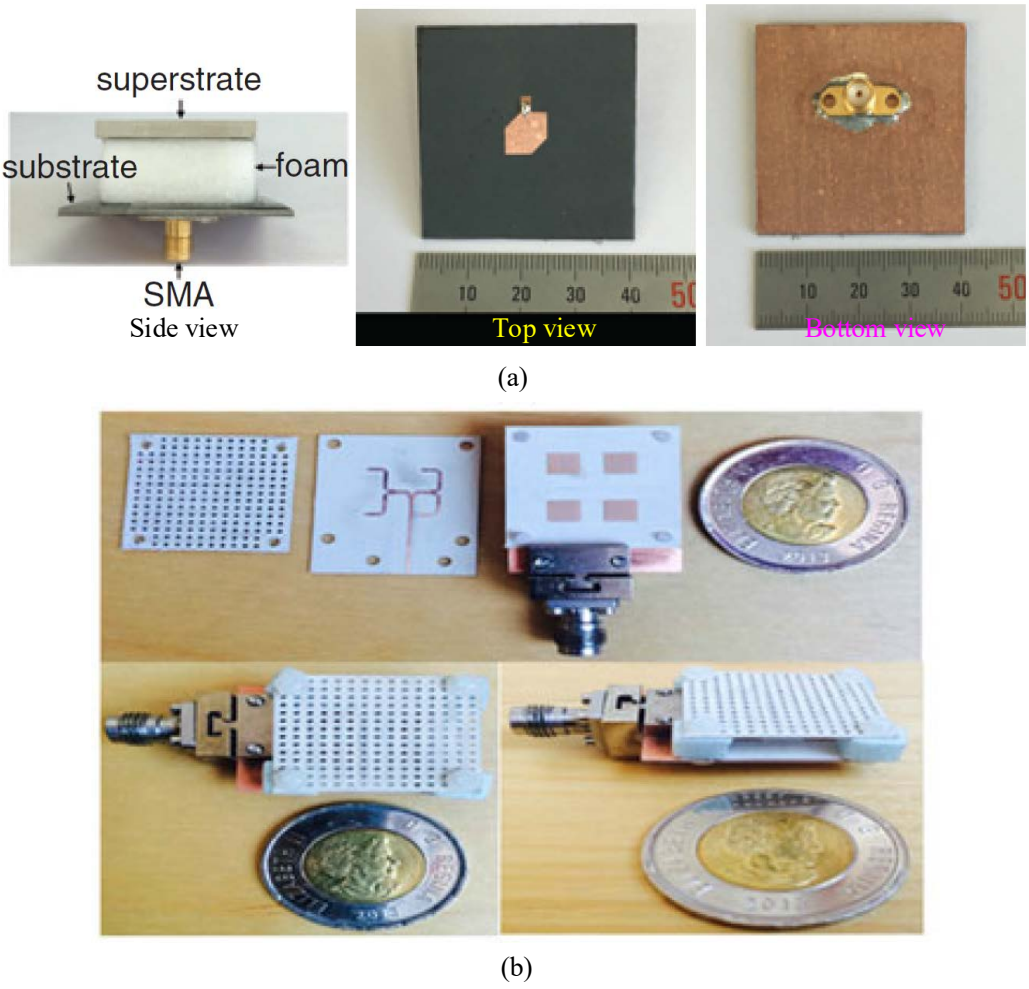

Figure 2.31: Geometry of antennas that uses dielectric superstrate to improve the gain and bandwidth of the antenna: (a) patch antenna [116], and (b) patch array [115].

Therefore, a dielectric superstrate as a dielectric load can be used to improve the impedance matching, increase the gain and directivity, and improve the impedance bandwidth of the antenna.

2.8 Microstrip Leaky-Wave Antenna

The microstrip leaky-wave antennas (MLWAs) are attractive because of their inherent beam scanning capabilities and low profile [117–122]. A microstrip line does not radiate in the fundamental mode (EH_0) because of the strongly bounded electric field between the microstrip line and ground plane [123]. However, a microstrip line radiates leaky-waves in some higher-order modes [124–126]. Fig. 2.32 shows the electric field distributions of a microstrip line operating in the fundamental mode (EH_0), first higher-order mode (EH_1), and second higher-order mode (EH_2). In both the EH_1 and EH_2 modes the antenna radiates as a leaky-wave.

A leaky structure supports fast wave and hence the wavenumber is complex and can be expressed as [122]

$$k_z = \beta - j\alpha \tag{2.4}$$

where, β is phase constant and α is attenuation constant. The attenuation constant α determines the amount of power leakage from a structure and β determines the position of the main beam. The direction of the main beam is given by [127]

$$\theta(f) = sin^{-1}\Big[\frac{\beta(f)}{k_0(f)}\Big] \tag{2.5}$$

where, θ is the angle between the boresight and the main beam direction.

The microstrip line shown in Fig. 2.32 (b) is a full-width (FW) microstrip line operating in its EH_1 mode. It can be seen from the electric field distribution that there is an electric field null at the center of the microstrip. Shorting the microstrip to the ground plane [see Fig. 2.33 (a)] will have no effect on the EH_1 mode operation [123]. The microstrip line is now symmetrical with respect to the shorting wall. Since the microstrip line is symmetric with respect to the center shorting wall, it is possible to remove one of the two sides from the antenna structure without affecting the performance of the antenna [123, 128, 129]. As LWA uses this method is called a half-width microstrip LWA (HW-MLWA). The

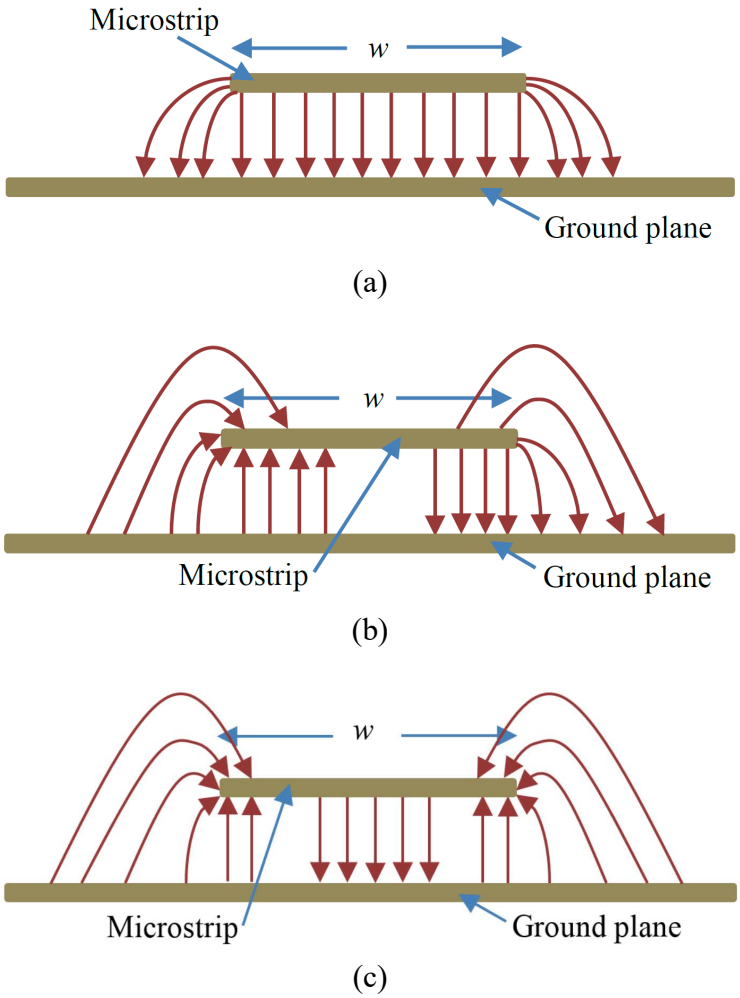

Figure 2.32: Electric field pattern of three different modes of a microstrip line (substrate omitted): (a) fundamental mode (EH_0) [123], (b) first higher-order mode (EH_1) [126], and (b) second higher-order mode (EH_2) [124].

generalized geometry of a HW-MLWA is shown in Fig. 2.33 (b). The boresight direction for this LWA is fixed, which is perpendicular to the plane of the antenna. The antenna shown in Fig. 2.33 are placed in the x-y plane, hence the boresight direction is along the z-axis.

The HW-MLWA have been studies well to achieve either forward or backward beam scanning or simultaneous beam scanning in the forward or backward directions [120, 129–

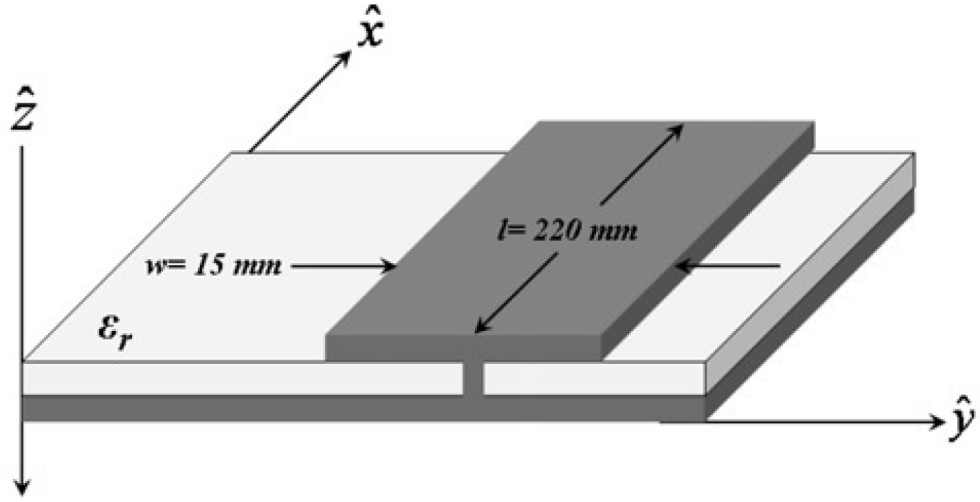

(a)

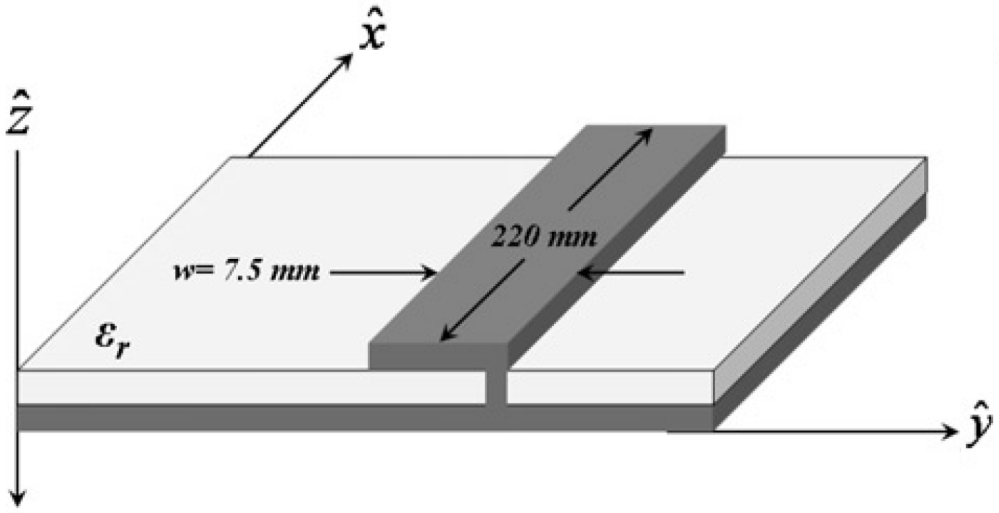

(b)

Figure 2.33: Cross-section of the (a) full-width (FW), and (b) half-width (HW) microstrip leaky wave antenna [123].

133]. Generally, an uniform LWA scans beam in the region between the boresight and endfire. An array of HW-MLWA can produce a boresight beam [117] and the configuration of the antenna is shown in Fig. 2.34. In this design the microstrip is terminated using a via, and arrays of vias at one edge of the microstrip act as a shorting wall. Also, a

slot-loaded patch antenna fed by a HW-MLWA has been analyzed to achieve boresight radiation [134].

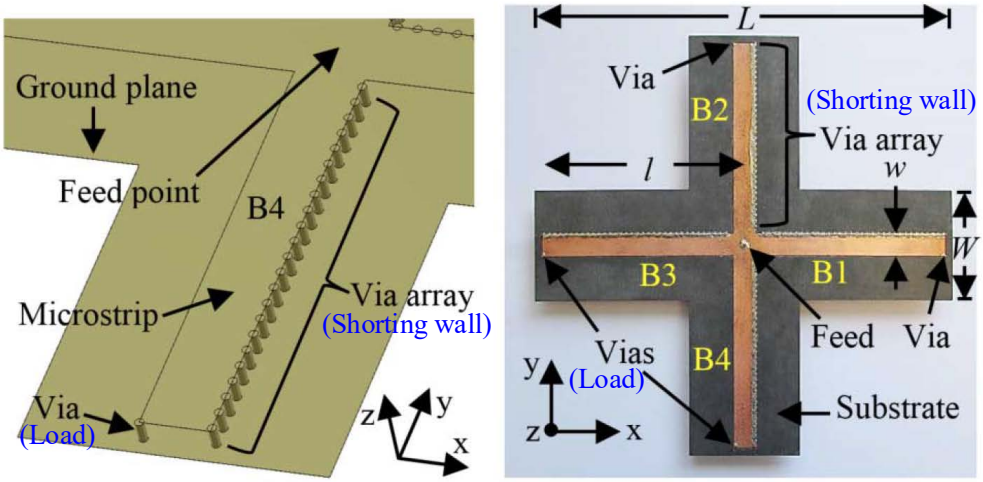

Figure 2.34: HW-MLWA with boresight radiation [117].

2.9 Summary

In this chapter, the frequency ranges that need to cover by future mobile phone antennas were studied. In order to cover all the LTE, LTE-advanced, LSA, and 28 GHz millimeter-wave bands, future mobile device antennas will be required to cover the frequency ranges 452-468, 698-960, 1427-2690, 3400-3800, 5150-5925 MHz, and 27.5-29.5 GHz. These bands were termed very-low-LTE, low-LTE, mid-LTE, high-LTE, very-high-LTE, and 28 GHz millimeter-wave bands, respectively, in this thesis.

The configurations of different types of 4G/LTE antennas for mobile devices were studied in this chapter. The antennas developed earlier were either categorized as planar inverted-F antenna (PIFA) or planar monopole antenna (PMA). All of the reported antennas are unable to cover the whole mid-LTE band and 1.5 GHz LSA band. However, they are able to cover the low, part of the mid, and high-LTE bands. Most of the reported

LTE/WWAN antennas have low antenna efficiency because of the use of input impedance matching circuit to cover those bands. Almost all the antennas consists of a single radiating element though some of them use a single feed point and others uses multiple points to feed the antenna. Importantly, most of these antennas suffer from nulls in the radiation patterns at the frequency close to the upper frequency limit of the mid-LTE band and also throughout the high-LTE band. Several antennas studied in the literature occupied a whole edge of the mobile device's substrate which is not feasible for practical applications. This is because they limit the integration of other components of a mobile phone like USB port, camera, speaker, microphone, etc.

In addition to the 4G/LTE antennas, this chapter gives an overview of the 28 GHz millimeter-wave antennas proposed for the 5G mobile device applications. Since the standards for 5G mobile antennas have not yet been finalized, this chapter discussed both the fixed beam antenna and pattern reconfigurable antenna. Most of the reported fixed beam antennas have good radiation characteristics but the size of those antennas was big compared to that of the 4G/LTE antennas. Conversely, the pattern reconfigurable antennas reported in the literature were mainly phased arrays. These antennas are able to scan beam either aligned with the boresight or endfire directions. The maximum scan range was ϕ = -70° to ϕ = +70° at θ = 90°, or θ = +35° to θ = -35° at ϕ = 0°. Yet the power consumed by an 8-bit phase shifter was almost 6 times more compared to the power consumed by the display for a 5 minute video playback. There are some planar multi-port antenna were developed to achieve beam switching. These planar antennas have a maximum scan range of θ = +48° to θ = -48° at ϕ = 0°. Importantly, all the reported antennas are able to scan the beam in 1-D but unable to scan in 2-D.

This chapter also gives an overview of the antennas with superstrate as a dielectric load in order to improve the performance of the antenna specifically bandwidth, gain, directivity, and impedance matching. These antennas either uses a cavity between the

antenna and the superstrate or directly placed the superstrate on top of the antenna without any gap.

Finally, in this chapter, the LWA which have inherent beam scanning capability and the half-width microstrip LWA (HW-MLWA) concept were discussed. The concept of the HW-MLWA will be used in this thesis to design a single beam antenna, a 1-D, and a 2-D beam switching antenna for 28 GHz millimeter-wave 5G mobile devices.

Chapter 3

28 GHz Millimeter-Wave 5G Antennas with Dielectric Load

3.1 Introduction

This chapter commences by describing the development of a highly efficient narrow-band PIFA (Ant-1) of compact size for the 28 GHz millimeter-wave band. In order to enhance the efficiency and achieve a large impedance bandwidth a single layer superstrate (dielectric load) is applied, which has the advantage of high gain and directivity. The influence of a mobile device battery on antenna performance has been investigated. Secondly, a wideband leaky-wave antenna (LWA) array (Ant-2) is developed. In LWA design a shorting pin/via or a 50 Ω load is usually employed at the end terminal to suppress any reflected wave as well as for impedance matching purposes. However, the radiation and subsequently the total efficiency of an antenna declines significantly at higher frequencies. Using a microstrip patch as a load the LWA antenna efficiency can be improved. It is possible to enhance the LWA array's efficiency by using a microstrip patch as a load for the element of the array and applying to it a superstrate as a dielectric load. Thirdly, the

narrow-band PIFA developed into a wideband PIFA (Ant-3) for the 28 GHz millimeter-wave band. Similar to the previous two developments, a superstrate acting as a dielectric load is applied in order to enhance the efficiency, hence the gain and directivity of the antenna. Owing to the good performance and convenience of fabrication, the proposed antennas are attractive for 5G mobile devices.

This chapter is organized as follows. Section 3.2 presents the narrow-band PIFA for 28 GHz millimeter-wave 5G mobile devices. The impact of the superstrate and a mobile device battery on the antenna's performance are briefly discussed in the same section. Section 3.3 presents the development of a highly efficient LWA array suitable for hand-held mobile devices. Section 3.4 presents the development of a highly efficient wideband PIFA for the 28 GHz millimeter-wave 5G mobile communication band. Comparing the performance between the antennas and reference antennas is presented in Section 3.5, and the main themes articulated in this chapter are summarized in Section 3.6.

3.2 Narrow-Band Planar Inverted-F Antenna (Ant-1) with Superstrate

The primary goal in this chapter is to develop antenna with reflection coefficient bandwidth 27.5-29.5 GHz with boresight radiation. The secondary goal is to achieve antenna gain above 7 dBi and half-power beamwidth above 30 degree.

This section presents the development of a planar inverted-F antenna (PIFA) with broadside radiation for 28 GHz millimeter-wave 5G hand-held mobile devices when a dielectric load is applied.

3.2.1 Antenna Configuration

The perspective view of the proposed millimeter wave 5G antenna is shown in Fig. 3.2 and detailed structure of the antenna is illustrated in Fig. 3.1; it is composed of a superstrate as a dielectric load. The antenna has been designed to print on a Rogers 5870 substrate ($\epsilon_r = 2.33$, and $\tan\delta = 0.0012$) with a thickness of 0.635 mm and a copper-cladding thickness of 0.035 mm.

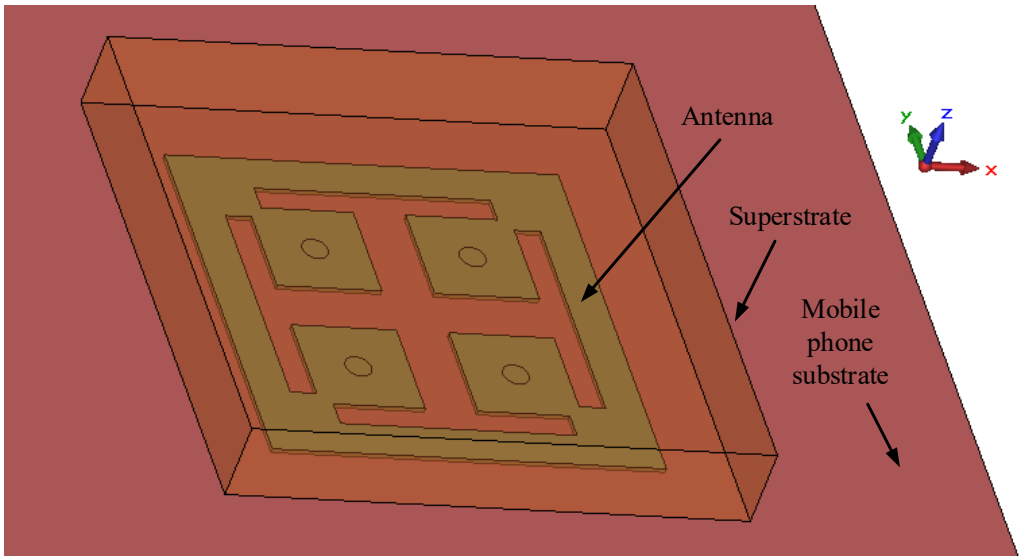

Figure 3.2: Perspective view of the narrow-band PIFA (Ant-1) with superstrate.

The presented realization includes two H-shaped slots in vertical and horizontal orientations, located at the center of an $L \times W$ patch, crossing each other in the center. Here the thickness of the wings and body of the H-slot are g_1 and g_2, respectively, as shown in Fig. 3.1 (a). Consequently, the four patch-shaped sections of dimensions $w_1 \times w_1$ are connected to the outer square loop with four individual high impedance lines at the four corners. Three shorting pins with a diameter of 0.1 mm, located at the center of each of three patch-like sections, connect them to the ground plane. The fourth patch-like section is used to feed the antenna from the bottom through to the fourth pin.

The design technique presented in [135] where a planar inverted-F antenna optimised

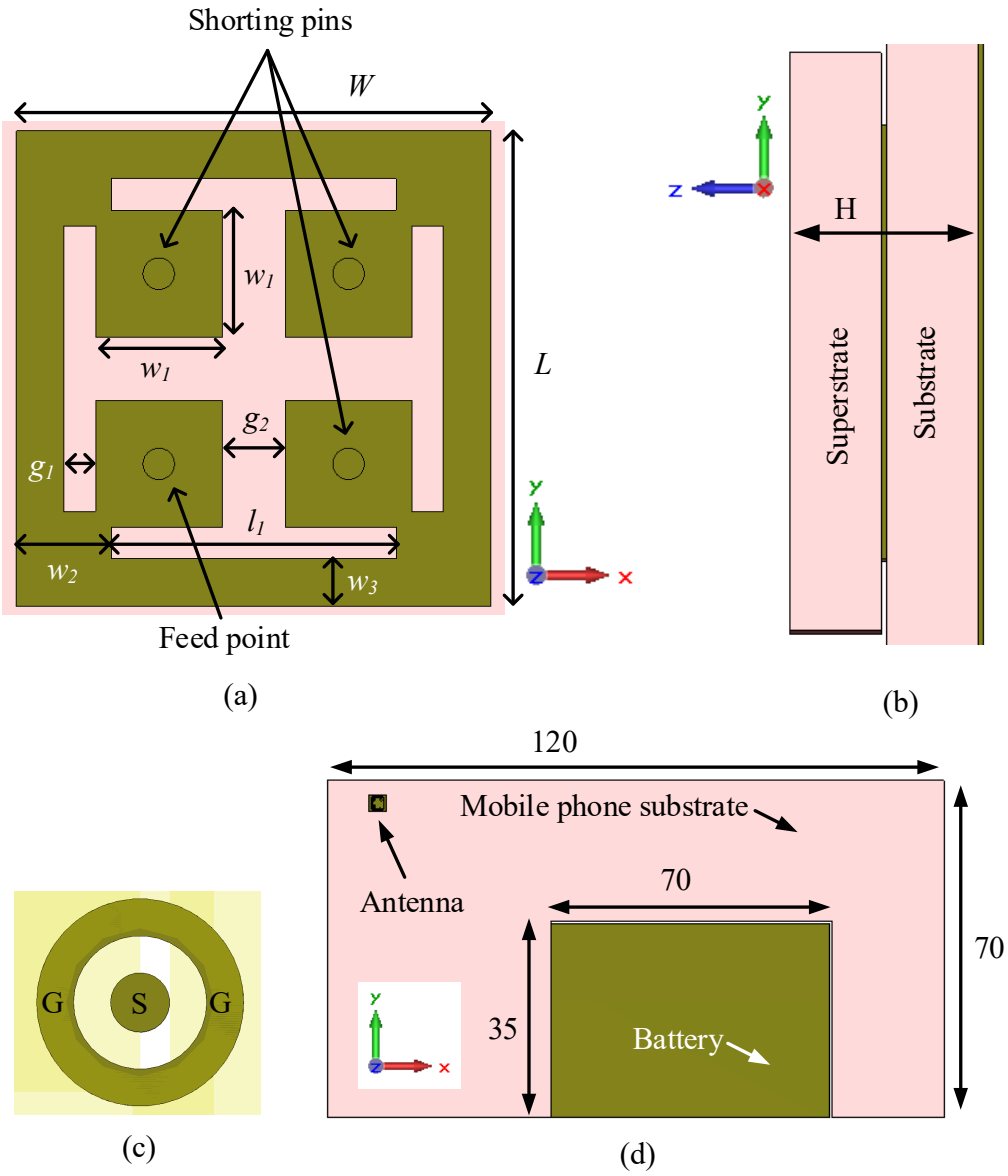

Figure 3.1: Configuration of the narrow-band PIFA (Ant-1) with superstrate and its placement in a mobile phone substrate: (a) top view without dielectric load, (b) side view with dielectric load, (c) back view of the ground-signal-ground (GSG) pad, and (d) antenna placement with respect to the substrate of a mobile device. All dimensions are in millimeters.

with a dielectric superstrate/load is considered during the design of the antenna and uses the fundamental equations for planar inverted-F antenna design are discussed in Section 2.3. Using the parameter analyses in CST the dimensions of the antenna presented in this section are optimized. The optimized design parameters of the narrow-band PIFA (Ant-1) are listed in Table 3.1.

Table 3.1: Design parameters of the narrow-band PIFA (Ant-1) with dielectric load. All dimensions are in millimeters.

$w_1 = 0.8$	$w_2 = 0.6$	$w_3 = 0.3$	$g_1 = 0.2$	$g_2 = 0.4$
$l_1 = 1.8$	$W = 3$	$L = 3$	$H = 1.34$	

A dielectric load ($\epsilon_r = 2.1$, and $\tan\delta = 0.0002$) that is 0.635 mm thick and has dimensions of $(L+1)$ mm $\times$ $(W+1)$ mm is placed on top of the radiating patch and the overall thickness of the antenna is 1.34 mm, as depicted in Fig. 3.1 (b). The effect of a mobile phone battery on the antenna performance is accounted for by inserting a metal box with the dimensions of a commercial battery.

The antenna is assumed to be fed by a ground-signal-ground (GSG) probe with a pitch of 50 microns and the GSG pad orientation is shown in Fig. 3.1 (c). The intention is integrate the proposed antenna with the front end of a mobile phone using a GSG probe or a 1.85 mm K-connector. The antenna is placed close to the top right-hand corner of a mobile phone, which has: firstly, a substrate with the dimensions 120 mm $\times$ 70 mm; and secondly, a battery with dimensions 70 mm $\times$ 35 mm, as shown in Fig. 3.1 (d). To visualize the effect of the battery a solid metal box is placed as a representative of a battery to have the maximum effect on antenna performance. In addition, the battery is connected to the ground plane of the mobile device in order to visualize the practical scenario. This leaves enough space for other RF and microwave components. A 1 mm gap

is allowed between the battery and the mobile device's substrate. The antenna dimensions are optimized using parametric analyses in CST Microwave Studio.

3.2.2 Effects of Superstrate

This section describes the effect of the superstrate which acts as a dielectric load, on the input impedance matching, directivity, gain and efficiency of the narrow-band planar inverted-F antenna (Ant-1). In this design, the dielectric load is chosen by parameter analyses in CST. A significant improvement in efficiency and input impedance matching, as well as improvements in directivity and gain, are observed when Teflon as a dielectric load is used.

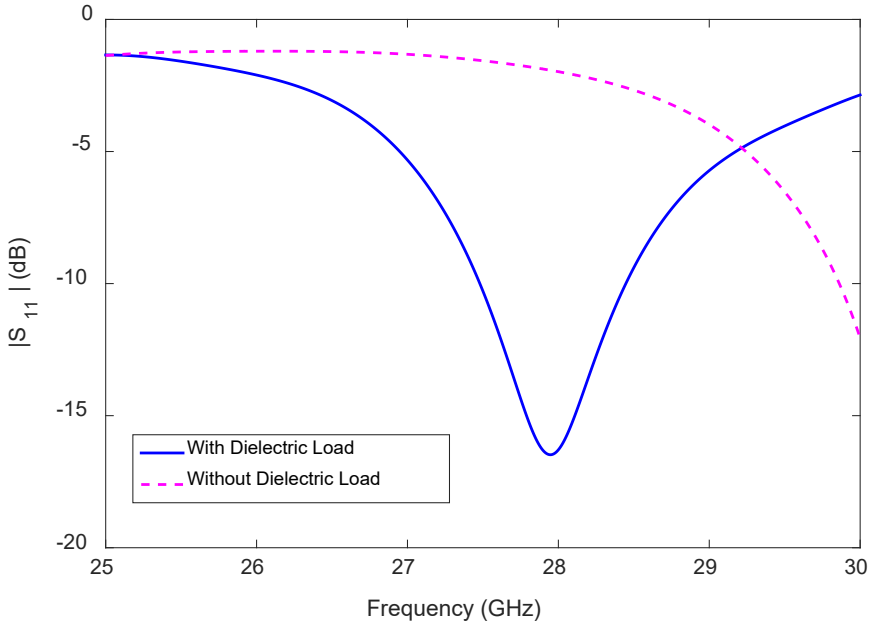

Figure 3.3: Effect of the dielectric load on the antenna input impedance matching of the narrow-band PIFA (Ant-1).

The effect of the dielectric load on the antenna reflection coefficient is shown in Fig. 3.3. The antenna input impedance matching in the frequency range 25-29 GHz is poor, but the input impedance matching improves as the frequency rises from 29 GHz to 30 GHz.

However, no resonance is observed within the presented frequency range 25-30 GHz. It is clear from the graph that the antenna without dielectric load resonates at a frequency which is above 30 GHz. On the other hand, the frequency of minimum reflection coefficient shifted towards a lower frequency and the antenna resonates at 27.95 GHz, as shown in Fig. 3.3. The -10 dB reflection coefficient bandwidth of Ant-1 is 980 MHz (27.47-28.45 GHz).

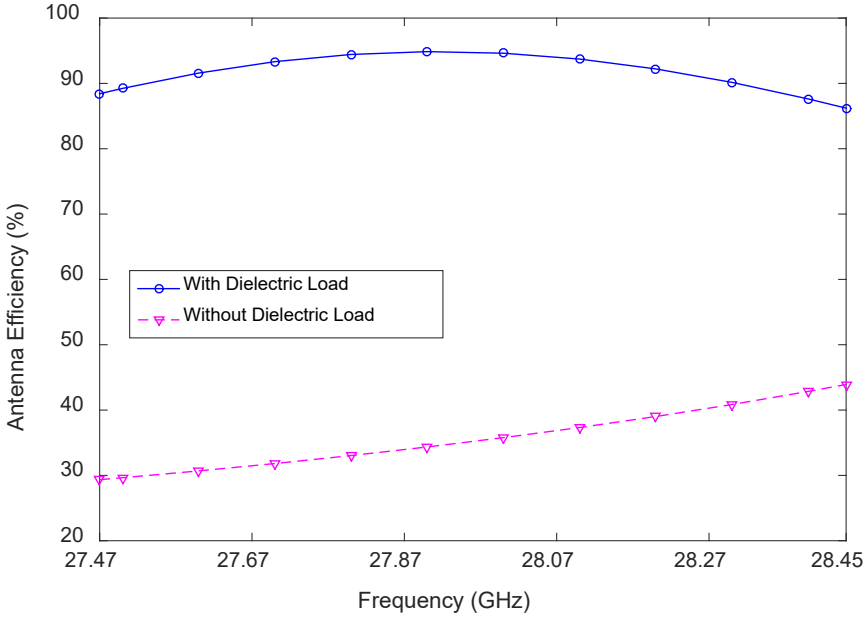

Figure 3.4: Effect of the dielectric load on the efficiency of the narrow-band PIFA (Ant-1).

Now the effects of the dielectric load on antenna efficiency are presented. Fig. 3.4 illustrates the effect of the dielectric load on the antenna efficiency within the reflection coefficient bandwidth. The antenna efficiency varies between 29% and 45% when the dielectric load is not present. The antenna efficiency encapsulates a minimum at 27.47 GHz and reaches its maximum at 28.45 GHz. When the dielectric load is employed on top of the antenna with a zero gap, the antenna efficiency is improved by more than 66%. With the use of the dielectric load, the antenna efficiency is a maximum at 27.9 GHz and a minimum at 28.45 GHz, i.e. are 95% and 84%, respectively.

The influence of the superstrate on the directivity, realized gain, and absolute gain of Ant-1 are analyzed. The results are compared within the frequency range 27.47-28.45 GHz. The gain and directivity of Ant-1 with and without the presence of the dielectric load are shown in Fig. 3.5. The maximum directivity is 8.5 dBi at 28.45 GHz and the minimum is 7.6 dBi at 27.47 GHz without the presence of the dielectric load. More than 1 dB of directivity improvement is observed when the appropriate dielectric load (chosen by parameter analysis in CST) is employed, as shown in Fig. 3.5. When the dielectric load is present, the directivity's variation within the reflection coefficient bandwidth is $\leq$ 0.3 dB, whereas this variation is $\leq$ 1 dB without the use of the dielectric load. The maximum and minimum directivity are 9.2 and 8.9 dBi, respectively, when the dielectric load is present.

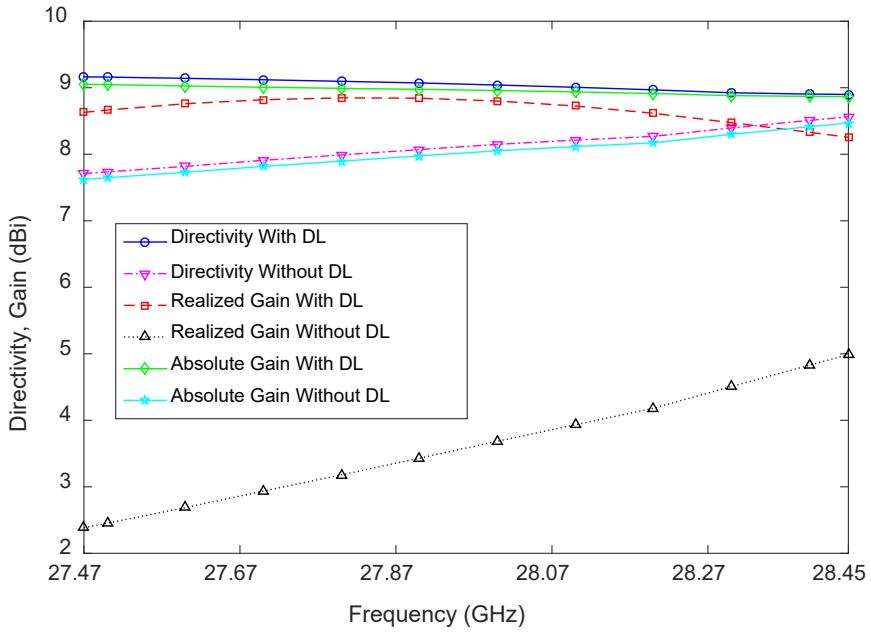

Figure 3.5: Effect of the dielectric load on the directivity and gain of the narrow-band PIFA (Ant-1).

Ant-1 has low gain, with $\leq$ 3 dB variation within the reflection coefficient bandwidth observed without the use of the dielectric load, as shown in Fig. 3.5. The minimum

and maximum realized gains are 2.2 and 5.2 dBi, at 27.47 and 28.45 GHz, respectively. When the dielectric load is employed, the maximum realized gain of the antenna is 8.6 dBi at 27.85 GHz and the minimum realized gain is 8.1 dBi at 28.45 GHz; therefore the realized gain variation within the reflection coefficient bandwidth is $\leq$ 0.5 dB. Based on the obtained results, the gain and directivity of the antenna are stable within the reflection coefficient bandwidth when the dielectric load is used. Also, around 6.4 dB improvement in realized gain is observed when using the dielectric load. In addition, the absolute gain of the antenna varies between 7.6 and 8.5 dBi without dielectric load is applied whereas the absolute gain varies between 8.9 and 9.1 dBi when dielectric load is applied.

3.2.3 Effects of Mobile Device Battery

In order to find the influence of a mobile device battery on antenna performance, the reflection coefficient, gain, directivity and efficiency of Ant-1 with no device battery are compared with the results when a mobile phone battery is added after removing a portion of the substrate and ground plane. Placement of the battery within the mobile phone substrate is shown in Fig. 3.1(d), as is the positioning of Ant-1. The dimensions of the battery chosen in this study are 70 mm $\times$ 35 mm.

The antenna has a -10 dB reflection coefficient bandwidth of 980 MHz (27.47 - 28.45 GHz) with the presence of a battery, as shown in Fig. 3.6, covering a portion of the 5G mobile communication band or millimeter-wave frequency bands for future mobile cellular devices. When the battery is removed the antenna reflection coefficient behavior remains the same, as depicted in Fig. 3.6.

The antenna efficiency of the narrow-band planar inverted-F antenna (Ant-1) has been studied with and without the presence of the battery, and the predicted results are shown in Fig. 3.7. The obtained minimum and maximum values of the antenna efficiency, with the presence of the battery, within the reflection coefficient bandwidth of the antenna are

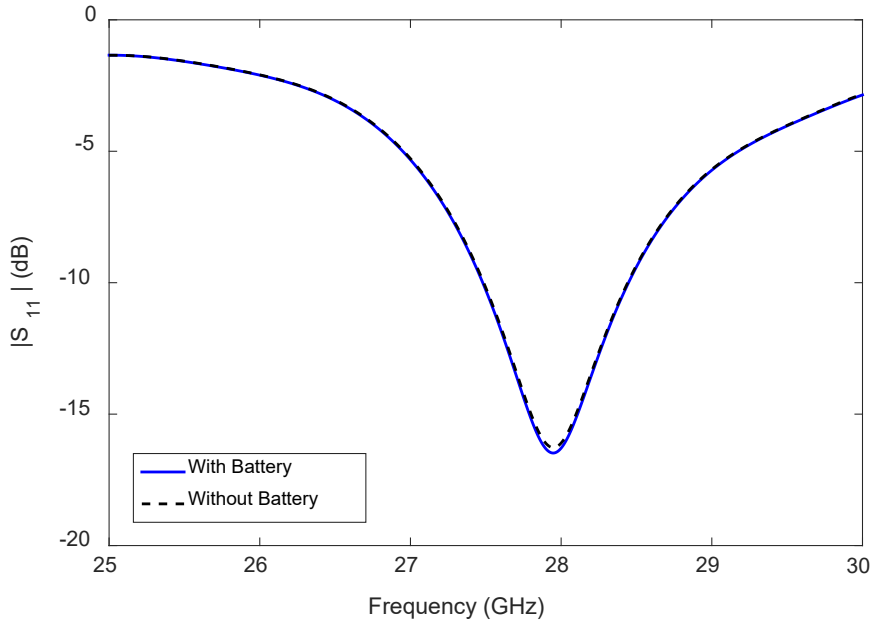

Figure 3.6: Reflection coefficient of the narrow-band PIFA (Ant-1) and with and without the presence of a mobile device battery while dielectric load is present.

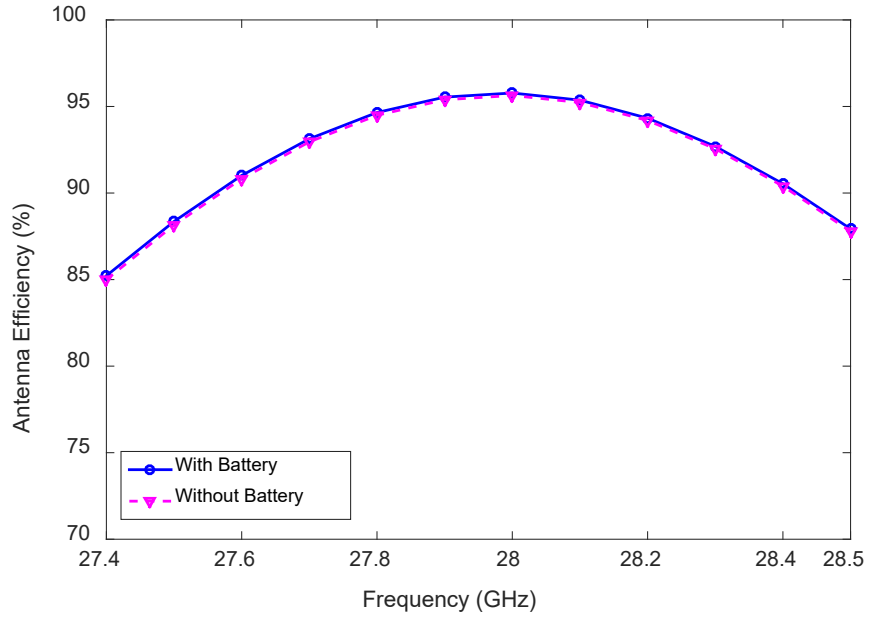

Figure 3.7: Efficiency of the narrow-band PIFA (Ant-1) with and without the presence of the battery while dielectric load is present.

88% and 96%, at 27.47 GHz and 27.9 GHz, respectively. The antenna efficiency of the antenna is unaffected by the presence of the battery, as depicted in Fig. 3.7.

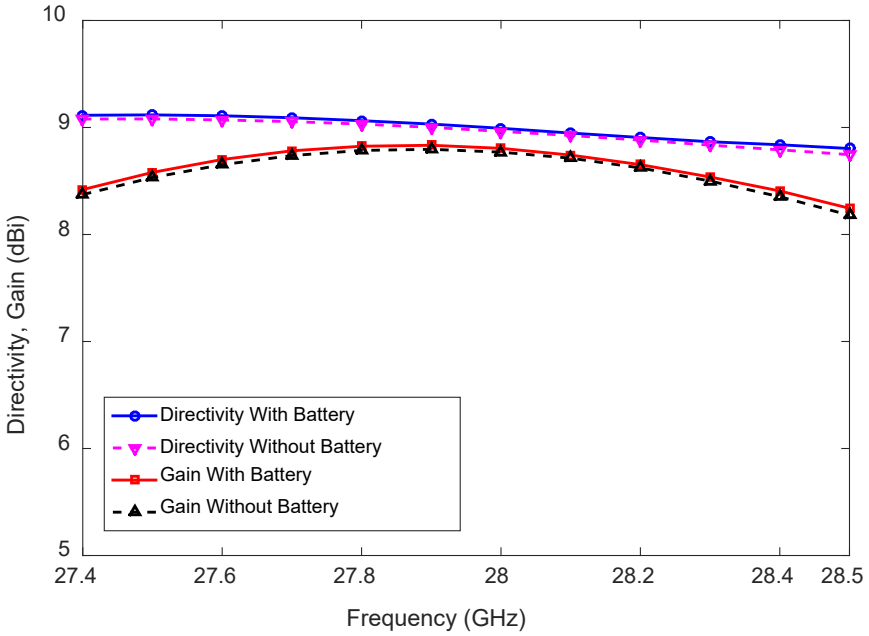

Figure 3.8: Directivity and gain of the narrow-band PIFA (Ant-1) with and without the presence of the battery while dielectric load is present.

The realized gain and directivity of the proposed antenna are shown in Fig. 3.8. The proposed antenna has a nearly constant gain within the antenna reflection coefficient bandwidth with a gain variation of only 0.55 dB, while the maximum and minimum gains are 8.6 dBi and 8.1 dBi, at 27.9 GHz and 28.5 GHz, respectively. The maximum and minimum directivities of the antenna are 9.2 dBi and 8.9 dBi, at 27.5 GHz and 28.5 GHz, respectively. A negligible decrease is observed in the gain and directivity when the battery is removed, as shown in Fig. 3.8.

It is therefore clear that the antenna reflection coefficient behavior together with the gain, directivity, and efficiency are unaffected by the battery's presence. Since the battery is connected to the ground plane of the mobile device, the antenna performance will be unaffected in practical. Therefore in the radiation pattern analysis the results for Ant-1

when the battery is present are presented and studied.

3.2.4 Radiation Patterns

Fig. 3.9 shows the normalized radiation patterns in the x-z plane, and Fig. 3.10 shows the normalized radiation patterns in the y-z plane of Ant-1 at 27.5, 27.75, 28, 28.25, and 28.5 GHz. At each frequency, the x-z plane and y-z plane radiation patterns are normalized with respect to the maximum at that frequency. The radiation patterns in the x-z plane and y-z plane at selected frequencies point towards the boresight, i.e. towards the z-axis.

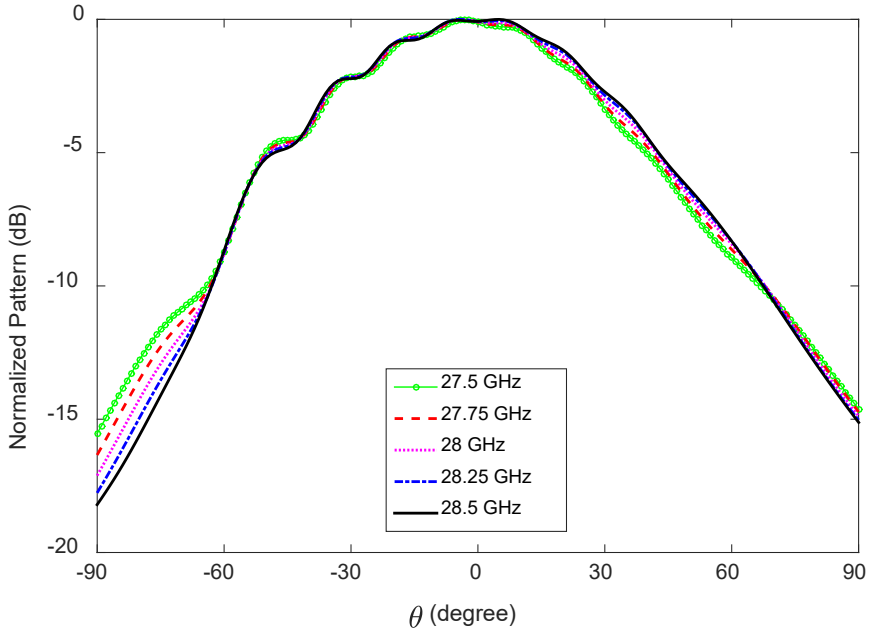

Figure 3.9: Normalized radiation patterns of the narrow-band PIFA (Ant-1) with dielectric load in the x-z plane.

Ant-1 has a quite constant radiation pattern over the antenna reflection coefficient bandwidth. The side-lobe level (SLL) and half-power beamwidth (HPBW) or 3-dB beamwidth for the x-z plane and y-z plane are listed in Table 3.2 at selected frequencies. The maximum and minimum HPBW are 69° and 64°, respectively, in the x-z plane, and the maximum and minimum HPBW are 69° and 65°, respectively, in the y-z plane.

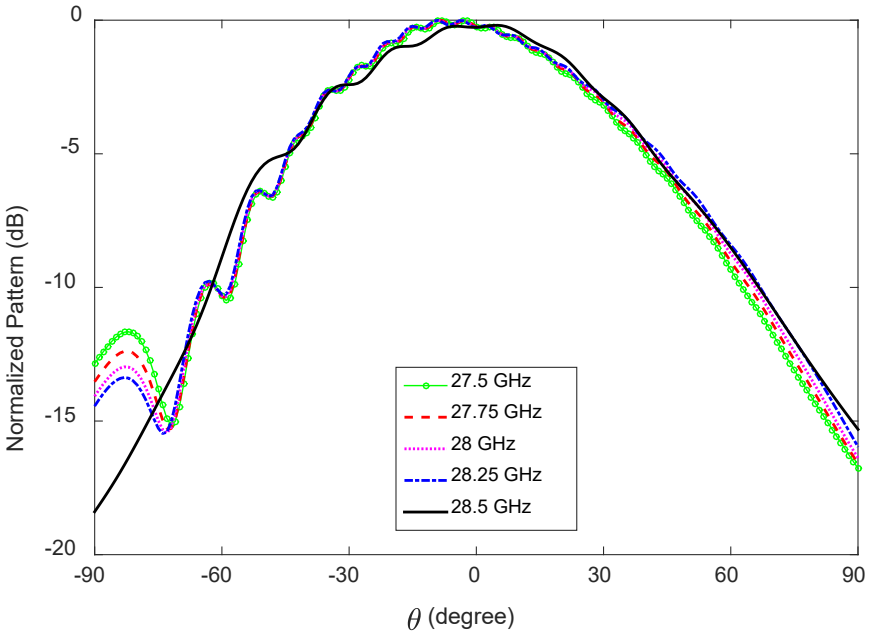

Figure 3.10: Normalized radiation patterns of the narrow-band PIFA (Ant-1) with dielectric load in the y-z plane.

Table 3.2: Side-lobe level (SLL) and half-power beamwidth (HPBW) of the narrow-band PIFA (Ant-1) with dielectric load in the x-z and y-z planes.

Frequency (GHz)		27.5	27.75	28	28.25	28.5
SLL (dB)	x-z plane	-18	-18	-20	-20	-20
	y-z plane	-14	-15	-16	-16	-20
HPBW (degree)	x-z plane	64	65	66	68	69
	y-z plane	65	66	67	67	69

The side-lobe level (SLL) of Ant-1 is always below -18 dB in the x-z plane. Also, the SLL is -18 dB at 27.5 and 27.75 GHz and -20 dB at 28, 28.25, and 28.5 GHz. The SLL is better in the x-z plane than in the y-z plane at presented frequencies. In the y-z plane, the SLL is always below -14 dB. The SLL of the radiation patterns decreases with increased frequency for both the x-z and y-z planes.

3.3 Wideband LWA Array (Ant-2)

The narrow-band PIFA (Ant-1) proposed in the previous section is unable to cover the 28 GHz millimeter-wave band (28-29.5 GHz) for future 5G mobile communications. In this section, a leaky-wave antenna (LWA) array (Ant-2) is proposed for the 28 GHz millimeter-wave band. This section also shows that a compact LWA array with high radiation efficiency and wide impedance bandwidth may be designed for 5G millimeter-wave application. This can be done by replacing the outer shorting pins by an appropriate radiating patch and using a superstrate as a dielectric load.

3.3.1 Antenna Configuration

The geometry of the presented LWA array (Ant-2) and its placement in a mobile device substrate are shown in Fig. 3.11. The array is designed on a Rogers 5870 substrate ($\epsilon_r = 2.33$ and $\tan\delta = 0.0012$) with a thickness of 0.8 mm, and a copper-cladding thickness of 0.013 mm. The proposed antenna array is composed of four half-width microstrip leaky wave antennas (HW-MLWAs) placed at right angles.

The antenna in this section is designed based on the design has been demonstrated for below 6 GHz operation in [117] with each element is loaded with a shorting pin and basic concept for designing HW-MLWA are discussed in Section 2.8. However, each element is composed of a HW-MLWA loaded with an $l_2 \times w_2$ radiating patch for the design presented in this section.

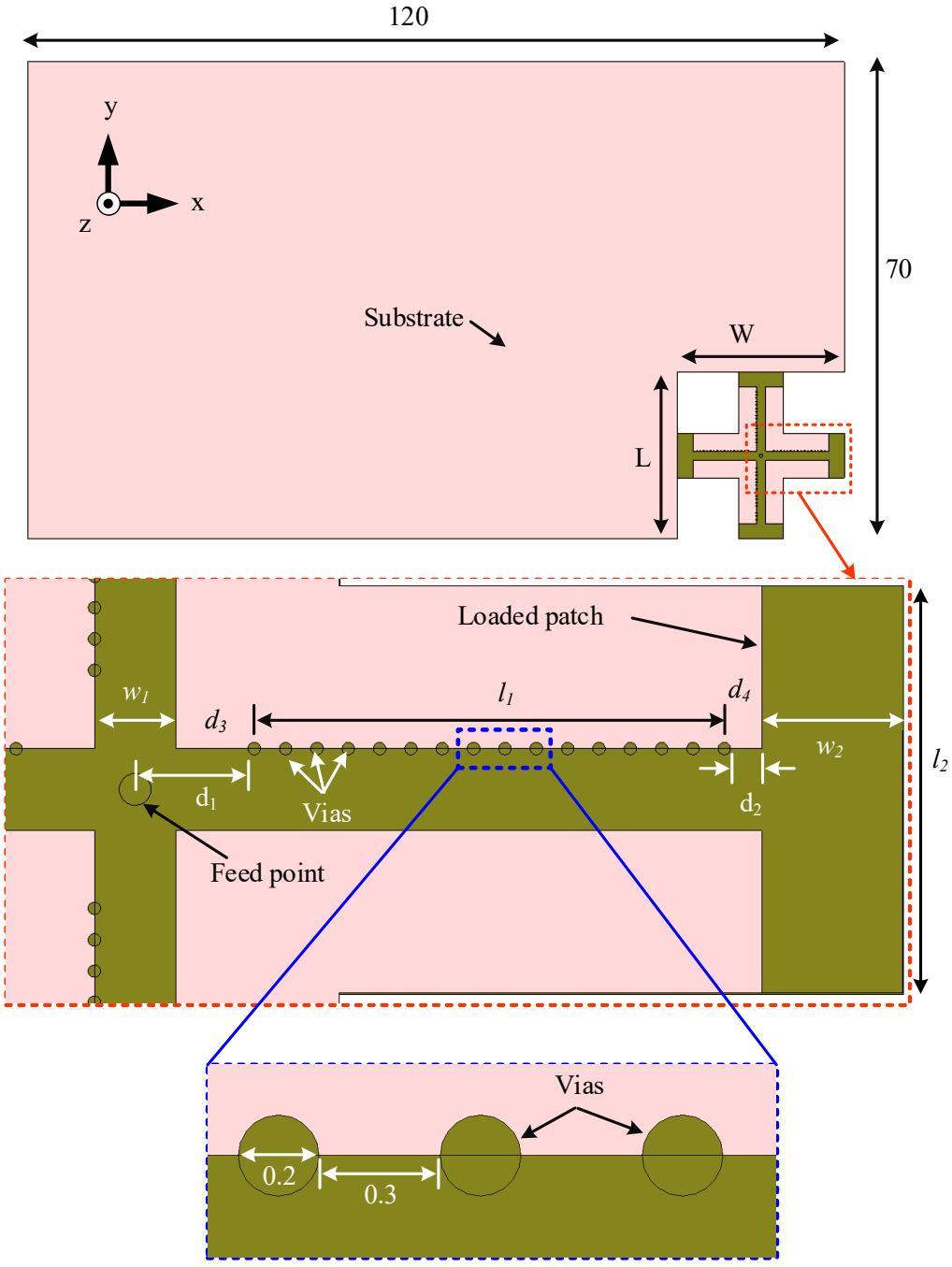

Figure 3.11: Configuration of the LWA array (Ant-2) radiating boresight for 28 GHz millimeter-wave 5G terminals and the placement of the LWA array in a mobile phone substrate (top view without dielectric load). All dimensions are in millimeters.

The array is fed at the center from the bottom of the substrate using a 2.92 mm coaxial connector. Note that most 2.92 mm connectors are of the panel-mount type. To ensure a guaranteed connection between the center pin of the coaxial connector with the antenna feed point, a cylindrical patch of inner and outer radius 0.2 and 0.3 mm, respectively, is employed as shown in the inset of Fig. 3.12. A copper circle of radius 0.8 mm is etched off from the ground in order to ensure isolation between the ground plane and the center pin of the coaxial connector.

For antenna input impedance matching the first shorting pin in each element is placed d_1 away from the center point of the array. For impedance matching between the leaky-wave antenna and the loaded patch, the location of the last shorting pin in each element is optimized using parameter analyses and is d_2 away from the patch. Here, the diameter of the shorting pin is 0.2 mm and the spacing between the two adjacent shorting pins is 0.5 mm (center to center).

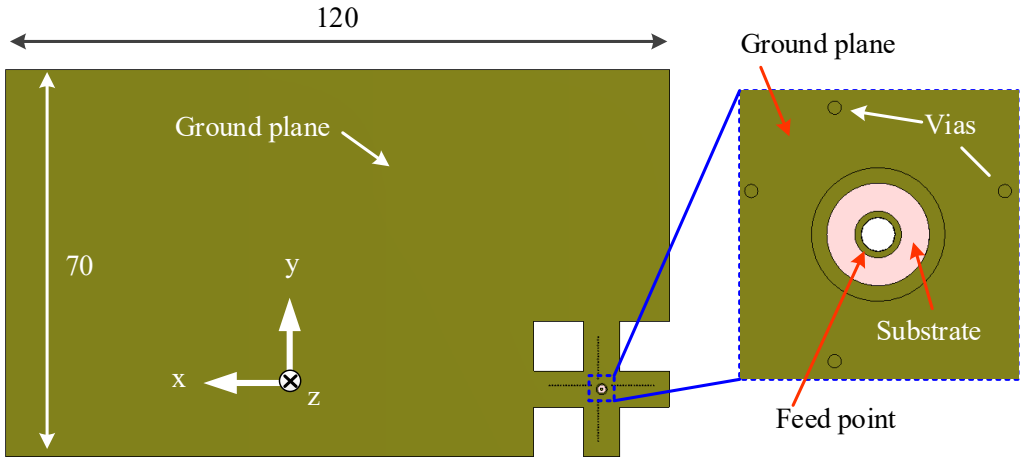

Figure 3.12: Back view of the LWA array (Ant-2) radiating boresight for 28 GHz millimeter-wave 5G terminals and the feed arrangement for 2.92 mm coaxial connector. All dimensions are in millimeters.

The overall dimensions of the array are 24.5 mm $\times$ 24.5 mm ($L \times W$) and it may

be placed in any corner of the substrate with a size of 120 mm × 70 mm. To improve of the antenna efficiency and impedance matching, a superstrate acting as a dielectric load is employed on top of the antenna, which is oriented with the center of the antenna. The dimensions of the antenna are optimized using parameter analyses in CST microwave studio. The optimized dimensions are listed in Table 3.3.

Table 3.3: Design Parameters of The Boresight-Radiating LWA Array (Ant-2). All dimensions are in millimeters.

$d_1 = 1.8$	$d_2 = 0.5$	$d_3 = 1.25$	$d_4 = 0.6$	$l_1 = 7.5$
$l_2 = 6.5$	$w_1 = 1.3$	$w_2 = 2.25$	$L = 24.5$	$W = 24.5$

The design of this highly efficient leaky-wave antenna (LWA) array (Ant-2) radiating towards the boresight direction is encompasses into two major steps. Initially, an LWA array radiating in the boresight direction is developed. Then a superstrate which acts as a dielectric load is employed in order to enhance the antenna efficiency. The presented array is designed using CST Microwave Studio and the dimensions are optimized using parameter analyses. It is found that the mobile device battery has no effect on antenna performance as by the study presented in the previous two sections. The following section presents results when no battery is present.

3.3.2 Effects of Superstrate and Simulation Results

The effects of the dielectric load on the antenna's performance are briefly presented here. A superstrate as a dielectric load with dimensions of 6 mm × 6 mm × 0.8 mm, and is placed at the top of the antenna in order to improve its performance. The center of the dielectric load is aligned with the feed point of the antenna array as shown in Fig. 3.13. The size and the material of the dielectric load are optimized using numerical analysis

in CST. In simulation, better impedance matching is observed when the superstrate is of Rogers 5870 substrate ($\epsilon_r = 2.33$ and $\tan\delta = 0.0012$) with a thickness of 0.8 mm. The overall size of the proposed antenna is 24.5 mm $\times$ 24.5 mm $\times$ 1.6 mm including the dielectric load.

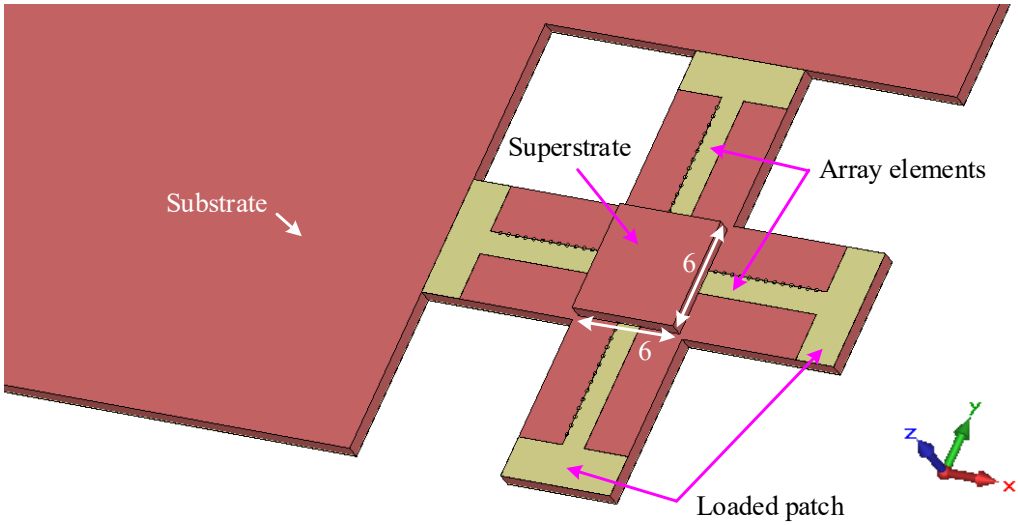

Figure 3.13: Perspective view of Ant-2 with the dielectric load. All dimensions are in millimeters.

The proposed LWA array covers the 28 GHz millimeter-wave 5G wireless communication band with a large impedance bandwidth ($|S_{11}| < -10$ dB) of 3.1 GHz (27.2-30.3 GHz) without the dielectric load, as illustrated in Fig. 3.14. The antenna impedance bandwidth becomes much greater with the use of a dielectric (see Fig. 3.14). With the presence of the dielectric load the array impedance bandwidth ($|S_{11}| < -13$ dB) is 6 GHz (26-32 GHz).

The antenna efficiency reaches its maximum when the dielectric load material is the same as the antenna substrate, Rogers 5870. Fig. 3.15 shows the antenna efficiency when the dielectric load is employed, and the results are compared with the antenna efficiency when no superstrate is applied.

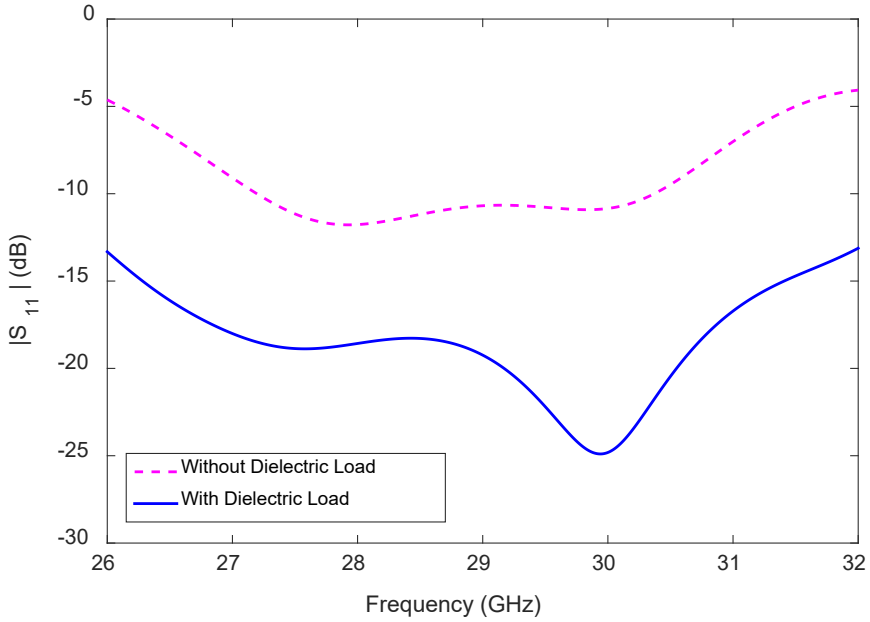

Figure 3.14: Reflection coefficient of the boresight-radiating LWA array (Ant-2) with and without dielectric load.

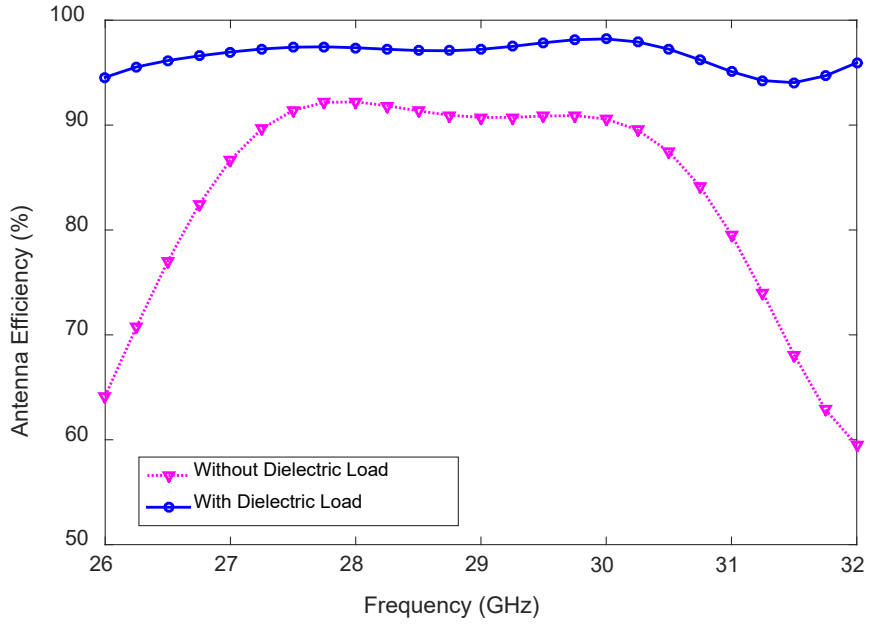

Figure 3.15: Antenna efficiency of the boresight-radiating LWA array (Ant-2) with and without dielectric load.

The antenna efficiency is almost flat within the 28 GHz millimeter-wave band (28-29.5 GHz) and an improvement of 6% is observed. The antenna efficiency varies between 60% and 92% without dielectric loading, within the reflection coefficient bandwidth. However, with the presence of the dielectric load the antenna efficiency improves significantly and varies between 95% and 98% within the reflection coefficient bandwidth. This efficient improvement because of the improvement in antenna impedance matching illustrated in Fig. 3.14.

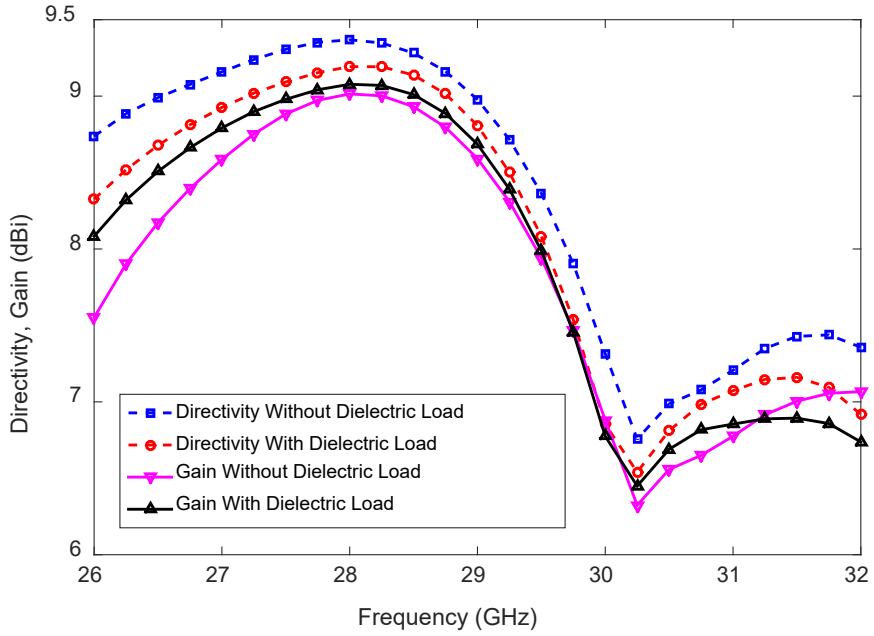

Figure 3.16: Directivity and gain of the boresight-radiating LWA array (Ant-2) with and without dielectric load.

The directivity and gain of the LWA array within the reflection coefficient bandwidth are shown in Fig. 3.16 with and without the dielectric load. The maximum directivity and gain for the array are 9.4 and 9 dBi, respectively at 28 GHz, and the minimum directivity and gain are 6.8 and 6.3 dBi, respectively, at 30.25 GHz, without the dielectric loading. The antenna directivity decreases slightly with the use of a dielectric load as shown in Fig. 3.16, however, the gain increases in the frequency ranges 26-29.5 GHz and 30-31.25

GHz. Nonetheless, a decrease in the antenna gain is observed when dielectric loading is applied in the 29.5-30 GHz and 31.25-32 GHz frequency ranges. With the dielectric loading, the maximum directivity and gain are 9.2 and 9.1 dBi, respectively, at 28 GHz, while the minimum directivity and gain are 6.5 and 6.4 dBi, respectively, at 30.25 GHz. The gain variation within the 28 GHz millimeter-wave band is only 1.1 dB, but within the antenna reflection coefficient bandwidth it is 2.7 dB.

3.3.3 Parameter Analysis

The distance between the feed point and the first via is d_1 (shown in Fig. 3.11), a key parameter that significantly affects the array's impedance matching and hence the antenna efficiency, as presented in this section. The results presented here are based on simulation with the dielectric load applied to the array.

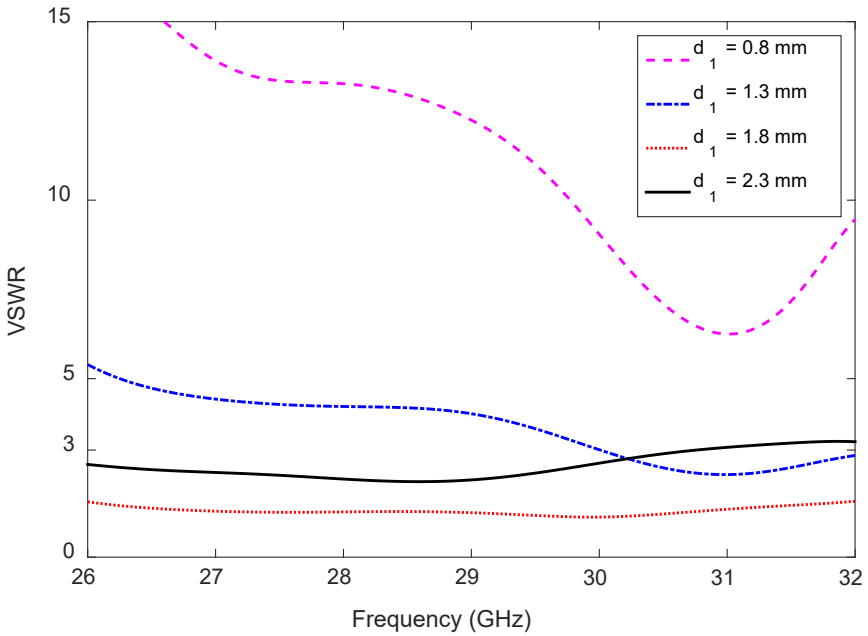

Figure 3.17: Antenna impedance matching at several locations of the first via in each array element.

The impedance matching within the antenna reflection coefficient bandwidth is very

poor when the distance d_1 is 0.8 mm as shown in Fig. 3.17. Impedance matching is improved with an increase in the distance of the first shorting pin to 1.8 mm and then worsens with a further increase in the distance d_1, as indicated in Fig. 3.17. Very good antenna input impedance matching is observed when $d_1 = 1.8$ mm and the dielectric load is present.

3.3.4 Radiation Patterns

The normalized radiation patterns of Ant-2 in the x-z and y-z planes are shown in Fig. 3.18 and Fig. 3.19, respectively. The patterns are presented in both planes at 27.5, 28, 28.5, 29, 29.5, and 30 GHz. At each frequency, the x-z plane and y-z plane radiation patterns are normalized with respect to the magnitude at that frequency. The radiation patterns point towards the +z-axis in both the x-z and y-z planes, as shown in Figs. 3.18 and 3.19.

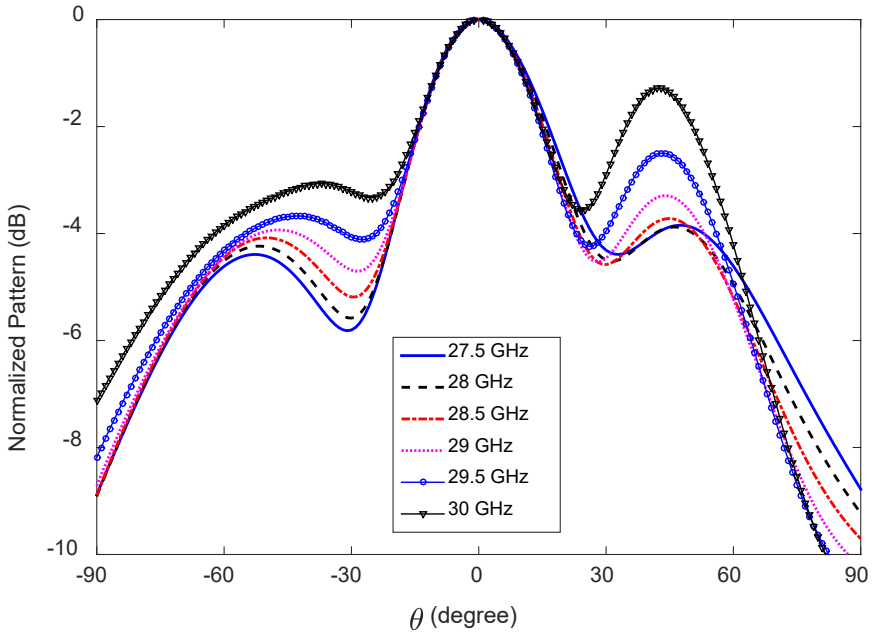

Figure 3.18: Normalized radiation patterns of the boresight-radiating LWA array (Ant-2), with the presence of the battery, in the x-z plane.

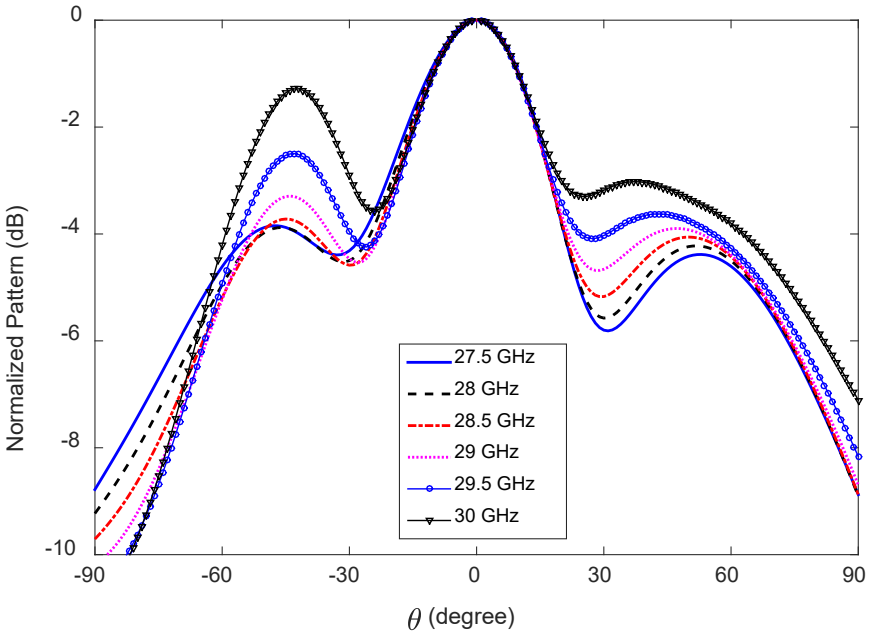

Figure 3.19: Normalized radiation patterns of the boresight-radiating LWA array (Ant-2), with the presence of the battery, in the y-z plane.

Table 3.4: Side-lobe level (SLL) and half-power beamwidth (HPBW) of the LWA array (Ant-2) radiation boresight in x-z and y-z planes.

Frequency (GHz)		27.5	28	28.5	29	29.5	30
SLL (dB)	x-z plane	-4	-4	-4	-3	-3	-1
	y-z plane	-4	-4	-4	-3	-3	-1
HPBW (degree)	x-z plane	39	38	37	36	36	39
	y-z plane	39	38	37	36	36	39

The side-lobe level (SLL) and half-power beamwidth (HPBW) for the x-z and y-z planes are listed in Table 3.4. In both the x-z and y-z planes, the HPBW varies between 36° and 39° and the HPBWs are equal in both planes at each frequency. Furthermore the SLLs are equal at each frequency in both the x-z and y-z planes, and the SLL decreases with increasing frequency in the frequency range 27.5-30 GHz. The SLL is -4 dB at 27.5

to 28.5 GHz, -3 dB at 29 and 29.5 GHz. The SLL is even worse at 30 GHz and is -1 dB.

3.4 Wideband PIFA (Ant-3) with Superstrate

The PIFA (Ant-1) with superstrate presented in Section 3.2 is a narrow-band antenna unable to cover the 28 GHz millimeter-wave 5G mobile communication band. On the other hand, the antenna presented in Section 3.3 (Ant-2) is a wideband antenna and covers the above mentioned band completely. Ant-1 has a very good SLL in both the x-z and y-z planes and it is always below -14 dB in the frequency range 27.5-28.5 GHz, but the SLL of Ant-2 is very poor within the 28 GHz millimeter-wave band and it varies in the range -4 dB to -1 dB within the frequency range 27.5-30 GHz. In this section another PIFA (Ant-3) with superstrate is developed which is the modification of Ant-1 targeting to increase the impedance bandwidth of the antenna.

3.4.1 Antenna Configuration

Similar to Ant-1 and Ant-2, the wideband PIFA has been designed to print on a Rogers 5870 substrate with a dielectric constant of $\epsilon_r = 2.33$ and loss tangent of tan $\delta = 0.0012$, having a thickness of $h = 0.635$ mm; the copper layer's thickness is 0.035 mm. The dimensions of the mobile phone substrate have been chosen as 120 mm $\times$ 70 mm.

The Ant-1 is investigated in CST using parameter analyses to identify the reason behind narrow-band operation. It is found that the two I-shaped slots at the center of the antenna, oriented at right angle, reduces the impedance bandwidth of the antenna. After removing both I-shaped slot from the centre of the Ant-1, the antenna is optimized using parameter analyses in CST for four I-shaped slot located close to the each edge of the patch.

A detailed configuration of the presented wideband millimeter-wave antenna (Ant-3)

is presented in Fig. 3.20 (a), which includes 4 I-shaped slots of dimensions w mm $\times$ l mm in vertical and horizontal orientations, located s mm away from each edge of an L mm $\times$ W mm square patch. In addition, the location of the fed via is optimized for better impedance matching using parameter analyses in CST.

The presented antenna uses a superstrate as a dielectric load, in order to enhance the directivity, gain and efficiency, made of the same material as the substrate, with equal thickness, and the overall thickness of the antenna is 1.34 mm. The size of the dielectric load is $(L + 1)$ mm $\times$ $(W + 1)$ mm.

The antenna is optimized using parameter analysis in CST microwave studio and the optimized dimensions are listed in Table 3.5. During simulation, the antenna is assumed to be fed with a ground-signal-ground (GSG) probe with a pitch of 200 microns and the orientation of the GSG pad shown in Fig. 3.20 (c). No external feed network is required for this design, which has the advantage of high efficiency.

Table 3.5: Design parameters of the wideband PIFA (Ant-3) with dielectric load. All dimensions are in millimeters.

$a = 1.1$	$b = 0.9$	$c = 0.5$	$d = 0.55$	$s = 0.3$
$w = 0.2$	$l = 1.9$	$p = 1.2$	$L = W = 3$	$H = 1.34$

The antenna is placed at the top-right corner of a mobile phone with a battery with the dimensions of 35 mm $\times$ 70 mm, as shown in Fig. 3.20 (d). A gap of 1 mm is allowed between the battery and the substrate of the mobile phone. The overall size of the proposed millimeter wave 5G antenna is $0.37\lambda_0 \times 0.37\lambda_0 \times 0.125\lambda_0$, where λ_0 is the free-space wavelength at 28 GHz.

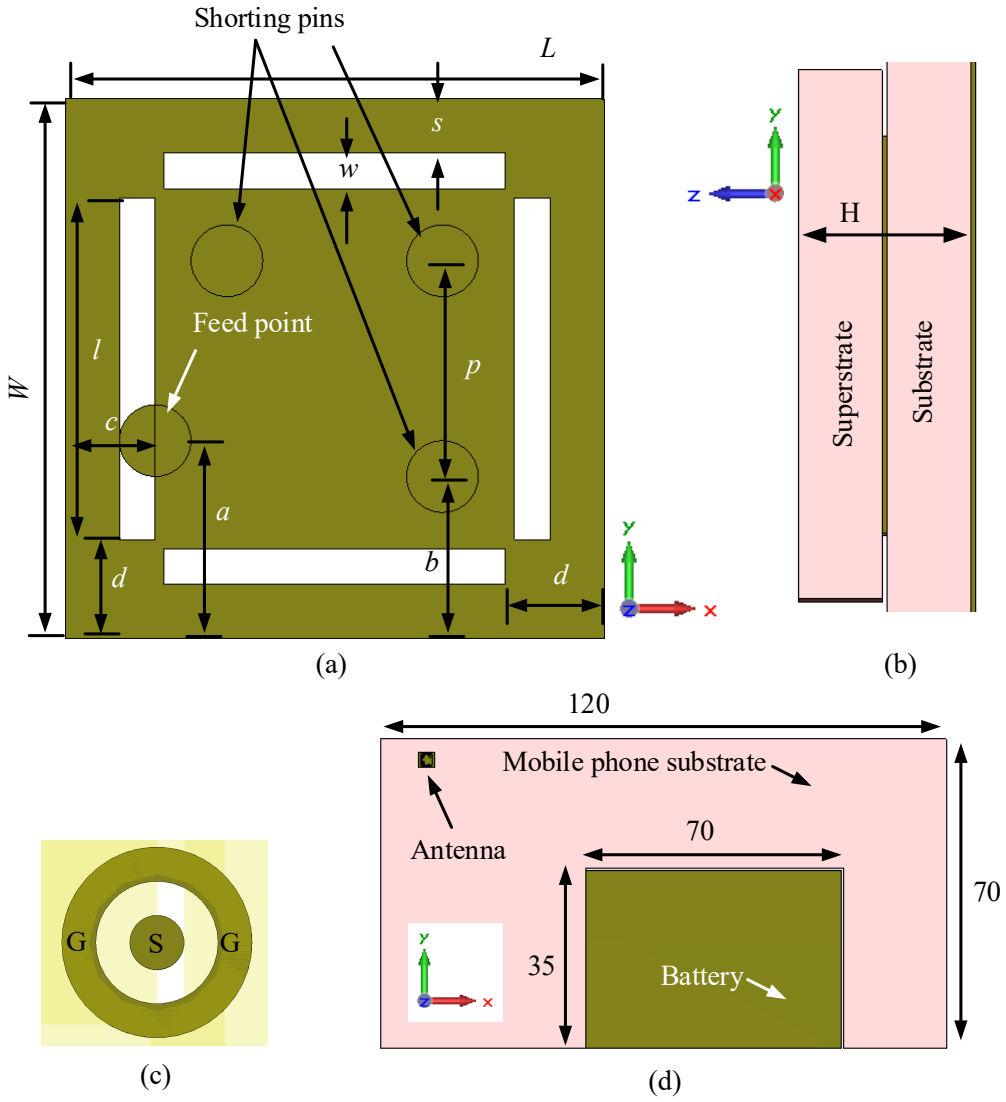

Figure 3.20: Configuration of the wideband PIFA (Ant-3) with dielectric load for millimeter wave 5G applications and its placement in a cell phone substrate: (a) top view of the radiating element without dielectric load, (b) side view of the antenna with dielectric load, (c) ground-signal-ground (GSG) pad for feeding, and (d) battery placement with respect to the antenna of the mobile phone. All dimensions are in millimeters.

3.4.2 Effects of Superstrate and Simulation Results

In this section the reflection coefficient, directivity, gain, and efficiency of Ant-3 with and without the presence of the superstrate as a dielectric load are presented and discussed. Since the performance of the antenna is unaffected when the battery is removed (demonstrated in Section 3.2) from the mobile phone substrate, the results presented in this section are based on the simulation when the battery is present.

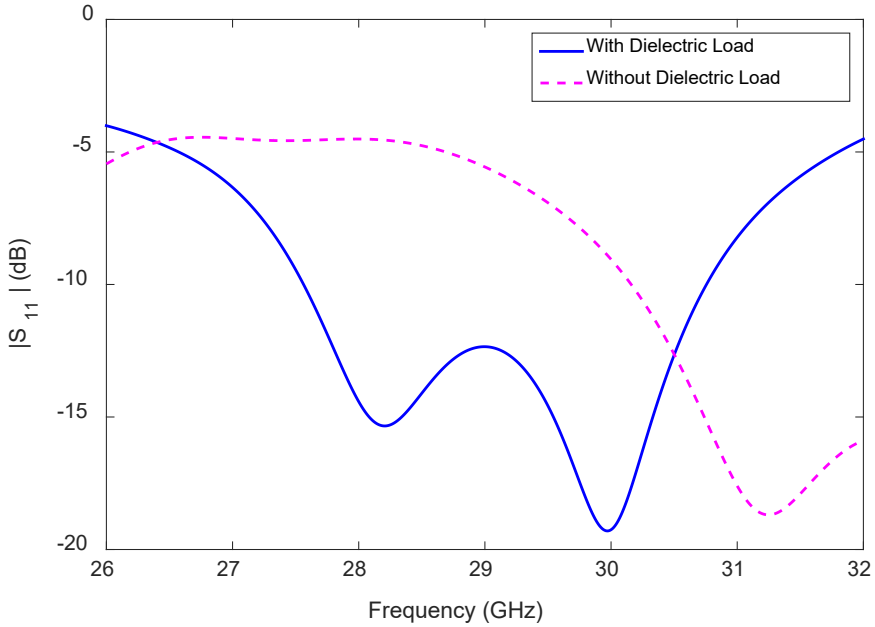

Figure 3.21: Reflection coefficient of the wideband PIFA (Ant-3) with dielectric load and when the battery is present.

The proposed antenna does not cover the 28 GHz millimeter-wave band when the superstrate is not present as shown in Fig. 3.21. It is clear from the figure that an improvement in antenna impedance matching is observed when the dielectric load is applied. When the superstrate is present, the antenna has a large impedance bandwidth of 3.18 GHz (27.57 - 30.75 GHz) measured at -10 dB, exhibited in Fig. 3.21, covering the 5G mobile communication band or millimeter-wave frequency band for future 5G mobile devices. Two resonances are observed within the reflection coefficient bandwidth, the first

at 28.3 GHz and the second at 30 GHz.

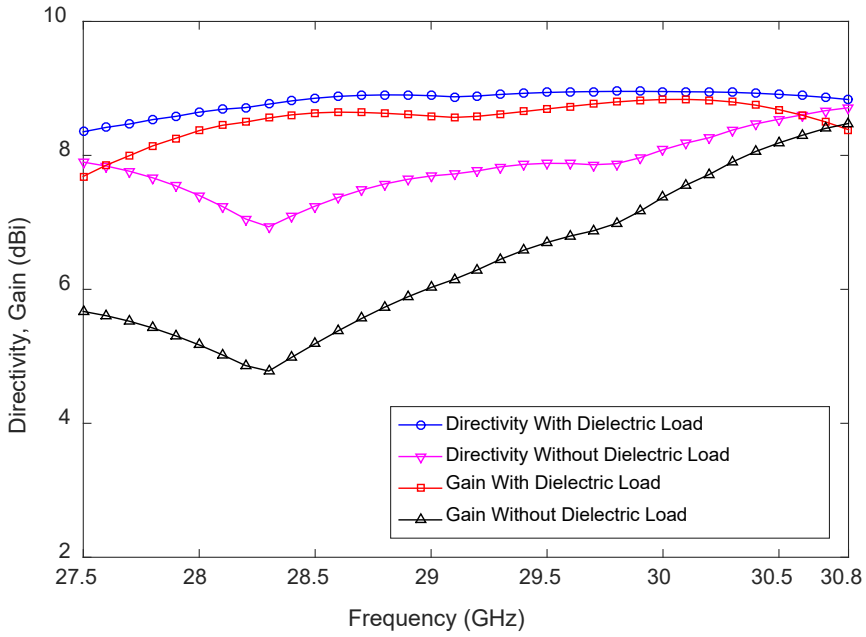

Figure 3.22: Effect of the dielectric load on the directivity and gain of the wideband PIFA (Ant-3).

Fig. 3.22 depicts the effects of the dielectric load on the antenna directivity and gain. The directivity varies between 6.9 and 8.7 dBi within the reflection coefficient bandwidth without the dielectric load and the minimum and maximum are observed at 28.3 and 30.8 GHz, respectively. A maximum of 2 dB improvement in directivity (at 28.3 GHz) is observed when the dielectric load is applied. With dielectric load, the minimum directivity of Ant-2 is 8.5 dBi at 27.5 GHz and the maximum directivity is 9 dBi at 30 GHz. Without the dielectric load, the variation of the directivity within the reflection coefficient bandwidth is $\leq$ 1.8 dB whereas this variation with the dielectric load is only $\leq$ 0.5 dB.

A significant improvement in the antenna gain is observed when the dielectric load is applied, as shown in Fig. 3.22. With the dielectric load, the minimum and maximum antenna gains are 7.7 and 8.8 dBi, at 27.5 and 30.1 GHz, respectively. Therefore, the gain variation within the reflection coefficient bandwidth is only 1.1 dB, indicating the

uniformity of the antenna radiation. On the other hand, without the dielectric load, the minimum antenna gain is 4.8 dBi and the maximum gain is 8.5 dBi, which indicates that the antenna gain variation is 3.7 dB; the antenna radiation is non-uniform within the reflection coefficient bandwidth.

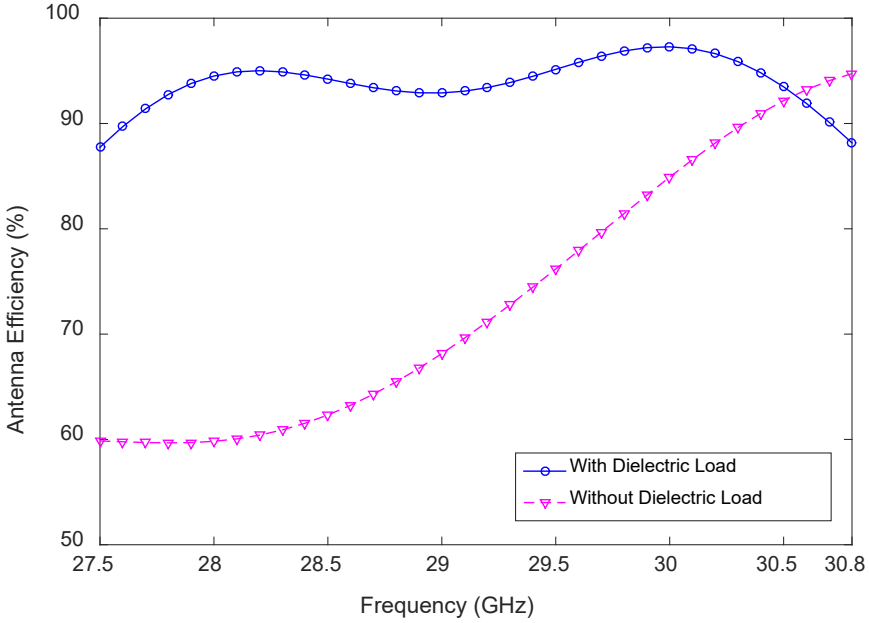

Figure 3.23: Effect of the dielectric load on the efficiency of the wideband PIFA (Ant-3).

Now, the effect of the dielectric load on the antenna efficiency is investigated. Fig. 3.23 shows the antenna efficiency with and without the presence of the dielectric load. The improvement in antenna efficient is due to the improvement in antenna input impedance matching when the dielectric load is applied. Because of the impedance matching improvement the gain of the antenna is increased hence efficiency improved. The antenna efficiency varies between 60% and 95% within the reflection coefficient bandwidth. Here, the minimum efficiency is observed at 27.5 GHz and the maximum at 30.8 GHz, with a nearly linear increase in the efficiency with frequency, as revealed in Fig. 3.23. With the dielectric load, a maximum 35% improvement in antenna efficiency is observed at 27.2 GHz. The minimum and maximum antenna efficiency are 86% and 97%, at 27.5 and

30.1 GHz, respectively. Therefore, the variation of the efficiency is below 10% within the reflection coefficient bandwidth, when the dielectric load is present.

3.4.3 Radiation Patterns

The normalized radiation patterns of Ant-3 in the x-z and y-z planes are shown in Fig. 3.24 and Fig. 3.25, respectively. The patterns are presented in both planes for the frequency range 27.5-30.5 GHz with a step of 0.5 GHz. At each frequency, the x-z plane and y-z plane radiation patterns are normalized with respect to the magnitude at that frequency.

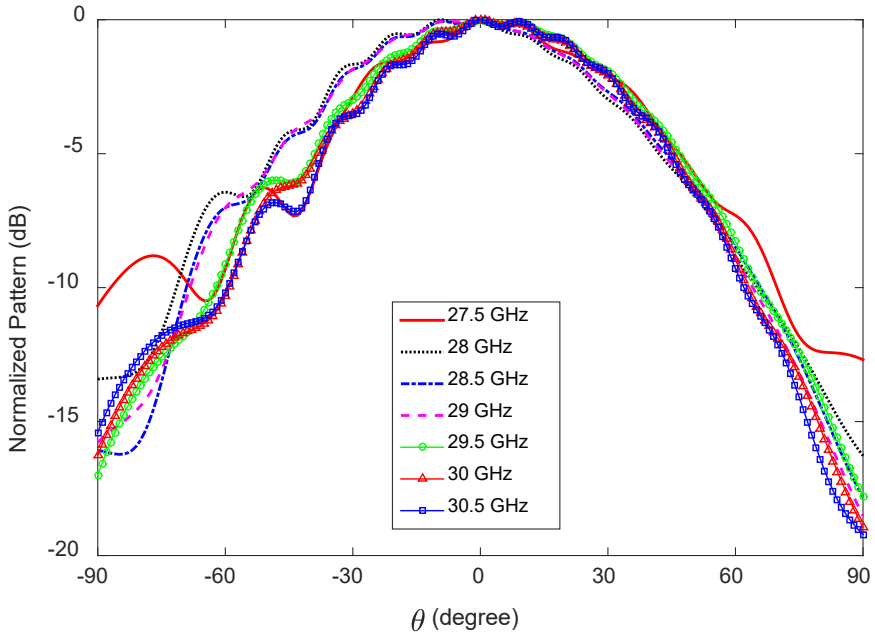

Figure 3.24: Normalized radiation patterns of the wideband PIFA (Ant-3) with dielectric load, and with the presence of the battery, in the x-z plane.

The radiation patterns point towards boresight, i.e. towards the +z-axis in both the x-z and y-z planes, within the reflection coefficient bandwidth. The side-lobe level (SLL) and half-power beamwidth (HPBW) or 3-dB beamwidth for the x-z and y-z planes radiation patterns are listed in Table 3.6. In the x-z plane, the maximum and minimum

HPBW are 68° and 61°, respectively, and in the y-z plane are 70° and 56°, respectively. The HPBW of Ant-3 in the x-z plane decreases from 68° to 61° with increasing frequency from 27.5 GHz to 30.5 GHz. On the other hand, the HPBW increases from 56° to 70° with increasing frequency from 27.5 GHz to 30.5 GHz. Ant-3 has a better SLL in the x-z plane than in the y-z plane. The SLL of Ant-3 in the x-z plane is always below -17 dB within the frequency range 28-30.5 GHz, but the SLL is -9 dB at 27.5 GHz. In the y-z plane, the SLL is -4, -6, and -8 dB at 27.5, 28, and 28.5 GHz, respectively. However, the SLL in the y-z plane is always below -19 dB in the frequency range 29-30.5 GHz. Overall, the SLL of Ant-3 in both the x-z and y-z planes are better at a frequency close to the second resonant (30 GHz) than is the SLL in the x-z and y-z planes at a frequency close to the first resonant (28.3 GHz).

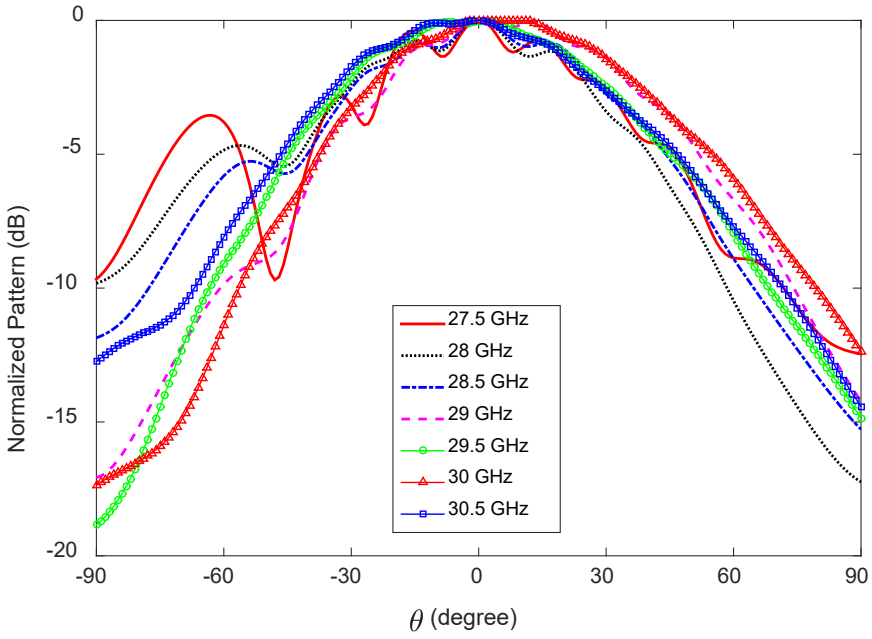

Figure 3.25: Normalized radiation patterns of the wideband PIFA (Ant-3) with dielectric load, and with the presence of the battery, in the y-z plane.

Table 3.6: Side-lobe level (SLL) and half-power beamwidth (HPBW) of the wideband PIFA (Ant-3) with dielectric load in x-z and y-z Planes.

Frequency (GHz)		27.5	28	28.5	29	29.5	30	30.5
SLL (dB)	x-z plane	-9	-17	-19	-22	-20	-20	-19
	y-z plane	-4	-6	-6	-19	-20	-21	-19
HPBW (degree)	x-z plane	68	67	68	68	67	62	61
	y-z plane	56	61	64	64	68	69	70

3.5 Comparison between Antennas

In this section, a comparison of the properties of the antennas presented in this chapter. Table 3.7 lists a performance comparison between Ant-1, Ant-2, and Ant-3. In terms of the achieved -10 dB reflection coefficient bandwidth, Ant-2 has 21% measured at -13 dB whereas Ant-1 has 4% (measured at -10 dB) and Ant-3 has 11% (measured at -10 dB) bandwidth. Yet, Ant-1 and Ant-3 are 97% smaller in size than Ant-2. The presented antennas have comparable efficiency, directivity and gain within the 28 GHz millimeter-wave 5G mobile communication band. Regarding the SLL, Ant-1 has a very low SLL in both the x-z and y-z planes compared to Ant-2. On the other hand, Ant-3 has a lower SLL in the x-z plane than in the y-z plane, and in both planes they are low compared to Ant-2. The HPBW of Ant-1 and Ant-3 are below 70° and for Ant-2 are below 38°. Overall, Ant-3 covers the 28 GHz millimeter-wave 5G mobile communication band and has a relatively low SLL together with comparable gain, directivity and efficiency to Ant-1 and Ant-2.

Table 3.7: Performance comparison of boresight-radiating narrow-band PIFA (Ant-1), LWA array (Ant-2), and wideband PIFA (Ant-3) antennas. Here, the results are compared within the 28 GHz millimeter-wave band (28-29.5 GHz).

Parameter		Ant-1	Ant-2	Ant-3
Physical Area (mm^2)		16	600	16
Bandwidth (GHz)		27.47-28.45	26-32*	27.57-30.75
Efficiency (%)		88-96	97-98	94-96
Directivity (dBi)		8.9-9.2	8.9-9.4	8.7-8.9
Gain (dBi)		8.1-8.6	8.4-9	8.4-8.8
SLL (dB)	x-z plane	$\leq$ -11	$\leq$ -3	$\leq$ -17
	y-z plane	$\leq$ -19	$\leq$ -3	$\leq$ -6
HPBW (degree)	x-z plane	$\leq$ 65	$\leq$ 38	$\leq$ 68
	y-z plane	$\leq$ 72	$\leq$ 38	$\leq$ 68

Here SLL means side-lobe level and HPBW means half-power beamwidth.

* -13 dB reflection coefficient bandwidth.

Now, the comparison of the performance of the proposed wideband PIFA (Ant-3) with reference antennas available for 28 GHz millimeter-wave 5G hand-held mobile devices having a directed beam. The size (area = length $\times$ width), gain, efficiency, and beam direction of the reference antennas together with Ant-3 are listed in Table 3.8. The proposed Ant-3 for 28 GHz millimeter-wave mobile devices has a higher efficiency than the reference antennas proposed for the same application. Owing to its compact size and good performance, the proposed antenna Ant-3 is attractive for future 5G mobile devices.

Table 3.8: The area, efficiency, gain, and beam direction of Ant-3 and the reference antennas proposed for the millimeter-wave 5G mobile communication band. Here, the results are compared within the 28 GHz millimeter-wave band (28-29.5 GHz).

References	Area (mm^2)	Efficiency (%)	Gain (dBi)	HPBW x-z and y-z planes
[136]	546	NA	10-13.5	NA
[41]	35	NA	4.6-6.7	NA
[43]	870	NA	9*	NA
[108]	7	72-75	2.3-2.8	180° and 170°
[51]	4445	60-75	9.95-10.19	10° and 80°
Ant-3	16	94-96	8.4-8.8	68° and 68°

Here, area = length × width; NA = not available;

*maximum value.

3.6 Summary

In this chapter three antennas radiating to the boresight were developed for 28 GHz millimeter-wave 5G mobile devices. A superstrate that acting as a dielectric load was applied to enhance the performance of the antenna, especially the efficiency.

Firstly, a narrow-band PIFA (Ant-1) was developed. A Teflon superstrate that acting as a dielectric load was applied to enhance the efficiency, gain and directivity of the antenna. The thickness of the Teflon superstrate was the same as the thickness (0.635 mm) of the substrate considered for antenna design. A maximum 66% improvement in antenna efficiency was observed when the superstrate was applied. Moreover, the antenna input impedance matching was improved for the same antenna when the dielectric load

was applied. However, Ant-1 is unable to cover the whole 28 GHz millimeter-wave 5G mobile communication band.

Secondly, a LWA array (Ant-2) radiating boresight was developed. The efficiency of the array was improved by applying a superstrate (made of the same material as the substrate) as a dielectric load to the LWA array and applying a microstrip patch as a load to the array elements. A maximum of 36% and minimum of 5% improvement in antenna efficiency was observed. The maximum improvement in gain and directivity, 2.9 and 2 dB, respectively, were perceived when the dielectric load was applied. The HPBW of Ant-1 (64°-69° in the x-z plane and 65°-69° in the y-z plane) was almost double the HPBW (36°-39° in both the x-z and y-z planes) of Ant-2.

Thirdly, another PIFA (Ant-3) with superstrate was developed. A similar effect on the input impedance matching, efficiency, gain and directivity of Ant-3 was observed as seen in Ant-1, because of the loading by superstrate. The HPBW (61°-68° in the x-z plane and 56°-70° in y-z plane) of Ant-3 was almost equal to the HPBW observed for Ant-1.

Finally, in this chapter three antennas were described. All of them were able to radiate towards the boresight direction. Beam scanning is not possible using these antennas. In the next chapter LWAs will be developed and investigated that are suitable for pattern reconfigurable antenna development for 28 GHz millimeter-wave 5G mobile devices.

Chapter 4

Leaky-Wave Antennas (LWAs) for 28 GHz Millimeter-Wave 5G for Beam Scanning

4.1 Introduction

In this chapter, firstly, a basic leaky-wave antenna (LWA) is investigated for radiating in the region between boresight and endfire, knows as the off-boresight direction, for 28 GHz millimeter-wave band where the length of the antenna is 5.1λ. Secondly, a small-size LWA suitable for mobile devices is developed for 28 GHz millimeter-wave 5G mobile communications. The working principles of the antenna are presented with the help of reflection coefficient, radiation performance, and surface current distribution (amplitude). Thirdly, a single element LWA antenna for mobile devices is developed that radiates towards boresight. Both the mobile device antennas are terminated at the far end by using a shorting pin for impedance matching and suppression of the reflected wave. The inherent property of a uniform LWA is to scan the main beam as the frequency increases.

The effects of the loading pin are analyzed in order to find the frequency at which the boresight beam starts to split into two off-boresight beams.

This chapter is organized as follows. Section 4.2 presents the design procedure and working principles of a basic HW-MLWA radiating off-boresight (the region between boresight and endfire) for mobile devices. In Section 4.3 a boresight radiating HW-MLWA is developed for 28 GHz millimeter-wave application. The design procedure and working principles together with the simulation results are presented in the same section. Section 4.4 summarizes the main themes that have been described in this chapter.

4.2 Antenna Radiating Off-Boresight

This section presents the design of a basic LWA for 28 GHz millimeter-wave 5G mobile devices. For design simplicity a half-width microstrip LWA (HW-MLWA) is chosen.

4.2.1 Antenna for 28 GHz Millimeter-Wave Band

The antenna is designed on an FR-4 substrate with relative permittivity $(\epsilon_r) = 4.3$, loss tangent $(\tan\delta) = 0.025$, and a thickness of 0.8 mm. The configuration of the antenna is shown in Fig. 4.1. Following the method proposed in [123] an HW-MLWA is modeled for 28 GHz millimeter-wave band, i.e. the fundamental method of designing HW-MLWA is considered during the design which is briefly presented in Section 2.8.

The design starts with a microstrip JKLO with one edge KL shorted to ground using periodically arranged shorting pins. Shorting one edge of a microstrip line can excite the first higher-order mode without using a special feed network [123]. In the dominant mode the electric field is tightly bound between the microstrip and the ground plane and hence the line is unable to radiate. In the first higher-order mode the microstrip line produces a radiating electric field as discussed in Section 2.8 of Chapter 2. In LWAs a load is used

at the far/other end to suppress the reflected wave from an antenna structure with finite length. If the wave reflects back from the other end a back lobe is produced. To reduce the back lobe the radiating microstrip needs to be infinitely long. The length of the microstrip line in this design is 54.4 mm or $5.1\lambda_0$ where λ_0 is the free-space wavelength at 28 GHz. The microstrip is fed using a narrow microstrip with a width of 0.6 mm and length of 2.95 mm at the side JK. A 2.92 mm surface-mount coaxial connector is used to feed the antenna from the bottom. To suppress the reflected wave and for better impedance matching the coaxial connector at I is terminated using a 50 Ω resistive load. The antenna is designed on a substrate of size 60 mm × 8 mm.

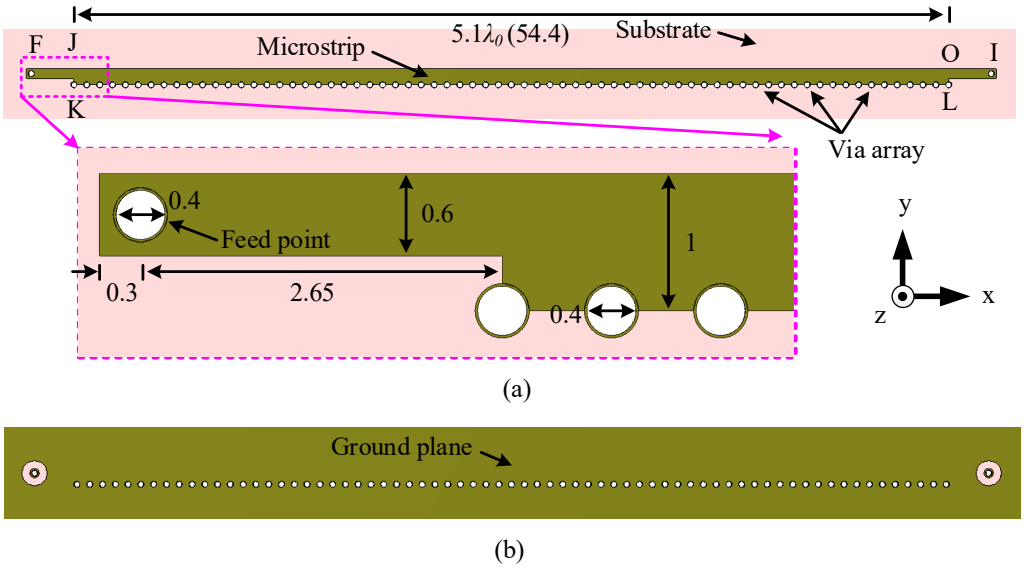

Figure 4.1: Configuration of the HW-MLWA (length = 5.1λ) for 28 GHz millimeter-wave band. All dimensions are in millimeters.

Fig. 4.2 shows the simulated reflection coefficient of the HW-MLWA. The antenna has a wide impedance bandwidth of 3.78 GHz (26.38-30.16 GHz). The surface current distribution (amplitude) at 27, 28, 29, 30, and 31 GHz, as shown in Fig. 4.3. It can be seen from the figure that as the frequency increases more energy travels toward the load, indicating an increase in the effective aperture of the antenna. A short effective aperture

widens the beam and hence the directivity is low. As the frequency increases the effective aperture increases (as illustrated in Fig. 4.3), which in turn reduces the beamwidth and improves the directivity.

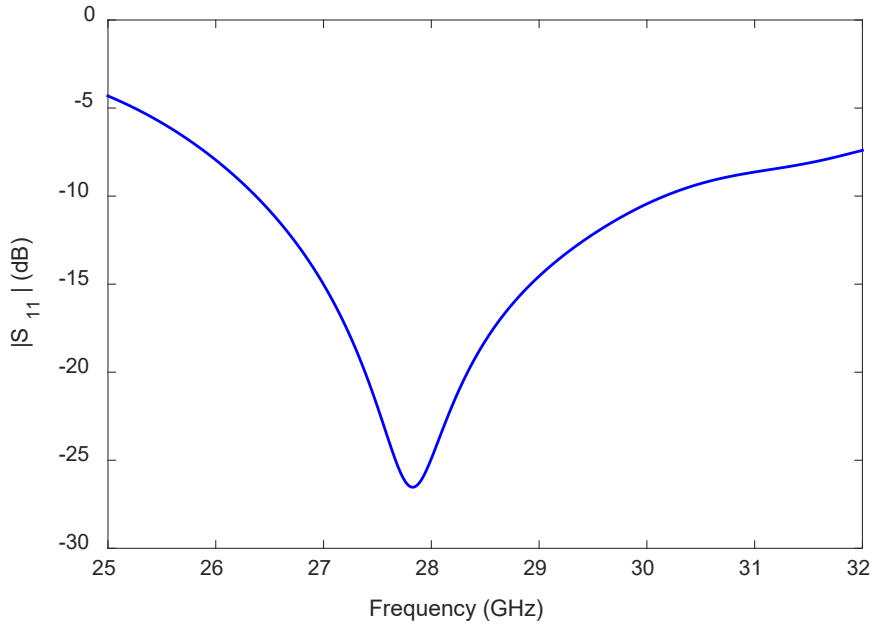

Figure 4.2: Reflection coefficient of the 28 GHz millimeter-wave HW-MLWA (length = 5.1λ) radiating off-boresight.

The predicted leakage rate (α/k_0) of the HW-MLWA (in Fig. 4.1) with length = $5.1\lambda_0$ operating in the 28 GHz millimeter-wave band is shown in Fig 4.4. The leakage rate has been calculated using the method presented in [122, 127]. It is evident from the figure that the leakage rate is maximum at 25 GHz, and it is minimum at 32 GHz within the frequency range 25-32 GHz. The leakage rate decreases gradually with increasing frequency. The leakage rates are 0.16, 0.13, 0.11, 0.09, and 0.07 at 27, 28, 29, 30, and 31 GHz, respectively. A higher value of leakage rate indicates that the most of the power radiates from a small section of the microstrip JKLO, which is close to the feed point F. Since the effective radiating aperture is low for a higher value of leakage rate it produces a wider beam and hence directivity and gain are low. On the other hand, low leakage rate

indicates that the input power propagates towards the load end of the antenna producing a larger effective aperture and hence produces a narrow beam with higher directivity and gain. These phenomena are explained using the surface current distributions shown in Fig. 4.3.

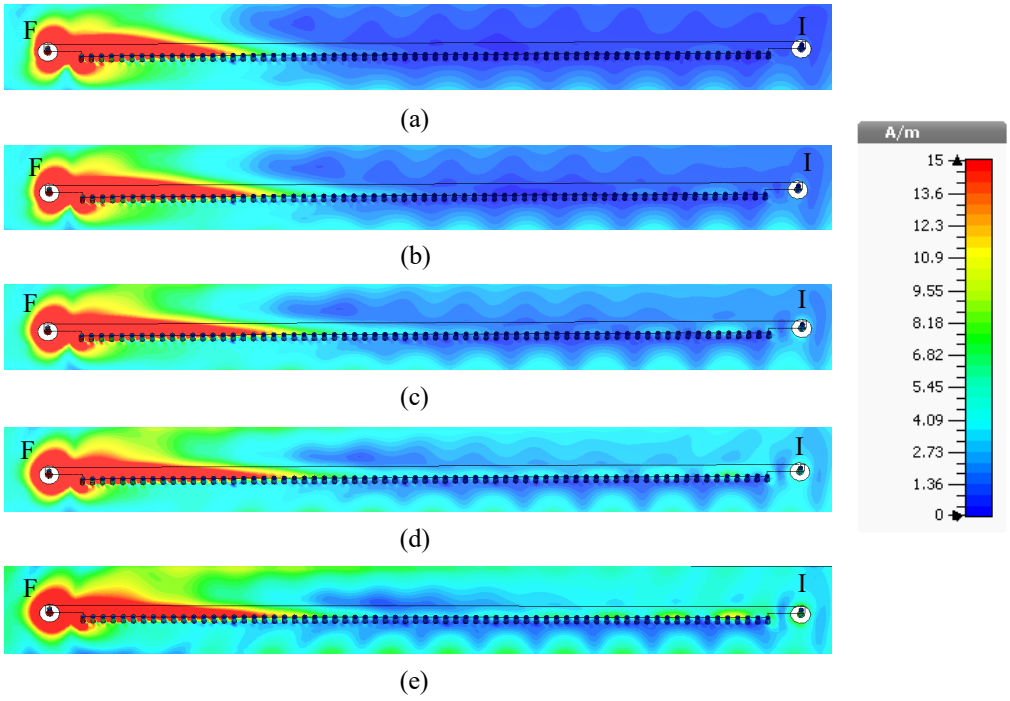

Figure 4.3: Surface current distributions (amplitude) of the 28 GHz millimeter-wave HW-MLWA (length = 5.1λ) at (a) 27, (b) 28, (c) 29, (d) 30, and (e) 31 GHz.

The normalized x-z plane radiation patterns of the HW-MLWA are shown in Fig. 4.5. The radiation patterns are presented in the frequency range 27-31 GHz with a step of 1 GHz. The direction of the main beam is $\theta = 39°$, $42°$, $57°$, $59°$, and $62°$ away from boresight at the frequency 27, 28, 29, 30, and 31 GHz, respectively, and the half-power beamwidth (HPBW) is 48°, 39°, 36°, 27° and 19° at 27, 28, 29, 30, and 31 GHz, respectively. As well, the directivity is 8, 8.8, 9.2, 9.9, and 10 dBi at 27, 28, 29, 30, and 31 GHz, respectively. Therefore, with increasing frequency the HPBW decreases, directivity increases, and the main beam shifts away from boresight. This happens because with increasing frequency

the effective aperture of the antenna increases (as shown in Fig. 4.3).

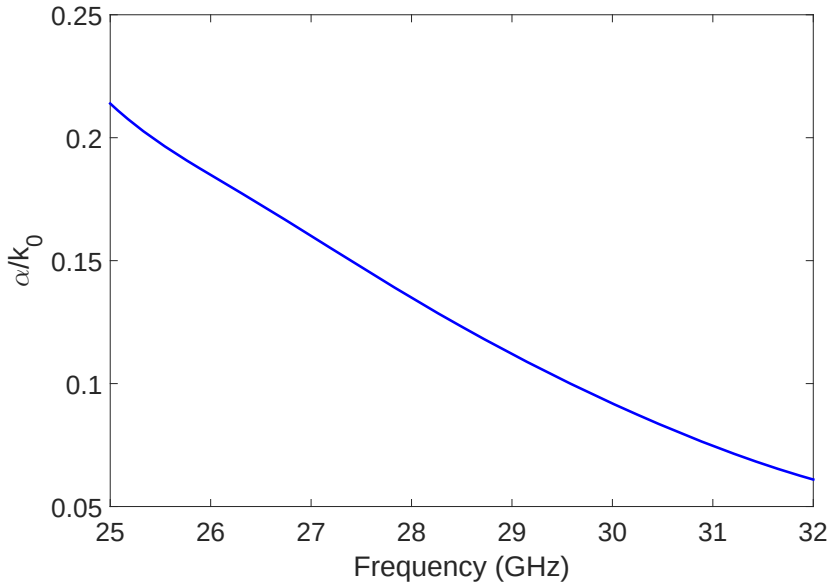

Figure 4.4: Predicted leakage constant (α/k_0) of the 28 GHz millimeter-wave HW-MLWA (length = 5.1λ) as a function of frequency.

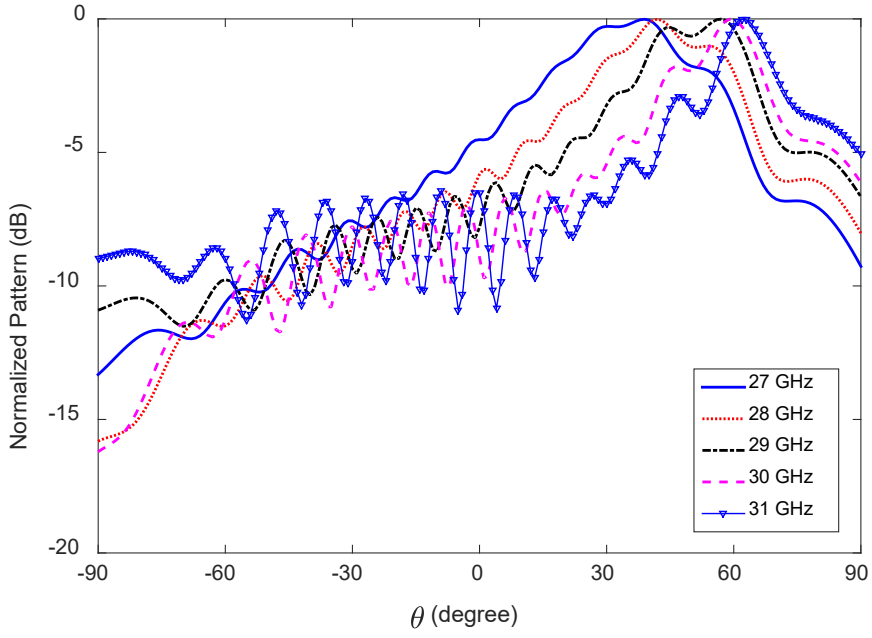

Figure 4.5: Normalized x-z plane radiation patterns of the 28 GHz millimeter-wave HW-MLWA (length = 5.1λ) radiating off-boresight.

4.2.2 Antenna for Mobile Devices

The antenna is designed on the same substrate with the same thickness. The configuration of the antenna is shown in Fig. 4.6. The size of the ground plane is equal to the size of the substrate, i.e. no ground clearance is considered for this design.

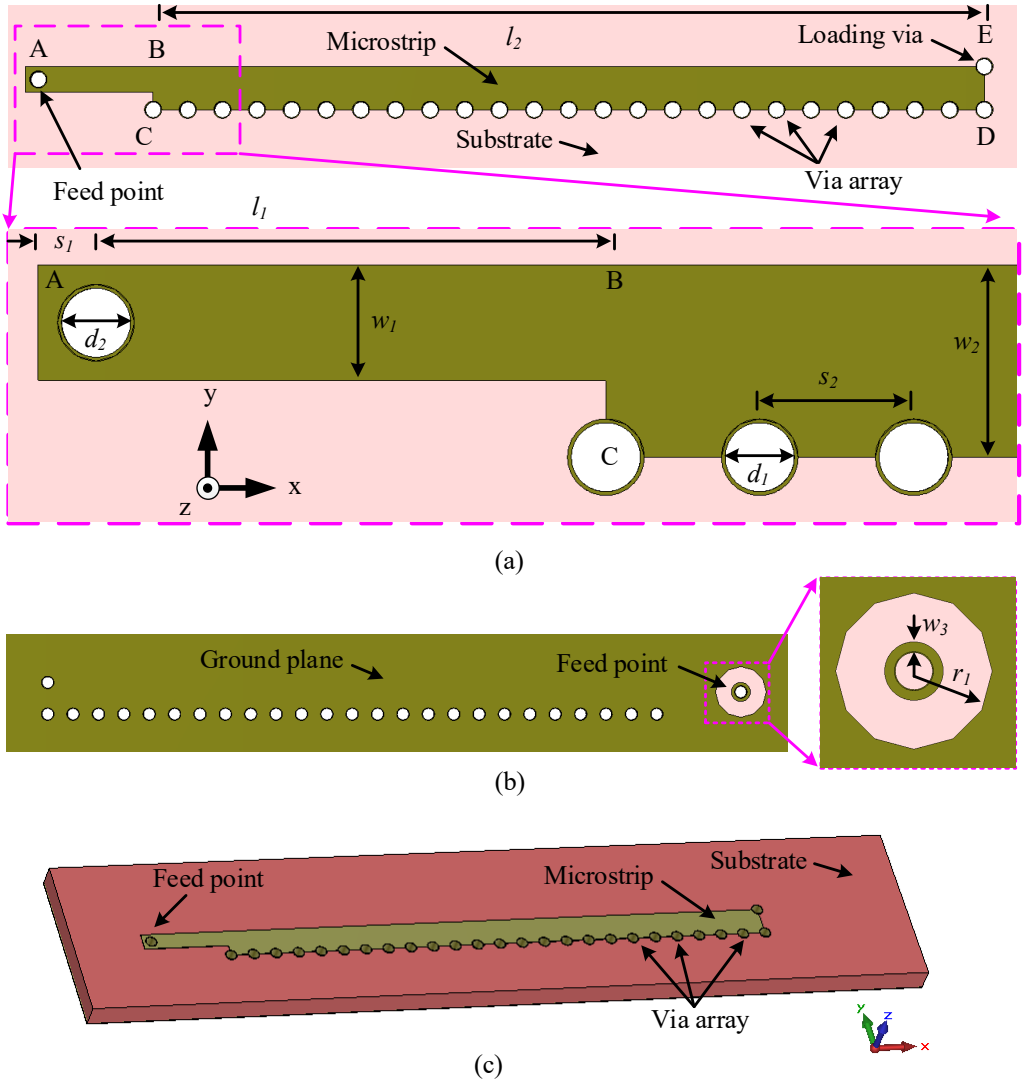

Figure 4.6: Configuration of the 28 GHz millimeter-wave HW-MLWA (length = $1.8\lambda_0$) radiating off-boresight: (a) top view, (b) back view, and (c) perspective view.

The antenna is composed of a uniform microstrip BCDE with one side, CD, shorted

to ground using periodically arranged shorting pins as shown in Fig. 4.6 (a). The design starts with a rectangular microstrip BCDE. The diameter of each shorting pin is d_1 and the center-to-center spacing between two consecutive shorting pins is s_2. For better impedance matching and to suppress the reflected wave a shorting pin is applied at the corner E of the microstrip BCDE. The diameter of this loading pin is the same as that of the shorting pins used at the edge CD. The microstrip BCDE is fed using a simple narrow microstrip of width w_1 and length $s_1 + l_1$. The dimensions of the feed line and microstrip are optimized using parameter analysis to cover the 28 GHz millimeter-wave band.

The antenna is fed using a 2.92 mm surface mount coaxial connector from the back of the substrate. The diameter of the feed via is $d_2 = 0.4$ mm. In order to ensure isolation between the feed via and the ground of the antenna, a circular-shaped segment of copper with radius $r_1 = 0.8$ mm is etched off from the ground plane. In addition, to ensure a guaranteed connection between the feed via and center pin of the coaxial connector, an annulus of copper with a width of $w_3 = 0.1$ mm (inner and outer radius 0.2 mm and 0.3 mm, respectively) is placed at the back of the antenna, as shown in Fig. 4.6 (b). The overall size of the microstrip BCDE is 19.2 mm $\times$ 1.4 mm or $1.8\lambda_0 \times 0.13\lambda_0$, where λ_0 is the free-space wavelength at 28 GHz. The optimized design parameters (using parameter analyses in CST) for the antenna are listed in Table 4.1.

Table 4.1: Design parameters of the 28 GHz millimeter-wave HW-MLWA (length = $1.8\lambda_0$) radiating off-boresight. All dimensions are in millimeters.

$d_1 = 0.4$	$d_2 = 0.4$	$s_1 = 0.3$	$s_2 = 0.8$	$w_1 = 0.6$
$w_2 = 1$	$w_3 = 0.1$	$l_1 = 2.65$	$l_2 = 19.2$	$r_1 = 0.8$

4.2.3 Working Principle

The reflection coefficient of the off-boresight radiating LWA in Fig 4.6 is shown in Fig. 4.7. The antenna has a large impedance bandwidth of 4.14 GHz (26.49-30.63 GHz), as indicated in Fig. 4.7, and covers the 28 GHz millimeter-wave 5G mobile communication band.

The two antenna parameters that mainly determine the operating band are studied. Firstly, the effect of the width w_2 of the microstrip BCDE on the antenna reflection coefficient is presented. Secondly, the impact of the width w_1 of the feed strip AB on the antenna reflection coefficient is presented.

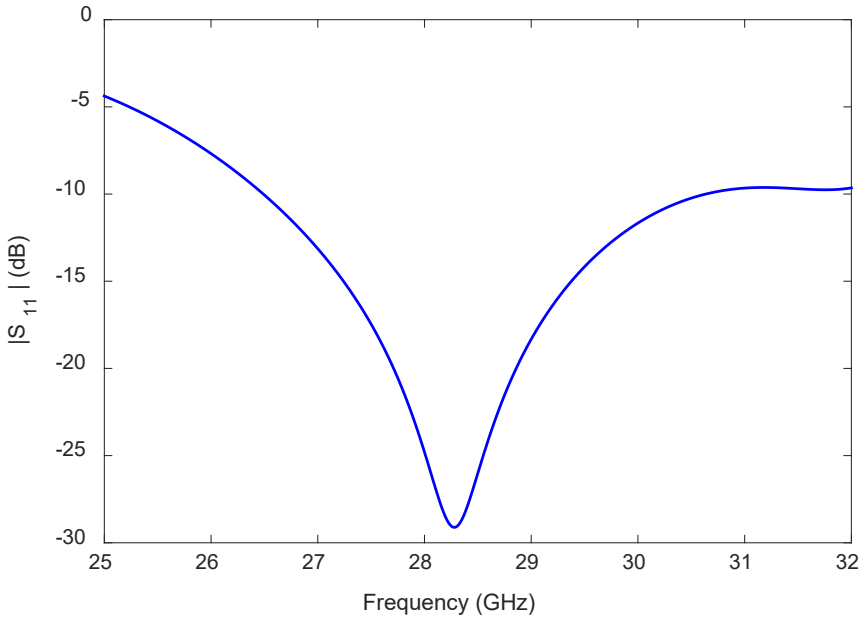

Figure 4.7: Reflection coefficient of the 28 GHz millimeter-wave HW-MLWA (length = $1.8\lambda_0$) radiating off-boresight.

The antenna reflection coefficient behavior for $w_1 = 0.5$ and 0.7 mm and $w_2 = 0.9$ and 1.1 mm is shown in Fig. 4.8. The lower frequency limit is shifted by 520 MHz when w_1 is varied from 0.5 mm to 0.7 mm. The antenna reflection coefficient bandwidth is 26.24-30.06 GHz for $w_1 = 0.5$ mm and the bandwidth is 26.76-32 GHz for $w_1 = 0.7$ mm. The reflection coefficient bandwidth is 27.81-31.81 GHz and 25.37-30.55 GHz when the patch

width w_2 is 0.9 and 1.1 mm, respectively. In order to cover the 28 GHz millimeter-wave band the values of w_1 and w_2 are carefully chosen to be 0.6 mm and 1 mm, respectively.

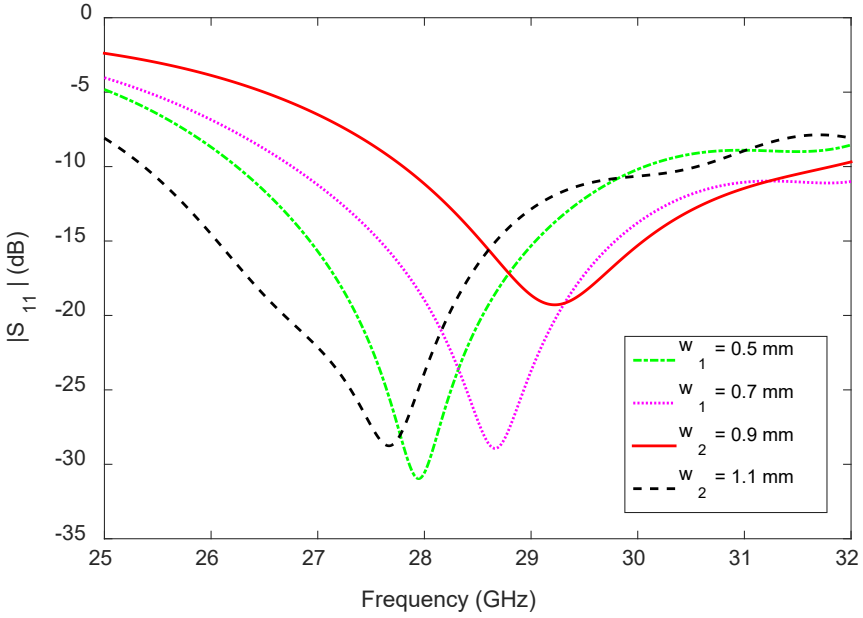

Figure 4.8: Effects of w_1 and w_2 on reflection coefficient of the 28 GHz millimeter-wave HW-MLWA (length = $1.8\lambda_0$) radiating off-boresight.

The working modes of the antenna are presented here. The surface current distribution (amplitude) at four different frequencies, i.e. 27, 28, 29, and 30 GHz is shown in Fig. 4.9. At low frequency the antenna radiates from a section close to the feed point, which can be seen by the strong surface current in the section that is close to the feed point A. The current decreases gradually and reaches a minimum before the end point E of the antenna. In the current antenna design, considering the application in a mobile device, the length is shortened significantly (1.8λ long) to increase the beamwidth. Moreover, the shorting pin does not support impedance matching for such a wide frequency range, which makes the beamwidth almost constant for the desired frequency range.

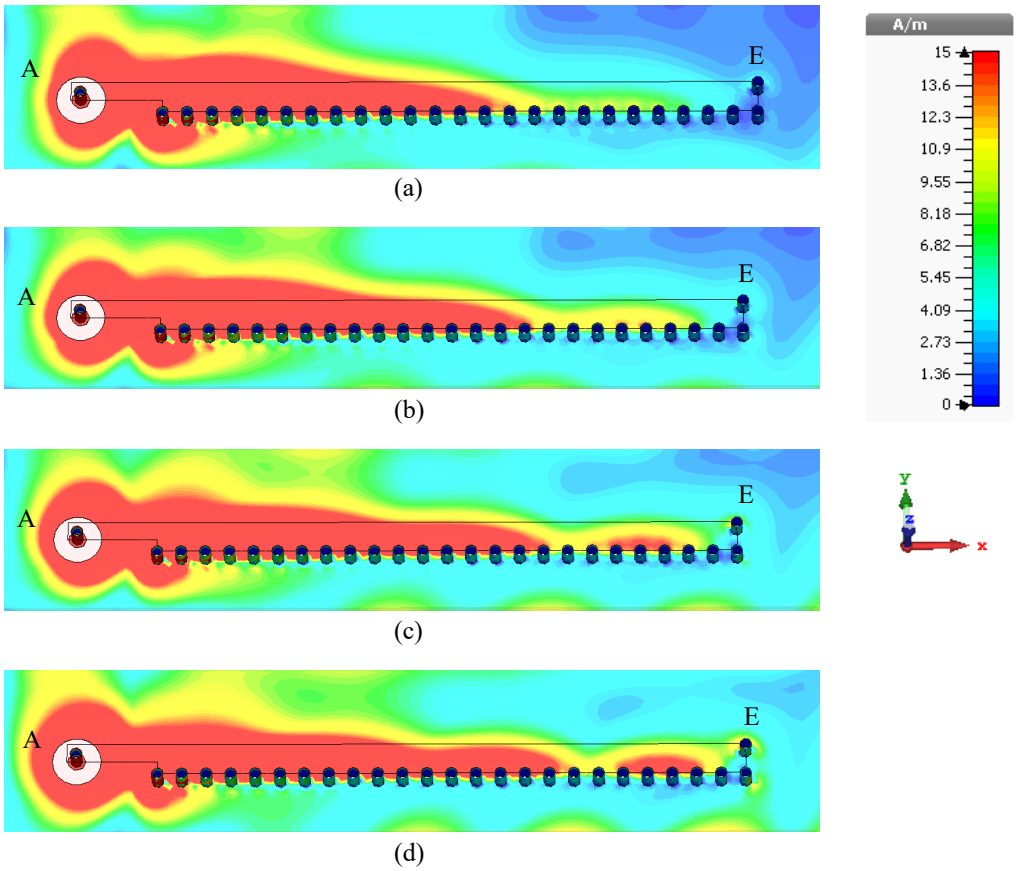

Figure 4.9: Surface current distributions (amplitude) of the 28 GHz millimeter-wave HW-MLWA (length = $1.8\lambda_0$) radiating off-boresight at (a) 27, (b) 28, (c) 29, and (d) 30 GHz.

4.2.4 Radiation Performance

The normalized radiation patterns of the antenna in the x-z and y-z planes are shown in Fig. 4.10 and Fig. 4.11, respectively. The side-lobe level (SLL) and half-power beamwidth (HPBW) of the radiation patterns in the x-z and y-z planes are listed in Table 4.2 together with the main lobe direction in the x-z plane.

The radiation patterns of the antenna in the x-z plane point in the region between boresight and endfire named the off-boresight region. At 27 GHz the main lobe direction is 36° away from the boresight direction whereas at 30.5 GHz the main lobe direction is

62° away from the boresight direction. When the frequency increases from 27 GHz to 30 GHz, giving the patterns presented in Fig. 4.10, the direction of the main lobe moves away from the boresight. This is because with increasing frequency more energy travels towards the load end (point F), as shown in Fig. 4.9. The SLL is always below -4 dB in the x-z plane at the presented frequencies and the half-power beamwidth (HPBW) varies between 46° and 51° in the x-z plane.

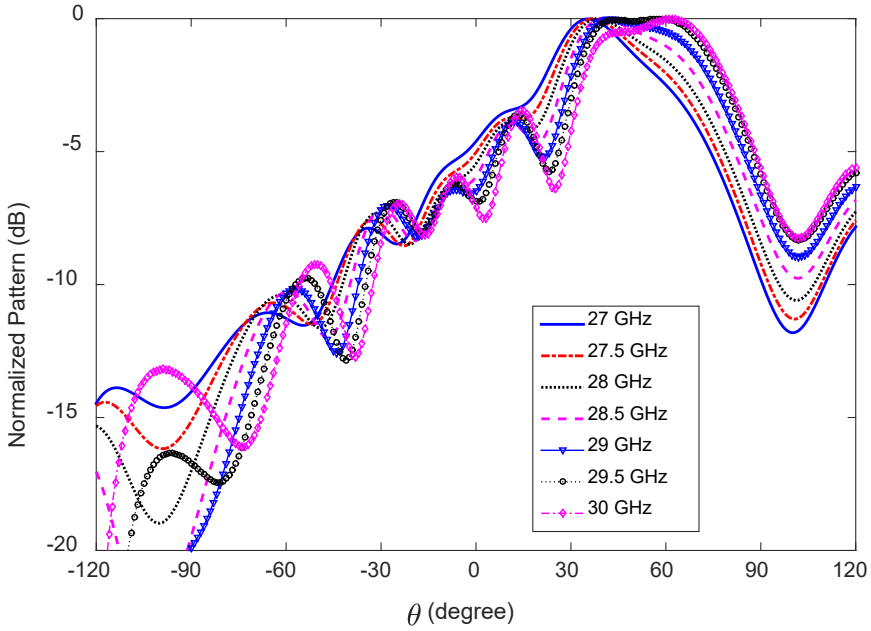

Figure 4.10: Normalized x-z plane radiation patterns of the 28 GHz millimeter-wave HW-MLWA (length = $1.8\lambda_0$) radiating off-boresight.

The radiation patterns in the y-z plane have a wider HPBW than in the x-z plane at each frequency, and the HPBW varies between 60° and 77°. The results in Figs. 4.10 and 4.11 confirm that the antenna produces a fan-shaped beam where the beamwidth is narrow in the x-z plane and wider in the y-z plane. Also the SLL in the y-z plane is much better than the SLL in the x-z plane. In the y-z plane the SLL varies between -9 and -18 dB, whereas in the x-z plane the SLL varies between -4 and -7 dB, in the frequency range 27-30 GHz.

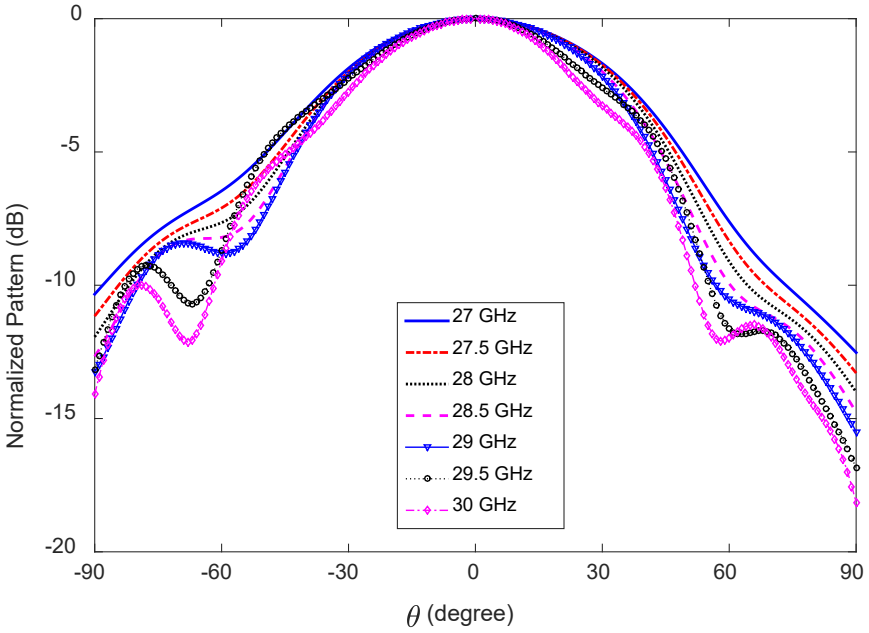

Figure 4.11: Normalized y-z plane radiation patterns of the 28 GHz millimeter-wave HW-MLWA (length = $1.8\lambda_0$) radiating off-boresight. The pattern cuts are taken at the main lobe direction.

Table 4.2: Side-lobe level (SLL), half-power beamwidth (HPBW), and main lobe direction of the 28 GHz millimeter-wave HW-MLWA (length = $1.8\lambda_0$) radiating off-boresight.

Frequency (GHz)		27	27.5	28	28.5	29	29.5	30
SLL (dB)	x-z plane	-7	-4	-4	-4	-4	-5	-4
	y-z plane	-15	-17	-18	-18	-9	-9	-10
HPBW (degree)	x-z plane	46	46	46	48	49	51	50
	y-z plane	77	74	72	71	69	69	60
Main Lobe Direction (θ°)	x-z plane	36	37	38	40	42	58	62

The side-lobes of the antenna become stronger as the frequency increases in the range 30-32 GHz, as shown in Fig. 4.12. The SLL of the antenna is -3.1, -2.6, -2.1, and -2 dB at 30.5, 31, 31.5, and 32 GHz, respectively, as shown in Fig. 4.12, whereas the SLL is -5.7

dB at 29.5 GHz, as shown in Fig. 4.10.

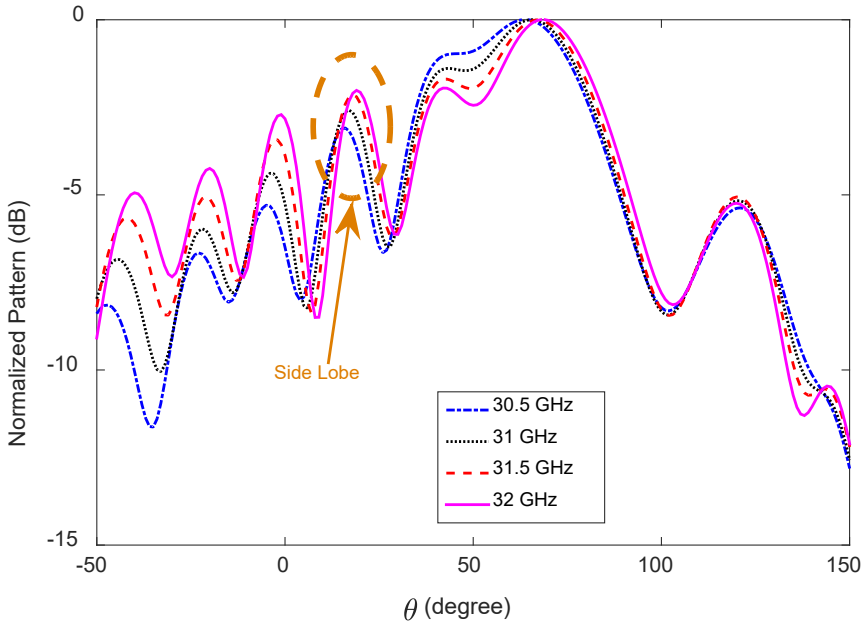

Figure 4.12: Changes in side-lobe levels with increasing frequency, of the 28 GHz millimeter-wave HW-MLWA (length = $1.8\lambda_0$) radiating off-boresight in the x-z plane.

Figs. 4.13 and 4.14 depict the simulated gain and directivity and efficiency, respectively, of the 28 GHz millimeter-wave LWA for the frequency range 27-30 GHz. The gain, directivity, and antenna efficiency are studied in the frequency range 27-30 GHz. The antenna gain varies between 6.93 and 7.2 dBi, as shown in Fig. 4.13, which means the antenna retains very stable radiation within the specified frequency range. The directivity of the antenna varies in the range 8.3-8.6 dBi, as shown in Fig. 4.13. The difference between the directivity and gain is due to the finite length of the antenna. Note that increases in the length of the antenna will reduce the difference between the directivity and gain. The antenna efficiency reaches its maximum at 27.75 GHz with 76% and its minimum at 30 GHz with 70%, as shown in Fig. 4.14.

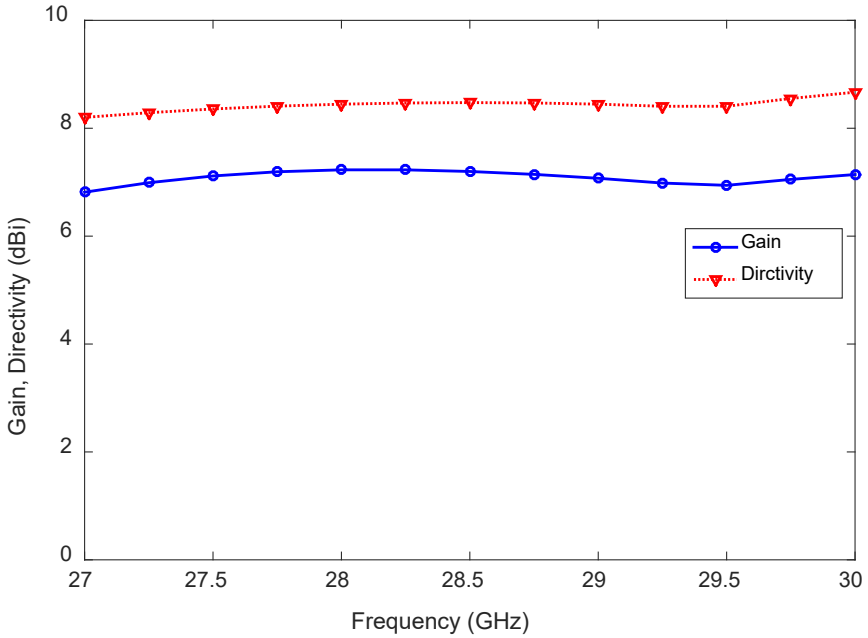

Figure 4.13: Directivity and gain of the 28 GHz millimeter-wave HW-MLWA (length = $1.8\lambda_0$) radiating off-boresight.

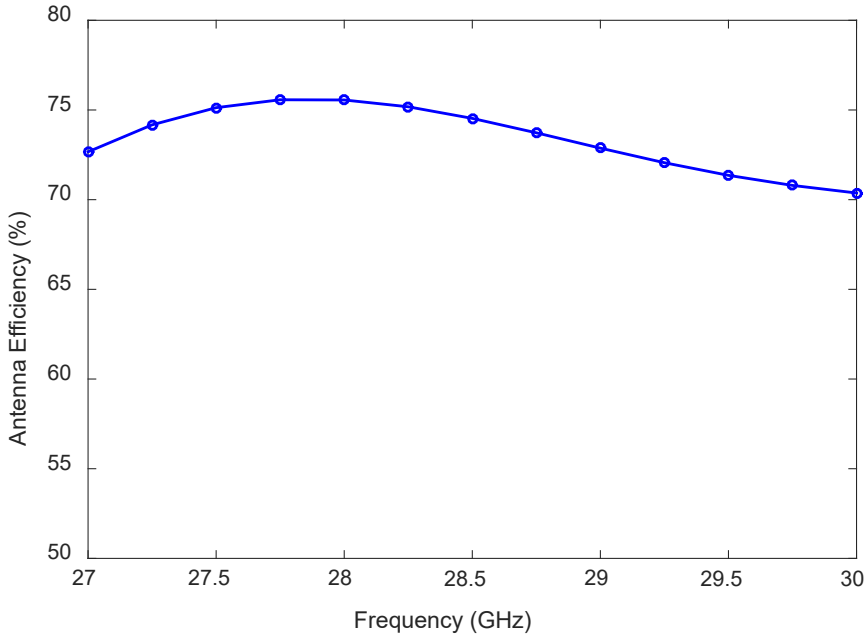

Figure 4.14: Antenna efficiency of the 28 GHz millimeter-wave HW-MLWA (length = $1.8\lambda_0$) radiating off-boresight.

4.3 Antenna Radiating Boresight

The antenna presented in the previous section is able to radiate in the off-boresight (between boresight and endfire) direction. This section describes the development of a leaky-wave antenna (LWA) radiating boresight, using a single element, for 28 GHz millimeter-wave 5G mobile communication application. The boresight direction for this antenna is fixed, which is perpendicular to the plane of the antenna. The antenna shown in Fig. 4.15 are placed in the x-y plane, hence the boresight direction is along the z-axis.

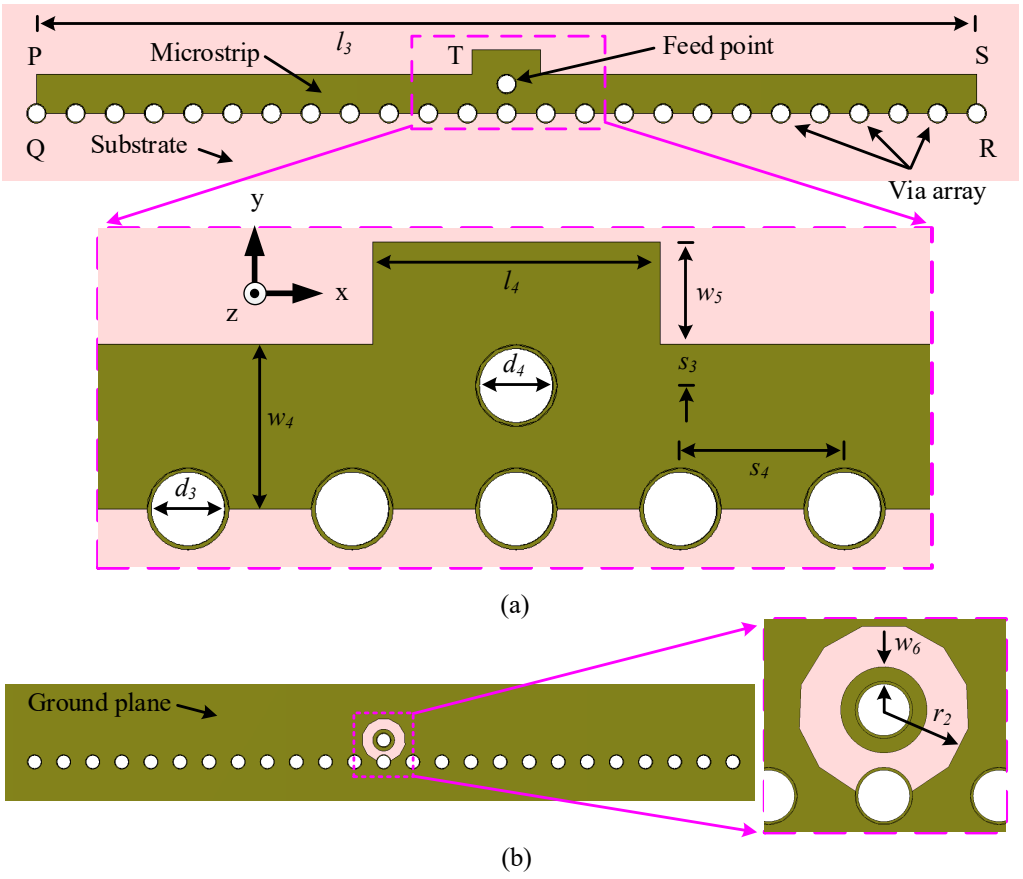

Figure 4.15: Configuration of the 28 GHz millimeter-wave HW-MLWA radiating boresight: (a) top view, and (b) back view.

4.3.1 Antenna Configuration

The boresight radiating 28 GHz millimeter-wave antenna is designed on the same substrate with the same thickness. The configuration of the antenna is shown in Fig. 4.15. The size of the ground plane is equal to the size of the substrate, i.e. no ground clearance is considered in this design.

The presented antenna has a longer microstrip PQRS with one side, QR, shorted to ground using periodically arranged shorting pins as shown in Fig. 4.15 (a). The diameter of each shorting pin and the center-to-center spacing between two consecutive shorting pins are the same as considered in the off-boresight radiating antenna design in Section 4.2. In this design no load has been applied to the antenna.

The microstrip PQRS is fed at the center T and a rectangular patch of length and width l_4 and w_5 is added to the antenna to further improve the antenna input impedance matching. The diameter of the feed via is $d_4 = 0.4$ mm. The feed arrangement of this antenna is almost the same as the technique presented in Section 4.2. The antenna is fed using a 2.92 mm surface mount coaxial connector from the back of the substrate. In order to ensure isolation between the feed via and the ground of the antenna, a circular segment of copper with radius $r_2 = 0.6$ mm is etched off from the ground plane. In addition, to ensure a guaranteed connection between the feed via and the center pin of the coaxial connector, an annulus copper with a width of $w_6 = 0.1$ mm (inner and outer radius 0.2 mm and 0.3 mm, respectively) is placed at the back of the antenna, as shown in Fig. 4.15 (b). The overall size of the antenna ($L \times W$) is 19.6 mm $\times$ 1.5 mm or $1.83\lambda_0 \times 0.14\lambda_0$, where λ_0 is the free-space wavelength at 28 GHz. The optimized design parameters (using parameter analyses in CST) for the antenna are listed in Table 4.3.

Table 4.3: Design parameters of the 28 GHz millimeter-wave HW-MLWA radiating boresight. All dimensions are in millimeters.

$d_3 = 0.4$	$d_4 = 0.4$	$w_4 = 0.8$	$w_5 = 0.5$	$w_6 = 0.1$
$s_3 = 0.2$	$s_4 = 0.8$	$r_2 = 0.6$	$l_3 = 19.2$	$l_4 = 1.4$

4.3.2 Design Procedure and Working Principle

In order to explain the working principles of the antenna, the evolution which consists of three steps is shown in Fig. 4.16. The design procedure concerning this antenna is described using the reflection coefficient and radiation performance of the antenna corresponding to the afore-mentioned three steps. Fig. 4.17 shows the antenna reflection coefficient, and Fig. 4.18 depicts the antenna gain and directivity corresponding to the three-steps of evolution of the antenna. The gain and directivity of the antenna corresponding to the design steps are analyzed within the frequency range 27-30 GHz.

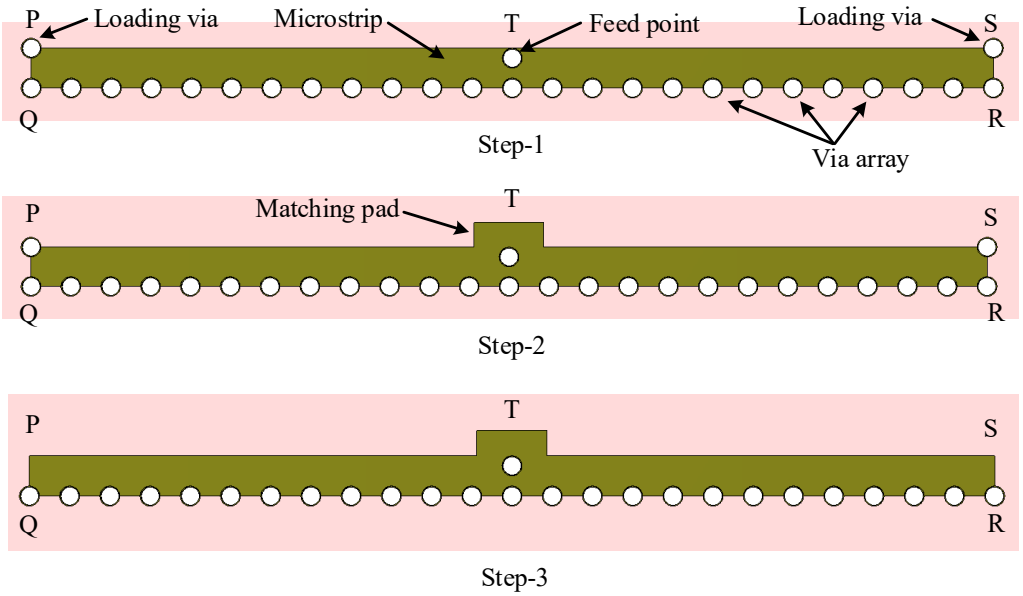

Figure 4.16: Evolution of the 28 GHz millimeter-wave HW-MLWA radiating boresight.

The antenna design starts with a microstrip PQRS of size $l_3 \times w_4$ having periodically arranged shorting pins on the edge QR and two loading vias applied at the corner points P and S, as shown in Fig. 4.16 (Step-1). The corresponding reflection coefficient of the antenna is shown in Fig. 4.17. The antenna of Step-1 has a reflection coefficient below -10 dB in the frequency range 31.39-32 GHz, which is outside the target frequency band. The gain of the antenna varies between 3.8 and 4.2 dBi, as shown in Fig. 4.18 and the directivity varies in the range 5.5-6.7 dBi.

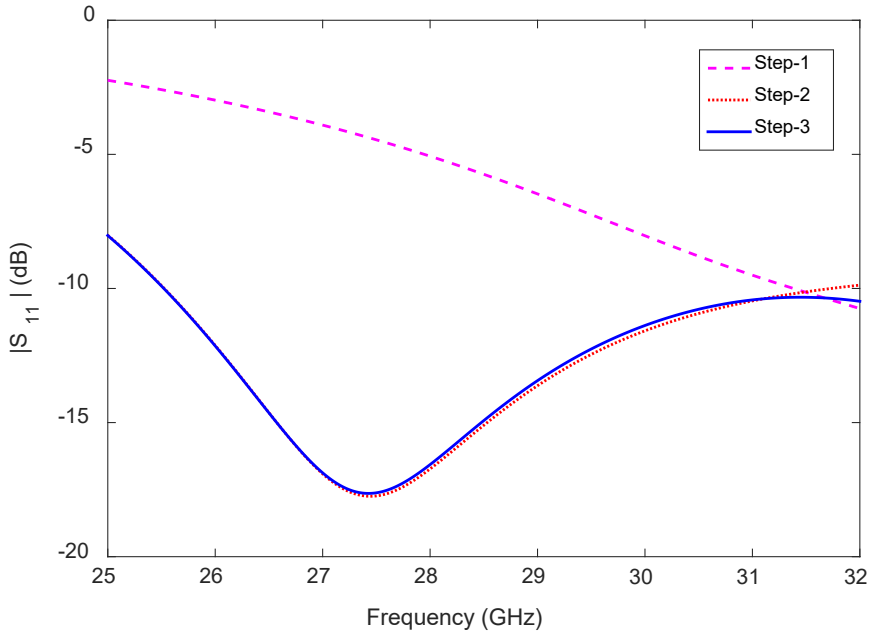

Figure 4.17: Reflection coefficient corresponding to the three-steps evolution of the 28 GHz millimeter-wave HW-MLWA radiating boresight.

The objective is to cover the 28 GHz millimeter-wave band (28-29.5 GHz) for future generation mobile device application. In Step-2, a rectangular patch of size $l_3 \times w_5$ is applied above the feed point for better impedance matching within the target band. The dimension of this matching pad is optimized using a parameter study in CST. The antenna covers a reflection coefficient bandwidth of 25.53-31.73 GHz, as shown in Fig. 4.17 (Step-2 curve), which covers the 28 GHz millimeter-wave band for 5G mobile communi-

cations. Also, the gain and directivity increases in Step-2 from the gain and directivity of the antenna in Step-1. In Step-2, the improvement in antenna directivity is almost equal throughout the presented frequency range 27.5-31 GHz, but a more noticeable improvement in antenna gain is observed in the lower frequency limit region than in the upper frequency limit region. The gain improvement at 27.5 GHz is 2.2 dB and at 31 GHz the improvement is 0.5 dB, as shown in Fig. 4.18. The gain variation within the frequency range 27-30 GHz is 1.3 dB.

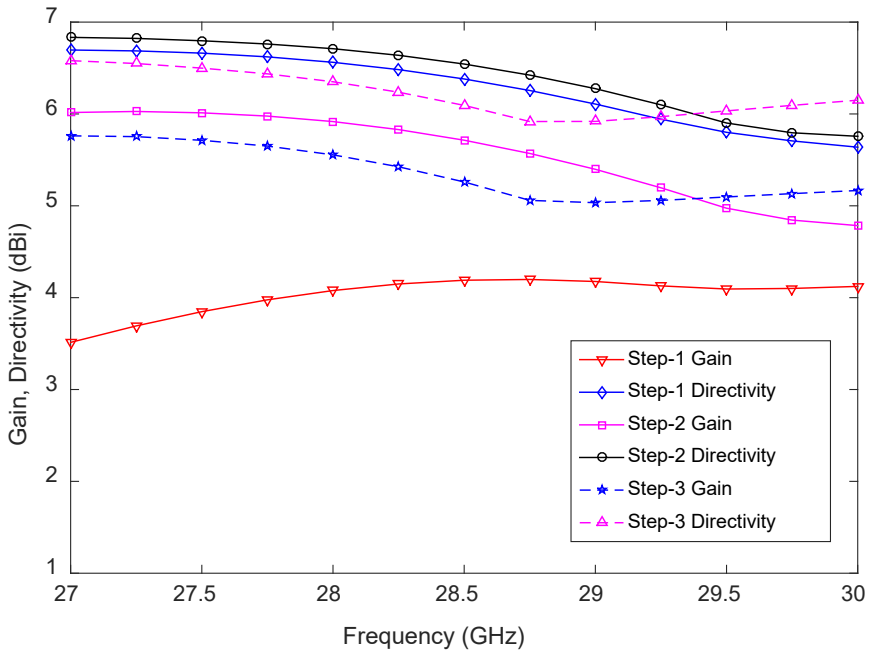

Figure 4.18: Gain and directivity corresponding to the three-steps of evolution of the 28 GHz millimeter-wave HW-MLWA radiating boresight.

The effect of the loading vias on the antenna performance is presented here. In Step-3, two loading vias are removed and the corresponding reflection coefficient is shown in Fig. 4.17 (Step-3 curve). The antenna reflection coefficient behavior within the frequency range 25-31 GHz is the same as seen for the Step-2 design. After removing these two loading vias, better impedance matching is observed at the upper frequency limit region

which makes the antenna reflection coefficient bandwidth even greater. The antenna gain and directivity for Step-3 are shown in Fig. 4.18 and compared with the results of the previous two steps. The gain and directivity variation is low in Step-3 compared to the gain and directivity variations for the other steps. The gain and directivity variation of the 28 GHz millimeter-wave antenna radiating boresight is only 0.7 and 0.5 dB, respectively.

In LWA design a termination (either a shorting pin or a 50 Ω load) is used at the far end. In this design two loading vias [Fig. 4.16 (Step-1, Step-2)] are applied as a matching load that helps in generating better antenna radiation patterns for a wide range of frequency than without using any matching load, while having the same reflection coefficient behavior for either case. The conversion of this boresight radiating antenna into a pattern reconfigurable antenna is presented in Chapter 5, where loading vias are not required.

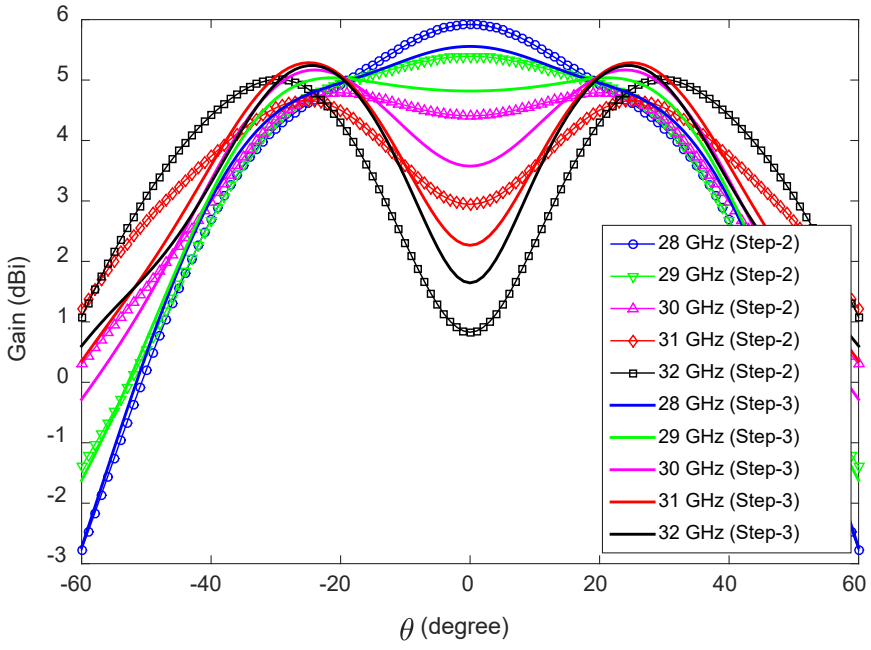

Figure 4.19: Effects of loading vias on HW-MLWA radiation patterns in the x-z plane.

The radiation patterns of the antenna [Fig. 4.15] in the y-z plane are unaffected whether the loading is applied or not. However, the x-z plane radiation patterns, especially

at frequencies close to the upper frequency limit of the reflection coefficient bandwidth, are affected by the type of loading applied. Here, the comparison between the radiation patterns of the antenna in the frequency range 28-32 GHz with a loading via [as shown in Fig. 4.16 (Step-2)] and without a loading via [as shown in Fig. 4.16 (Step-3)] is presented. Both antennas, Step-2 and Step-3, have radiation with a single beam at 28, 29, and 30 GHz, as shown in Fig. 4.19. However, at 31 GHz the antenna with a loading via has single-beam radiation whereas the antenna without a loading via has dual-beam radiation (single beam split at boresight into two beams).

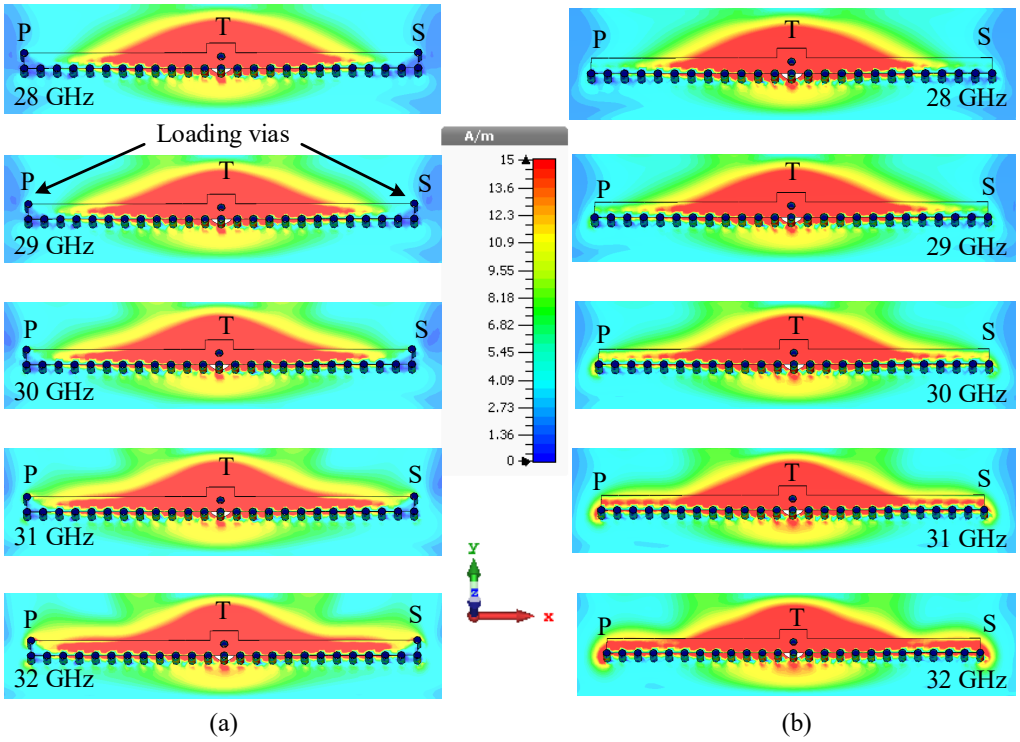

Figure 4.20: Surface current distributions (amplitude) at 28, 29, 30, 31, and 32 GHz of the 28 GHz millimeter-wave HW-MLWA radiation boresight: (a) with loading vias (Step-2 design), and (b) without loading vias (Step-3 design).

The main lobe of the antenna at Step-3 starts to split at lower frequency (31 GHz) than the frequency (32 GHz) when the main lobe starts to split for the antenna of Step-2.

This occurs because at higher frequencies more energy travels towards the load end (P and S) of the antenna after Step-3. Since no loading is applied at the end the energy reflects back and produces a backward beam, whereas in the antenna of Step-2 the remaining energy is grounded through the matching via, as shown in Fig. 4.20. For both antennas (Step-2 and Step-3), a strong surface current (magnitude) is observed at the location of feed point T. The magnitude of the surface currents gradually decreases and a minimum is observed at the end points (P and S). That is, the antenna has one maximum and two minima, indicating that the antenna is operating in the half-wavelength modes.

4.3.3 Radiation Performance

The gain and directivity of the 28 GHz millimeter-wave antenna radiating boresight were already presented in Section 4.3.2. This section presents the antenna efficiency together with the normalized radiation patterns in the x-z and y-z planes. The presented antenna does not radiate perfectly in the boresight, i.e. along the z-axis. The direction of the main lobe is -16° to -25° away from boresight in the y-z plane within the frequency range 27-30 GHz, as shown in Fig. 4.21. However, the half-power beamwidth (HPBW) of the antenna is large enough to cover the boresight direction. The HPBW of the antenna in the x-z and y-z planes is listed in Table 4.4.

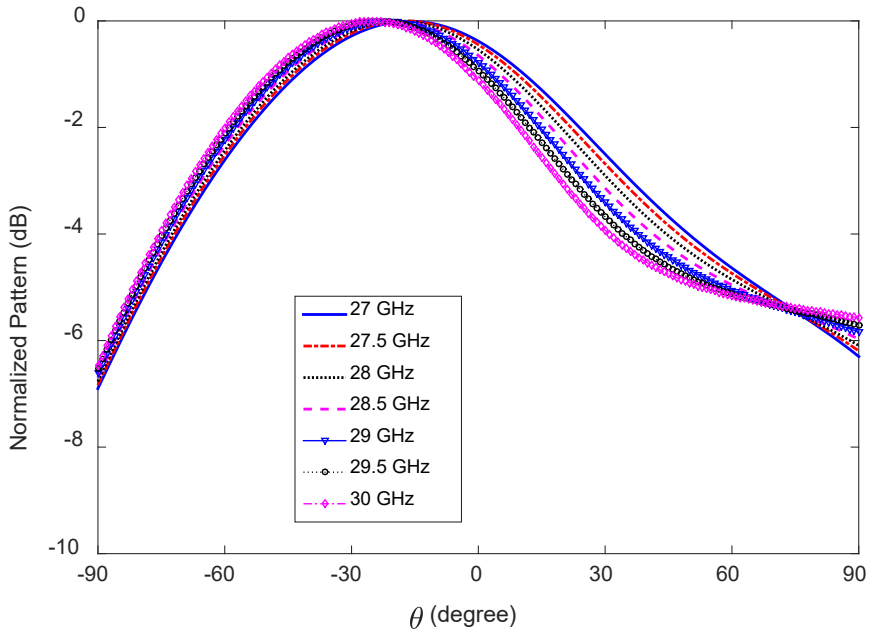

Figure 4.21: Normalized radiation patterns in the y-z plane of the 28 GHz millimeter-wave HW-MLWA radiating boresight.

The direction of the main lobe at 27 GHz is -16° and at 30 GHz is -25°. The main lobe shifts away slightly with increasing frequency, as shown in Fig. 4.21, and the direction of the main lobe for all the presented frequencies is included in Table 4.4. Fig. 4.22 shows the normalized radiation patterns of the antenna in the x-z plane. The antenna gain (in the x-z plane) at boresight gradually decreases with increasing frequency. The magnitude along the boresight ($\theta = 0°$) is 0.9 dB below the peak value at 29.5 GHz, whereas the magnitude is 1.6 dB below the peak value at 30 GHz, as illustrated in Fig. 4.22. In addition, at 31 GHz the magnitude along the boresight ($\theta = 0°$) is more than 3 dB below the peak value, resulting in a single beam split into dual-beam radiation, as previously shown in Fig. 4.19.

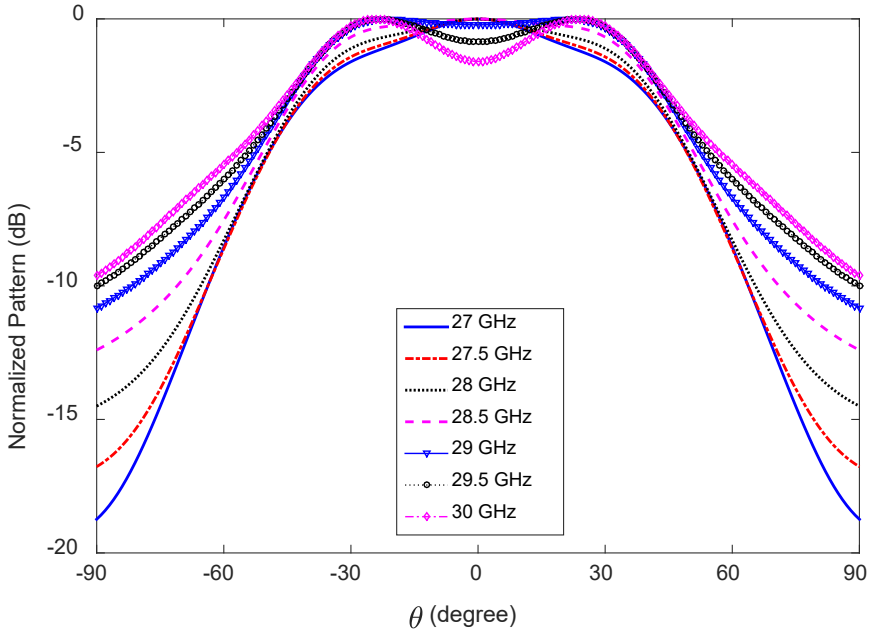

Figure 4.22: Normalized radiation patterns in the x-z plane of the 28 GHz millimeter-wave HW-MLWA radiating boresight.

The side-lobe level (SLL) of the antenna in the x-z plane is much better than the SLL of the antenna in the y-z plane, as listed in Table 4.4. In the x-z plane the SLL improves gradually with increasing frequency; the SLL is -13 and -17 dB at 27 and 30 GHz, respectively. However, in the y-z plane the SLL at each frequency is -8 dB within the frequency range 27-30 GHz.

Table 4.4: Side-lobe level (SLL), half-power beamwidth (HPBW), and main lobe direction of the 28 GHz millimeter-wave HW-MLWA radiating boresight.

Frequency (GHz)		27	27.5	28	28.5	29	29.5	30
SLL (dB)	x-z plane	-13	-14	-15	-15	-16	-16	-17
	y-z plane	-8	-8	-8	-8	-8	-8	-8
HPBW (degree)	x-z plane	82	83	84	87	89	90	92
	y-z plane	100	98	96	94	92	90	88
Main Lobe Direction (θ°)	y-z plane	-16	-17	-19	-20	-22	-23	-25

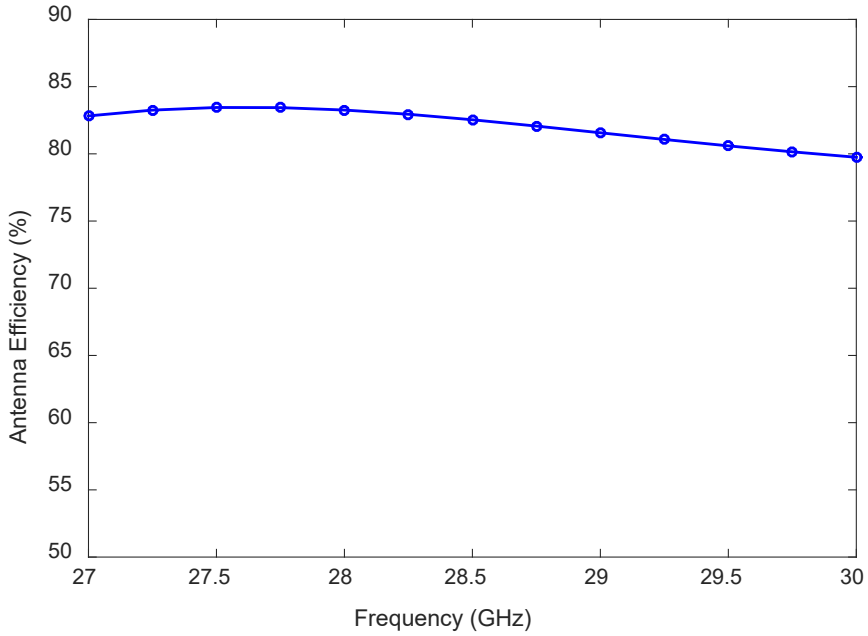

Figure 4.23: Antenna efficiency of the 28 GHz millimeter-wave HW-MLWA radiating boresight.

The antenna efficiency (total efficiency) varies between 80% and 84% within the frequency range 27-30 GHz, as shown in Fig. 4.23. The antenna efficiency reaches its maximum at 27.5 GHz while the minimum occurs at 30 GHz. As the frequency increases

more energy travels towards the end, resulting in more loss and therefore poorer antenna efficiency.

4.4 Summary

In this chapter, firstly, a basic half-width microstrip leaky-wave antenna (HW-MLWA) for 28 GHz millimeter-wave band was investigated. Secondly, a HW-MLWA was developed for 5G mobile devices which has a -10 dB reflection coefficient bandwidth of 4.14 GHz (26.49-30.63 GHz) that covers the 28 GHz millimeter-wave 5G mobile communication band. The antenna radiated in the off-bore-right (region between the +z and +x-axes) direction. The developed antenna was able to scan the beam along the x-axis with scan angles from $\theta = 36^\circ$ to $\theta = 62^\circ$ in the frequency range from 27 GHz to 30 GHz.

Thirdly, a novel single-element HW-MLWA with a -10 dB reflection coefficient bandwidth of 6.2 GHz (25.53-31.73 GHz) was developed to radiate towards the boresight direction and cover the 28 GHz millimeter-wave 5G mobile communication band. The half-power beamwidth (HPBW) in the y-z plane ($\phi = 90^\circ$) was sufficiently wide and varied between 98° and 88°, with the main lobe pointing in the boresight direction with a tilt angle of θ = -16° to θ = -25°, indicating complete coverage of the boresight direction. Investigated in this chapter as well was the frequency beyond which the single-beam antenna became a dual-beam antenna, generating a null in the boresight direction because of the energy distribution towards the load.

In the next chapter, a 1-D, and a 2-D pattern reconfigurable antenna for 28 GHz millimeter-wave 5G mobile devices will be developed based on the study presented in this chapter.

Chapter 5

Pattern Reconfigurable Antennas for 28 GHz Millimeter-Wave 5G

5.1 Introduction

In this chapter, firstly, a novel antenna is developed for 1-D pattern reconfigurable operation using the properties of the antennas presented in the previous chapter. The 1-D pattern reconfigurable antenna has three feed points: one at the center and two at the sides of the antenna. By selecting between these three feeds it is possible to switch the beam in three different directions along the antenna axis. The antenna performance is optimized for each feed while the other feeds are inactive. The 1-D pattern reconfigurable antenna is prototyped and the operation is verified through measurements.

Secondly, a method is presented to achieve 2-D pattern reconfigurable operation using two 1-D beam switching antennas. The performance of the 2-D beam switching antenna is tested after placing the antenna at the corner of a ground plane of the mobile device. The 2-D beam switching antenna with device ground plane is prototyped and tested experimentally. A comparison with the reference antennas to date justifies the the proposed

antenna's suitability for future 5G mobile device application.

This chapter is structured as follows. Section 5.2 presents the development of a novel antenna for 1-D pattern reconfigurable operation. The simulation results of the 1-D pattern reconfigurable antenna are verified through measurements in Section 5.3. A strategy is presented to achieve 2-D pattern reconfigurable operation using two 1-D pattern reconfigurable antennas in Section 5.4. Also, the measured and simulation results of the 2-D pattern reconfigurable antenna are presented after integrating the antenna with the ground plane of a mobile device. A comparison of the performance with the reference antennas to date is presented in Section 5.4. Section 5.5 summarizes the chapter and specifically the main points articulated in it.

5.2 1-D Pattern Reconfigurable Antenna

This section presents the design of a multiple-feed 1-D pattern reconfigurable antenna for 28 GHz millimeter-wave 5G mobile communications, which can switch the beam in three different directions along the antenna axis.

5.2.1 Antenna Configuration

The 1-D pattern reconfigurable antenna is designed on an FR-4 substrate with relative permittivity $\epsilon_r = 4.3$, loss tangent $\tan\delta = 0.025$, and a thickness of 0.8 mm. The size of the ground plane is 7 mm $\times$ 30 mm, which is equal to the size of the substrate, i.e. no ground clearance is considered in this design. The configuration of the antenna is shown in Fig. 5.1. The antenna for 1-D pattern reconfiguration is an integration of the two designs presented in Chapter 4, for boresight and off-boresight radiating antennas.

Similar to the previous two antennas, i.e. the radiating off-boresight and radiating boresight antennas, this antenna has one rectangular microstrip GHVU with edge HV

shorted to ground using periodically arranged shorting pins. The diameter of the shorting pins and the center-to-center distance between two consecutive shorting pins are the same as those used in the two antennas presented in the previous chapter.

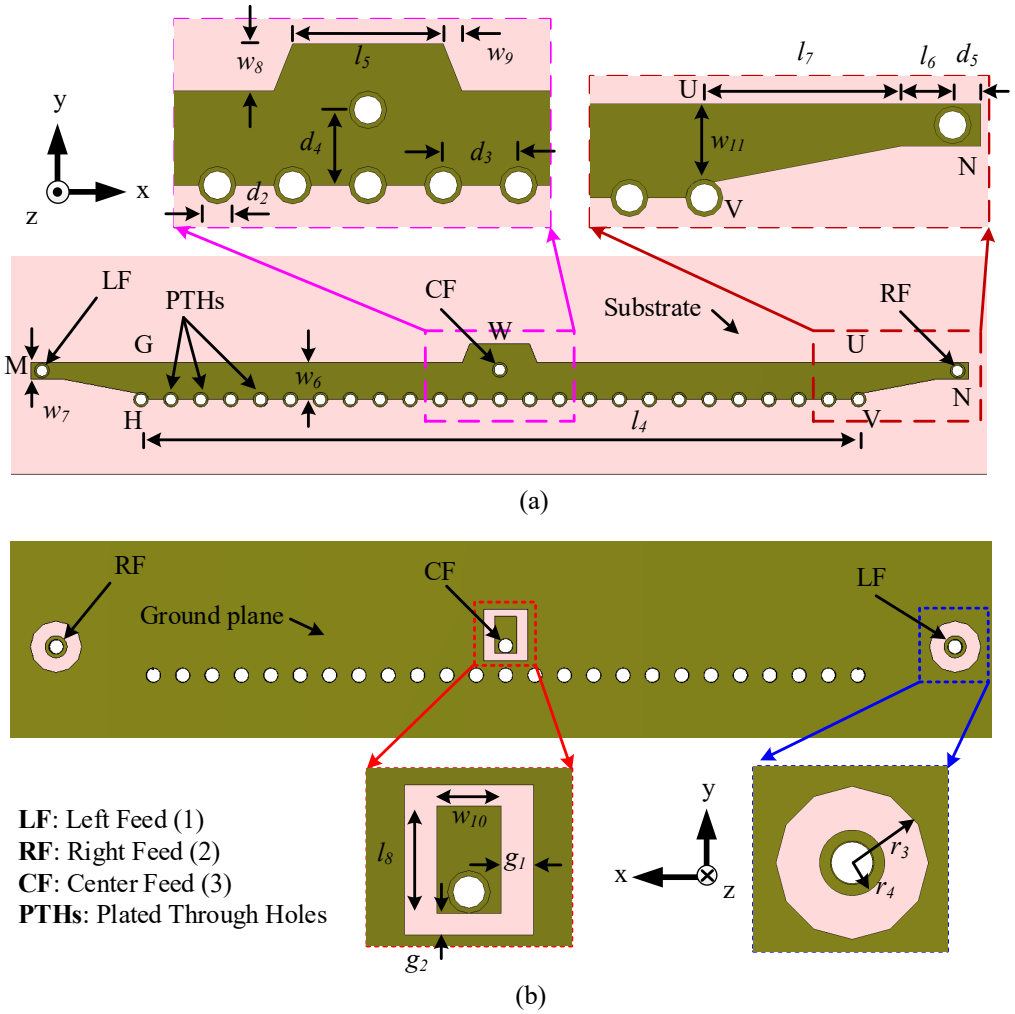

Figure 5.1: Configuration of the 1-D pattern-reconfigurable antenna for 28 GHz millimeter-wave 5G communication: (a) top view, and (b) back view.

The antenna is feed at three different locations titled left feed (LF), right feed (RF), and center feed (CF), as shown in Fig. 5.1 (a). In order to have better impedance matching between the coaxial connector and the microstrip GHVU the tapered microstrip lines MG and NU are used for LF and RF, respectively. Also a tapered microstrip line is placed at

the location W to improve the impedance matching when the center feed is applied. In this design consideration, only one feed is active at a time while the other two feeds are inactive. Therefore, when LF is active the other two coaxial connectors RF and CF act as an open-ended 50 Ω matched load and vice versa.

During simulation the antenna is assumed to be fed using the 2.92 mm coaxial connector from the back of the antenna. A copper annulus of radius r_3 and a rectangular copper of size $(l_8 + 2g_2) \times (w_{10} + 2g_1)$ is etched from the ground plane in order to ensure isolation between the center pin of the coaxial connector and the ground plane at the location of the side feeds and the center feed, respectively, as shown in Fig. 5.1 (b). In addition, to ensure a guaranteed connection between the feed via and the center pin of the coaxial connector, a copper annulus of radius r_4 and a copper rectangle of size $l_8 \times w_{10}$ is placed at the location of the edge feeds and the center feed, respectively.

The antenna has been designed to switch the beam to three different directions: firstly, off-bore-right (in the region between the +z and +x-axes); secondly, off-bore-left (in the region between the +z and -x-axes); and thirdly, boresight (along the +z-axis). They employ three feeds LF, RF, and CF, respectively. The overall size of the antenna is 25.1 mm × 1.6 mm or $2.34\lambda_0 \times 0.15\lambda_0$, where λ_0 is the free-space wavelength at 28 GHz. The optimized design parameters (using parameter analyses in CST) for the antenna are listed in Table 5.1.

Table 5.1: Design parameters of the 1-D pattern reconfigurable antenna for 28 GHz millimeter-wave 5G hand-held devices. All dimensions are in millimeters.

$d_2 = 0.4$	$d_3 = 0.8$	$d_4 = 0.8$	$d_5 = 0.3$	$l_4 = 19.2$
$l_5 = 1.6$	$l_6 = 0.55$	$l_7 = 2.1$	$l_8 = 1$	$w_6 = 0.9$
$w_7 = 0.45$	$w_8 = 0.5$	$w_9 = 0.2$	$w_{10} = 0.6$	$w_{11} = 0.75$
$g_1 = 0.3$	$g_2 = 0.2$	$r_3 = 0.7$	$r_4 = 0.3$	

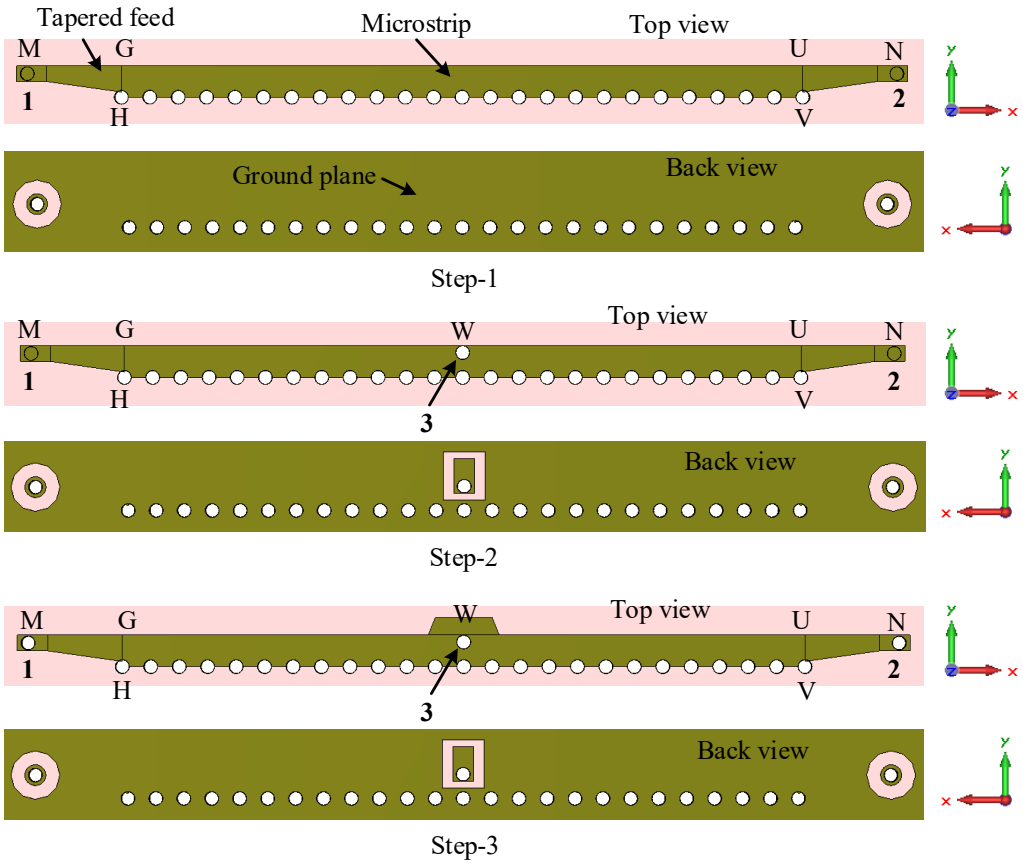

Figure 5.2: Evolution of the 1-D pattern reconfigurable antenna for 28 GHz millimeter-wave 5G hand-held devices.

5.2.2 Design Procedure and Working Principle

The design procedure and working principle of the 1-D pattern reconfigurable antenna are presented in this section using the three step evolution depicted in Fig. 5.2, and the corresponding reflection coefficients are shown in Fig. 5.3. The working principle is presented with the help of the antenna parameters listed in Table 5.1.

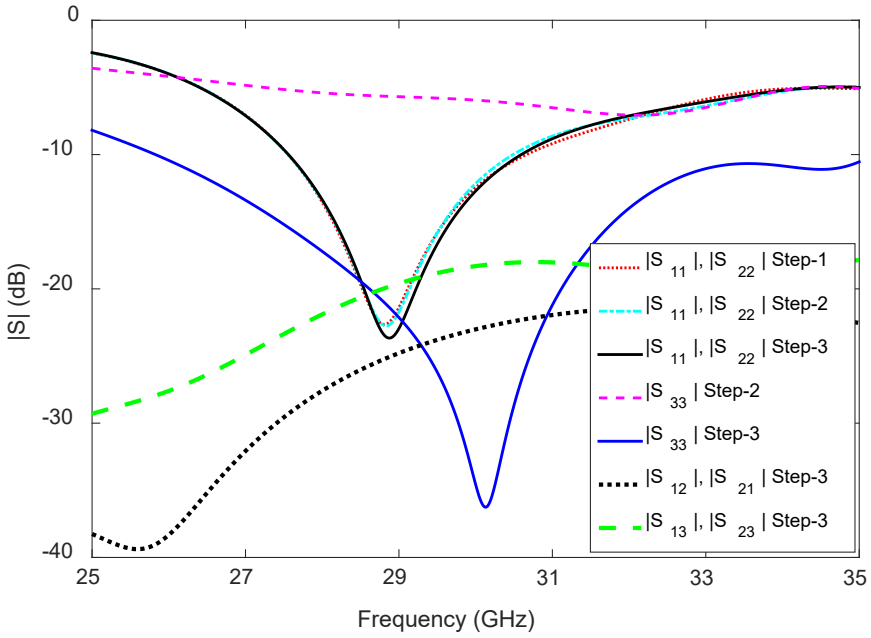

Figure 5.3: S-parameters corresponding to the three steps of evolution of the 1-D pattern reconfigurable antenna for 28 GHz millimeter-wave 5G hand-held devices.

In the first step (Step-1) the antenna is fed from either end by activating one at a time, as shown in Fig. 5.2 (Step-1). The antenna in Step-1 has a -10 dB reflection coefficient bandwidth of 3.2 GHz (27.5-30.7 GHz), as shown in Fig. 5.3 ($|S_{11}|, |S_{22}|$ Step-1 curve).

The antenna in Step-1 is capable of switching the radiation pattern to two different directions. The radiation pattern direction is in the off-bore-right when Feed-1 (LF) is active, as shown in Fig. 5.4. The radiation pattern moves to the region between the +z and -x-axes, named off-bore-left, when Feed-2 (RF) is active. The angle measured from the boresight is the same in both cases due to the symmetric antenna structure. For example, the direction of the main lobe is 35° (i.e. $\theta = +35°$) away (at 28.5 GHz) from boresight and is in the off-bore-right region when LF is active, as revealed in Fig. 5.5. Therefore, at 28.5 GHz the direction of the main lobe is 35° away (i.e. θ = -35°) from boresight and is in the off-bore-left region when RF is active (see Fig. 5.5).

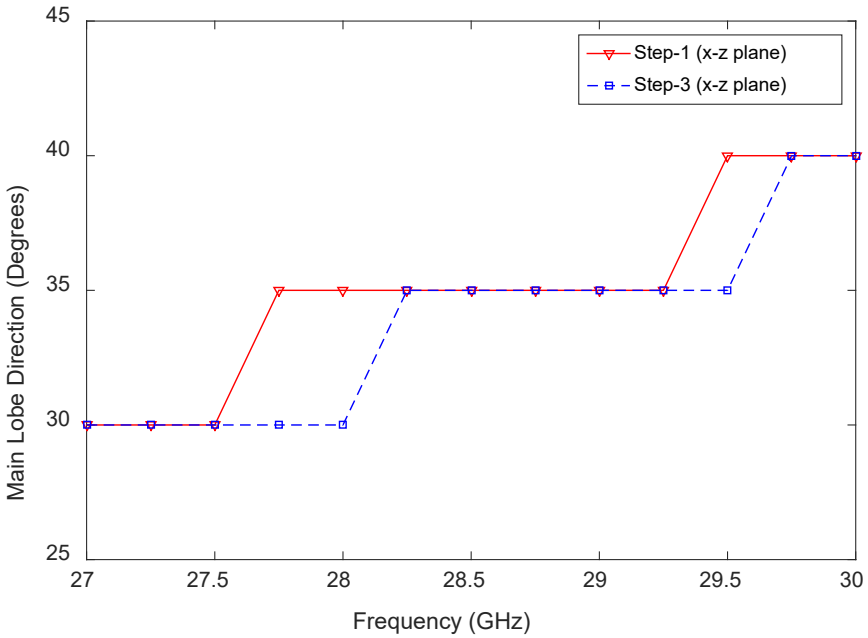

Figure 5.4: Effects of the center feed via on the main lobe direction of the 1-D pattern reconfigurable antenna when left feed (LF) is active.

In Step-2, firstly, a plated through hole is applied at the location W in order to provide a feed at the center of the microstrip GHVU in order to achieve broadside radiation, as shown in Fig. 5.2 [top view (Step-2)]. Step-2 ends with placing a copper rectangle [shown in Fig. 5.2 back view (Step-2)] of length l_8 and width w_{10} with maintaining gaps of g_1 and g_2, as indicated in Fig. 5.1, with the ground plane along the x and y directions, respectively. These gaps ensure isolation between the feed via and the ground plane. The patch determines the input impedance of the antenna for the center feed. It also helps to ensure a guaranteed connection between the center pin of the coaxial connector and the antenna. In Step-2, the reflection coefficients of the side feeds remain unaffected, as indicated in Fig. 5.3 ($|S_{11}|, |S_{22}|$ Step-2 curve). However, the center feed via at the location W affects the radiation performance of the side feeds LF, and RF. These results will be discussed at the end of this section.

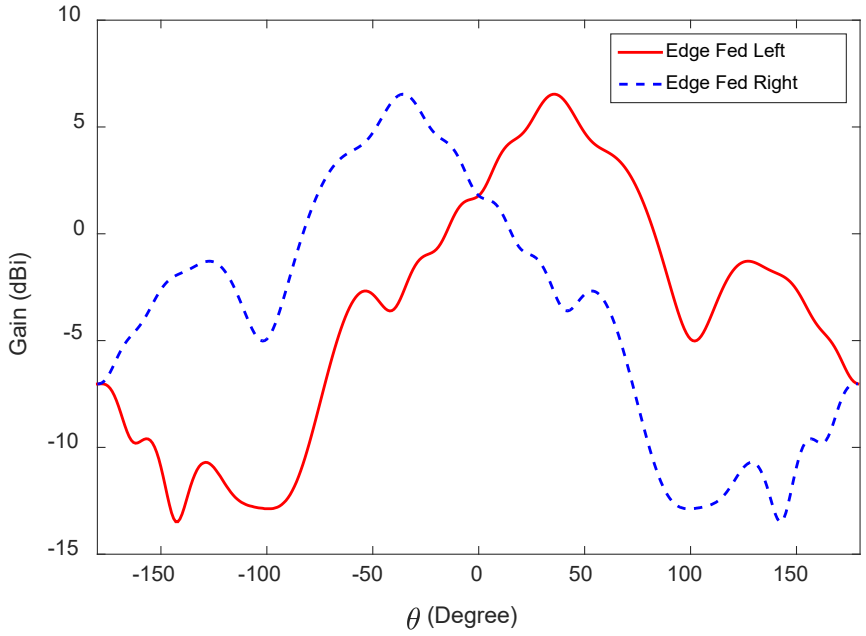

Figure 5.5: Radiation patterns of the antenna in the x-z plane for Step-1 at 28.5 GHz for left feed (LF) and right feed (RF).

In Step-3, a trapezoidal patch is added at the center of the microstrip GHVU which is aligned with the center of the free edge GU, as shown in Fig. 5.2 (Step-3). As discussed earlier, the length and width of this trapezoidal patch significantly control the input impedance of the antenna for the CF and the effects are presented in Section 5.2.3. The dimensions of this trapezoidal patch are optimized using parameter analysis in CST. The S-parameters for the optimized structure are shown in Fig. 5.3. The impedance bandwidth for the LF and RF remains unaffected (27.45-30.7) but improves significantly for the CF (25.8-35 GHz). The transmission coefficients ($|S_{12}|$, $|S_{21}|$) between the LF and RF are always below -24 dB within the reflection coefficient bandwidth of the antenna, as illustrated in Fig. 5.3 ($|S_{12}|, |S_{21}|$ Step-3 curve), which indicates the antenna's good radiation properties. Also, the transmission coefficients ($|S_{13}|$, $|S_{31}|$, $|S_{23}|$, $|S_{32}|$) between the side feed LF/RF and center feed CF are always below -18 dB within the reflection coefficient bandwidth of the antenna, as shown in Fig. 5.3 ($|S_{13}|, |S_{23}|$ Step-3 curve).

Concerning the analysis on the effects of the center feed via on the radiation performance of the side feed, the results in the target frequency range 27-30 GHz are used, which covers all the proposed 28 GHz millimeter-wave band (27.5-28.5 or 28-29.5 GHz). Fig. 5.4 shows the direction of the main lobe for Step-1 (center feed via is absent in the design) and Step-3 (including center feed via) when LF is active. Here, as expected, the main lobe is in the off-bore-right region. The direction of the main lobe is in the range 30°-40° within the 28 GHz millimeter-wave band when center feed via is absent. The direction of the main lobe shifts slightly towards boresight by 5° when the center feed via is present at 27.75, 28, and 29.5 GHz. That is, the direction of the main lobe is $\theta = +30°$ with the center feed via and $\theta = +35°$ without the center feed via at 28 GHz. Within the target frequency range, the main lobe points at three different angles are $\theta = +30°$, $+35°$, and $+40°$ with or without the presence of the center feed via. However, this switching happens at different frequencies for both cases. The first shift of the main beam is observed at 27.75 and 28.25 GHz for Step-1 and Step-3, respectively, and second shifting is observed at 29.5 and 29.75 GHz for Step-1 and Step-3, also respectively. Importantly, in all cases the direction of the main beam is between 30° and 40°.

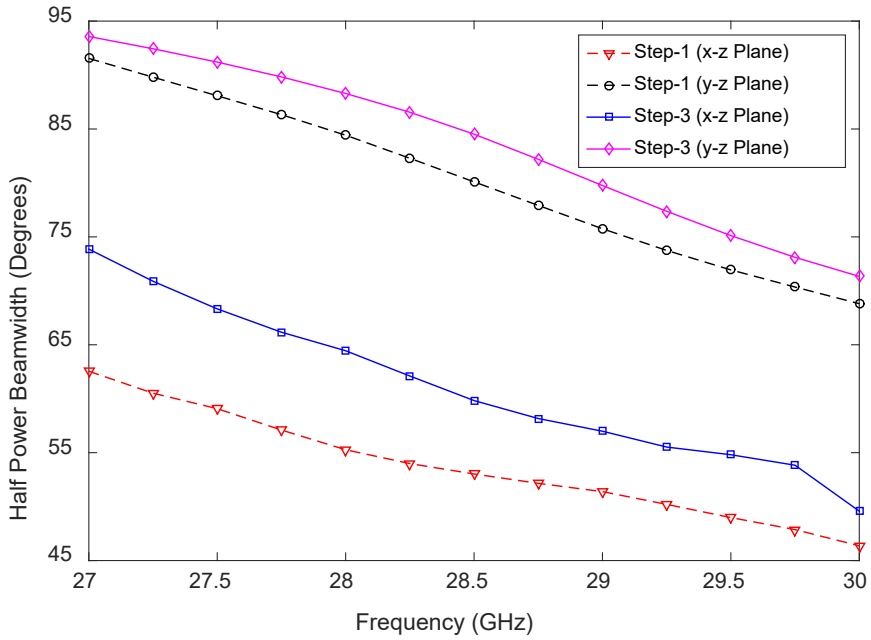

Figure 5.6: Effects of the center feed via on the half-power beamwidth of the 1-D pattern reconfigurable antenna when the left feed (LF) is active.

Fig. 5.6 shows the effects of the center feed via on the half power beamwidth (HPBW) of the antenna in x-z and y-z planes when LF is active. In the x-z plane the HPBW becomes wider by 5° at 30 GHz and widens almost linearly with a decrease in the frequency from 30 GHz to 27 GHz, a 10° improvement in beamwidth is observed at 27 GHz. This is because the center feed via acts as a wall and prohibits energy from travelling towards the RF end. This is further illustrated by the surface current distribution (amplitude) depicted in Fig. 5.7. As well, the beamwidth is improved by 4° in the y-z plane because of the center feed via as shown in Fig. 5.6.

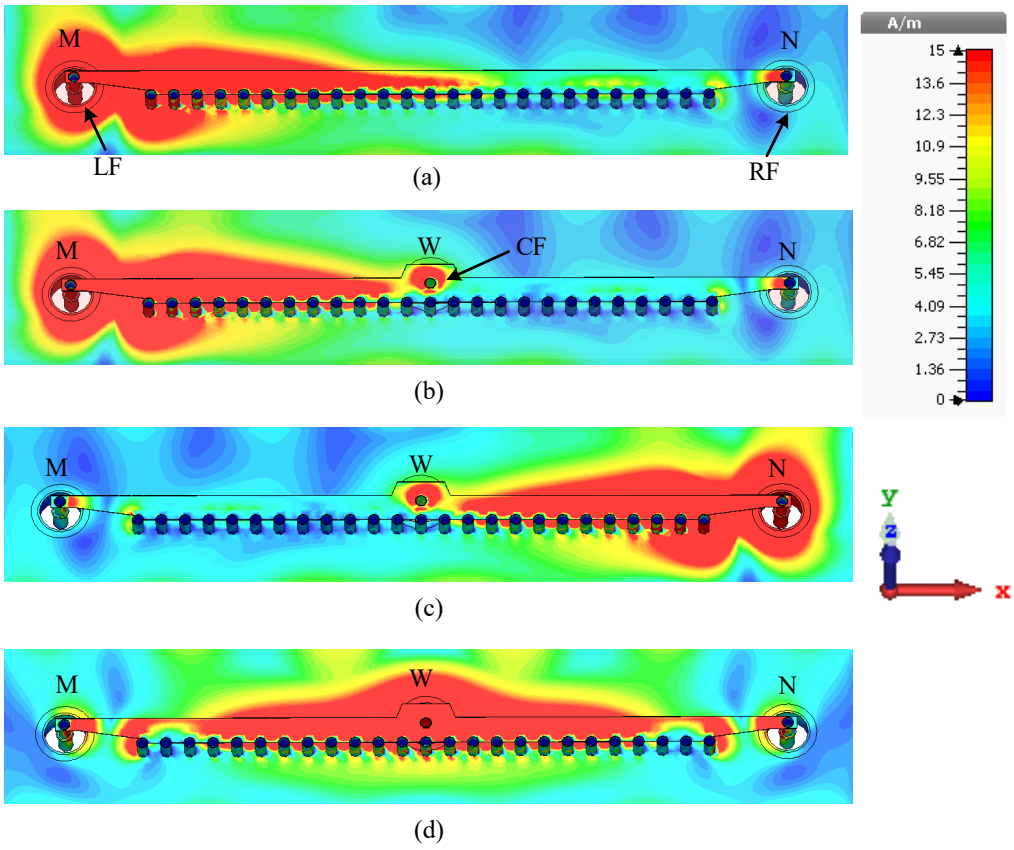

Figure 5.7: Surface current distributions (amplitude) of the 1-D pattern reconfigurable antenna at 29.5 GHz: (a) evolution Step-1 with LF active, and evolution Step-3 with (b) LF active, (c) RF active, and (d) CF active.

The center feed via also helps to improve the side-lobe level (SLL) for the x-z plane radiation. The SLL is below -7 dB in the frequency range 27-28.5 GHz for the x-z plane radiation and the SLL is below -4 dB in the frequency range 28.75-30 GHz when no center feed via is present (see Fig. 5.8). However, the SLL is always below -7 dB in the frequency range 27-30 GHz when the center feed via is present. A small change in the SLL is observed for the y-z plane radiation when the center feed via is present, which is negligible because in either case the SLL is always below -14 dB in the frequency range 27-30 GHz.

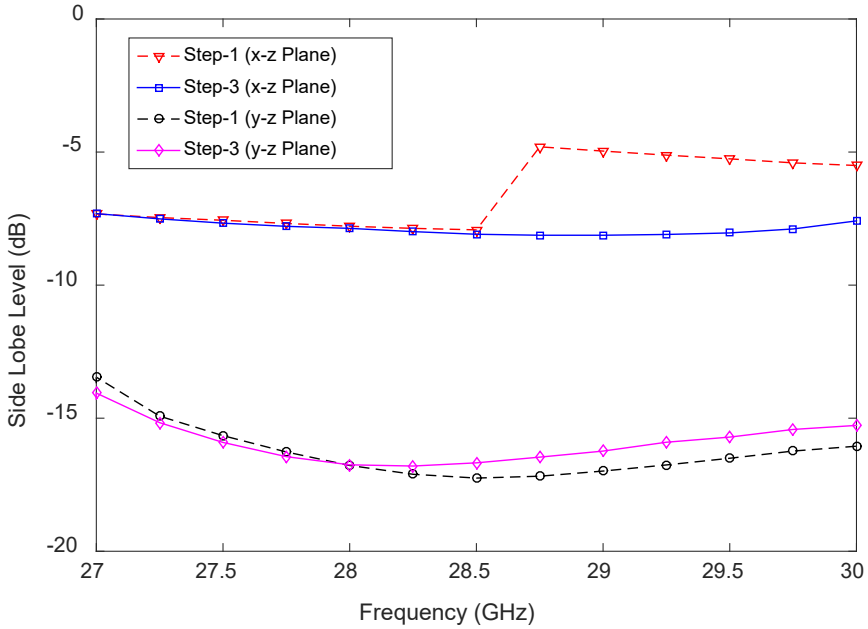

Figure 5.8: Effects of the center feed via on the side-lobe level of the 1-D pattern reconfigurable antenna when the left feed (LF) is active.

Turning to the surface current distribution of the antenna to understand the working modes and to illustrate the effects of the center feed via on the side feed LF/RF, when the side feed LF/RF is active, the center feed via restricts the energy to travel towards the other side of the antenna. This is evident in Figs. 5.7 (b) and (c). Therefore, the direction of the main lobe shifts slightly towards the boresight and improves the isolation between the two side feeds LF and RF because it is known from the previous study presented in Chapter 4 that the further the energy travels towards the load (other side of the antenna) the more is the antenna beam tilted towards end fire. When LF/RF is active, the current is strong within the feed side of the microstrip GHUV and a minimum at the other side, indicating that the antenna is operating in the quarter wavelength mode. The antenna is operating in the half wavelength mode when the CF is active because the current reaches its maximum at the center of the microstrip GHVU, while the minimum occurs at the two sides M and N, as shown in Fig. 5.7 (d).

5.2.3 Parameter Analysis

This section studies the parameters of the antenna that significantly control the reflection coefficient of the 1-D pattern reconfigurable antenna. The width w_7 of the tapered section MG and NU, and the width w_6 of the microstrip GHVU, control the operating bandwidth of the antenna when LF/RF is active. A similar effect using the parameters w_1 and w_2 that are equivalent to w_7 and w_6, respectively, was previously investigated for off-boresight radiating antennas, presented in Section 4.2.3. Now, the effects of the feed pad (parameters l_8 and w_{10}) and matching pad (parameters l_5, w_8, and w_9) on the reflection coefficient of the antenna are discussed when the CF is active. During the parameter analysis the parameters of the antenna are retained as listed in Table 5.1 except for the parameter that is varying.

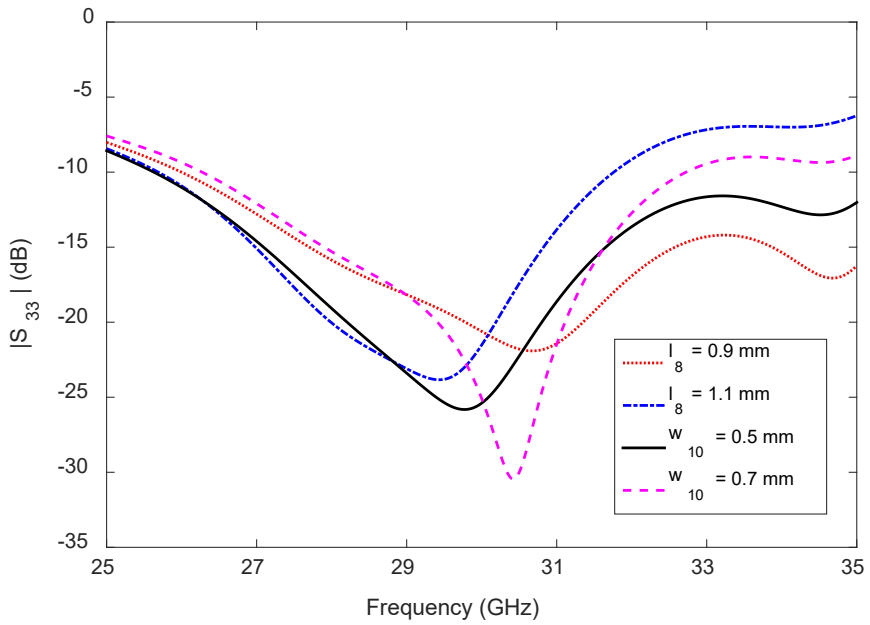

Figure 5.9: Effects of the length l_8 and width w_{10} of the feed pad on the reflection coefficient of the antenna when the CF is active.

Fig. 5.9 shows the antenna reflection coefficient behavior with changes in the length l_8 and width w_{10} of the feed pad [used for center feed at the back of the antenna, shown

in Fig. 5.1 (b)]. A change in the length and width of the feed pad influences the antenna impedance matching significantly in the frequency range 30-35 GHz. However, the effect in the frequency range 25-30 GHz is less. By controlling the length l_8 and width w_{10} of the feed pad it is possible to control the upper frequency limit of the impedance bandwidth when the CF is active, but they wield negligible effect on the lower frequency limit of the antenna impedance bandwidth. Using parameter analysis in CST the value of the length l_8 and width w_{10} are chosen to be 1 mm and 0.6 mm, respectively.

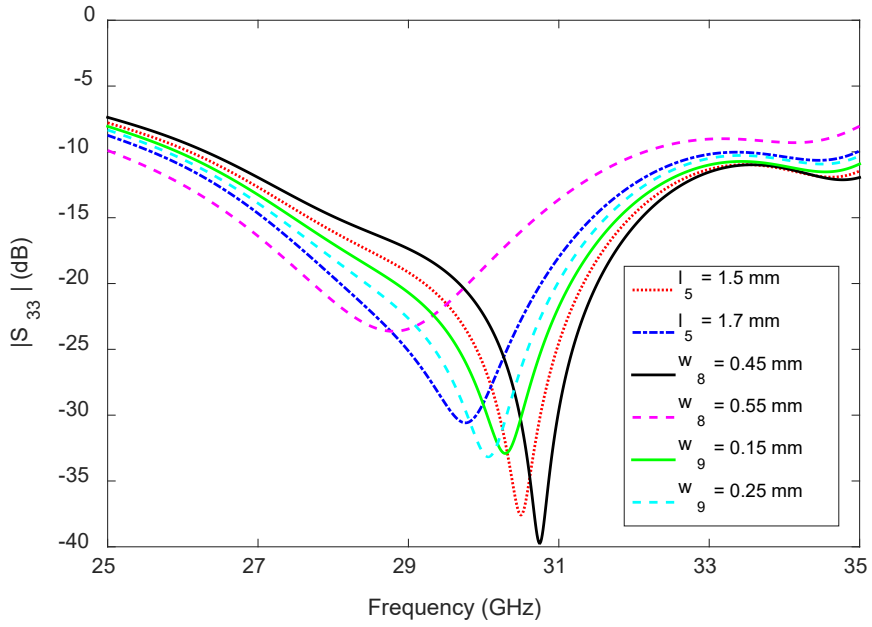

Figure 5.10: Effects of the matching pad dimensions (l_5, w_8, and w_9) on the reflection coefficient of the antenna when the CF is active.

The effects of the geometry of the trapezoidal matching pad (used for the center feed which is aligned with the free edge GU) are presented here. Fig. 5.10 displays the antenna reflection coefficient behavior when the length l_5, width w_8, and width of the tapered section w_9 are changed. A small change of the length l_5 and width w_9 has only a slight effect, but a small change in the width w_8 has a significant impact on the antenna reflection coefficient, as shown in Fig. 5.10. With decreasing width w_8, the antenna

impedance bandwidth decreases. Using parameter analysis in CST the values of l_5, w_8, and w_9 are chosen to be 1.6 mm, 0.5 mm, and 0.2 mm, respectively.

5.2.4 Effects of Coaxial Connector Misalignment

In order to have a low-cost design, the antenna is designed using a 2.92 mm coaxial connector instead of a waveguide feed. Most of the available 2.92 mm coaxial connectors in the market are of the surface mount type. During simulation, the center pin of the 2.92 mm coaxial connector is placed at the center of the feed pad used for LF, RF, and CF, as shown in Fig. 5.11. After prototyping, there is a possibility of misalignment of the center pin with the simulation model and prototype. The effects of misalignment of the coaxial connector in order to understand the impact on the antenna reflection coefficient are studied. The shifts of the center pin of the coaxial connector along the x-axis and y-axis are denoted by dx and dy, respectively, as shown in Fig. 5.11.

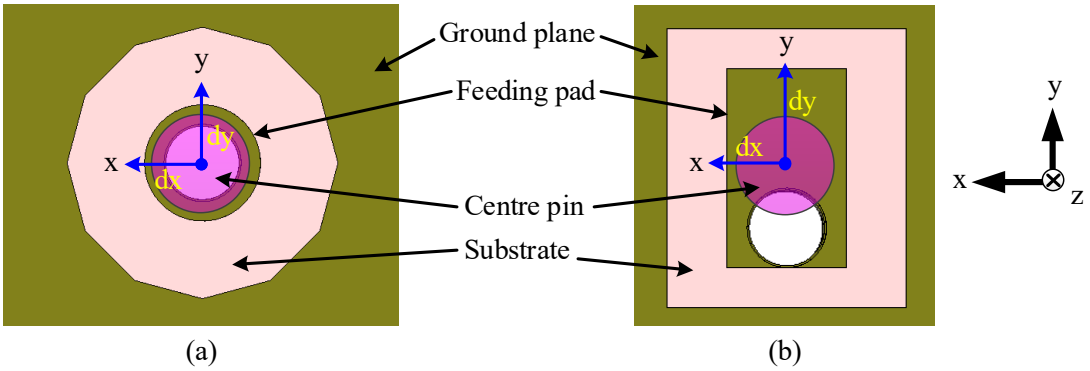

Figure 5.11: Orientation of the center pin of the surface mount coaxial connector and the feed pad in (a) LF and RF, and (b) CF.

Firstly, the effects of coaxial connector misalignment are studied for the LF and RF . Fig. 5.12 shows the antenna reflection coefficient behavior due to the displacement of the center pin along the x and y-axes. In this analysis, the considered range are +0.2

mm to -0.2 mm along both these axes. The misalignment of the center pin of the coaxial connector for the LF and RF has a small effect on the lower frequency limit, but the upper frequency limit shifts by 330 MHz to 630 MHz towards lower frequency when the misalignment is in either the ±x or the ±y direction. However, a maximum 220 MHz shift in the lower frequency limit is observed when the misalignment is along the -x-axis by 0.2 mm.

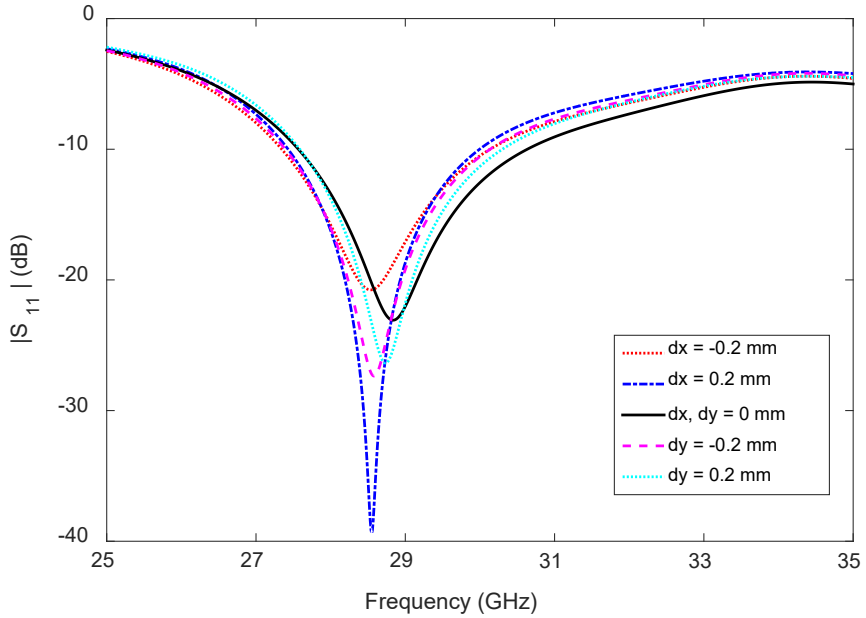

Figure 5.12: Effects of misalignment between the center pin of the surface mount coaxial connector and the center of the feed pad when the LF is active.

Secondly and finally, the effects of coaxial connector misalignment are studied for the CF. Due to the symmetric structure of the antenna with respect to the CF along the x-axis, a shift of the center pin by dx along the +x-axis has the same effect as misalignment -dx along the -x-axis. For presentation simplicity, only results for a change of dx along the +x-axis are shown. The shift of the center pin along the +x direction has negligible effect on the antenna reflection coefficient bandwidth, as shown in Fig. 5.13. However, a shift of the center pin of the coaxial connector along the -y direction (towards the free

edge GU of the microstrip GHVU) does significantly influence on the antenna reflection coefficient's behavior. The antenna reflection coefficient is almost unaffected if the center pin moves away from the edge GU of the microstrip GHVU (+y direction). When the center pin shifts by dy = -0.05 mm along the -y direction, the antenna reflection coefficient bandwidth changes from 26.17-35 GHz to 27.57-32.87 GHz, as shown in Fig. 5.13.

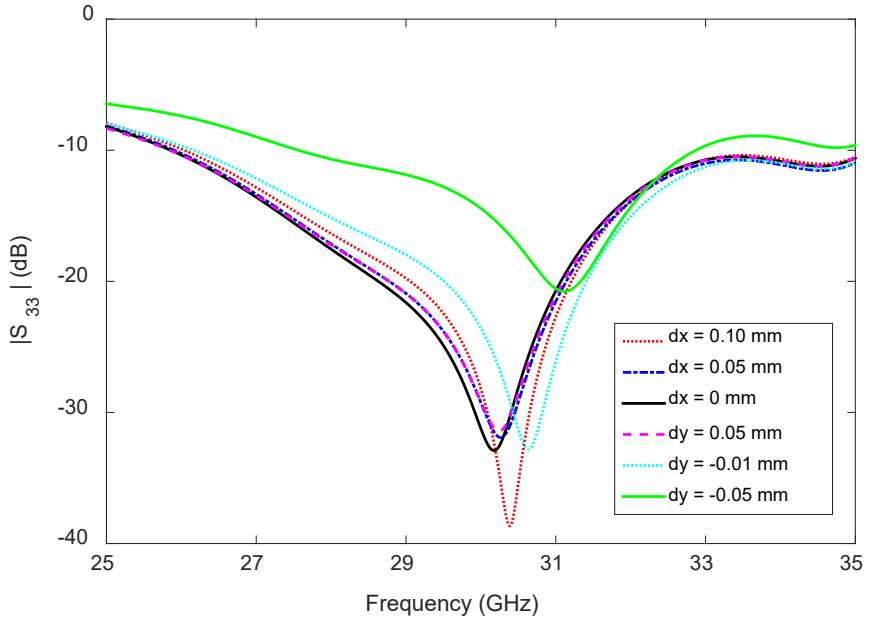

Figure 5.13: Effects of misalignment between the center pin of the surface mount coaxial connector and the center of the feed pad when the CF is active.

5.3 Measured and Predicted Results

This section presents the measured S-parameters, directivity, gain, efficiency and radiation patterns of the 1-D pattern reconfigurable antenna, and compares with the corresponding simulated results. The radiation performance of the fabricated antenna was measured at the Antenna & RF Measurements Facility, Politecnico di Torino, Italy, and the S-parameters were measured using a Vector Network Analyzer at Macquarie University, Australia and at MACOM, Sydney, Australia. The top and bottom views of the prototype

are shown in Fig. 5.14. The 2.92 coaxial connector is used to fed the antenna during simulation and measurement, but a smaller 1.85 mm coaxial connector can be used.

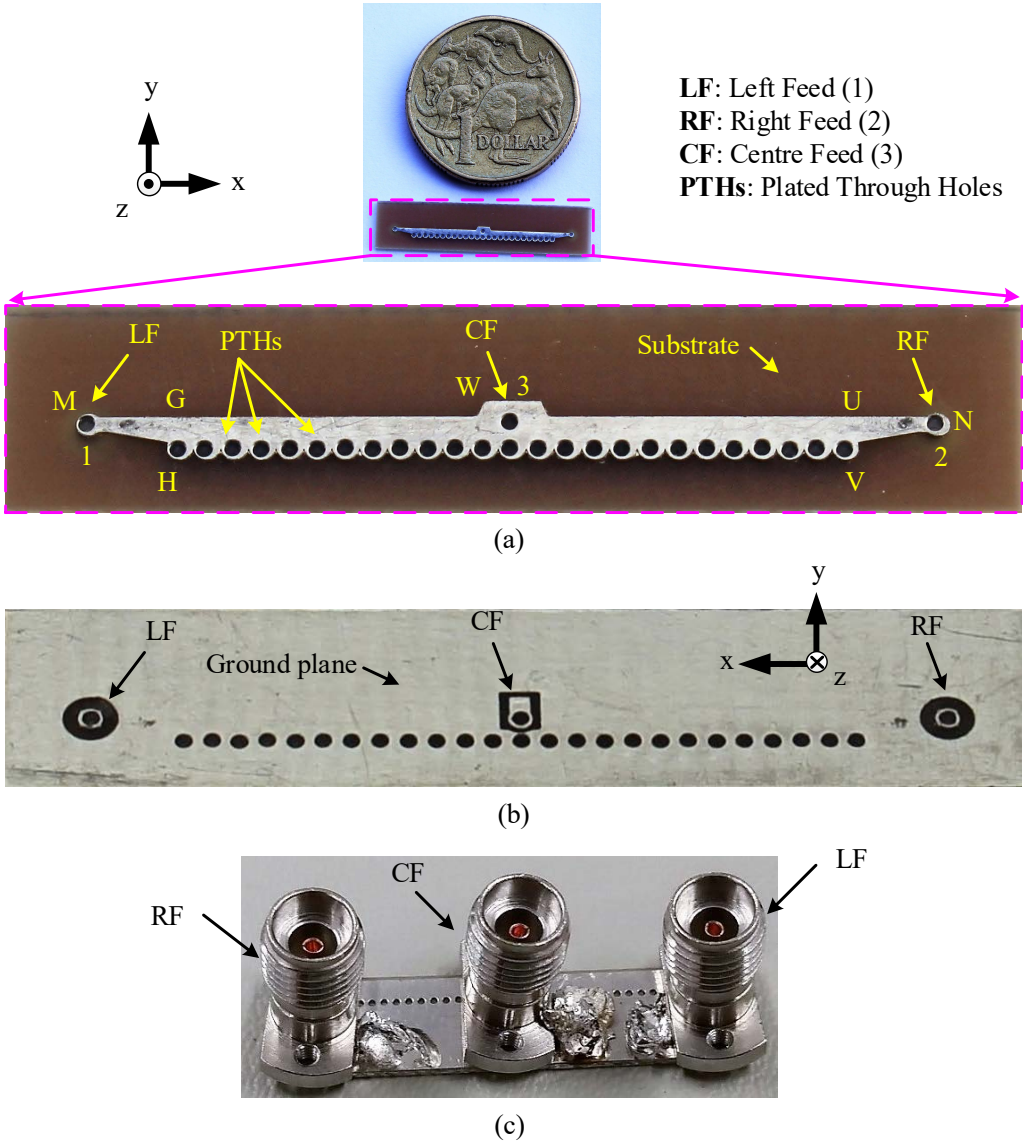

Figure 5.14: Fabricated 1-D pattern reconfigurable antenna for 28 GHz millimeter-wave 5G hand-held devices: (a) top view, (b) back view (before adding the coaxial connector), and (c) back view (after adding the coaxial connector).

5.3.1 S-Parameters

The measured S-parameters of the 1-D pattern reconfigurable antenna are shown in Fig. 5.15 together with the predicted results; an excellent agreement is observed between the measured and the predicted results. The measured -10 dB reflection coefficient bandwidth of the antenna is 3.2 GHz (27.3-30.5 GHz) for the left feed (LF) while the predicted bandwidth is 3.2 GHz (27.5-30.7 GHz). The measured and predicted reflection coefficients of the antenna for LF are the same as for RF. For this reason, the reflection coefficient of the antenna for LF is presented in Fig. 5.15. Also, the measured -10 dB reflection coefficient bandwidth of the antenna is 9.4 GHz (25.6-35 GHz) for the center feed (CF) and the predicted reflection coefficient bandwidth is 9.2 GHz (25.8-35 GHz).

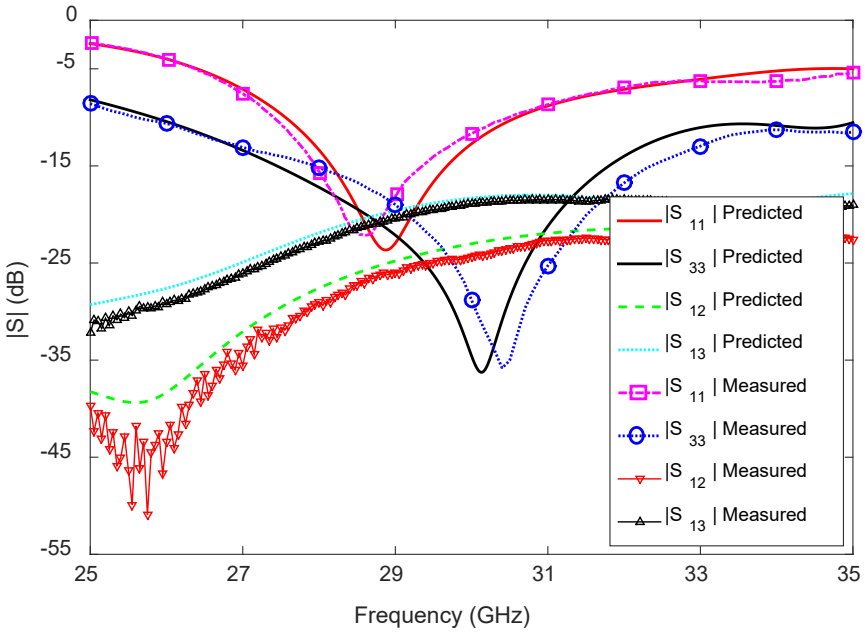

Figure 5.15: Measured and simulated S-parameters of the 1-D pattern reconfigurable antenna for 28 GHz millimeter-wave 5G hand-held devices.

The measured transmission coefficients ($|S_{12}|$, $|S_{21}|$) between the LF and RF are below -24 dB within the -10 dB reflection coefficient bandwidth (27.3-30.5 GHz) of the antenna,

whereas the simulated $|S_{12}|$, $|S_{21}|$ is below -22 dB within the -10 dB reflection coefficient bandwidth. Apart from this, the measured transmission coefficients ($|S_{13}|$, $|S_{31}|$, $|S_{23}|$, $|S_{32}|$) between the edge feeds (LF, RF) and the center feed (CF) are below -19 dB within the -10 dB reflection coefficient bandwidth (25.6-35 GHz) of the antenna, whereas the simulated $|S_{13}|$, $|S_{31}|$, $|S_{23}|$, $|S_{32}|$ are below -18 dB within the -10 dB reflection coefficient bandwidth. Therefore, an excellent agreement is observed between the simulated and measured transmission coefficients between the three feeds, i.e. LF, RF, and CF.

5.3.2 Radiation Performance

The directivity, gain, efficiency and radiation patterns in the y-z plane of the antenna for LF is the same as for RF, except for the radiation patterns in the x-z plane. For this reason, the measured directivity, gain, efficiency and radiation patterns in the y-z plane of the antenna for LF are presented in this section together with the simulated results.

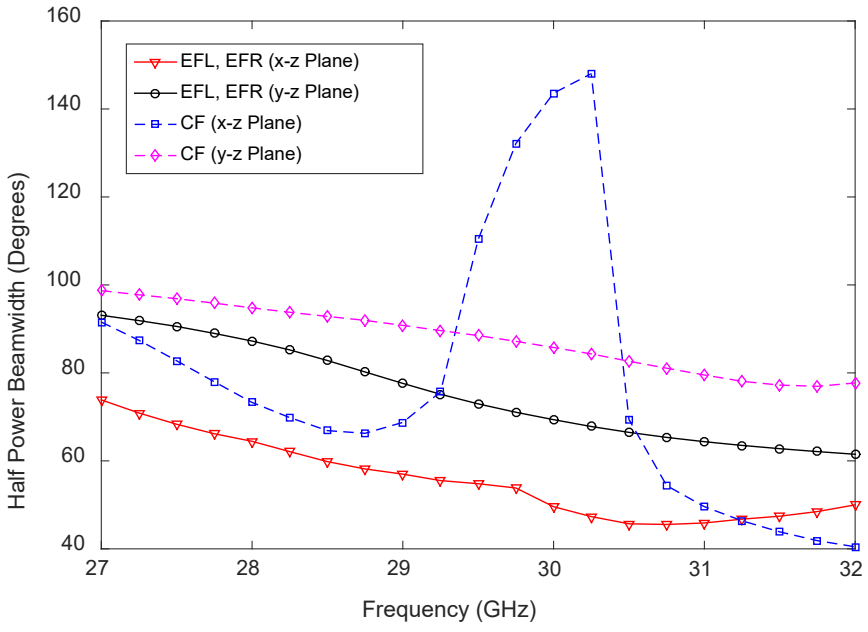

Figure 5.16: Simulated half power beamwidth in x-z and y-z planes of the 1-D pattern reconfigurable antenna for CF, LF, and RF.

Before discussing the antenna's radiation performance it is important to know the frequency when the radiation patterns for CF in the x-z plane start to split, meaning that the single-beam pointing boresight splits into two beams pointing off-bore-right and off-bore-left. Fig. 5.16 shows the half-power beamwidth (HPBW) of the 1-D pattern reconfigurable antenna with LF, RF and CF active one at a time. Note that the HPBW for LF and RF is equal at each frequency point. The HPBW for LF and RF in both the x-z and y-z planes becomes continuously narrower with increasing frequency. As this frequency increases, more energy travels towards the load end of the antenna for LF and RF resulting in an increase in directivity, as shown in Fig. 5.17. Thus a decrease in the HPBW occurs but no beam split is recorded. However, the side-lobe level (SLL) becomes worse as the frequency increases.

The HPBW of the antenna for CF in the y-z plane continuous to narrow with increasing frequency, as shown in Fig. 5.16. The reason is that, with increasing frequency, more energy travels towards both ends of the antenna and the energy at the location of the feed point (center of the antenna) gradually becomes weaker, as previously indicated in Fig. 4.20. The HPBW in the x-z plane decreases with increasing frequency up to the frequency 28.5 GHz, because more energy is concentrated at the center of the antenna and hence the directivity of the antenna increases, as shown in Fig. 5.18. As the frequency increases from 28.5 GHz to 30.25 GHz the concentrated energy from the center of the antenna starts to distribute towards both load ends of the antenna, and so the HPBW of the antenna for CF starts to increase, up to 30.25 GHz. Fig. 5.18 shows that the directivity of the antenna for CF decreases. The boresight gain of the antenna for CF in the x-z plane at 30.5 GHz is 3 dB lower than the maximum, hence the single-beam radiation completely splits into two beams pointing off-bore-right and off-bore-left. However, the antenna performs very well in the target frequency range 27-30 GHz. The directivity, gain, efficiency and radiation patterns of the antenna are presented for this target frequency

range 27-30 GHz.

The measured gain and directivity of the antenna for LF and CF are shown in Fig. 5.17 and Fig. 5.18, respectively, and compared with the simulated results in the frequency range 27-30 GHz; an excellent agreement is observed between the simulated and measured results. The maximum and minimum directivity of the antenna for LF are 8.6 and 6.8 dBi between 27 and 30 GHz. For CF the maximum and minimum directivity of the antenna are 6.9 and 5.1 dBi within the frequency range 27-30 GHz. The directivity of the antenna for LF increases with increasing frequency, but for CF the directivity increases in the frequency range 27-28.5 GHz and decreases in the frequency range 28.5-30 GHz.

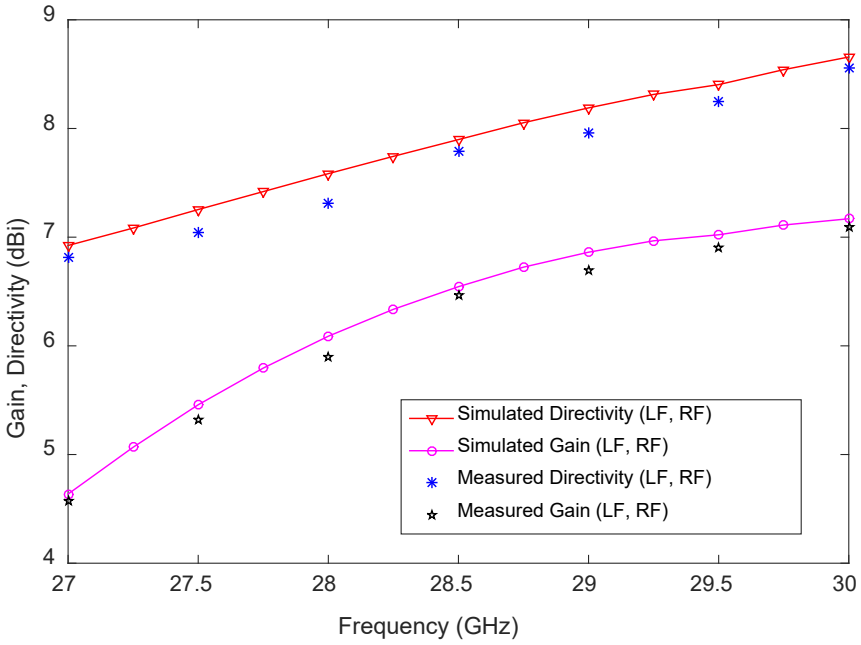

Figure 5.17: Measured and simulated directivity and gain of the 1-D pattern reconfigurable antenna with EFL or EFR active.

The maximum and minimum measured gains of the antenna for LF are 7.1 and 4.6 dBi, respectively, at frequency 30 and 27 GHz, respectively, i.e. the gain variation within the frequency range 27-30 GHz is 2.5 dB. The maximum and minimum measured gain of the antenna for CF are 6.1 and 4.1 dBi, respectively, at frequency 28.5 and 30 GHz,

respectively, i.e. the gain variation within the frequency range 27-30 GHz is 2 dB. As the frequency increases more energy propagates towards the load end of the antenna for LF and RF, resulting in a more directive radiation patterns as well as an increase in the gain of the antenna with increasing frequency. Therefore, the gain vs frequency behavior of the antenna for LF and RF in the frequency range 27-30 GHz is similar to the directivity vs frequency behavior of the antenna for LF and RF. As the frequency increases in the frequency range 27-28.5 GHz more energy is concentrated at the center of the antenna resulting in an increase in the directivity and gain of the antenna for CF, but with increasing frequency in the range 28.5-30 GHz more energy is distributed towards both load ends of the antenna, resulting in a decrease in the directivity and gain of the antenna. Therefore, the gain vs frequency behavior of the antenna for CF in the frequency range 27-30 GHz is similar to the directivity vs frequency behavior of the antenna for CF.

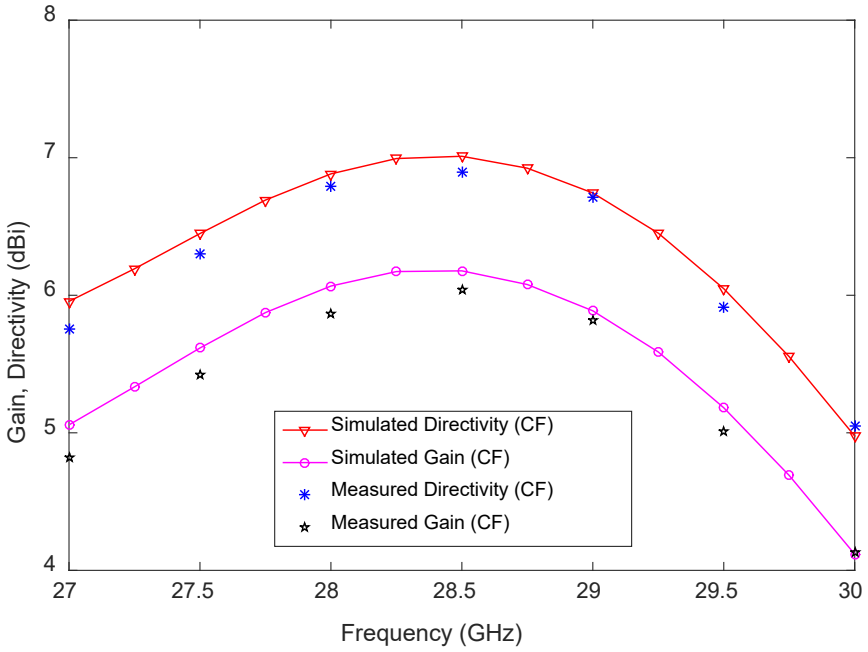

Figure 5.18: Measured and simulated directivity and gain of the 1-D pattern reconfigurable antenna with CF active.

Fig. 5.19 shows the measured antenna efficiency for LF and CF together with the simulated results; a good agreement is observed between the simulated and measured results. The antenna efficiency is estimated from the measured gain and directivity of the antenna and using the fundamental equation of efficiency calculation from directivity and gain [122]. The measured antenna efficiency is at its maximum at 28.5 GHz and the minimum appears at 27 GHz for LF. The maximum and minimum measured antenna efficiencies are 72% and 58%, respectively. The antenna efficiency for CF is 8% higher than the antenna efficiency for LF, as depicted in Fig. 5.19. The maximum and minimum antenna efficiencies of the antenna for CF are 82% and 80%, respectively, at 28.5 GHz and 27 GHz, respectively.

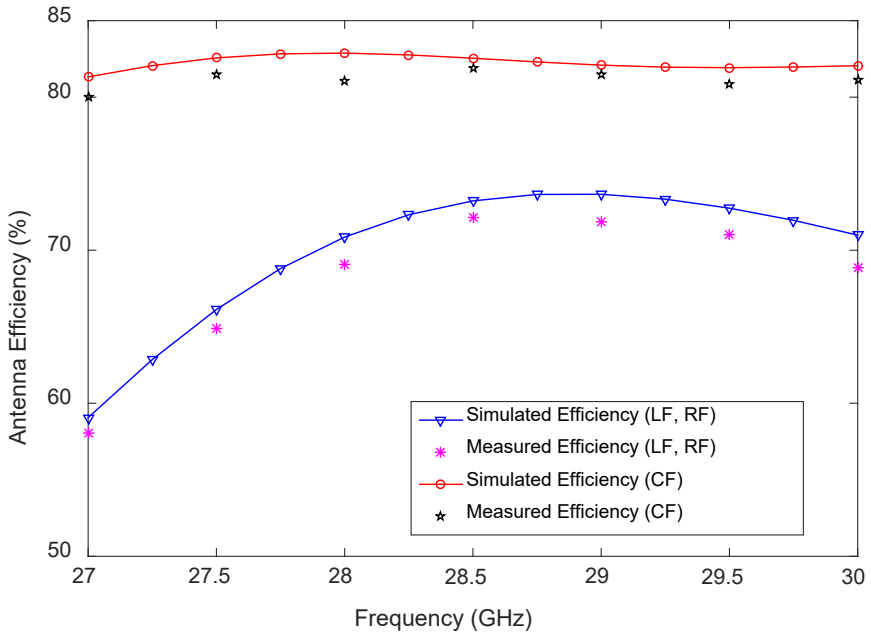

Figure 5.19: Measured and simulated antenna efficiency of the 1-D pattern reconfigurable antenna.

Regarding the normalized radiation patterns of the 1-D pattern reconfigurable antenna for EFL, EFR and CF, the radiation pattern at each frequency in each plane is normalized using the peak gains in the corresponding plane at that frequency. The predicted and

measured radiation patterns are normalized separately. The measured radiation patterns are presented for the frequency range 27-30 GHz with a step of 1 GHz but the predicted radiation patterns are presented for the same frequency range with a step of 0.5 GHz.

Fig. 5.20 illustrates the predicted and measured radiation patterns in the x-z plane of the 1-D pattern reconfigurable antenna with LF active. The measured main lobe for LF points in the region off-bore-right and at an angle of $\theta = 30°$, $33°$, $35°$, $37°$ at 27, 28, 29 and 30 GHz, respectively, as shown in Fig. 5.20 (b). The predicted main lobe direction in the x-z plane is $\theta = 30°$, $32°$, $36°$, $38°$ at 27, 28, 29 and 30 GHz, respectively, as shown in Fig. 5.20 (a).

The measured and predicted radiation patterns in the x-z plane of the antenna with RF active are exhibited in Fig. 5.21. An excellent agreement is observed between the measured and predicted radiation patterns. The measured main lobe for RF points in the region off-bore-left and the pointing angle is equally away from boresight at each frequency as was found for LF.

Table 5.2: Measured side-lobe level (SLL), half-power beamwidth (HPBW), and main-lobe direction (MLD) of the 1-D pattern reconfigurable antenna with LF/RF active for 28 GHz millimeter-wave 5G hand-held devices.

Frequency (GHz)		27	28	29	30
SLL for LF/RF (dB)	x-z plane	-9	-8	-9	-9
	y-z plane	-13	-15	-14	-13
HPBW for LF/RF (degree)	x-z plane	78	68	61	53
	y-z plane	97	92	80	73
MLD for LF ($\theta°$)	x-z plane	30	33	35	37
MLD for RF ($\theta°$)	x-z plane	-30	-33	-35	-37

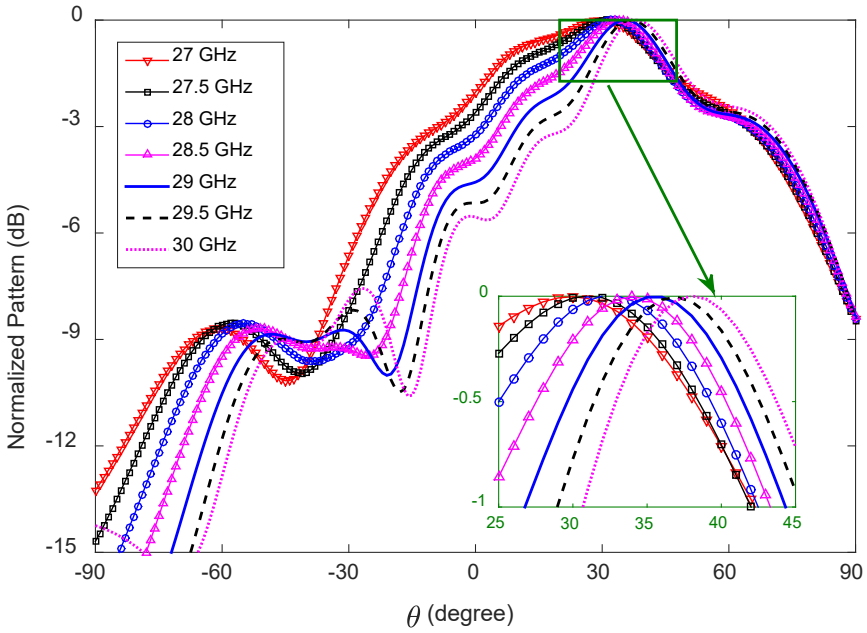

(a)

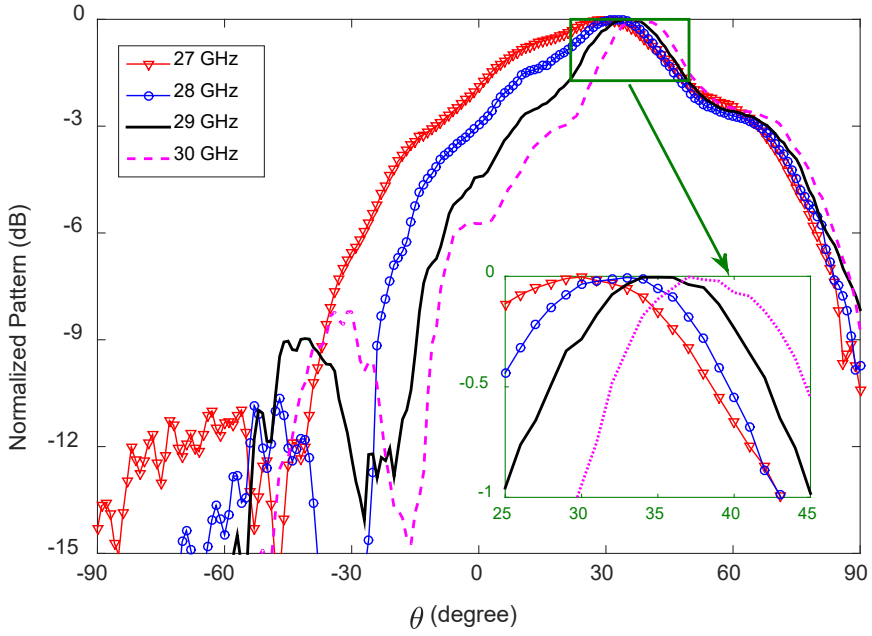

(b)

Figure 5.20: Radiation patterns (normalized) in the x-z plane of the 1-D pattern reconfigurable antenna: (a) predicted, and (b) measured when LF is active.

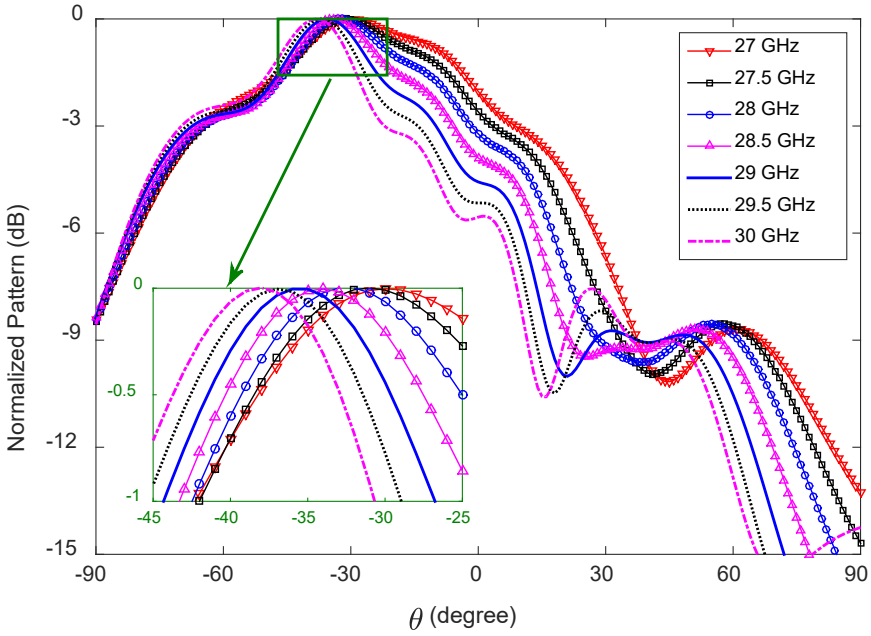

(a)

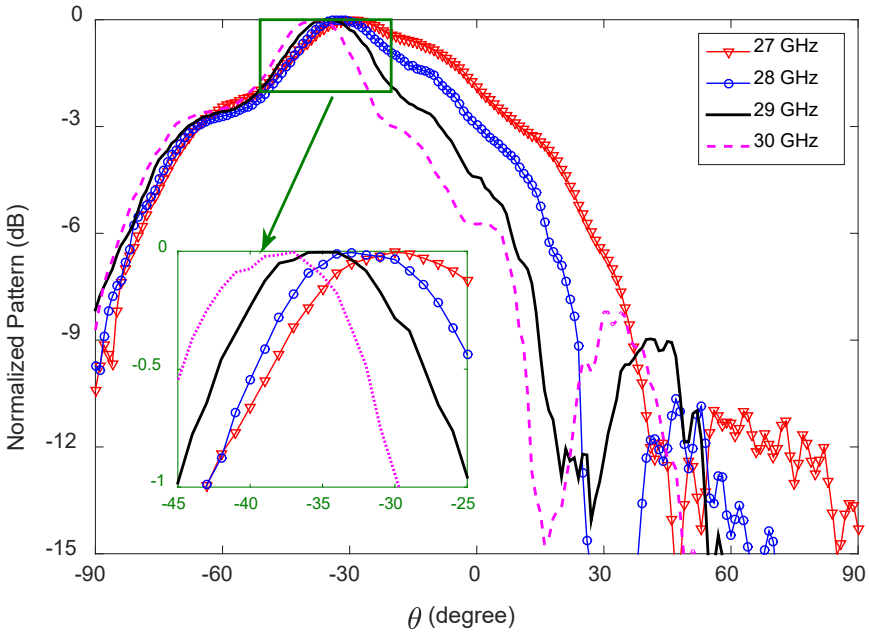

(b)

Figure 5.21: Radiation patterns (normalized) in the x-z plane of the 1-D pattern reconfigurable antenna: (a) simulated, and (b) measured, when RF is active.

The measured side-lobe level (SLL), half-power beamwidth (HPBW), and main lobe direction (MLD) of the radiation pattern in the x-z plane are listed in Table 5.2. The measured SLL for LF and RF is always below -8 dB in the x-z plane. The HPBW decreases with the increase of the frequency and the maximum and minimum HPBW in the x-z plane are 78° and 53° at 27 and 30 GHz, respectively.

Fig. 5.22 shows the measured and simulated y-z plane radiation patterns of the antenna with LF and RF active. The radiation patterns in the y-z plane for LF and RF are the same and pointing towards boresight. The measured SLL, HPBW, and main lobe direction of the radiation pattern in the y-z plane are listed in Table 5.2. Like the simulation observation, the HPBW in the y-z plane is wider than the HPBW in the x-z plane at each frequency. Added to this, the HPBW decreases with the increase of the frequency; the maximum and minimum HPBWs in the y-z plane are 97° and 73° at 27 and 30 GHz, respectively. The SLL in the y-z plane is below -13 dB and is better than the SLL in the x-z plane.

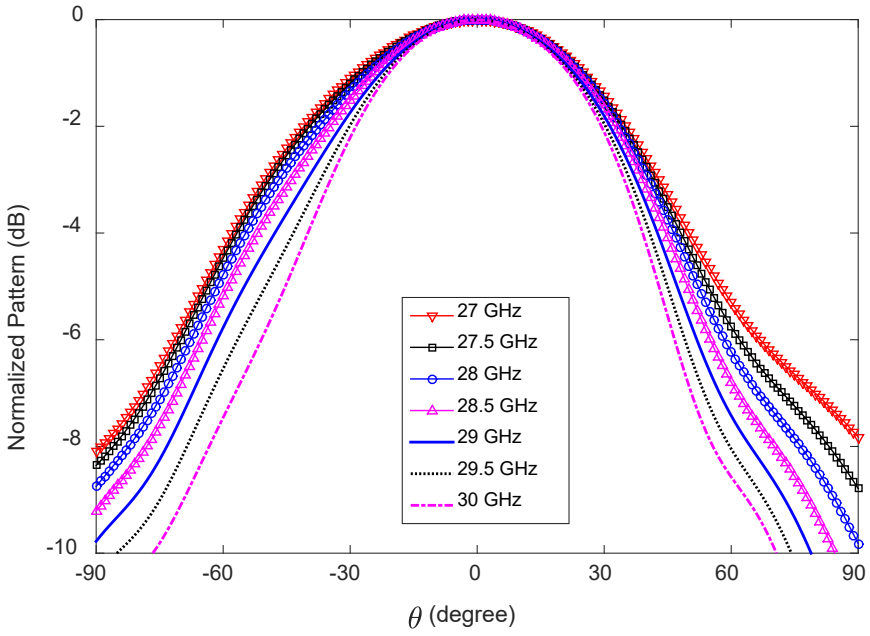

(a)

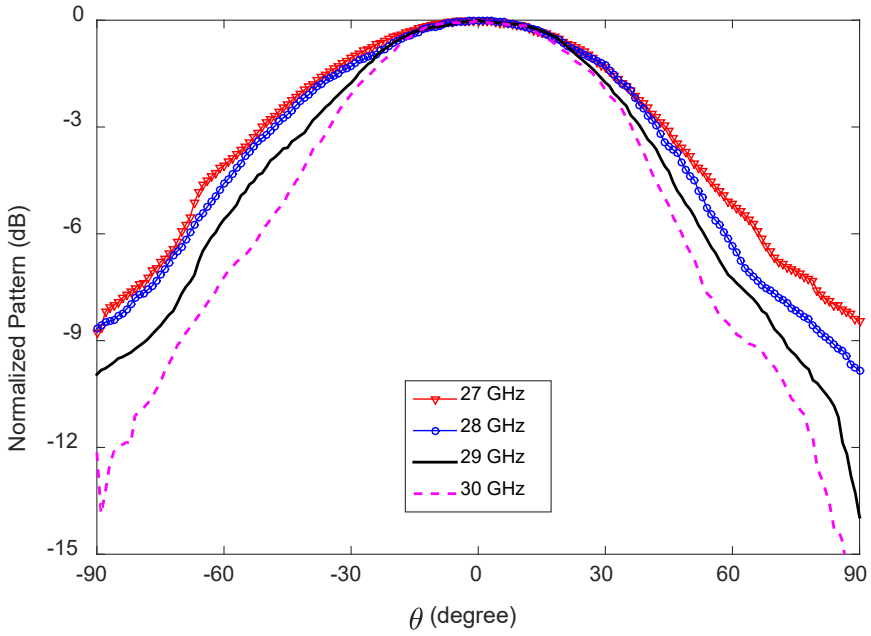

(b)

Figure 5.22: Radiation patterns (normalized): (a) simulated, and (b) measured, in the y-z plane of the 1-D pattern reconfigurable antenna with LF or RF active for 28 GHz millimeter-wave 5G hand-held devices.

The measured and predicted radiation patterns in the x-z plane and y-z plane of the antenna with CF active are shown in Fig. 5.23 and Fig. 5.24, respectively. The radiation patterns in the x-z plane point towards boresight and no beam splitting is observed within the frequency range 27-30 GHz. The radiation patterns in the y-z plane point -20° to -27° away from boresight and with the increase in the frequency the main lobe's direction shifts away from boresight. Table 5.3 lists the measured SLL, HPBW, and MLD of the antenna with CF active. The beamwidth becomes narrower with the increase of the frequency till 28.5 GHz, and then beamwidth becomes wider when frequency increases. The maximum and minimum beamwidth in the x-z plane of the antenna with CF active are 146° and 74° at 30 and 29 GHz, respectively. The measured beamwidth vs frequency behavior in the x-z and y-z planes of the antenna are the same as those observed in the simulation (Fig. 5.16). The SLL of the antenna in the x-z plane is better than that in the y-z plane. The SLL in the x-z and y-z planes is always below -12 dB and -9 dB, respectively.

Table 5.3: Measured side-lobe level (SLL), half-power beamwidth (HPBW), and main-lobe direction (MLD) of the 1-D pattern reconfigurable antenna with CF active for 28 GHz millimeter-wave 5G hand-held devices.

Frequency (GHz)		27	28	29	30
SLL (dB)	x-z plane	-17	-15	-14	-12
	y-z plane	-10	-9	-11	-10
HPBW (degree)	x-z plane	94	77	74	146
	y-z plane	102	98	95	89
MLD (θ°)	y-z plane	-20	-20	-23	-27

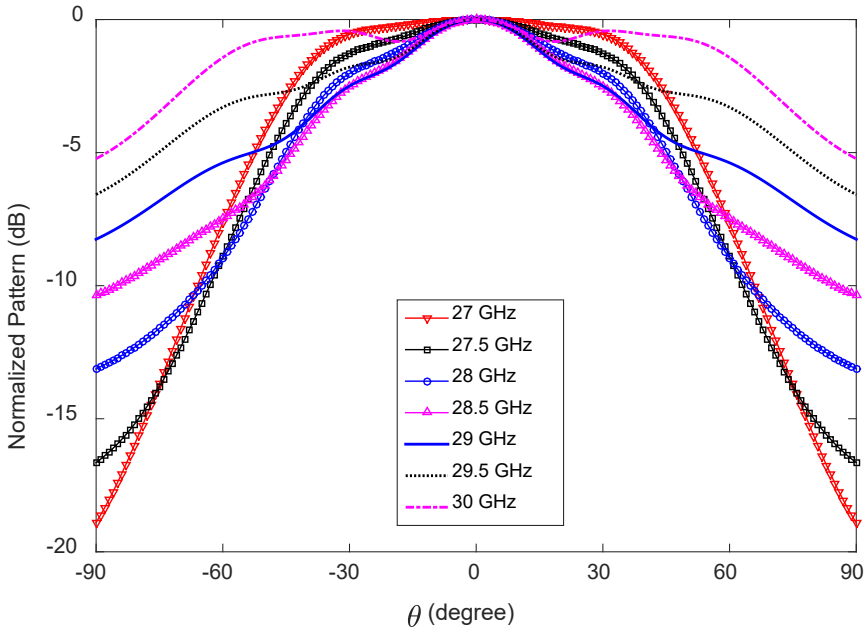

(a)

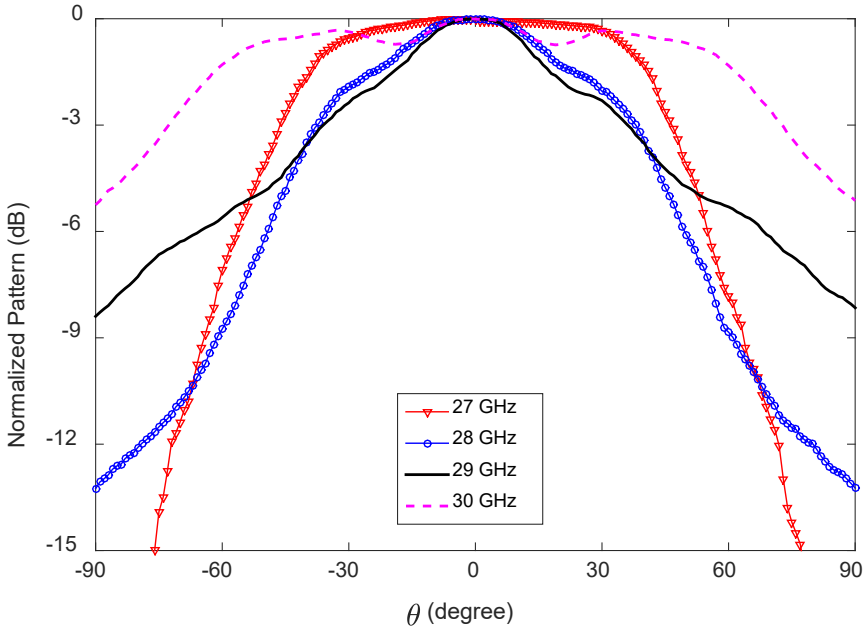

(b)

Figure 5.23: Radiation patterns (normalized): (a) simulated, and (b) measured, in the x-z plane of the 1-D pattern reconfigurable antenna with CF active for 28 GHz millimeter-wave 5G hand-held devices.

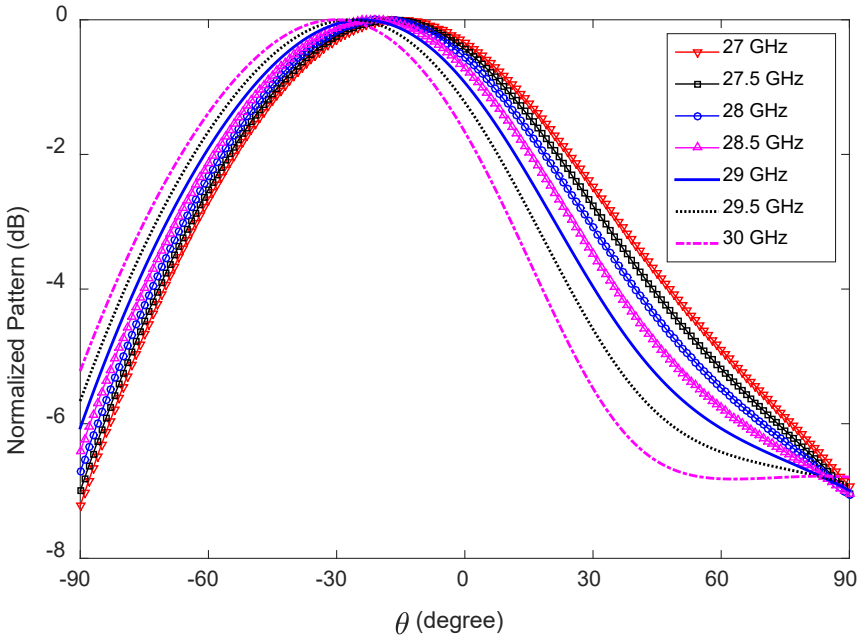

(a)

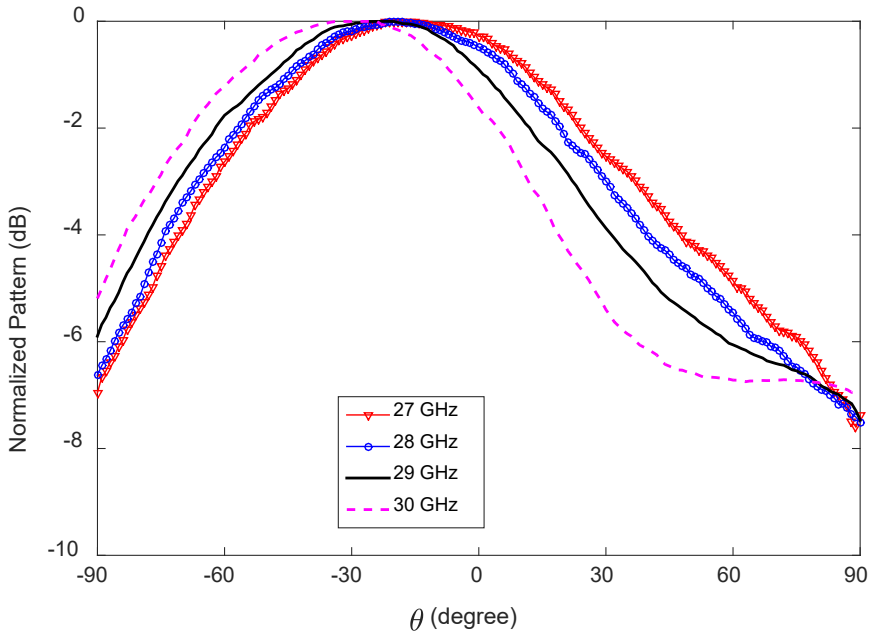

(b)

Figure 5.24: Radiation patterns (normalized): (a) simulated, and (b) measured, in the y-z plane of the 1-D pattern reconfigurable antenna with CF active for 28 GHz millimeter-wave 5G hand-held devices.

5.4 2-D Pattern Reconfigurable Antenna

The antenna presented in Section 5.2 is developed to switch the beam to three different directions along the x-axis, i.e. 1-D pattern reconfiguration is achieved. In this section, the way to use two similar antennas placed at right angles in order to achieve the beam switching along two axes (along x and y-axes), i.e. to have 2-D beam switching, is presented. The measured and simulated results are described after integrating the antenna into a mobile device ground.

5.4.1 Antenna Configuration

The configuration of the antenna for 2-D beam switching is shown in Fig. 5.25 together with the prototype. The area required for each element (mmAnt-1 and mmAnt-2 indicated in Fig. 5.25) of the 2-D beam switching antenna is 30 mm × 7 mm (length × width). These two elements are identical to each other.

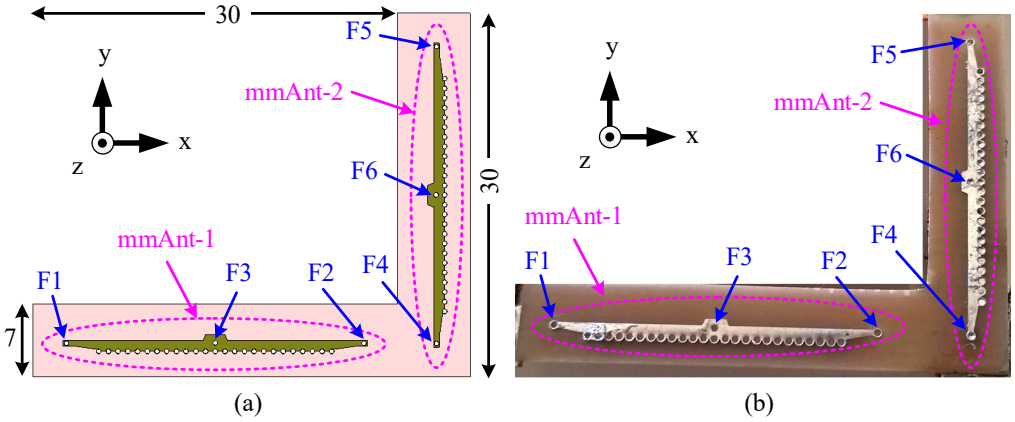

Figure 5.25: Configuration of the 2-D pattern-reconfigurable antenna for 28 GHz millimeter-wave 5G hand-held devices: (a) CST model, and (b) prototype. All dimensions are in millimeters.

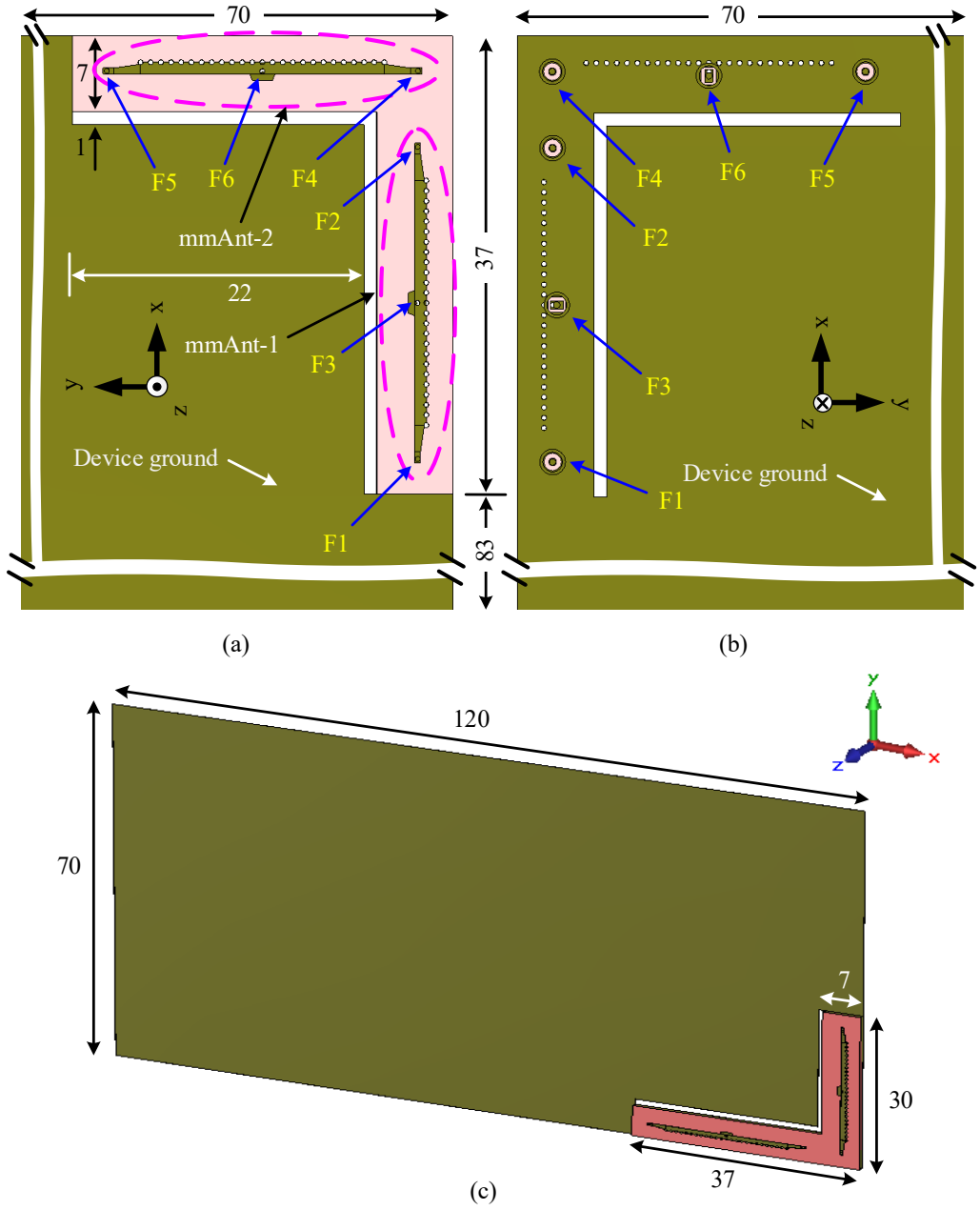

Figure 5.26: CST model of the 2-D pattern-reconfigurable antenna integrated into a mobile device ground that is 120 mm × 70 mm in size: (a) top, (b) back, and (c) perspective views. All dimensions are in millimeters.

The 1-D pattern reconfiguration along the x-axis is achieved using the element mmAnt-1 and the directions of radiation are in off-bore-right (the region between the +z and +x

axes), off-bore-left (the region between the +z and -x axes) and boresight (along the +z axis) when the feeds F1, F2, and F3, respectively, are active. Also, 1-D pattern reconfiguration along the y-axis is achieved using the element mmAnt-2 and the direction of radiation is in off-bore-up (the region between the +z and +y axes), off-bore-down (the region between the +z and -y axes) and boresight (along the +z axis) when the feeds F4, F5, and F6, respectively, are active.

5.4.2 Integration into Mobile Device

This section presents the configuration of the 2-D pattern reconfigurable antenna after integrating the antenna into a mobile device ground plane with a size of 120 mm × 70 mm. The proposed 2-D beam switching antenna is placed at a corner of the ground plane of a mobile device, as depicted in Fig. 5.26. A 1 mm gap, as indicated in Fig. 5.26 (a), is ensured between the mobile device's ground plane and the substrate of the antenna in order to limit the distribution of energy from the antenna to the ground plane.

5.4.3 Measured and Predicted Results

Fig. 5.27 shows the prototype of the 2-D pattern reconfigurable antenna after integrating into a mobile device ground. The simulated and measured S-parameters of the antenna are shown in Fig. 5.28, and an excellent agreement is observed between the simulated and measured results.

The measured -10 dB reflection coefficient bandwidth of the antenna is 3.2 GHz (27.3-30.5 GHz) for the side feeds F1, and F2, and 2.9 GHz (27.4-30.3 GHz) for the side feeds F4, and F5. Also, the measured -10 dB reflection coefficient bandwidths of the antenna are 9.4 GHz (25.6-35 GHz) for the center feed F3 and 9.3 GHz (25.7-35 GHz) for the center feed F6.

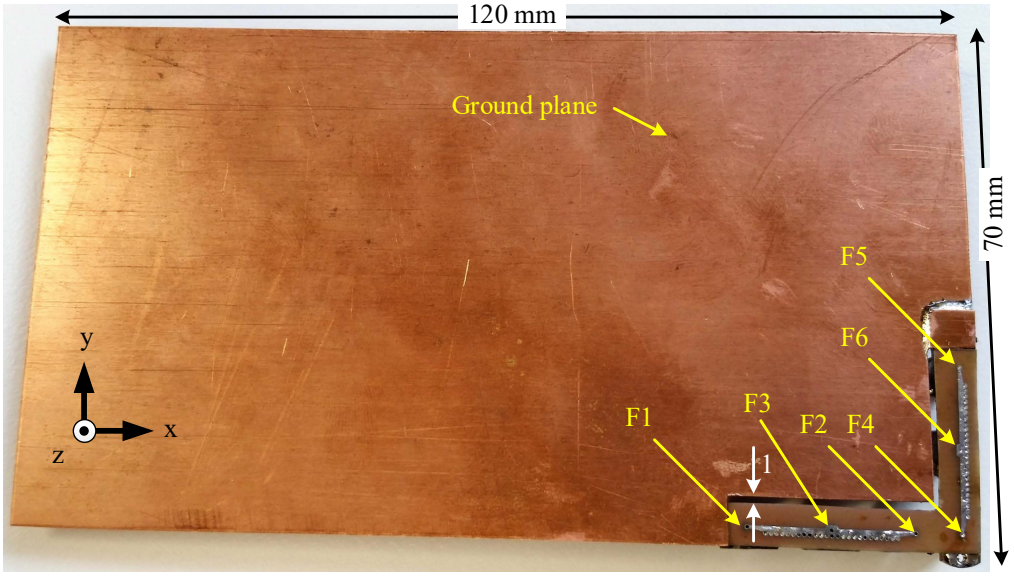

(a)

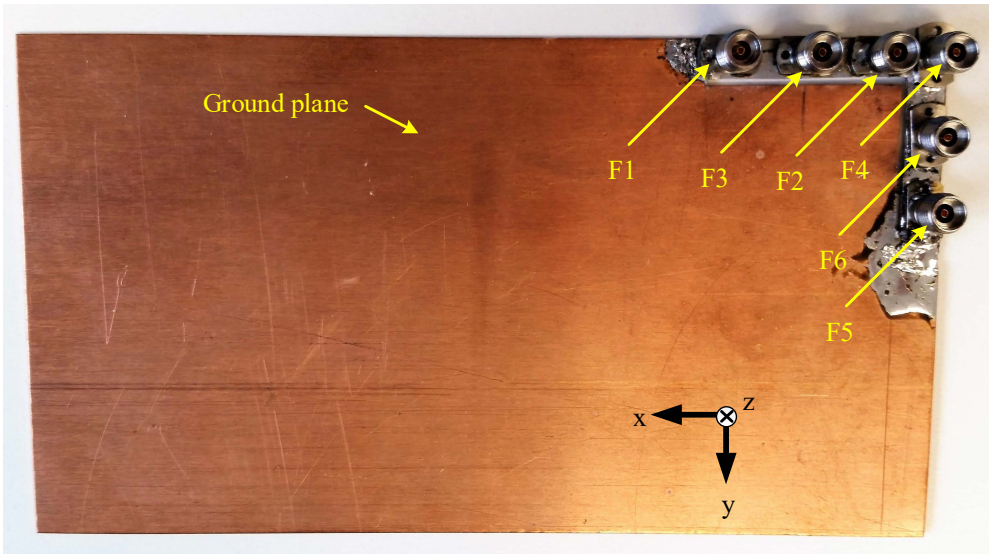

(b)

Figure 5.27: Prototype of the 2-D pattern-reconfigurable antenna after integrating into the mobile device's ground plane: (a) top view, and (b) back view.

The measured transmission coefficients ($|S_{12}|$, $|S_{21}|$) between F1 and F2 are below -24 dB within the -10 dB reflection coefficient bandwidth (27.3-30.5 GHz) of the antenna, and the measured $|S_{45}|$, $|S_{54}|$ are below -27 dB within the -10 dB reflection coefficient bandwidth (27.4-30.3 GHz) of the antenna. Furthermore the measured transmission coef-

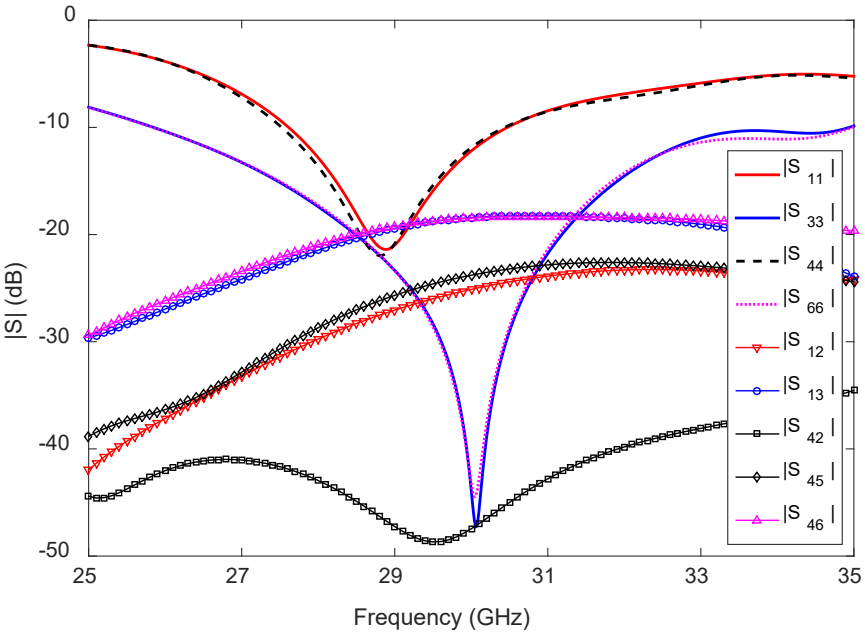

(a)

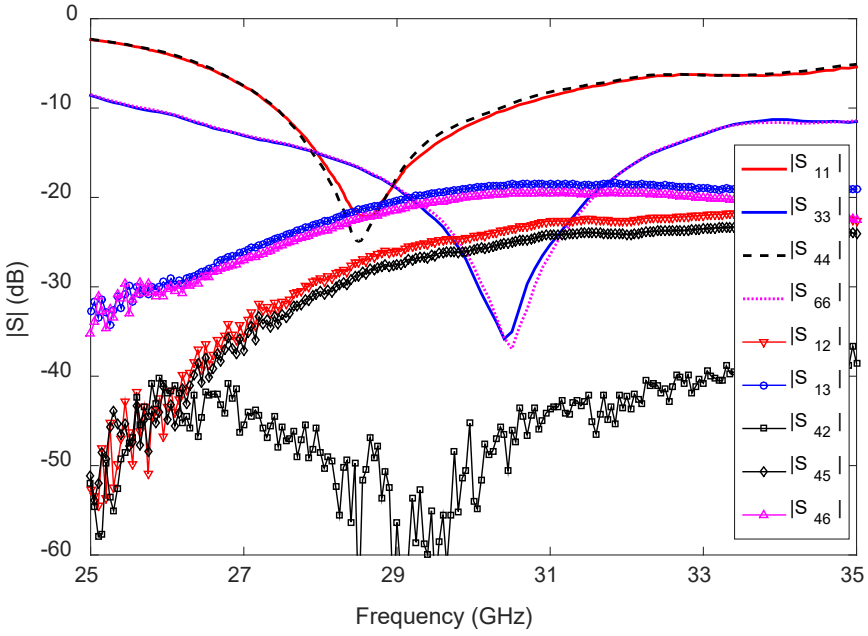

(b)

Figure 5.28: S-parameters of the 2-D pattern reconfigurable antenna for 28 GHz millimeter-wave 5G hand-held devices: (a) simulated, and (b) measured.

ficients ($|S_{13}|$, $|S_{31}|$, $|S_{23}|$, $|S_{32}|$) between the side feeds F1, F2, and center feed F3 of the antenna are below -19 dB. This occurs within the -10 dB reflection coefficient bandwidth (25.6-35 GHz) of the antenna. Meanwhile the measured $|S_{46}|$, $|S_{64}|$, $|S_{56}|$, $|S_{65}|$ between the side feeds F4, F5 and center feed F6 of the antenna are below -20 dB within the -10 dB reflection coefficient bandwidth.

In order to ensure isolation between the elements mmAnt-1 and mmAnt-2 the transmission coefficients between F2 of mmAnt-1 and F4 of mmAnt-2 are measured since these two feed points are very close to each other and a maximum transmission is possible between these two feed points. The measured $|S_{42}|$ is always below -38 dB within the frequency range 25.6-35 GHz, indicating that the elements mmAnt-1 and mmAnt-2 do not affect each other's performance.

The directions of the main lobe of the 2-D pattern reconfigurable antenna at 27, 28, 29, and 30 GHz are listed in Table 5.4 when F1, F2, F3, F4, F5, and F6 are on (one feed at a time). Also, their half-power beamwidth (HPBW) or 3-dB beamwidth are listed in Table 5.5. For better understanding, firstly, the 3-D radiation patterns of the antenna at 27 and 30 GHz are shown in Fig. 5.29; secondly, the 2-D radiation patterns at 28 GHz (in Cartesian coordinates) are shown in Fig. 5.30.

Table 5.4: Main-lobe direction (MLD) of the 2-D pattern reconfigurable antenna at 27, 28, 29, and 30 GHz when feeds F1, F2, F3, F4, F5, and F6 are on (one feed at a time).

Feed	27 GHz (θ, ϕ)	28 GHz (θ, ϕ)	29 GHz (θ, ϕ)	30 GHz (θ, ϕ)
F1	+24°, -45°	+27°, -35°	+42°, -20°	+46°, 0°
F2	-25°, +50°	-33°, +45°	-30°, +25°	-59°, 0°
F3	-24°, +90°	-22°, +90°	-27°, +90°	-33°, +90°
F4	+24°, +30°	+29°, +60°	+35°, +90°	+47°, +90°
F5	-28°, +150°	-29°, +140°	-38°, +90°	-39°, +90°
F6	+21°, 0°	+19°, 0°	+27°, 0°	+30°, 0°

Table 5.5: Half-power beamwidth (HPBW) of the 2-D pattern reconfigurable antenna in the x-z and y-z planes at 27, 28, 29, and 30 GHz when feeds F1, F2, F3, F4, F5, and F6 are on (one feed at a time).

Feed	27 GHz (x-z, y-z planes)	28 GHz (x-z, y-z planes)	29 GHz (x-z, y-z planes)	30 GHz (x-z, y-z planes)
F1	67°, 98°	61°, 88°	74°, 78°	63°, 99°
F2	65°, 97°	59°, 90°	65°, 82°	59°, 84°
F3	87°, 104°	75°, 90°	42°, 85°	32°, 84°
F4	102°, 69°	89°, 66°	84°, 85°	77°, 69°
F5	89°, 67°	86°, 82°	99°, 65°	83°, 66°
F6	93°, 83°	91°, 59°	91°, 38°	85°, 40°

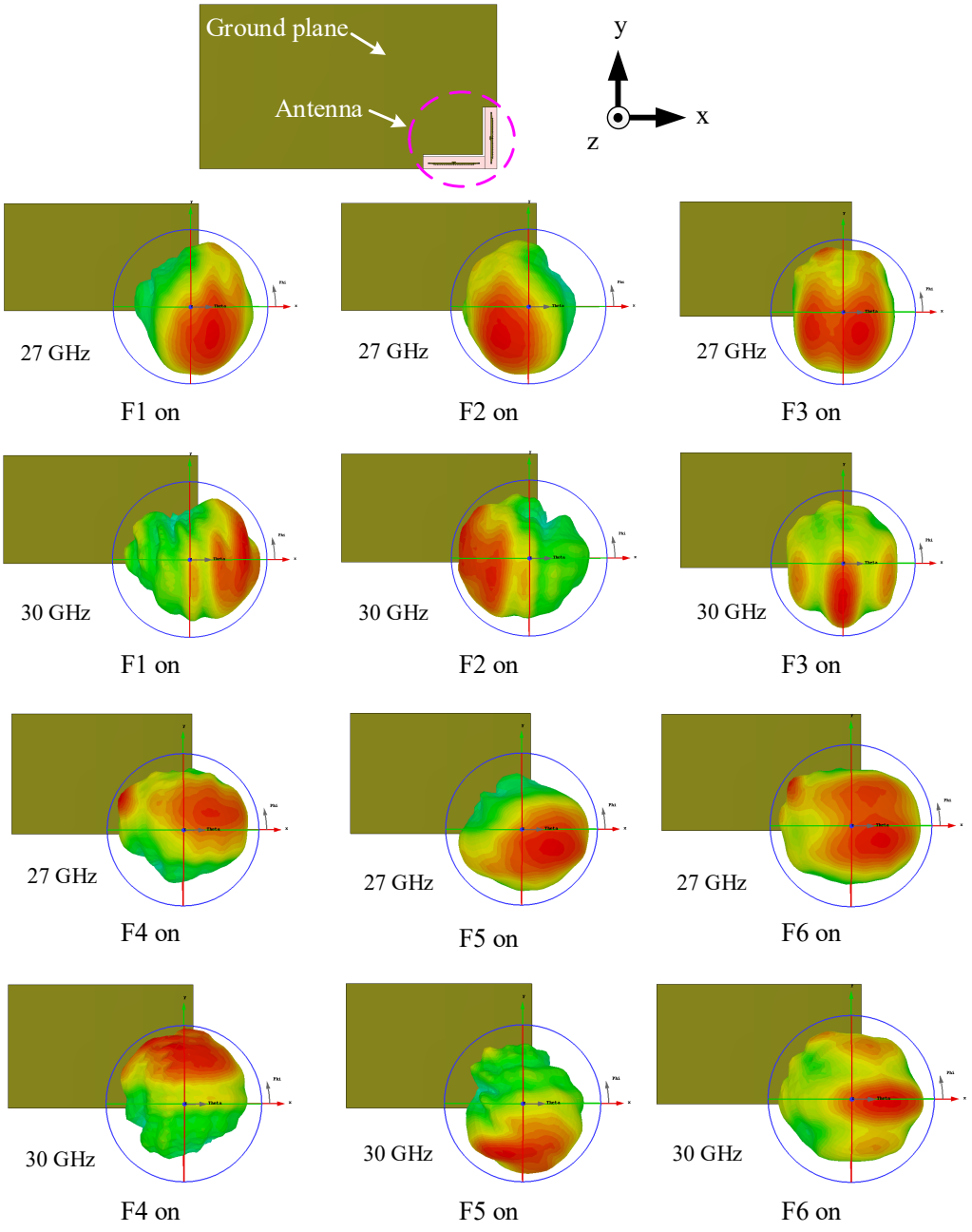

Figure 5.29: 3-D radiation patterns of the 2-D pattern-reconfigurable antenna at 27 and 30 GHz after integrating the antenna into the ground plane of a mobile device.

From the 3-D radiation patterns it is clear that the antenna radiation patterns are not perfectly aligned with the x-axis or y-axis after integrating the antenna into the device

ground plane. At 27 GHz, the radiation pattern of the antenna is in the region between the +x and -y axes, θ = +24°, ϕ = -45°, when F1 is on but the HPBW in the y-z plane is 98° which is wide enough to cover the ϕ = 0° region. The radiation patterns of the antenna slowly shift to the x-z plane (ϕ = 0°) with an increasing tilting angle from θ = +24° to θ = +46° in the frequency range 27-30 GHz, as illustrated in Fig. 5.29. The obtained results are listed in Table 5.4.

A similar behavior for the radiation patterns of F2 is observed. At 27 GHz, the main lobe points at (θ, ϕ) = (-25°, +50°), and at 30 GHz the direction of the radiation pattern is aligned with the x-z plane (ϕ = +180°). For F3, the direction of radiation is always aligned with the y-z plane (ϕ = -90°) but -24° to -33° tilting along the -y-axis is observed within the frequency range 27-30 GHz. Again, the HPBW in the y-z plane is always above 84°, which is sufficient to cover the boresight direction, i.e. the +z-axis.

Therefore, using the element mmAnt-1 it is possible to scan along the x-axis (ϕ = 0°) from θ = +46° to θ = -59° and along the y-axis (ϕ = 90°) from θ = -24° to θ = -33°. This can be done while having a 3-dB coverage of 167° (from θ = +78° to θ = -89°) along the x-axis and 103° along the y-axis (from θ = +28° to θ = -75°). In this way the boresight direction is covered.

For the feeds F4 to F6 a similar scanning behavior is observed along the y-z plane (ϕ = 90°) to that observed for F1 to F3 along the x-z plane (ϕ = 0°). Using the element mmAnt-2 it is possible to scan along the y-axis (ϕ = 90°) from θ = +47° to θ = -39° and along the x-axis (ϕ = 0°) from θ = +21° to θ = +30° while having a 3-dB coverage of 154° (from θ = +82° to θ = -72°) along the y-axis and 99° along the x-axis (from θ = -26° to θ = +73°). This covers the boresight direction.

It can therefore be suggested that the proposed 2-D pattern reconfigurable antenna to achieved 3-dB coverage is 167° [(θ, ϕ) = (-89°, 0°) to (78°, 0°)] along the x-axis, and 154° [(θ, ϕ) = (-72°, 90°) to (82°, 90°)] along the y-axis.

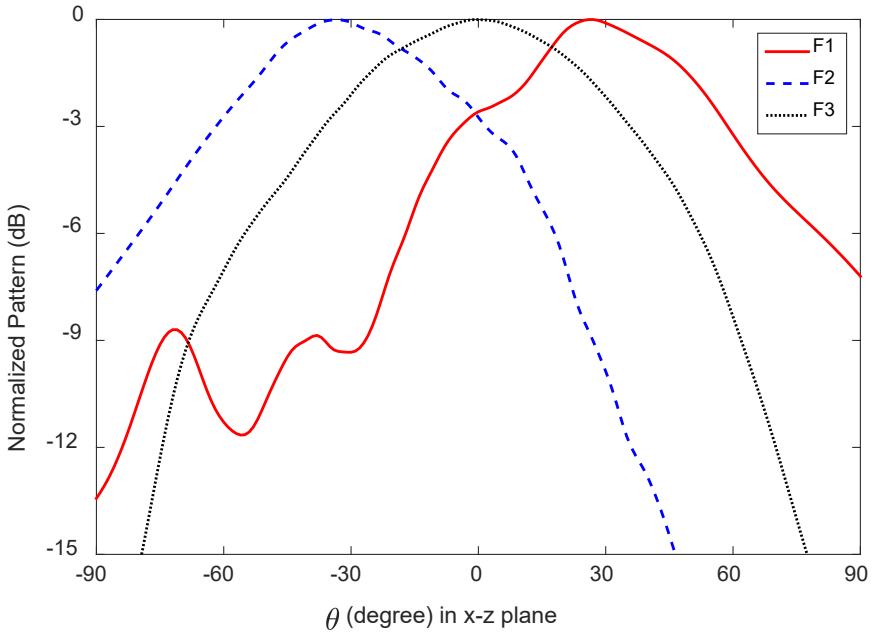

(a)

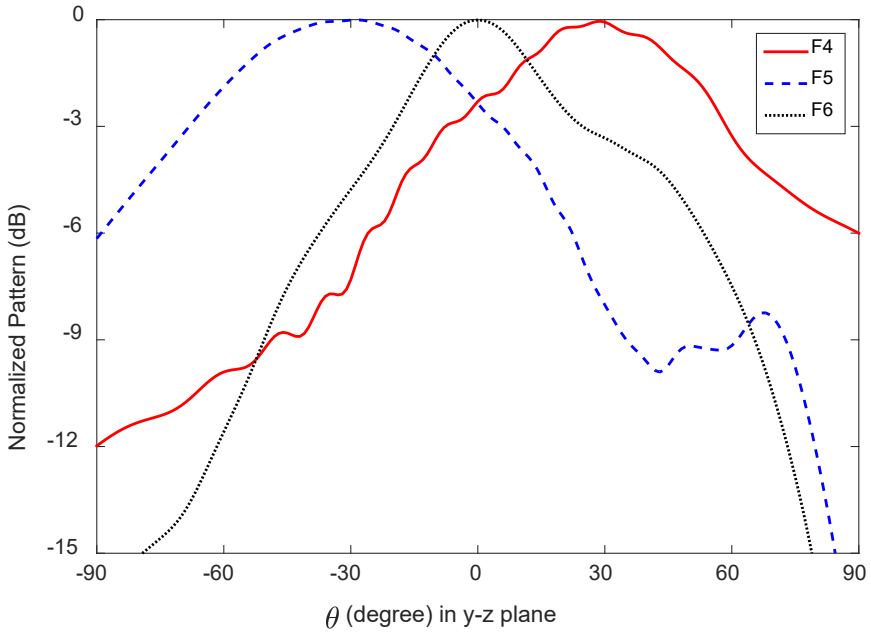

(b)

Figure 5.30: Radiation patterns of the 2-D pattern reconfigurable antenna at 28 GHz: (a) for F1, F2, and F3 in the x-z plane (cut angle $\phi = 0°$), and (b) for F4, F5, and F6 in the y-z plane (cut angle $\phi = 90°$).

From the presented results in Fig. 5.30 it is clear that the proposed antenna scans the beam along the x-axis using the element mmAnt-1 and along the y-axis using the element mmAnt-2. The direction of the radiation for the three feed points F1, F2, and F3 of element mmAnt-1 are θ (along x-axis, $\phi = 0°$) = +27°, -33°, and 0°, respectively. Meanwhile the direction of the radiation for the three feed points F4, F5, and F6 of element mmAnt-2 are θ (along y-axis, $\phi = 90°$) = +29°, -29°, and 0°, respectively.

Table 5.6: Design comparison between the proposed 1-D/2-D pattern reconfigurable antenna and the reference antennas reported to date for millimeter-wave 5G mobile devices.

Ref.	Area (mm^2)	1-D/2-D Scan	Scan Angle (θ)	No. of Ports	Type
[57]	446	1-D	-60° to +65°	16	phased array
[53]	1156	1-D	NA	4	microstrip
[54]	NA	1-D	-45° to +45°	4	phased array
[52]	1534	1-D	-48° to +48°	8	slot array
[55]	1035	1-D	0° to +70°	8	microstrip
[56]	385	1-D	0° to +50°	10	phased array
[58]	1505	1-D	-45° to +45°	4	microstrip
This Work	480	2-D	+46° to -59° +47° to -39°	6	microstrip

Here, area = length × width; NA = not available.

Now the comparison between the performances of the proposed 2-D beam switching antenna with the pattern reconfigurable millimeter-wave 5G mobile device antennas reported to date is discussed. Table 5.6 compares the area, scan directions, scan angle, number of ports and type of the proposed antenna with the reference antennas. This is the only antenna to date capable of 2-D beam scanning proposed for 28 GHz millimeter-wave

5G mobile devices. The performance of the antennas reported in [53, 55–57] was verified by adding the antenna to a device ground plane but the performance of the antennas proposed in [52, 54, 58] are not tested when placed on a mobile device ground plane. The performance of the antenna proposed in this chapter was verified after integrating the antenna into the mobile device's ground plane.

5.5 Summary

In this chapter, firstly, a novel single element LWA with 3 ports was developed to achieve 1-D beam scanning capability. The proposed 1-D beam switching antenna was prototyped and tested experimentally. The proposed antenna was optimized to have good side-lobe levels and a wide beam scanning angle. Using the side feeds, the prototyped antenna was able to switch the beam from θ = -37° to θ = +37° with a 3-dB coverage of 128° (θ = -64° to θ = +64°) along the x-axis (ϕ = 0°) within the frequency range 27-30 GHz. Using the center feed, the antenna was able to scan the beam from θ = -20° to θ = -27° with a 3-dB coverage of 103° (θ = +31° to θ = -72°) along the y-axis (ϕ = 90°) within the frequency range 27-30 GHz, illustrating complete coverage of boresight direction.

Secondly, a novel antenna with 6 ports was developed using two 1-D beam switching antennas to achieve 2-D beam switching, and it was placed at the corner of a ground plane of the mobile device. The 2-D beam switching antenna was prototyped and tested experimentally. Using the element (mmAnt-1) whose axis was aligned with the x-axis (ϕ = 0°) it was able to scan the beam from θ = +46° to θ = -59° with the side feeds. Also, mmAnt-1 was able to scan from θ = -24° to θ = -33° along the y-axis (ϕ = 90°) with the center feed. The achieved 3-dB coverage was 167° (from θ = +78° to θ = -89°) along the x-axis and 103° (from θ = +28° to θ = -75°) along the y-axis. Using the element mmAnt-2 whose axis was aligned with the y-axis (ϕ = 90°) could scan the beam from θ = +47° to θ

= -39° with the side feeds. Also, the element mmAnt-2 was able to scan along the x-axis (ϕ = 0°) from θ = +21° to θ = +30° with the center feed. The achieved 3-dB coverage was 154° (from θ = +82° to θ = -72°) along the y-axis and 99° along the x-axis (from θ = -26° to θ = +73°). Overall, using the proposed 2-D pattern reconfigurable antenna the achieved 3-dB coverage is 167° [(θ, ϕ) = (-89°, 0°) to (78°, 0°)] along the x-axis. Along the y-axis covering the boresight direction (the +z-axis) it is 154° [(θ, ϕ) = (-72°, 90°) to (82°, 90°)]. Finally, the performance of the proposed antenna was compared with other referenced beam switching antennas to date proposed for 28 GHz millimeter-wave 5G mobile device applications.

Antennas were presented for 28 GHz millimeter-wave band in the previous chapters of this thesis. The following chapters will discuss on the design and development of antennas for LSA (cognitive radio technology for 5G), 4G/LTE, 2.4 GHz WLAN, and 3.3 GHz WiMAX bands.

Chapter 6

Planar Antennas for LSA and Mid-LTE Bands

6.1 Introduction

This chapter presents the design and development of two novel planar antennas for mobile devices. Firstly, a planar antenna (Ant-4) with an O-shaped ground plane is presented for small mobile devices. The Ant-4 performance is tested with and without the presence of a mobile-device battery. Secondly, another novel planar antenna (Ant-5) for hand-held mobile devices is presented. The substrate size of Ant-4 is equivalent to a USB modem whereas the substrate size of Ant-5 is equivalent to a hand-held smart phone. Both planar antennas cover the LSA bands (1452-1492 and 2300-2400 MHz) and mid-LTE band (1427-2690 MHz). In these designs and developments no vertical plate has been used.

This chapter is organized as follows. Section 6.2 presents the design, working modes, and radiation performance of the planar antenna (Ant-4) with O-shaped ground plane. The planar antenna (Ant-5) design for hand-held mobile devices is presented in Section 6.3 together with the working modes, and radiation performance. A comparison between Ant-

4 and Ant-5 is presented in Section 6.4. Section 6.5 summarizes the chapter.

6.2 Antenna (Ant-4) for Small Mobile Devices

This section presents a wideband planar antenna (Ant-4) for LSA bands and mid-LTE band operation. The antenna is suitable for small mobile devices.

6.2.1 Antenna Configuration

The antenna shown in Fig. 6.1 was deigned to be printed on a Rogers 5880 substrate with a substrate thickness of 1.575 mm and copper-cladding thickness of 0.035 mm. The dimensions of the substrate considered for this design, 40 mm × 100 mm, have been a commonly used substrate in small mobile devices like a USB modem. The antenna dimensions of 15 mm × 40 mm occupy a complete edge of the substrate. The ground plane and the antenna are designed in the same plane, leaving a gap of 5 mm as depicted in Fig. 6.1 (a). A hole is considered between the radiating element and the ground plane for a simple feed arrangement with dimensions of 5 mm × 10 mm as shown in Fig. 6.1 (a). The antenna is fed with an SMA connector from the bottom of the substrate. A shorting pin (connector between the ground plane of the antenna and the ground of the SMA connector) that is 0.5 mm × 0.5 mm × 1.61 mm in dimension is located at the center of the top edge of the ground plane as indicated in Figs. 6.1 (b) and (c). A detailed configuration of the antenna is presented in Fig. 6.1 (d), where all the dimensions are in millimeters. A battery is placed at the bottom-left corner of the substrate, with dimensions of 20 mm × 40 mm × 5 mm. There is a gap between the battery and the substrate of the antenna, and their detailed dimensions are presented in Fig. 6.1 (e). The antenna dimensions were optimized using parameter analysis in CST Microwave Studio. The dimensions of the antenna shown in Fig. 6.1 are optimum values.

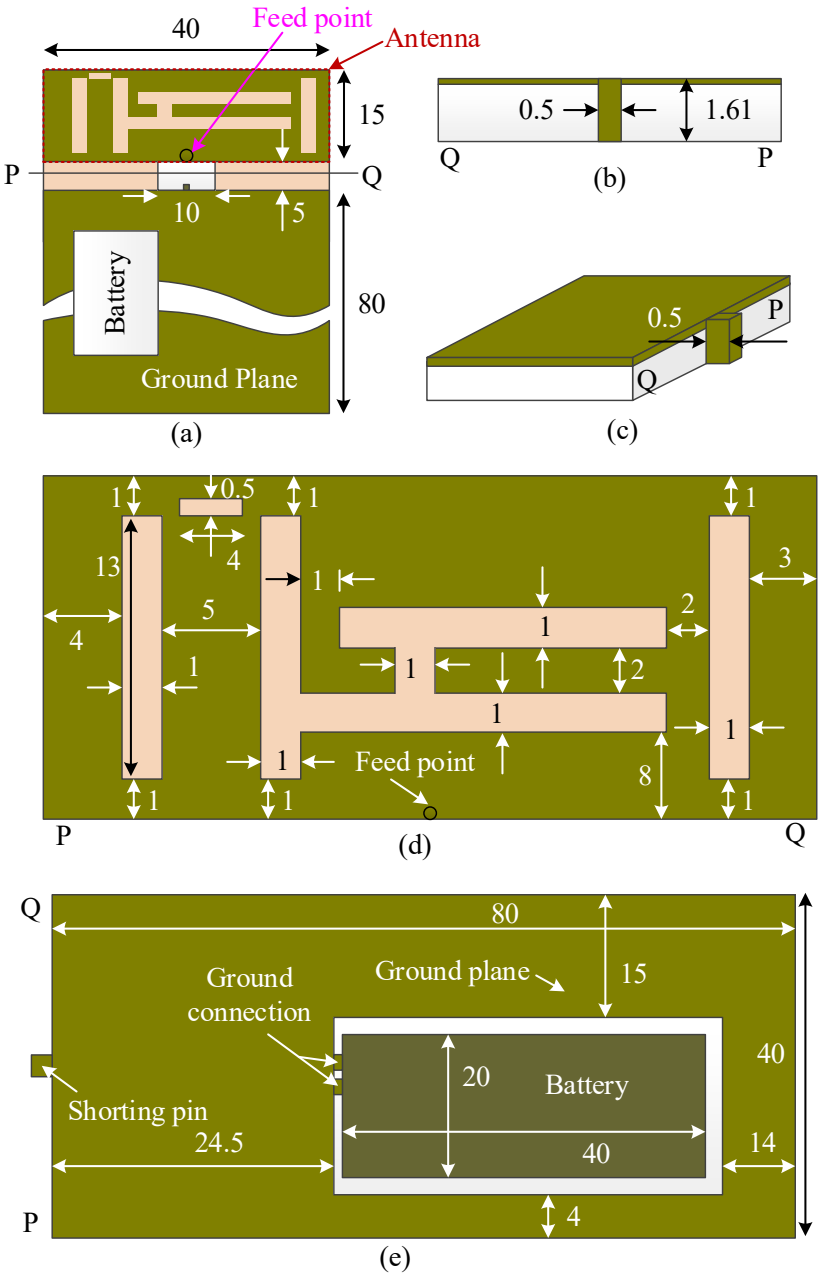

Figure 6.1: Geometry of the wideband planar antenna (Ant-4) for LSA and mid-LTE bands: (a) top view, (b) shorting pin (cross-section along line PQ), (c) shorting pin (perspective view), (d) detailed geometry, and (e) placement of the battery. All dimensions are in millimeters.

6.2.2 Design Procedure and Working Modes

The wideband planar design started with a patch antenna of size 40 mm × 15 mm fed at the center. In this design the antenna and the ground plane of the mobile device are on the same side of the substrate as indicated in Fig. 6.1. The antenna was designed without using active and passive elements, e.g. diode, capacitor, inductor, etc, and uses fundamental equations discussed in Section 2.3. In Step-1, an L-shaped slot ABC is inserted at the center of the structure. In Step-2, an I-shaped slot DE is introduced to the structure. Step-2 ends with creating a connecting slot between the L-shaped slot ABC and I-shaped slot DE. Finally, in Step-3, to ensure a sufficiently wide operating band, three I-shaped slots F, G and H are inserted into the structure. The simulated reflection coefficient behavior of Step-3 is shown in Fig. 6.3 (without-battery curve). The antenna has a -6 dB reflection coefficient bandwidth of 2.13 GHz (1.03-3.16 GHz) in the absence of the battery, with three resonant frequencies at 1.27, 1.93 and 2.94 GHz. Note that 'in the absence of the battery' means that the O-shaped ground plane is left blank.

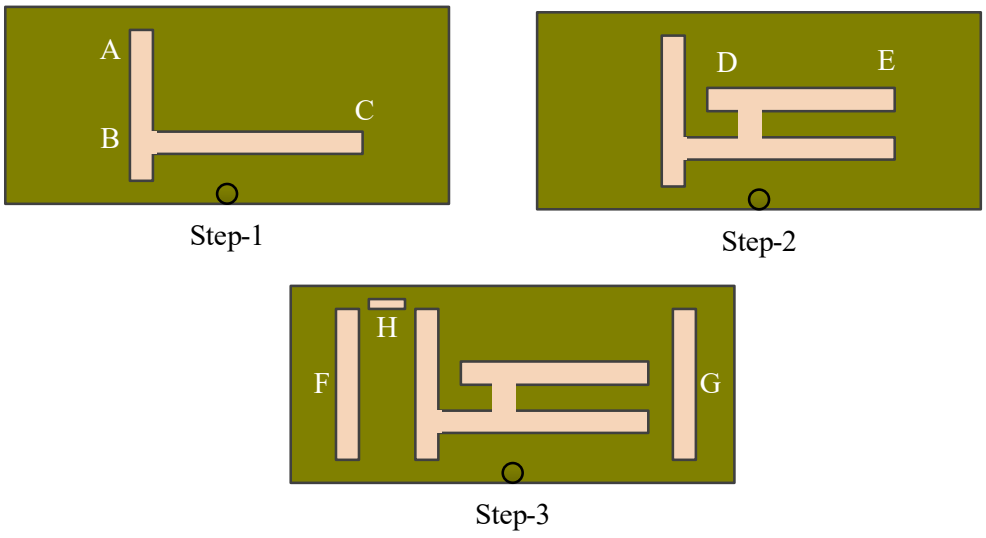

Figure 6.2: Three-steps of evolution of the geometry of wideband planar antenna (Ant-4).

In order to verify the battery's effect on the operating band of the antenna, a battery

is placed within the gap of the O-shaped ground plane. The substrate of the mobile device is removed from the ground clearance area chosen for battery installation. To visualize the effect of the battery a solid metal box is placed as a representative of a battery to have the maximum effect on antenna performance. The proposed wideband planar antenna has a reflection coefficient bandwidth of 2.02 GHz (1.12-3.14 GHz) with the presence of the battery, as shown in Fig. 6.3 (with-battery curve), covering the LSA and complete mid-LTE bands. After using the battery, the antenna still has three resonant frequencies, specifically at 1.26, 1.92 and 2.95 GHz.

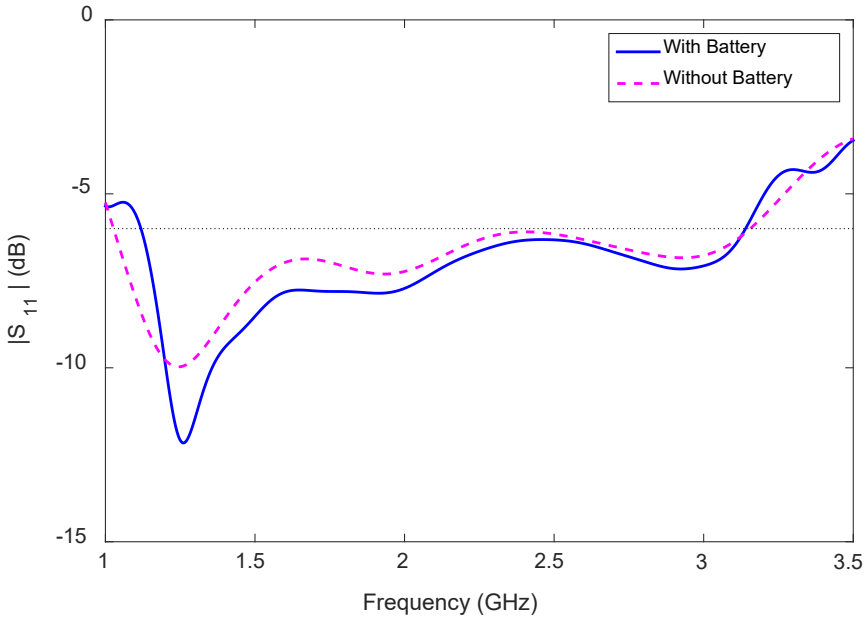

Figure 6.3: Predicted reflection coefficient of the wideband planar antenna (Ant-4) with and without the presence of a battery.

After placing the battery, a negligible effect on the antenna operating bandwidth is observed. It is evident that the antenna input impedance matching improves within the operating bandwidth while maintaining three resonant frequencies.

Turning to the surface current distributions at the three frequencies to understand the working modes of the antenna. Fig. 6.4 shows the simulated surface current distribution

at three frequencies 1.3, 2 and 2.6 GHz. The surface current in the ground plane is omitted for presentation simplicity. The surface current is at maximum from the feed point to the slot BCF at the three resonant frequencies. Another maximum is observed at the slot end-point E and there is a null at the location D (between C and E), indicated by the magenta circle. Therefore two maxima with a null exist at the middle, and subsequently the antenna is operating in the half-wavelength mode at the three resonant frequencies.

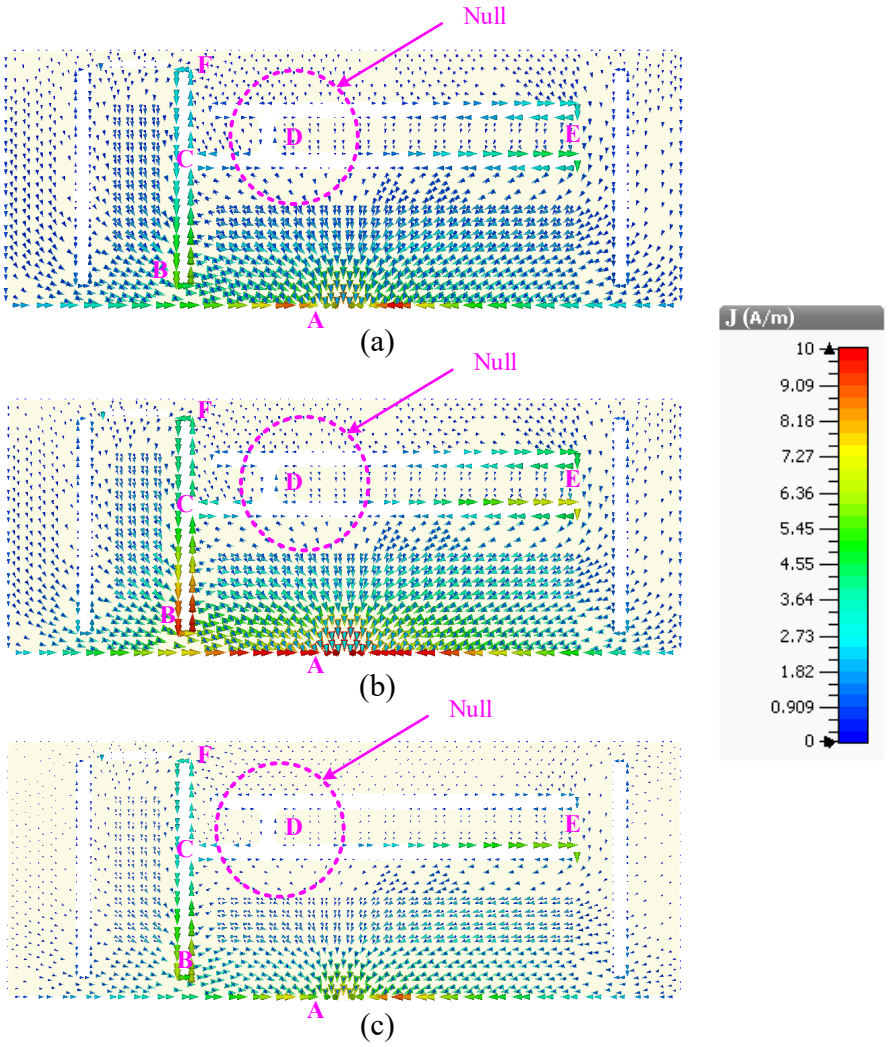

Figure 6.4: Predicted surface current distributions for the wideband planar antenna (Ant-4) at three resonant frequencies: (a) 1.3, (b) 2, and (c) 2.6 GHz.

6.2.3 Radiation Performance and Discussion

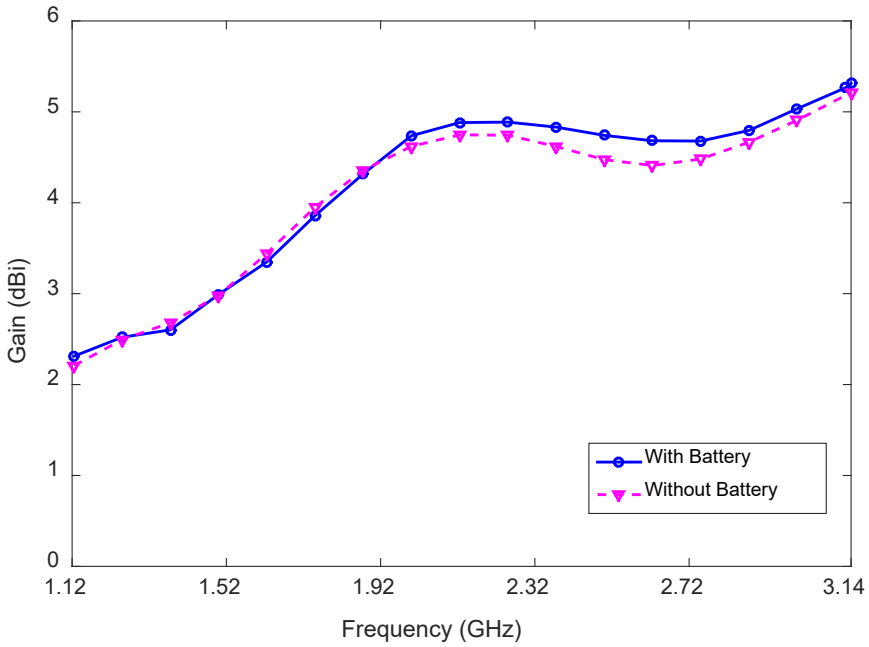

Figure 6.5: Gain of the wideband planar antenna (Ant-4) within the -6 dB reflection coefficient bandwidth.

The antenna radiation performance was tested with and without placing the battery on the substrate; the gains within the -6 dB reflection coefficient bandwidth are compared in Fig. 6.5. The antenna gain is minimum at 1.03 GHz and maximum at 3.16 GHz, of 1.8 and 5.4 dBi, respectively, when the battery is not present. With the presence of the battery the antenna gain reaches its minimum at lower frequency limit and maximum at upper frequency limit, these being 2.3 and 5.3 dBi, respectively. Let the gain variation be denoted by $G_{\triangle}$. $G_{\triangle}$ within the total operating band of the proposed antenna is quite large ($\approx$ 3 dB) but in an individual band it is less than 0.5 dB. For example, $G_{\triangle} \leq 0.48$ dB in the LTE 1 band, $G_{\triangle} \leq 0.35$ dB in LTE 11, $G_{\triangle} \leq 0.20$ dB in LTE 16, and $G_{\triangle} \leq 0.40$ dB in the PCS band. Therefore, the antenna has a stable gain in sub-operating bands. The gain variations of the antenna without the placement of the battery are almost the

same as or slightly less than the gain with battery, as presented in Fig. 6.5.

Fig. 6.6 depicts the antenna efficiency of Ant-4 as a function of frequency. The antenna efficiency of the proposed planar antenna was studied with and without the presence of a battery. The antenna efficiency is minimum at the lower frequency limit and maximum at 1.25 GHz, 65% and 91%, respectively, without the presence of the battery. When the battery is installed the antenna efficiency is minimum at 3.16 GHz while the maximum at 1.25 GHz, 74% and 89%, respectively.

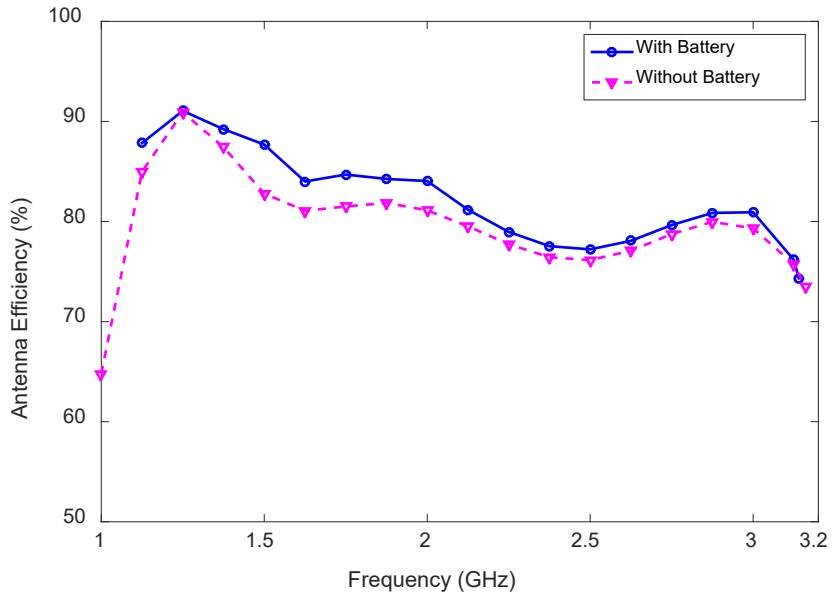

Figure 6.6: Antenna efficiency of the wideband planar antenna (Ant-4) within the -6 dB reflection coefficient bandwidth.

The antenna radiation patterns in the three principal planes, x-z, y-z, and x-y, were studied for three different frequencies. The simulated E_θ and E_ϕ radiation patterns, in normalized form, of the antenna at 1.5 and 2.0 GHz are shown in Fig. 6.7, and at 2.5 GHz are shown in Fig. 6.8. The E_θ and E_ϕ radiation pattern in each plane is normalized by the magnitude of the maximum in that plane. The difference in the magnitudes of E_θ and E_ϕ radiation in the x-z plane is 30, 25, 20 dB at 1.3, 2.0, and 2.6 GHz, respectively.

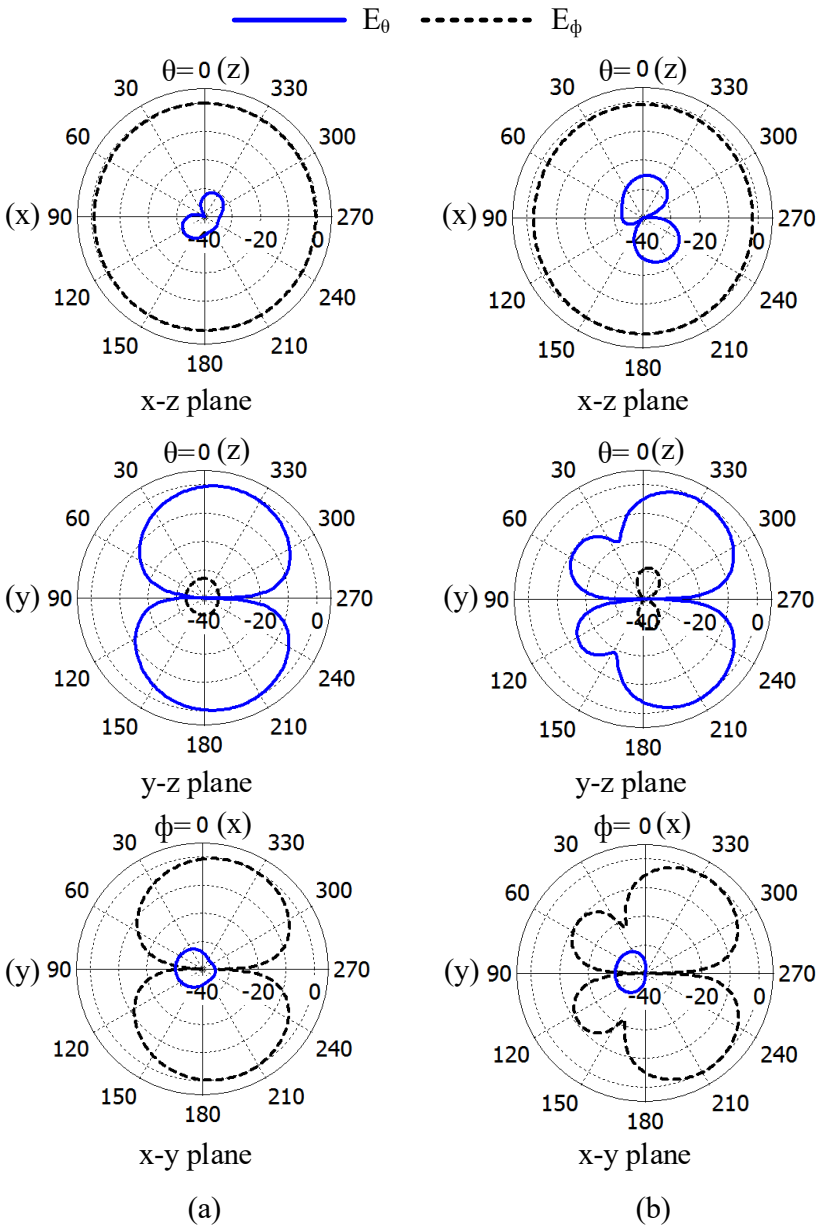

Figure 6.7: Radiation patterns (E_θ and E_ϕ) of the wideband planar antenna (Ant-4) in the three principal planes (x-z, y-z, and x-y planes) at (a) 1.3, and (b) 2.0 GHz.

It is observed that the E_ϕ radiation patterns in the x-z plane are omnidirectional over the antenna operating band, which is similar to the pattern of a dipole oriented in the y direction. In the x-y plane, the E_ϕ radiation pattern is significantly higher along the

±x direction but is the opposite along ±y. The patterns are comparable in the y-z plane at all represented frequencies. Therefore, the antenna radiation pattern is nearly omnidirectional in the x-z plane at all frequencies. However, two nulls have been observed in the radiation patterns of the antenna over the operating band.

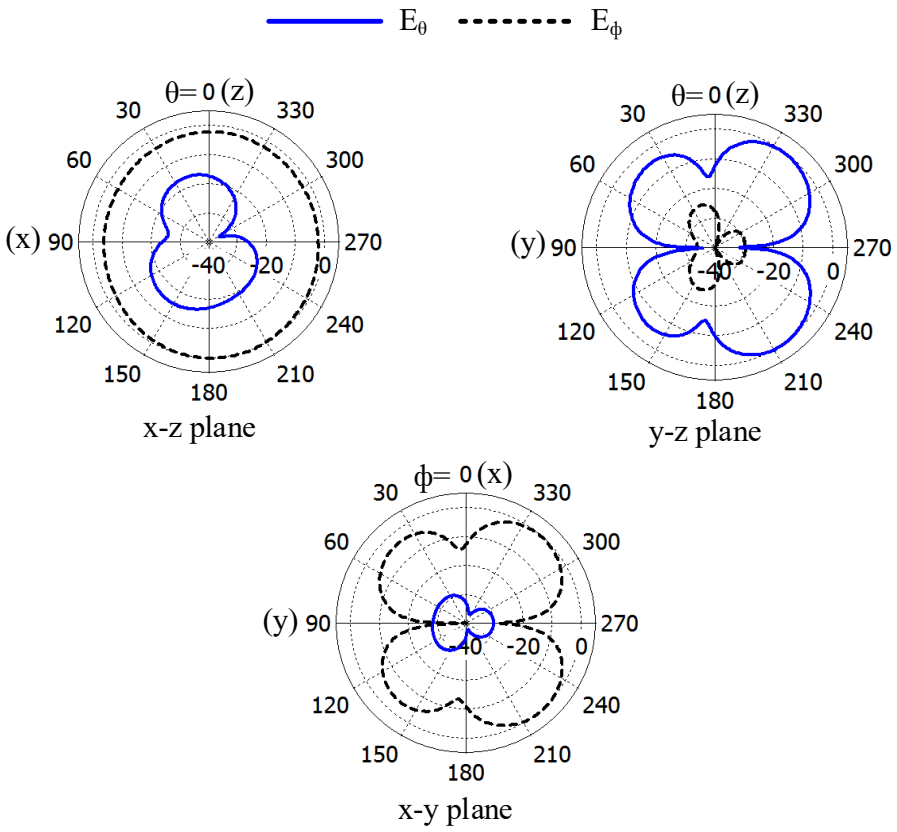

Figure 6.8: Radiation patterns (E_θ and E_ϕ) of the wideband planar antenna (Ant-4) in the three principal planes (x-z, y-z, and x-y planes) at 2.6 GHz.

6.3 Antenna (Ant-5) for Regular-Sized Mobile Devices

The antenna (Ant-4) presented in Section 6.2 occupies a complete edge of the substrate, limiting the space for other electronic components. Moreover the gain variation within

the operating band for Ant-4 is high ($\approx$ 3 dB). In addition, two nulls in the radiation patterns of the antenna are observed over the operating band. Ant-4 is suitable for small mobile devices like USB modem operating in the LSA bands and mid-LTE band, but is expensive because of the substrate (Rogers 5880) used.

This section presents a planar antenna (Ant-5), on a low-cost FR-4 substrate, suitable for hand-held mobile devices like smart phones. Ant-5 is developed for the 1.5 and 2.3 GHz LSA bands and mid-LTE band operation.

6.3.1 Antenna Configuration

This novel printed antenna (Ant-5) has been designed to operate in the 1452-1492 and 2300-2400 MHz LSA bands, and its detailed geometry with top and bottom views is shown in Fig. 6.9. The total area covered by the antenna is 40 mm $\times$ 15 mm, or $0.18\lambda_0 \times 0.07\lambda_0$, where λ_0 is the free-space wavelength at 1.38 GHz. For simulation purposes, the antenna is assumed to be fed from an SMA connector at the bottom. To ensure isolation between the ground plane and the center pin of the SMA connector, a circular portion of copper with radius r has been etched off from the ground plane as depicted in Fig. 6.9 (b). The antenna is placed at the top-right corner of a mobile device substrate with the dimensions of 120 mm $\times$ 70 mm. A substrate commonly used in mobile devices is FR-4 with relative permittivity (ϵ_r) and loss tangent ($\tan\delta$) of 4.3 and 0.025, respectively. Its thickness is assumed to be 0.8 mm. The overall area of the ground plane is equal to the area of the substrate. A segment of copper with dimensions of 50 mm $\times$ 11 mm has been removed from the top-right corner of the ground plane as shown in Fig. 6.9 (b).

The proposed antenna is composed of two elements: firstly, an L-shaped element to the left of the feed point (left element) to cover the 1.5 GHz LSA band; and secondly, an L-shaped element to the right (right element) to cover the 2.3 GHz LSA band. CST Microwave Studio was used for the design and analysis of the antenna. The dimensions were

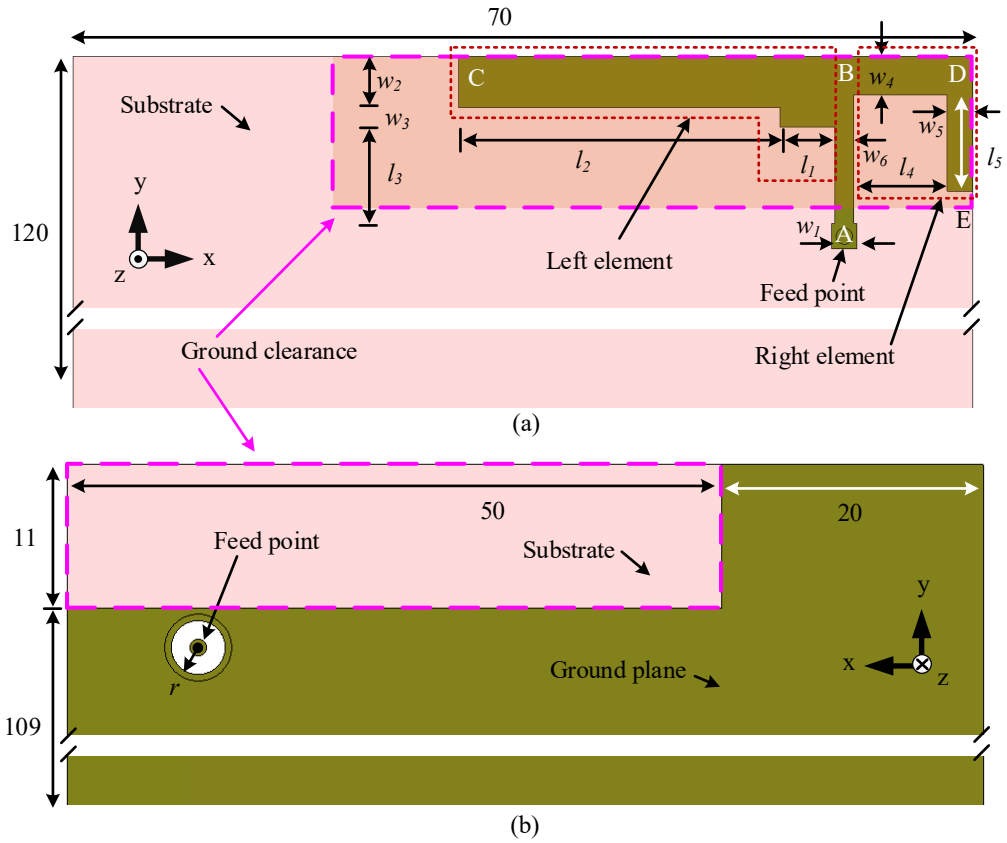

Figure 6.9: Geometry of the planar antenna (Ant-5) for LSA and mid-LTE bands operation: (a) top view with detailed antenna geometry, and (b) bottom view. All dimensions are in millimeters.

Table 6.1: Design parameters of the planar antenna (Ant-5) for the LSA bands. All dimensions are in millimeters.

$w_1 = 2$	$w_2 = 4$	$w_3 = 1.5$	$w_4 = 3$	$w_5 = 2$
$w_6 = 1.5$	$l_1 = 4.25$	$l_2 = 25$	$l_3 = 7.5$	$l_4 = 7.25$
$l_5 = 7.5$	$W = 15$	$L = 40$		

optimized using a parameter analysis conducted in CST for good impedance matching.

6.3.2 Design Procedure and Working Principle

The proposed planar antenna (Ant-5) evolution in three steps is shown in Fig. 6.10 and the corresponding reflection coefficient behavior is shown in Fig. 6.11. In addition, the antenna is designed based on the fundamental equations discussed in Section 2.3. The Ant-5 design procedure and working principle are explained with the help of Fig. 6.10, the parameters listed in Table 6.1, and the results presented in Fig. 6.11.

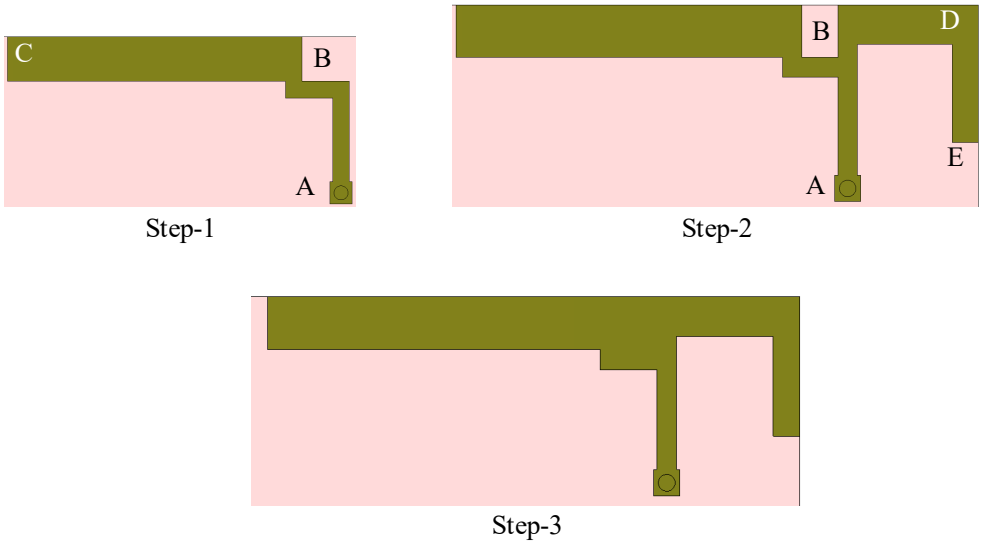

Figure 6.10: Three-steps of evolution of the geometry of the planar antenna (Ant-5) to cover the LSA bands.

Firstly, an I-shaped element AB of width w_4 was made and a $w_1 \times w_1$ square element was placed at point A to ensure proper connection between the center pin of the SMA and the antenna elements as shown in Fig. 6.10 (Step-1). Then another I-shaped element BC was added to the left of the previous I-shaped element AB, with length and width of l_2 and w_2, respectively. Step-1 was completed by adding a rectangular element with length and width of $l_1$and w_3, respectively, to ensure better impedance matching in the 1.5 GHz LSA band at the location of B as shown in Fig. 6.10 (Step-1). The antenna in Step-1 has a -6 dB reflection coefficient bandwidth of 600 MHz (1.38-1.98 GHz) as depicted in

Fig. 6.11 (Step-1 curve) and resonating at 1.56 GHz. The effective length of the antenna in Step-1 is about 44 mm, which is close to the quarter wavelength at 1.56 GHz.

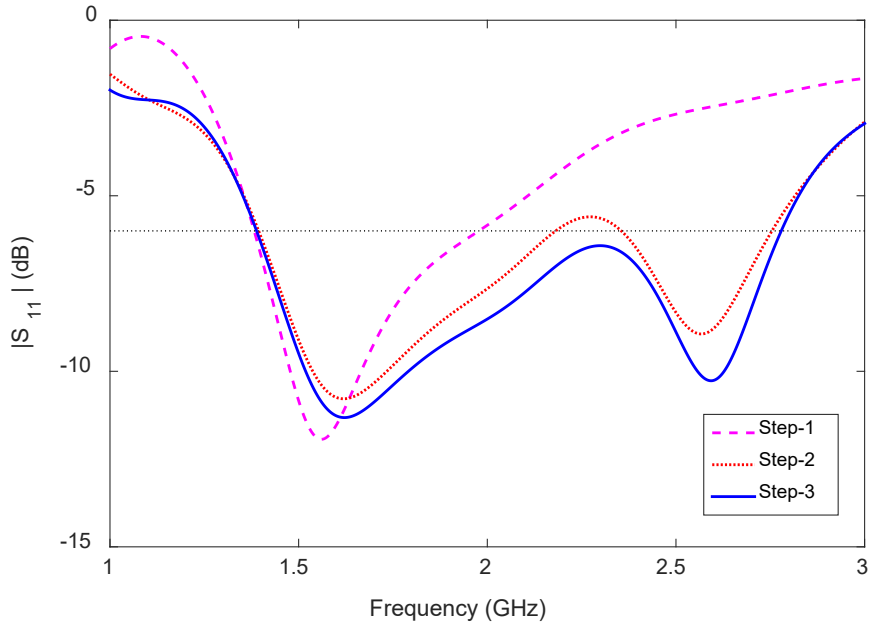

Figure 6.11: The simulated reflection coefficients corresponding to the evolution of the planar antenna (Ant-5).

In Step-2 the target is to create another resonant band close to the upper frequency limit of the mid-LTE band in order to have complete mid-LTE band coverage as well as 1.5 and 2.3 GHz LSA band coverage. To create a second resonant band close to the upper frequency limit, an L-shaped element BDE was added to the right of the antenna of Step-1 as shown in Fig. 6.10 (Step-2). The length and width of the element BDE were optimized using parameter analysis in CST. The finalized antenna in Step-2 generates two resonant bands with 190 MHz improvement in the reflection coefficient bandwidth over the previously achieved band. The new resonant band is at 1.62 GHz with a -6 dB reflection coefficient bandwidth of 790 MHz (1.39-2.18 GHz). After the addition of element BDE, a second resonant band is generated at 2.56 GHz with a -6 dB reflection coefficient bandwidth of 400 MHz (2.35-2.75 GHz) as shown in Fig. 6.11 (Step-2 curve). However,

the antenna in Step-2 does not have complete coverage of the mid-LTE band. Also it did not cover the 2.3 GHz high-LTE band. There is a null of 170 MHz (2.18-2.35 GHz) in the 2.3 GHz LSA band in the reflection coefficient bandwidth.

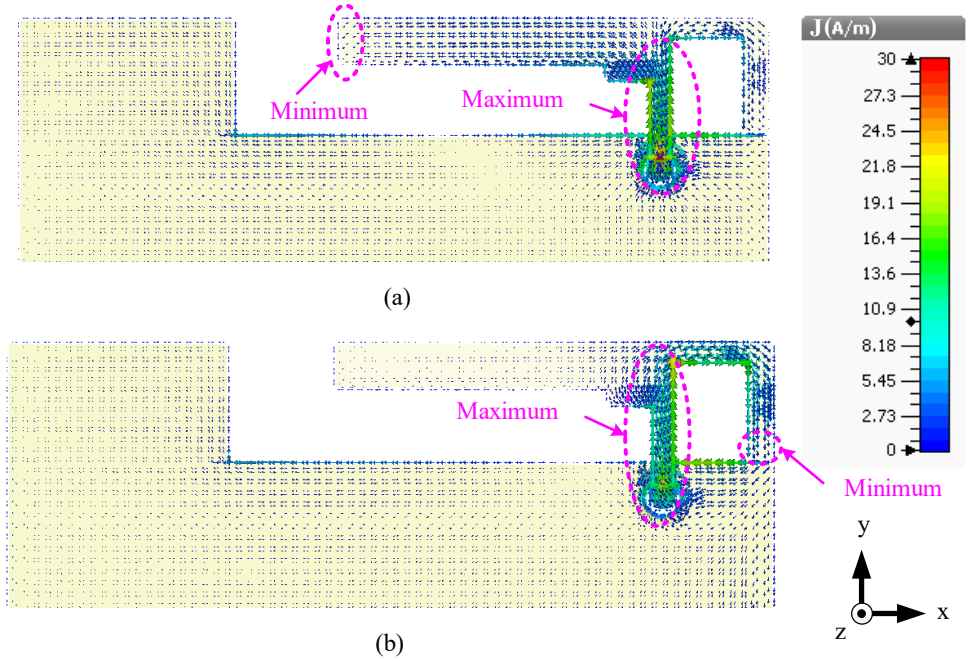

Figure 6.12: Predicted surface current distributions for the planar antenna (Ant-5) operating in the LSA bands at (a) 1.8, and (b) 2.6 GHz.

In Step-3 the aim is to achieve complete coverage of the mid-LTE band which will ensure coverage of the LSA bands as well, since the antenna in Step-2 has two resonances with lower and upper frequency limit coverage. Now try to merge both the resonant bands by removing the reflection coefficient null present in the 2.3 GHz LSA band. In Step-3 a rectangular element is added to the gap between the left and right elements as shown in Fig. 6.10 (Step-3). The finalized antenna has a wide reflection coefficient bandwidth of 1390 MHz (1.39-2.78 GHz) measured at -6 dB and covering both LSA bands and the LTE mid-band. The antenna resonates at 1.62 and 2.59 GHz within the mid-LTE band. The effective length for the right element is around 31 mm which is equal to a

quarter-wavelength at 2.59 GHz, and for the left element is 44 mm which is equal to a quarter-wavelength at 1.62 GHz.

Referring to the surface current distributions that are shown in Fig. 6.12, at 1.8 and 2.6 GHz in order to further understand the operation of the antenna, at both frequencies the surface current is a maximum around the feed point and a minimum at the end of the left or right element. This means that the antenna is resonating in the quarter-wavelength modes at both frequencies. The left element contains strong currents at 1.8 GHz and the right element comprises strong currents at 2.6 GHz. However, in both cases moderate currents are observed in the ground plane that is close to the antenna structure.

6.3.3 Parameter Analysis

Antenna parameter analysis is organized into two stages. Firstly, the study of the effects of the antenna parameters on the lower frequency limit is presented. Secondly, the effects of the antenna parameters on the upper frequency limit are presented. Also the influence of the antenna parameters on input impedance matching within the operating band are studied.

The length l_2 and width w_2 of element BC control the lower frequency limit and the antenna input impedance matching within the operating band, specifically close to the 1.62 GHz as shown in Fig. 6.13. This is because the element ABC controls the antenna operating band within the lower frequency limit region. When the length changes from l_2 = 26 mm to 24 mm with down steps of 1 mm, the antenna impedance matching becomes very good in the 2.3 GHz LSA band but the lower frequency limit shifts from 1.37 to 1.41 GHz. Note that the targeted lower frequency limit is 1427 MHz. Therefore, for the length $l_2 = 24$, 25 and 26 mm, the lower frequency limit always remains below the targeted value. However, there is a null in the reflection coefficient behavior in the 2.3 GHz LSA band when $l_2 = 26$ mm, which is not expected. A similar effect is observed for a change in

the width w_2 from 5 mm to 3 mm. Therefore, the length and width are carefully chosen to be 25 and 4 mm to avoid nulls in the 2.3 GHz LSA bands.

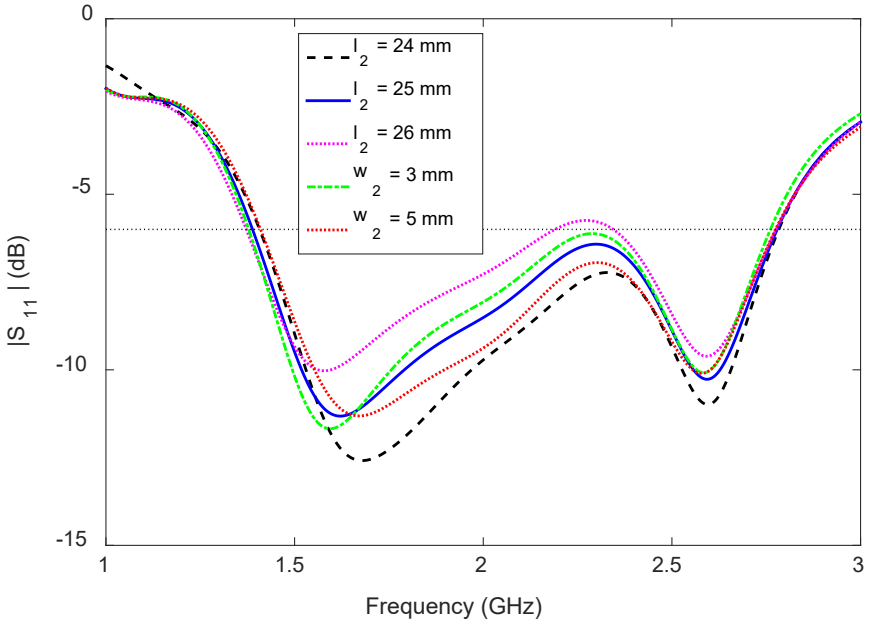

Figure 6.13: Effects of l_2 and w_2 on lower frequency limit and input impedance matching of Ant-5.

For the parameters that controlling the upper frequency limit and input impedance matching within the operating band, the right element BDE controls the second resonant of the antenna as well as the upper frequency limit. Fig. 6.14 shows the impact of the length l_5 and width w_4 on the reflection coefficient of Ant-5. The two resonant bands of the antenna generated by the two elements BC and BDE separate significantly, with a null in the 2.3 GHz LSA band when l_5 is 6.5 mm. With an increase of the length l_5 from 6.5 to 8.5 mm with a step of 1 mm, the two resonances merge while the input impedance of the antenna improves significantly. However, the bandwidth of the antenna becomes smaller. A similar effect on antenna reflection coefficient is observed for a change of width w_4 from 4 to 2 mm. Therefore, the length l_5 and width w_4 are carefully chosen to be 7.5 and 3 mm, respectively, in order to cover the LSA bands and mid-LTE band.

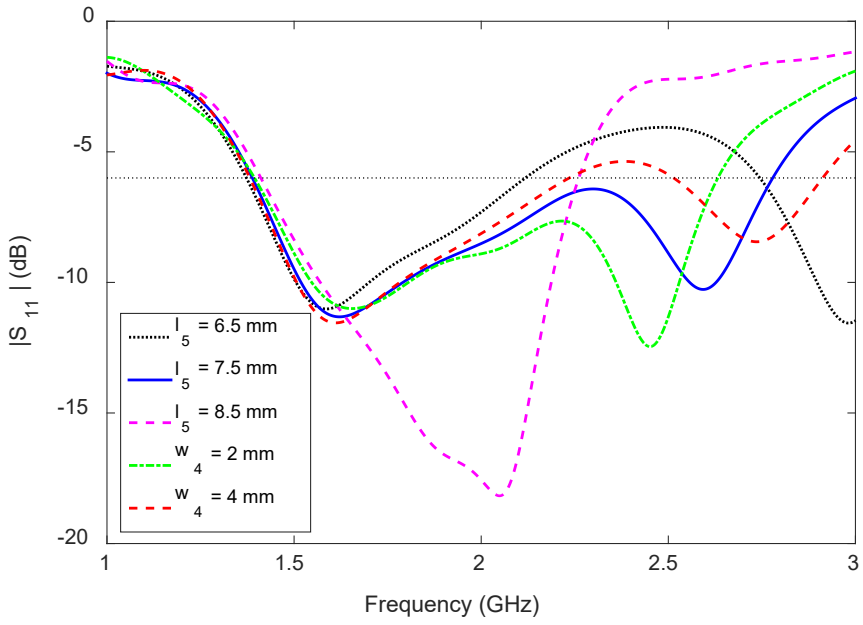

Figure 6.14: Effects of l_5 and w_4 on upper frequency limit and antenna input impedance matching of Ant-5.

6.3.4 Radiation Performance and Discussion

The proposed planar antenna (Ant-5) has a gain varying with frequency within the -6 dB reflection coefficient bandwidth as shown in Fig. 6.15. The minimum gain of the proposed antenna is 1.3 dBi at 1.39 GHz and the maximum gain is 3.6 dBi at 2.78 GHz. Therefore, the gain variation within the reflection coefficient bandwidth is 2.3 dB, which is lower than the Ant-4 gain variation (3 dB).

The Ant-5 efficiency with varying frequency within the -6 dB reflection coefficient bandwidth is illustrated in Fig. 6.16. The minimum and maximum antenna efficiencies are 67% and 90%, at 2.78 and 1.7 GHz, respectively. Consequently, the antenna efficiency is always above 50% within the antenna operating band which makes the antenna suitable for hand-held device application.

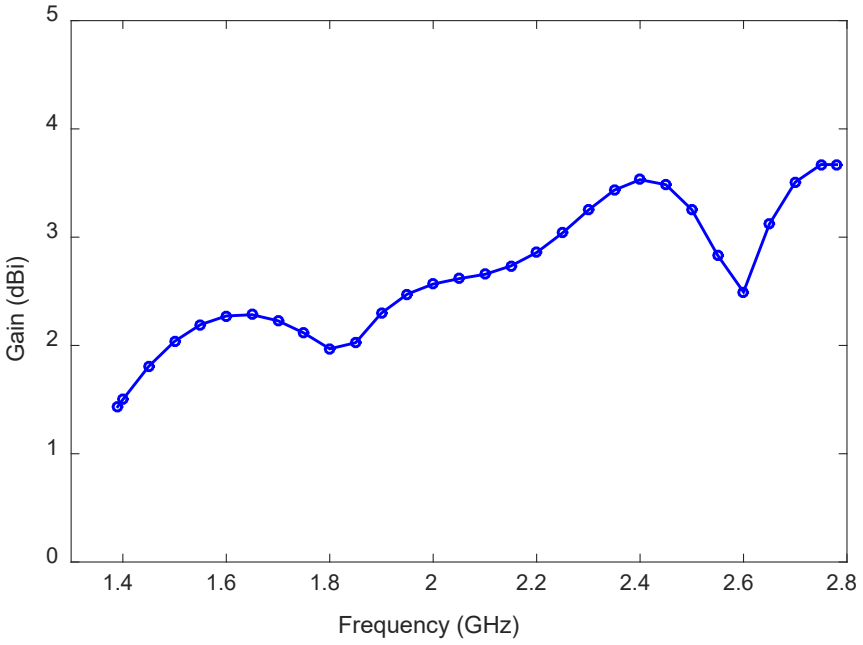

Figure 6.15: Predicted gain of the planar LSA antenna (Ant-5).

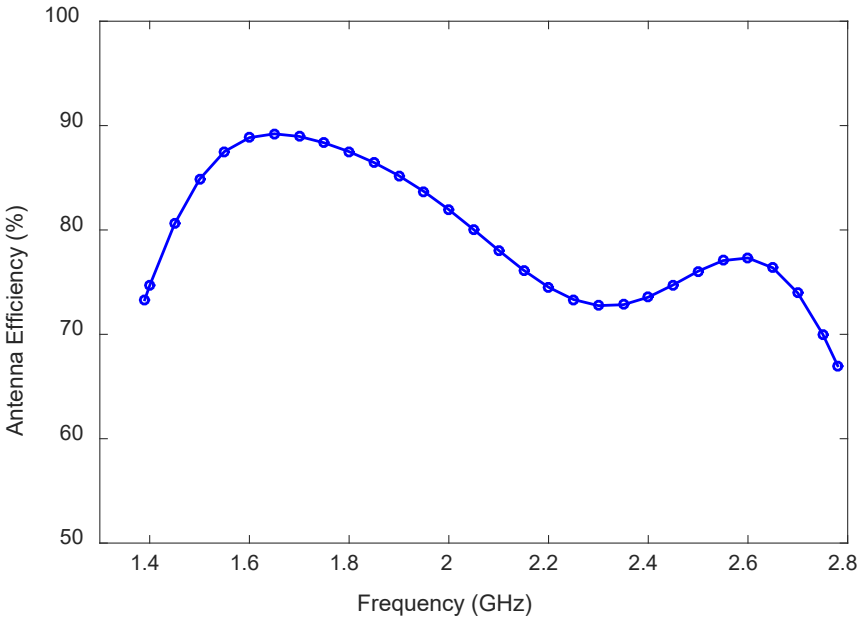

Figure 6.16: Predicted efficiency of the planar LSA antenna (Ant-5).

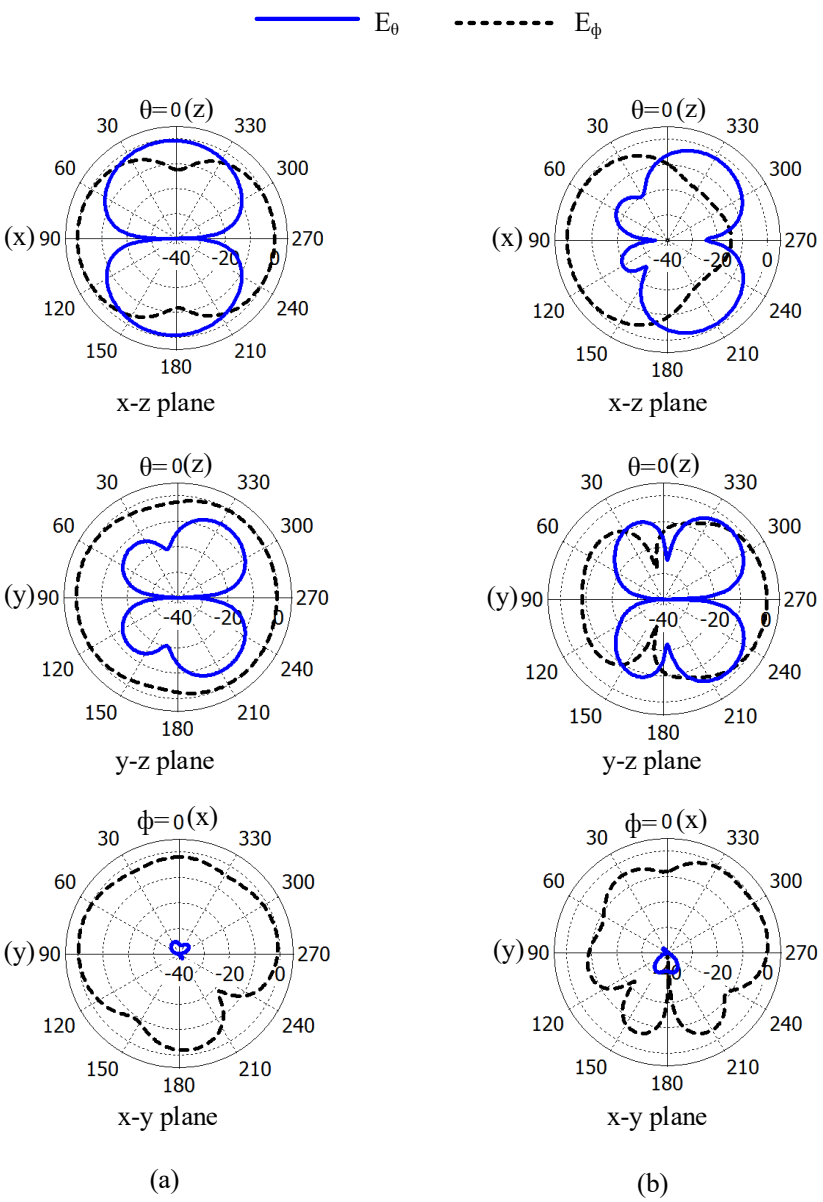

Figure 6.17: Predicted normalized radiation patterns of the planar LSA antenna (Ant-5) in two LSA bands at (a) 1.8, and (b) 2.6 GHz.

Fig. 6.17 shows the normalized E_ϕ and E_θ radiation patterns of Ant-5 in the three principal planes at 1.8 and 2.6 GHz. Here, the patterns are normalized with respect to the maximum in the corresponding principal plane. From the presented results, no nulls have been observed at 1.8 GHz but a null has been observed at 2.6 GHz in the x-y plane

radiation patterns. The E_ϕ radiation in the y-z plane at 1.8 GHz is more uniform (i.e. somewhat omnidirectional) compared to the E_ϕ radiation in the same plane at 2.6 GHz. An almost directed E_ϕ radiation pattern is observed in the x-z plane at 2.6 GHz.

6.4 Comparison between Ant-4 and Ant-5

Table 6.2: Performance comparison between Ant-4 (for small mobile devices) and Ant-5 (regular hand-held mobile devices).

Parameter	Ant-4	Ant-5
Physical Area (mm^2)	600	600
Bandwidth (GHz)	1.12-3.14	1.39-2.78
Efficiency (%)	74-89	67-90
Gain (dBi)	2.3-5.3	1.3-3.6
Nulls in Radiation Patterns	2 null	1 null

A performance comparison between Ant-4 and Ant-5 is presented in Table 6.2. Ant-4 and Ant-5 occupy an equal area but the substrate of Ant-4 is much smaller than the substrate of Ant-5. Both antennas cover the LSA bands and mid-LTE band with more than 50% efficiency within the operating band. The gain variation of Ant-5 is much smaller than the gain variation of Ant-4 within the -6 dB reflection coefficient bands. Ant-4 has nulls in its radiation patterns in the x-y plane while Ant-5 has nulls in the y-z plane. Ant-4 has omnidirectional radiation patterns over the operating band in the x-z plane but the radiation pattern of Ant-5 is omnidirectional in the y-z plane at close to the lower frequency limit. It starts to generate nulls in the same plane up near the upper frequency limit.

6.5 Summary

In this chapter, a wideband planar antenna (Ant-4) was developed and analyzed for small mobile device applications. The antenna impedance bandwidth covers the LSA, mid-LTE and 2.4 GHz WLAN bands. Detailed design considerations for the antenna were described, especially the feed arrangement. The antenna performance was analysed in the presence and absence of a battery, and negligible effects were observed regarding the antenna's performance. Two nulls are exist in the radiation patterns within the entire reflection coefficient bandwidth (1.12-3.14 GHz) of the antenna. Then another novel planar antenna (Ant-5) was designed, targeting a reduced number of nulls in the radiation patterns. The operating bandwidth of Ant-5 is 1390 MHz (1.39-2.78 GHz), which covers both the LSA frequency bands and the mid-LTE band. Ant-5 cover the 1.5 GHz LSA band without null in the radiation patterns, but a null exist at frequencies close to the upper frequency limit of the reflection coefficient bandwidth. Ant-4 and Ant-5 are of equal size and the gain of Ant-5 is more stable than that of Ant-4. However, nulls in the radiation patterns were observed for both the presented antennas. Both cover the LSA bands (1452-1492 and 2300-2400 MHz) and the mid-LTE band (1427-2690 MHz) but they do not cover the high-LTE band (3400-3800 MHz). In the next chapter, a dual-band antenna will be designed and developed in order to cover the LSA bands and the mid and high-LTE bands.

Chapter 7

Dual-Band Antenna for LSA, Mid-LTE and High-LTE Bands

7.1 Introduction

The previous chapter showed it is possible to cover both the LSA bands and mid-LTE band using a planar structure. However, the proposed antennas do not cover the high-LTE band. In this chapter, a dual-band antenna (Ant-6) for hand-held mobile devices is presented with the help of the design developed in the previous chapter. The primary focus here is to develop an antenna that covers both the LSA bands, mid-LTE and high-LTE bands, i.e. to cover 1427-2690 and 3400-3800 MHz bands. The antenna proposed in this chapter consists of a planar structure loaded with an I-shaped vertical plate. Most of the available solutions use passive or active lumped component-based input impedance matching circuits to cover the above mentioned bands. A novel antenna is developed without using an input impedance matching circuit. The detailed design and working principle of the antenna are presented together with a summary of the antenna's radiation performance.

This chapter is organized as follows. Section 7.2 presents the proposed antenna configuration. The antenna design procedure together with the working principles are presented in Section 7.3. Section 7.4 presents the effects of the antenna's geometrical parameters on the antenna's reflection coefficient behavior. Section 7.5 describes the radiation performance of the antenna. The suitability of the antenna for different-sized mobile devices is discussed in Section 7.7. Section 7.8 summarizes the important point made in this chapter.

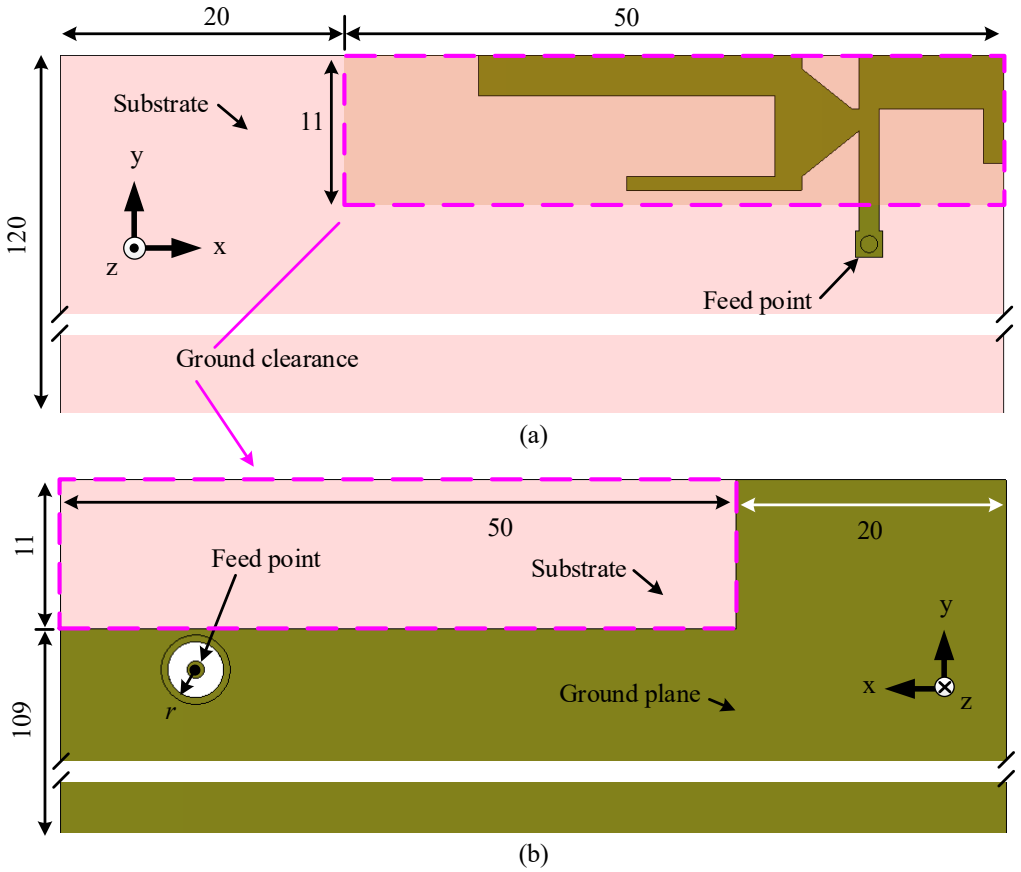

Figure 7.1: Placement of the dual-band antenna (Ant-6) on a mobile phone substrate: (a) top view without vertical plate, and (b) back view. All dimensions are in millimeters.

7.2 Antenna Configuration

A novel dual-band antenna (Ant-6) is designed, operating in the 1427-2690 and 3300-3800 MHz bands for LSA, TDD/FDD LTE, UMTS, DCS, PCS, GSM1800, GSM1900, WLAN (2.4 GHz), and WiMAX (2.5 and 3.3 GHz) applications, and is displayed in Figs. 7.1 and 7.2. Fig. 7.1 shows the top and back views of the antenna without the vertical plate and reveals the placement of the antenna in the mobile device substrate. Fig. 7.2 is a perspective view of the antenna and its detailed geometry. There is a vertical plate in the antenna design which is shown as unfolded along the +y-axis in Fig. 7.2 (b) for better presentation. To ensure isolation between the ground plane and the center pin of the SMA connector, a circular portion of copper with radius r is etched off from the ground plane as shown in Fig. 7.1 (b).

Table 7.1: Design parameters of the dual-band antenna (Ant-6). All dimensions are in millimeters.

$w_1 = 2$	$w_2 = 1.5$	$w_3 = 1.6$	$w_4 = 0.5$	$w_5 = 3$
$w_6 = 3.4$	$w_7 = 2$	$w_8 = 1$	$w_9 = 1$	$w_{10} = 3$
$w_{11} = 4$	$w_{12} = 1.5$	$l_1 = 7.4$	$l_2 = 4.25$	$l_3 = 22$
$l_4 = 11$	$l_5 = 7.75$	$l_6 = 4$	$l_7 = 20$	$l_8 = 50$
$h_1 = 4$	$w_{13} = 11$	$r = 2$	$L_1 = 39$	$W_1 = 15$

The overall dimensions of the antenna are 39 mm $\times$ 15 mm $\times$ 4 mm or $0.18\lambda_0 \times 0.08\lambda_0 \times 0.02\lambda_0$, where λ_0 is the free-space wavelength at 1.39 GHz. The antenna is assumed to be fed from an SMA connector from the bottom. The proposed antenna is placed at the top-right corner of a mobile device substrate with the following dimensions: 120 mm $\times$ 70 mm. A commonly used low cost substrate for a mobile device is FR-4 with relative permittivity (ϵ_r) and loss tangent ($\tan\delta$) of 4.3 and 0.025, respectively, and a thickness

of 0.8 mm. The overall size of the ground plane is equal to the size of the substrate. A segment of copper with dimensions of 50 mm × 11 mm is removed from the top-right corner of the ground plane. CST Microwave Studio is used for the design and analysis. The optimized design parameters for the proposed antenna are listed in Table 7.1.

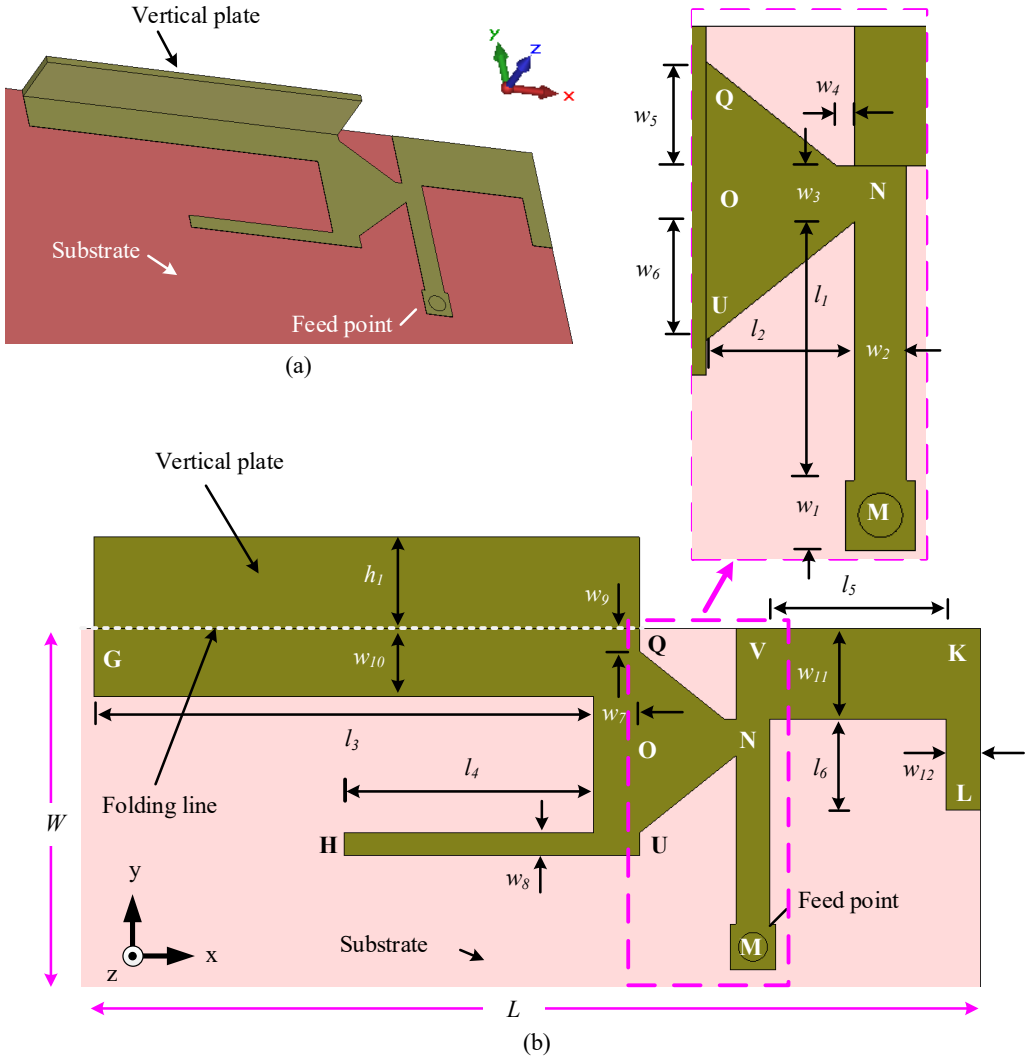

Figure 7.2: Geometry of the dual-band antenna (Ant-6) for the mid and high bands: (a) perspective view with vertical plate, and (b) top view with unfolded vertical plate along +y axis.

The proposed antenna is composed of three elements: firstly, the L-shaped element

MNO in the middle; secondly, a U-shaped large element GQUH loaded with the vertical plate on the left; and thirdly, an L-shaped monopole antenna VKL on the right. Here, the vertical plate is aligned with the edge GQ. The dimensions are optimized using a parameter analysis conducted in CST for good impedance matching in both bands.

7.3 Design Procedure and Working Principle

The proposed dual-band antenna (Ant-6) design procedure can be divided into two major steps; firstly, an antenna design for the LSA and mid-LTE (1427-2690 MHz) bands; and secondly, addition of a new element in the antenna design to cover the high-LTE (3300-3800 MHz) band. These two major steps are divided into four basic stages to explain the working principle. Also the predicted surface current distributions for the final design at the resonant frequencies are shown so that the working modes are better understood. In addition, the antenna is designed based on the fundamental equations discussed in Section 2.3. The geometry evolution for the antenna and the corresponding predicted reflection coefficients are shown in Figs. 7.3 and 7.4, respectively.

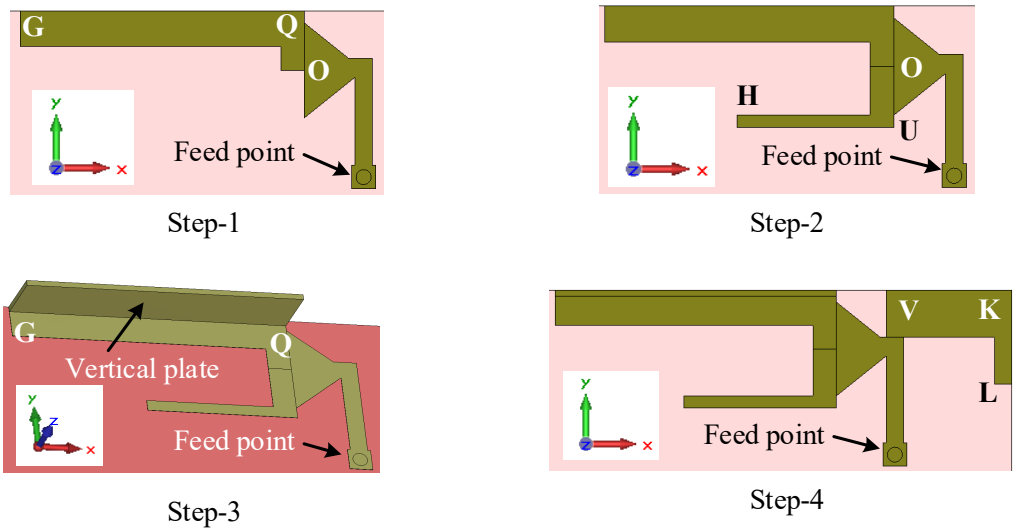

Figure 7.3: Four-steps of evolution of the geometry of the dual-band antenna (Ant-6).

The four basic steps of the antenna evolution are exhibited in Fig. 7.3 and the design parameters are indicated in Fig. 7.2 (b). In the first step, the middle element MNUOQ [inset of Fig. 7.2 (b)] is designed and optimized. The effective length of this element is $l_{ILE} = l_1 + l_2 + (w_1 + w_2 + w_3)/2 = 14.2$ mm. Later on, an L-shaped strip OQG with an effective length of $w_3/2 + w_5 + w_7/2 + l_3 = 26.8$ mm is added to the edge OQ of the middle element MNUOQ such that the antenna covers the mid (1427-2690 MHz) band. In this band the antenna resonates at 1.67 GHz. The effective length of the antenna ($l_{ILE} + 26.8 = 41$ mm) is close to the quarter wavelength at 1.67 GHz.

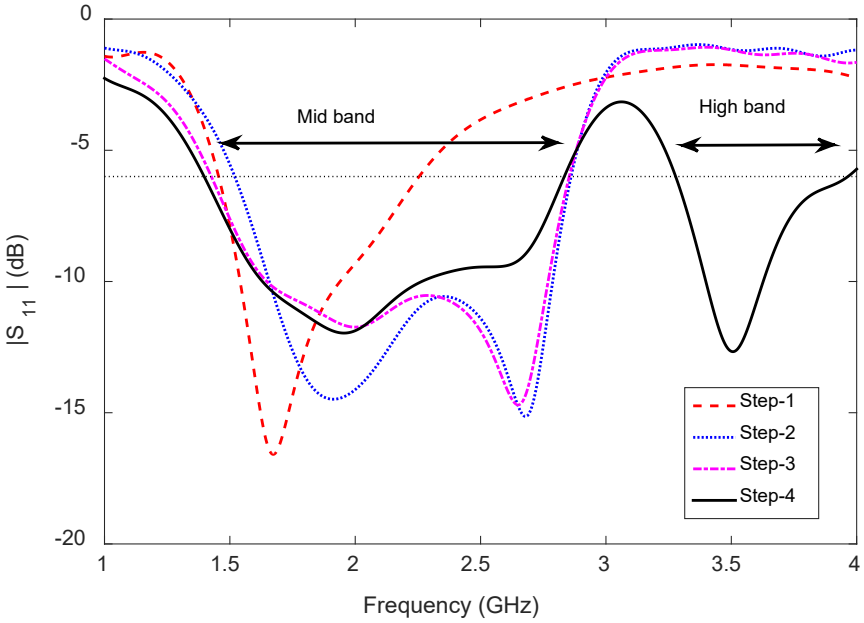

Figure 7.4: Predicted reflection coefficient corresponding to the evolution of the dual-band antenna (Ant-6).

In Step-2, another L-shaped strip OUH with a length of $w_3/2+w_6+w_8/2+l_4 = 15.7$ mm is added to the edge OU of the feed element; the additional electrical length in the antenna structure is around 29.9 mm. As can be seen from Fig. 7.4, the antenna resonates at two different frequencies, 1.98 and 2.68 GHz, because of the two separate electrical paths MNOQG and MNOUH, respectively.

Again in Step-2, a -6 dB reflection coefficient bandwidth of 1.35 GHz (1.51 - 2.86 GHz) is achieved by the design. However, it is required to shift the lower edge frequency to 1.42 GHz to cover all the mid-LTE and LSA bands. To make this possible a vertical plate of height h_1 is loaded to the edge GQ (Step-3). The vertical plate loading shifts the lower edge frequency to 1.41 GHz with a negligible variation of the upper edge frequency (2.85 GHz).

Now the aim is to cover the high-LTE (3300-3800 MHz) band together with the mid-LTE band with the same antenna. To do so, an L-shaped element VKL with an effective length of $w_2 + l_5 + w_{12} + l_6$ is loaded to the top of the middle element MN in Step-4. The effective length (right side of the middle element) of the new element is around 24.75 mm, which in turn generates a resonant band at 3.51 GHz.

The finalized antenna design [Fig. 7.2 (b)] consists of three electrical paths MNOQG (= 41 mm), MNOUH (= 29.9 mm), and MNVKL (= 24.75 mm), and makes the antenna resonate at 1.96, 2.65, and 3.51 GHz, respectively. At all resonant frequencies the antenna resonates in the quarter-wavelength mode. The -6 dB reflection coefficient bandwidths of the proposed monopole-based antenna are 1.45 GHz (1.39-2.84 GHz) and 700 MHz (3.27-3.97 GHz), respectively, covering the targeted mid (1427-2690 MHz) and high (3300-3800 MHz) bands.

The current distributions of this antenna at three frequencies are shown in Fig. 7.5 to illustrate the working modes. For better presentation the vertical plate is unfolded along the +y-axis. It can be seen from Fig. 7.5 (a) that the current is a minimum close to G and a maximum close to M, meaning that the antenna resonates in the quarter-wavelength mode at 1.8 GHz. Also, strong currents are observed in the element OUH at 1.8 GHz, meaning that the element OUH is radiating at this frequency. At 2.6 GHz, the current is a maximum close to M and there are two minima at H and G as shown in Fig. 7.5 (b). This also indicates that the antenna is resonating in the half-wavelength mode. Fig. 7.5 (c)

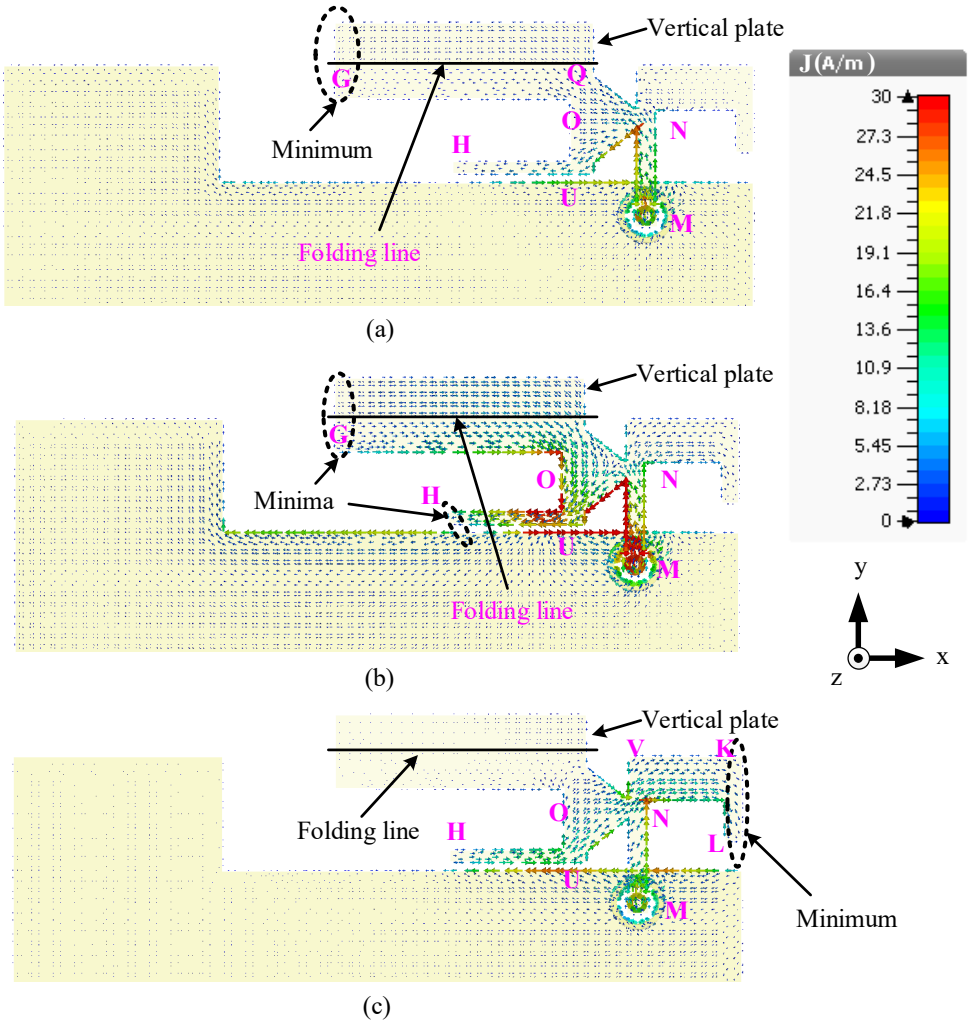

Figure 7.5: Surface current distributions of the dual-band antenna (Ant-6) at (a) 1.8, (b) 2.6, and (c) 3.6 GHz.

illustrates that the antenna resonates in the quarter-wavelength mode at 3.6 GHz since the current reaches its maximum at M while the minimum occurs at edge KL.

7.4 Parameter Analysis

The antenna parameter analysis is organized into three steps. Firstly, the effects of the antenna parameters on the mid-LTE band is studied. Secondly, the effects of the antenna

parameters on the high-LTE band are presented. Thirdly and finally, the influence of the antenna parameters on both the bands are assessed.

Referring to Figs. 7.2 and 7.5, the widths w_{10}, w_7 and lengths l_3, l_4 of the antenna element GQOUH control the impedance matching and impedance bandwidth in the mid operating band. For the high-LTE band, the impedance matching and impedance bandwidth are controlled by the width w_{11} and length l_6 of the antenna element NVKL, and the width w_7 and length l_4 of the antenna element OUH. When one geometry parameter is analyzed the other parameters of the antenna are retained as listed in Table 7.1.

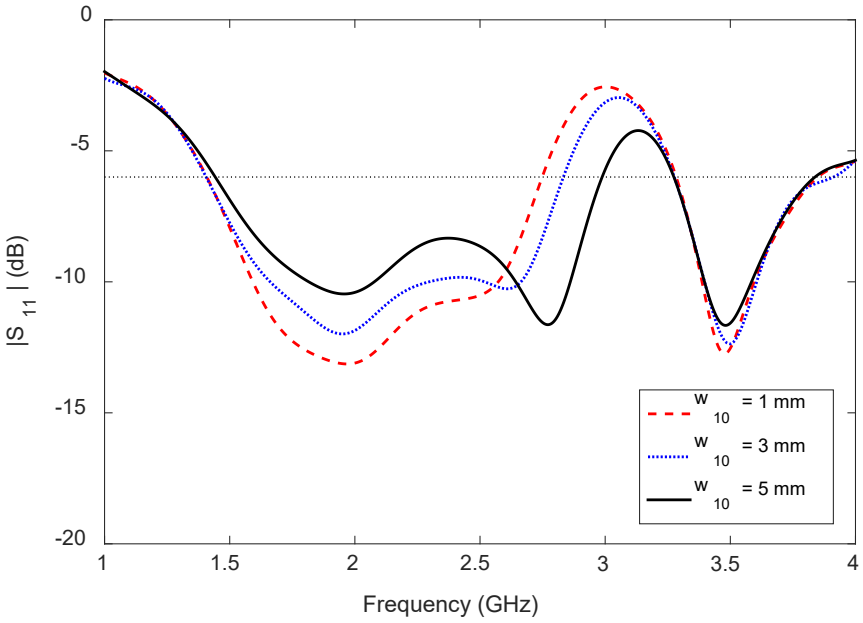

Figure 7.6: Influence of w_{10} on the operating bandwidth and impedance matching at mid-LTE band of the dual-band antenna (Ant-6).

The reflection coefficient behavior with changes of the width w_{10} is shown in Fig. 7.6, and with changes of the length l_3 is shown in Fig. 7.7. However, the width w_8 of the antenna element UH has less effect on the mid-LTE band than the above mentioned two parameters. The width w_{10} controls the higher edge frequency in the mid-band significantly but has a negligible effect on the lower edge frequency. Yet the dual resonance

in the mid-LTE band is always maintained for w_{10} = 1, 3 and 5 mm.

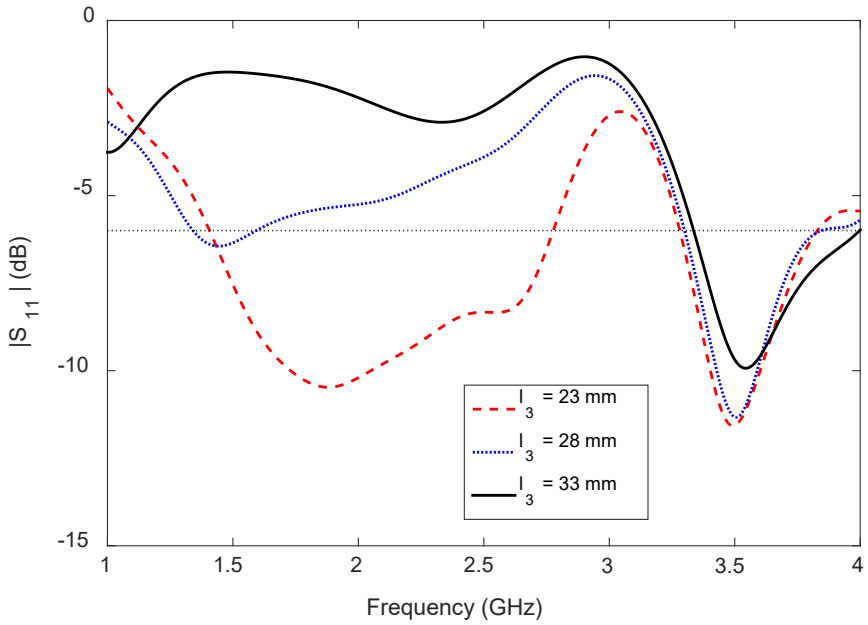

Figure 7.7: Influence of l_3 on operating bandwidth and impedance matching at mid-LTE band of the dual-band antenna (Ant-6).

The dual resonance for l_3 = 23 mm is converted to a single resonance for l_3 = 28 and 33 mm in the mid-LTE band, and the antenna impedance matching becomes worse as the length of the element QG (l_3) increases. Here, resonances are counted when the reflection coefficient value falls below -6 dB. In all the above cases the high-LTE band remains unaffected but a slight change in the frequency of minimum reflection coefficient is observed (see Figs. 7.6 and 7.7).

The antenna element VKL was loaded to the middle element MNO to cover the high-LTE band, and the corresponding results are presented in Fig. 7.4. When considering the effect of two major parameters, the width w_{11} and length l_6 of the element VKL, this refers to impedance matching and the reflection coefficient bandwidth within the high-LTE band. This is explained in more detail below.

The antenna reflection coefficient behavior for width w_{11} = 2, 4 and 6 mm is shown

in Fig. 7.8, and for length l_6 = 0, 3 and 6 mm is shown in Fig. 7.9. The frequency of minimum reflection coefficient shifts towards high frequency when width w_{11} changes from 2 to 6 mm since the effective length of the element VKL decreases. Besides this, increases of the width of the element VK help to improve the antenna impedance matching at the high-LTE band as well as increase the reflection coefficient bandwidth. To cover the high-LTE band the value of the width w_{11} is carefully chosen to be 4 mm.

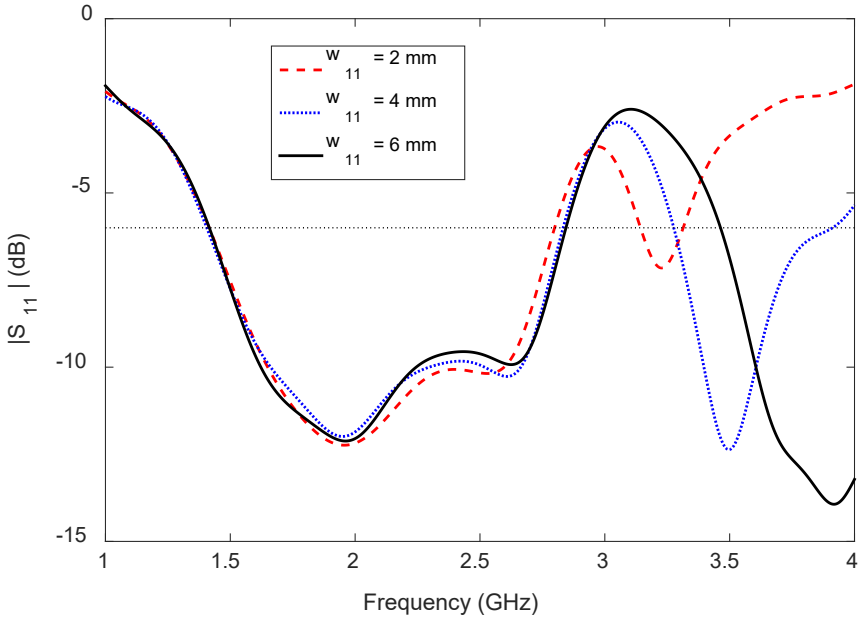

Figure 7.8: Effects of w_{11} on operating bandwidth and impedance matching at high-LTE band of the dual-band antenna (Ant-6).

The other way to increase the effective length of the antenna element VKL is to increase the length of the element KL. Consequently, the increase of length l_6 shifts the frequency of minimum reflection coefficient towards lower frequency as made clear in Fig. 7.9. For l_6 = 0 mm, the L-shaped element VKL becomes an I-shaped element VK, resulting in a less effective length than before, which shifts the antenna operating band in the high-LTE band region towards higher frequency. By tuning the width of the element VK (w_{11}) and the length of the element KL (l_6) it is possible to tune the bandwidth and operating band

to cover the high-LTE band. In both cases, with changes in the width w_{11} and length l_6, a negligible effect on the lower frequency limit of the mid-LTE band is observed; however, a slight change in the upper frequency limit of the mid-LTE band is observed. In order to cover the complete mid-LTE band and high-LTE band the value of l_6 is carefully chosen to be 4 mm.

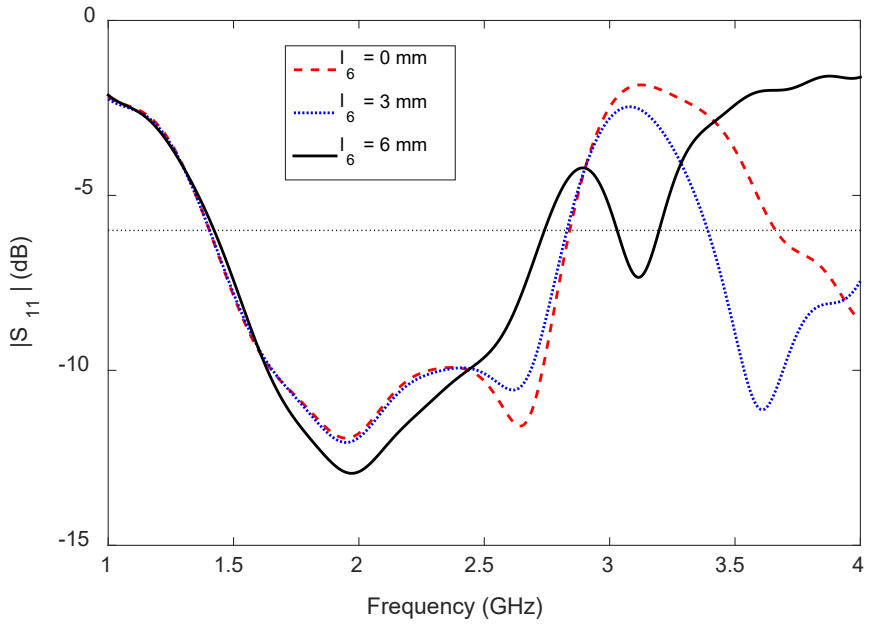

Figure 7.9: Effects of l_6 on operating bandwidth and impedance matching at the high-LTE band of the dual-band antenna (Ant-6).

The antenna element OUH (length l_4 and width w_7) which contributes to the mid and high-LTE band impedance matching that was previously illustrated by the surface current distribution (shown in Fig. 7.5), is now considered here. The length l_4 and width w_7 have a negligible effect on the lower frequency limit of the mid-LTE band because this frequency is mainly controlled by the element OQG and the vertical plate. With changes in the width w_7 from 0 to 4 mm the reflection coefficient bandwidth in the mid-LTE band widens but the reflection coefficient bandwidth in the high-LTE band becomes narrower. The result is reduced impedance matching as demonstrated in Fig. 7.10.

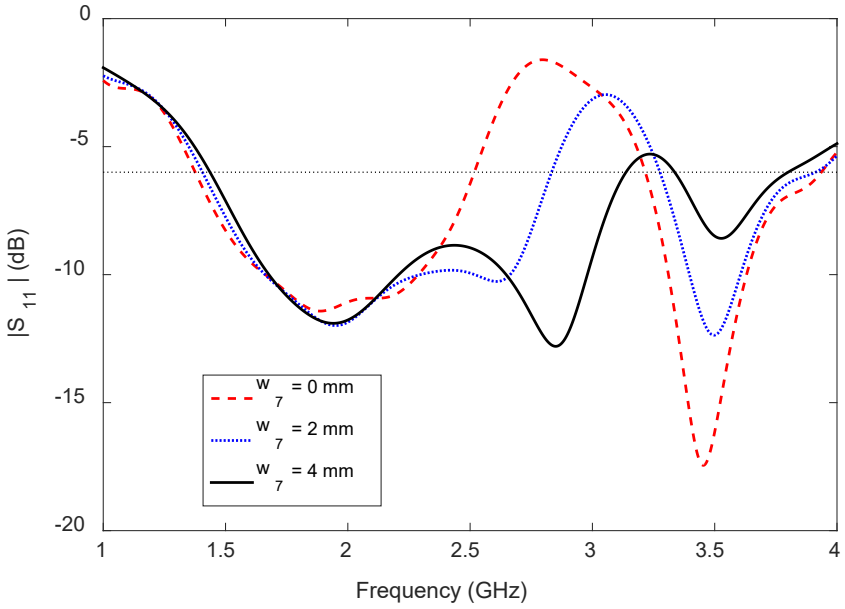

Figure 7.10: Effects of w_7 on operating bandwidth and impedance matching at mid and high bands of the dual-band antenna (Ant-6).

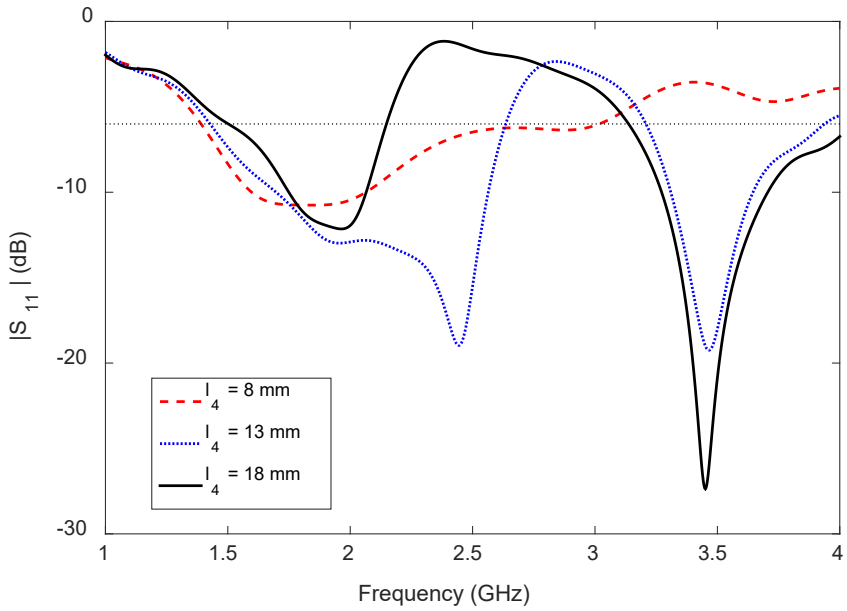

Figure 7.11: Effects of l_4 on operating bandwidth and impedance matching at mid and high bands of the dual-band antenna (Ant-6).

Antenna impedance matching in the high-LTE band is very good when $l_4 = 13$, and 18 mm but the reflection coefficient bandwidth in the mid-LTE band becomes narrower with the increase in length l_4 from 8 to 18 mm (see Fig. 7.11). For $l_4 = 8$ mm the antenna impedance matching is very poor in both the mid and high bands. In order to have good impedance matching over the mid and high bands and to have sufficient reflection coefficient bandwidth in both the bands the length l_4 and width w_7 are carefully chosen so that they are 11 mm and 2 mm, respectively.

7.5 Radiation Performance and Discussion

The predicted antenna efficiency within the -6 dB reflection coefficient bandwidth as a function of frequency is shown in Fig. 7.12. The maximum and minimum antenna efficiencies in the mid-LTE band are 90% and 61%, at 1.85 and 2.8 GHz, respectively. The antenna efficiency at its minimum is 66% at 3.3 GHz in the high-LTE band while the maximum is 89% at 3.5 GHz. Thus the antenna efficiency is always above 61% in both the mid and high-LTE bands.

The predicted antenna gain within the -6 dB reflection coefficient bandwidth as a function of frequency is shown in Fig. 7.13. The maximum and minimum gain in the mid-LTE band are 3.4 and 1.4 dBi, at 2.55 and 1.4 GHz, respectively. The gain is a minimum of 4.2 dBi at 3.3 GHz in the high-LTE band and is a maximum of 6.1 dBi at 3.55 GHz. Therefore the gain variations of the antenna in the mid and high bands are less than 2 and 1.9 dB, respectively, which means that the antenna has stable gain in both bands.

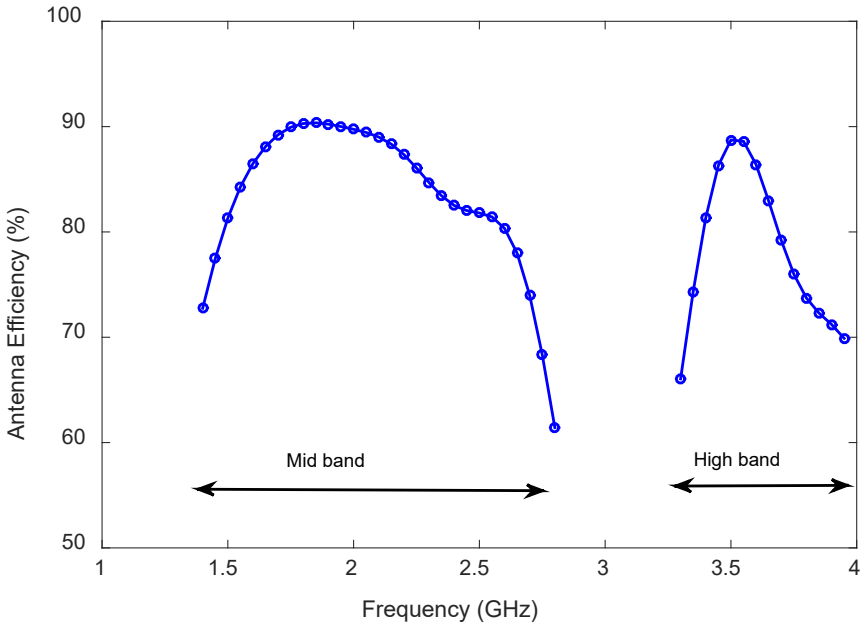

Figure 7.12: Predicted antenna efficiency of the dual-band antenna (Ant-6) for the mid and high bands.

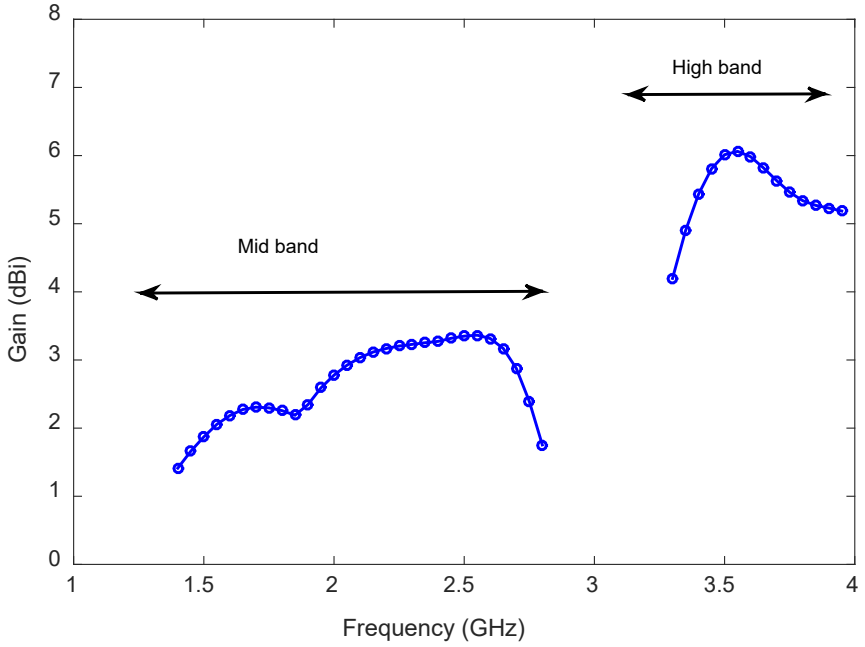

Figure 7.13: Predicted antenna gain of the dual-band antenna (Ant-6) for the mid and high bands.

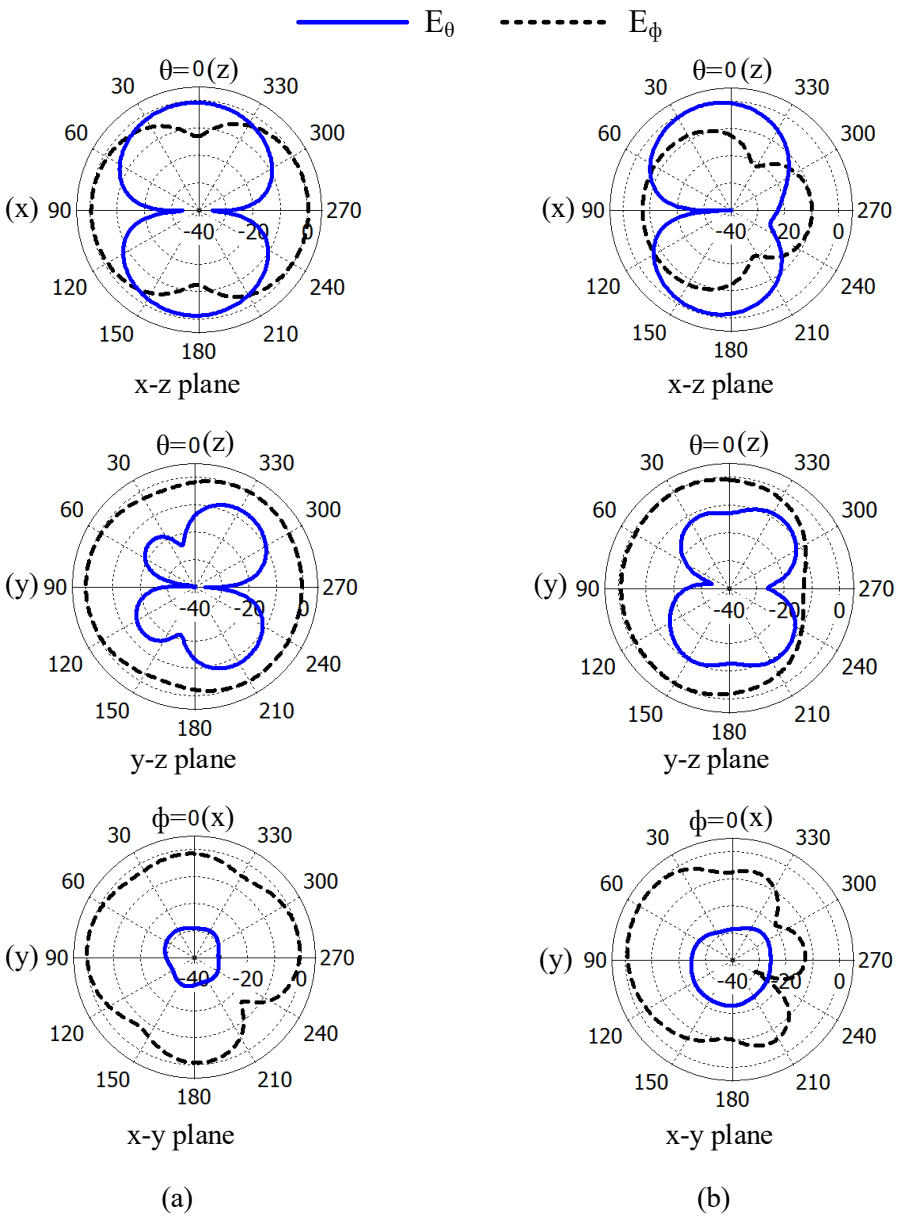

Figure 7.14: Predicted normalized radiation patterns of the dual-band antenna (Ant-6) at (a) 1.8, and (b) 2.6 GHz.

The normalized E_θ and E_ϕ radiation patterns of the antenna for both mid and high bands are presented. The predicted radiation patterns in the three principal planes at 1.8 and 2.6 GHz are shown in Fig. 7.14, while the radiation patterns at 3.6 GHz are depicted

in Fig. 7.15. The radiation patterns in each plane are normalized with respect to the maximum of the corresponding principal plane.

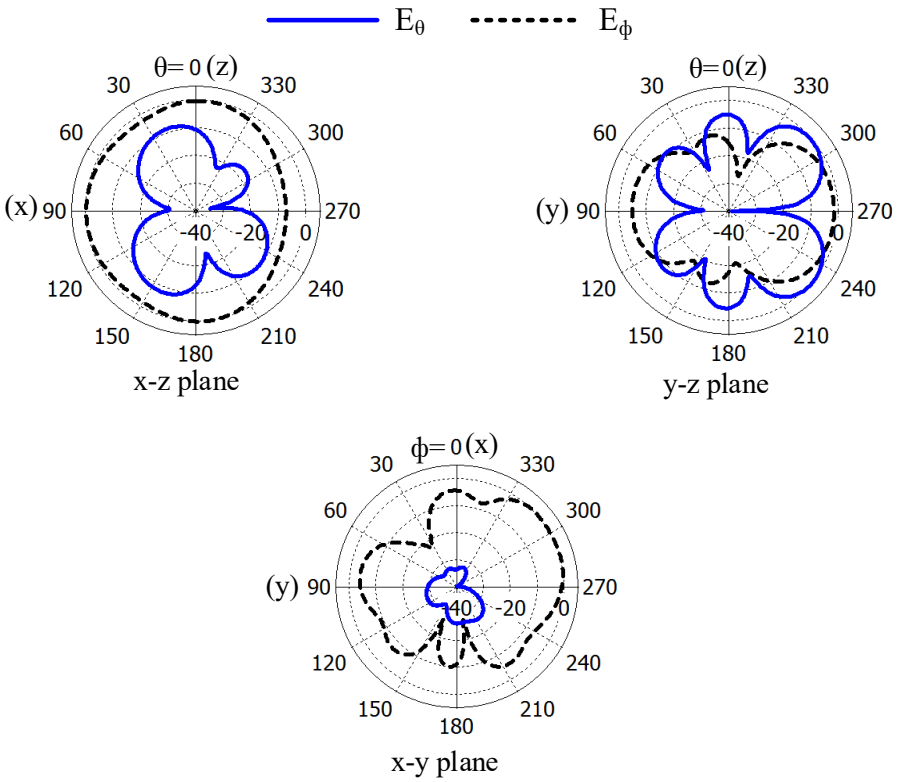

Figure 7.15: Predicted normalized radiation patterns of the dual-band antenna (Ant-6) at 3.6 GHz.

The E_ϕ pattern in the x-z plane at 3.6 GHz is more uniform (nearly omnidirectional) than the E_ϕ pattern in the same plane at 1.8 and 2.6 GHz. A uniform E_ϕ pattern is observed in the y-z plane at 1.8 GHz. Strong E_ϕ radiation is observed along the y-axis at 3.6 GHz compared to the z-axis. Also the E_ϕ pattern is more uniform in the x-y plane at 1.8 GHz than the E_ϕ pattern at 3.6 GHz. The E_ϕ pattern in the x-y plane has two nulls at 3.6 GHz and one null at 2.6 GHz. Overall, the E_ϕ component is always stronger than E_θ in the y-z and x-y planes at 1.8 and 2.6 GHz and in the x-z and x-y planes at 3.6 GHz. As well, the E_ϕ and E_θ levels are comparable in the x-z plane at 1.8 and 2.6 GHz and

in the y-z plane at 3.6 GHz, an additional benefit in practical applications with complex propagation environments [73, 137, 138].

7.6 Compatibility with Different-Sized Mobile Devices

This section presents simulated reflection coefficients for the dual-band antenna (Ant-6) when fitted into different-sized mobile phones and tablet computers. Selected devices with their typical dimensions that are considered for the proposed antennas compatibility validation are listed in Table 7.2. In each device, the antenna (Ant-6) to cover mid and high bands is placed at the top-right corner of the selected mobile device substrate. In this study the antenna parameters are the same as those presented in Table 7.1. The ground clearance is kept the same as previously mentioned in the antenna design section (Section 7.2).

The reflection coefficient behavior for the dual-band antenna (Ant-6) with changes in the size of the mobile device is shown in Fig. 7.16. With changes in the substrate size of a mobile device the antenna lower frequency limit is affected in the mid-LTE band for the dual-band antenna (Ant-6). This is because of the change in the ground plane size. However, the upper frequency limit is almost unaffected with an alteration of the substrate size. In the case of a smart phone plus, three resonances have been observed in the mid-LTE band. Yet only two resonances are clearly seen for the other three mobile devices, as shown in Fig. 7.16. Moreover, good antenna input impedance matching has been observed over the mid operating band for all the sizes of hand-held devices listed in Table 7.2.

Table 7.2: Substrate dimensions of commonly used hand-held mobile devices and tablet computers for the compatibility test of the dual-band antenna (Ant-6).

Device Name	Length (mm)	Width (mm)
Smart Phone (SP)	120	70
Smart Phone Plus (SP Plus)	160	80
Mini Tablet Computer (Mini TC)	200	135
Tablet Computer (TC)	240	170

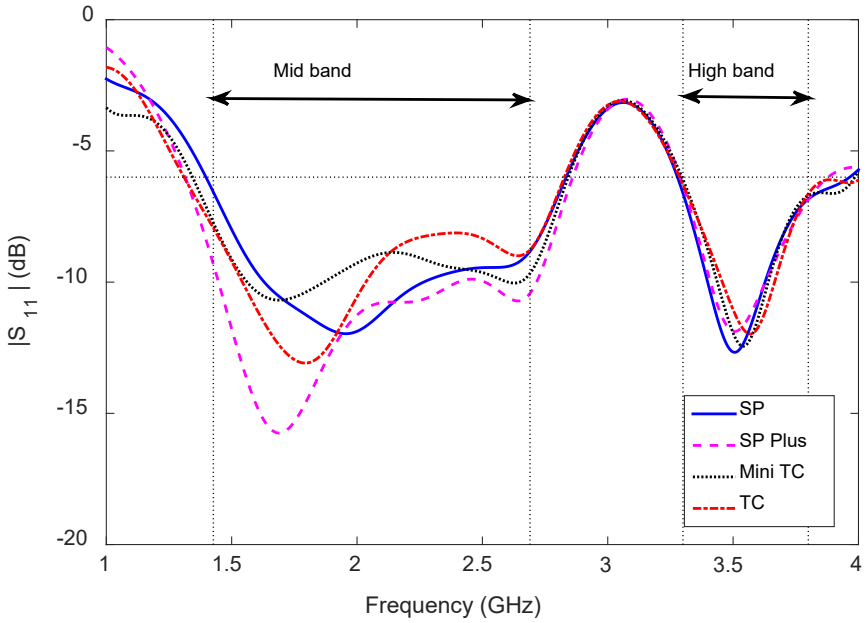

Figure 7.16: Effect of the device size on the reflection coefficient of the dual-band antenna (Ant-6). Here, SP: smart phone, and TC: tablet computer.

The lower and upper frequency limits are completely unaffected by changes in the size of the mobile device substrate in the high-LTE band. A negligible effect on the antenna impedance matching at the frequency of minimum reflection coefficient in the high-LTE band is observed. A slight change in the frequency of minimum reflection coefficient when

the size of the mobile device substrate changes is also observed. From the results presented here, the antenna is suitable for the smart phone, smart phone plus, mini tablet computer and tablet computers operating in the mid and high bands.

7.7 Comparison between Ant-5 and Ant-6

Table 7.3: Comparing performance between Ant-5 (presented in Chapter 6, Section 6.3) and Ant-6 (proposed in this chapter).

Parameter	Ant-5	Ant-6
Physical Area (mm^2)	600	585
Bandwidth (GHz)	1.39-2.78	1.39-2.84, 3.27-3.97
Efficiency (%)	67-90	62-90 (M), 66-88 (H)*
Gain (dBi)	1.3-3.6	1.4-3.4 (M), 4.2-6.1 (H)
Null in Radiation Patterns	1 null	1 null (M), 2 nulls (H)

*Here M and H stand for the mid-LTE and high-LTE bands, respectively.

A comparison of the performance between the planar antenna (Ant-5 presented in Chapter 6 Section 6.3) and Ant-6 (proposed in this chapter) is presented in Table 7.3. The area (length $\times$ width) required for Ant-6 is less than the area occupied by Ant-5. Ant-6 is a dual-band antenna whereas Ant-5 is a single-band antenna. Ant-6 covers both the LSA bands, mid-LTE and high-LTE bands but Ant-5 is unable to cover the high-LTE band. Both antennas are designed on the same substrate of equal size (120 mm $\times$ 70 mm). The gain variation of Ant-6 is lower than the gain variation of Ant-5 within the mid-LTE band. The gain variation of Ant-6 within the high-LTE band is almost equal to the gain variation of the antenna within the mid-LTE band. The efficiency of Ant-6 and Ant-5 is

always above 62% within their -6 dB reflection coefficient bandwidths. Ant-6 cover the lower LSA band without null in the radiation patterns. However, a null is observed at the frequency close to the higher frequency limit of the mid-LTE band for both antennas, although the antennas have nearly omnidirectional radiation patterns at frequency close to the lower frequency limit of the mid-LTE band. In addition, Ant-6 has two nulls in the radiation patterns in the high-LTE band.

7.8 Summary

A novel dual-band antenna (Ant-6) for mobile devices was proposed in this chapter. The antenna was composed of a planar structure loaded with an I-shaped vertical plate. Ant-6 covers both the LSA bands, mid-LTE and high-LTE bands, having a -6 dB reflection coefficient bandwidth of 1450 MHz (1.39-2.84 GHz) and 700 MHz (3.27-3.97 GHz). The suitability of the antenna for different-sized (120 mm × 70 mm, 160 mm × 80 mm, 200 mm × 135 mm, and 240 mm × 170 mm) mobile devices was verified through simulation. The antenna operates in the quarter and half-wavelength modes at resonant frequencies. The antenna parameters that affect the reflection coefficient bandwidth and antenna input impedance matching were analyzed. The antenna's efficiency varies in the 62%-90% and 66%-88% ranges within the mid-LTE and high-LTE bands, respectively. The gain variation of the antenna is 2 and 1.9 dB within the mid-LTE and high-LTE bands, respectively. Despite the proposed antennas covering the mid-LTE and high-LTE bands, a null in the radiation patterns is exist at a frequency close to the upper frequency limit of the mid-LTE band, and 2 nulls are exist in the high-LTE band radiation patterns. However, nearly omnidirectional radiation patterns were observed at a frequency close to the lower frequency limit of the mid-LTE band. In the next chapter, a wideband antenna will be developed in order to cover the above mentioned bands without any null in the radiation

patterns.

Chapter 8

Wideband Antenna for LSA, Mid-LTE and High-LTE Bands

8.1 Introduction

In this chapter a wideband antenna (Ant-7) loaded with an L-shaped vertical plate is developed. Unlike the previous dual-band antenna (Ant-6 presented in Chapter 7), this is a single wideband antenna covering both the LSA and mid-LTE and high-LTE bands. In this design approach the aim is to design a smaller antenna with no null in the radiation patterns. Similar to Ant-6 the proposed antenna in this chapter does not require any active or passive lumped component-based input impedance matching. In order to verify the proposed development Ant-7 was prototyped and tested experimentally.

This chapter is organized as follows. The proposed antenna's configuration is presented in Section 8.2. The working principle with the help of the design procedure is presented in Section 8.3. As well, the surface current distributions of the antenna are analyzed at three different frequencies to further understand the working modes of the antenna (see Section 8.3). Extensive parameter studies are conducted and described in Section 8.4 to

understand the parameters that significantly affect the impedance matching and operating bandwidth of the antenna. In order to test the developed antenna's design the simulated reflection coefficient and radiation performance are compared with the measured results in Section 8.5. The suitability of the proposed antenna with different-sized mobile devices is evaluated in Section 8.6. Comparing the performance between Ant-7 and reference antennas is described in Section 8.7 while the final part of this chapter, Section 8.8, summarizes the major findings presented here.

8.2 Antenna Configuration

A novel wideband antenna (Ant-7), designed to operate in the mid and high bands for LSA, TDD/FDD LTE, UMTS, DCS, PCS, GSM1800, GSM1900, 2.4 GHz WLAN, and WiMAX (2.5 and 3.3 GHz), is shown in Figs. 8.1 and 8.2. Fig. 8.1 displays the top and back views of the antenna without a vertical plate and the antenna's placement within the mobile device substrate. Fig. 8.2 is a perspective view of the antenna and its detailed geometry. There is an L-shaped vertical plate in the antenna design which is shown as unfolded along the +y-axis in Fig. 8.2 (b), for better presentation. The antenna is fed with an SMA connector. To ensure isolation between the ground plane and the center pin of the SMA connector, a circular portion of copper with radius r is etched off from the ground plane as indicated in Fig. 8.2 (b). The overall size of the antenna (Ant-7) is 34 mm $\times$ 15 mm $\times$ 4 mm or $0.16\lambda_0 \times 0.07\lambda_0 \times 0.02\lambda_0$, where λ_0 is the free-space wavelength at 1.41 GHz. This means that the proposed antenna is 13% smaller than the dual-band antenna (Ant-6) presented in Chapter 7.

The wideband antenna (Ant-7) is composed of three elements: a U-shaped large element (PQOR) loaded with an L-shaped vertical plate (aligned with the edge PQ) to cover the mid-LTE band on the left; an L-shaped loop antenna (NSTS) on the right to

cover the high-LTE band; and an L-shaped element at the middle, to provide impedance matching for both left and right elements. The middle element is the same as the element used in Ant-6. The optimized design parameters for the proposed antenna are listed in Table 8.1.

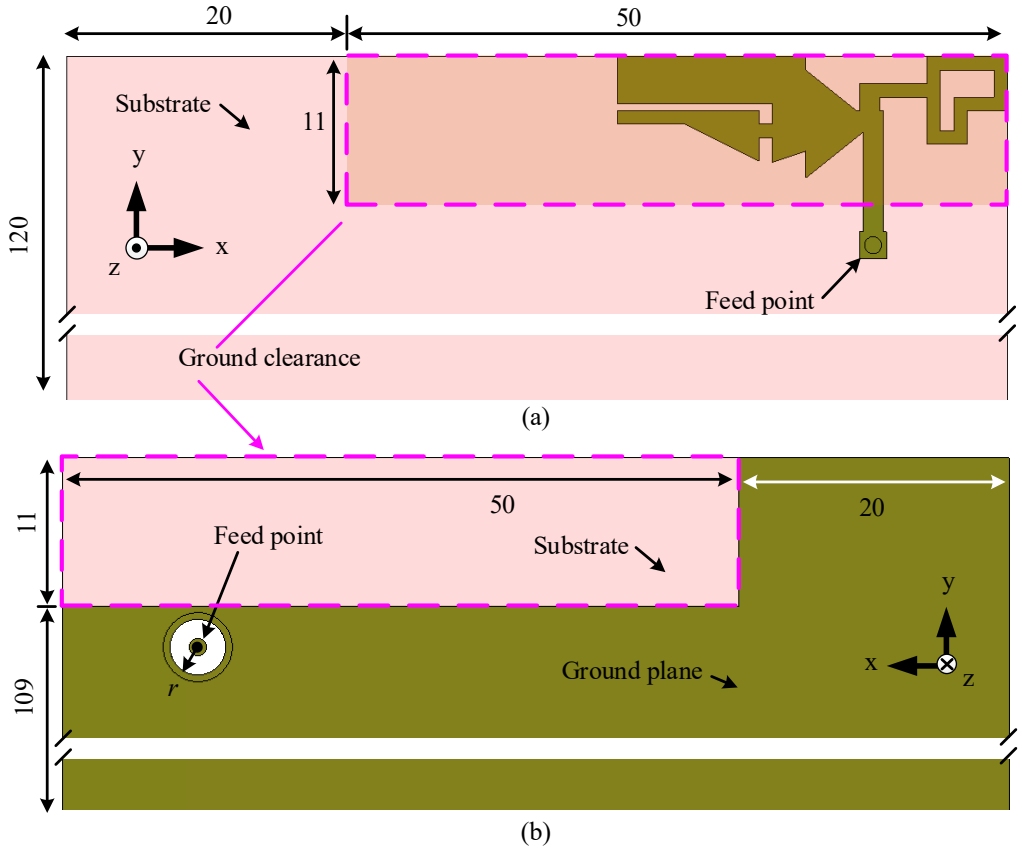

Figure 8.1: Placement of the wideband antenna (Ant-7) on a mobile phone substrate: (a) top view without vertical plate, and (b) back view. All dimensions are in millimeters.

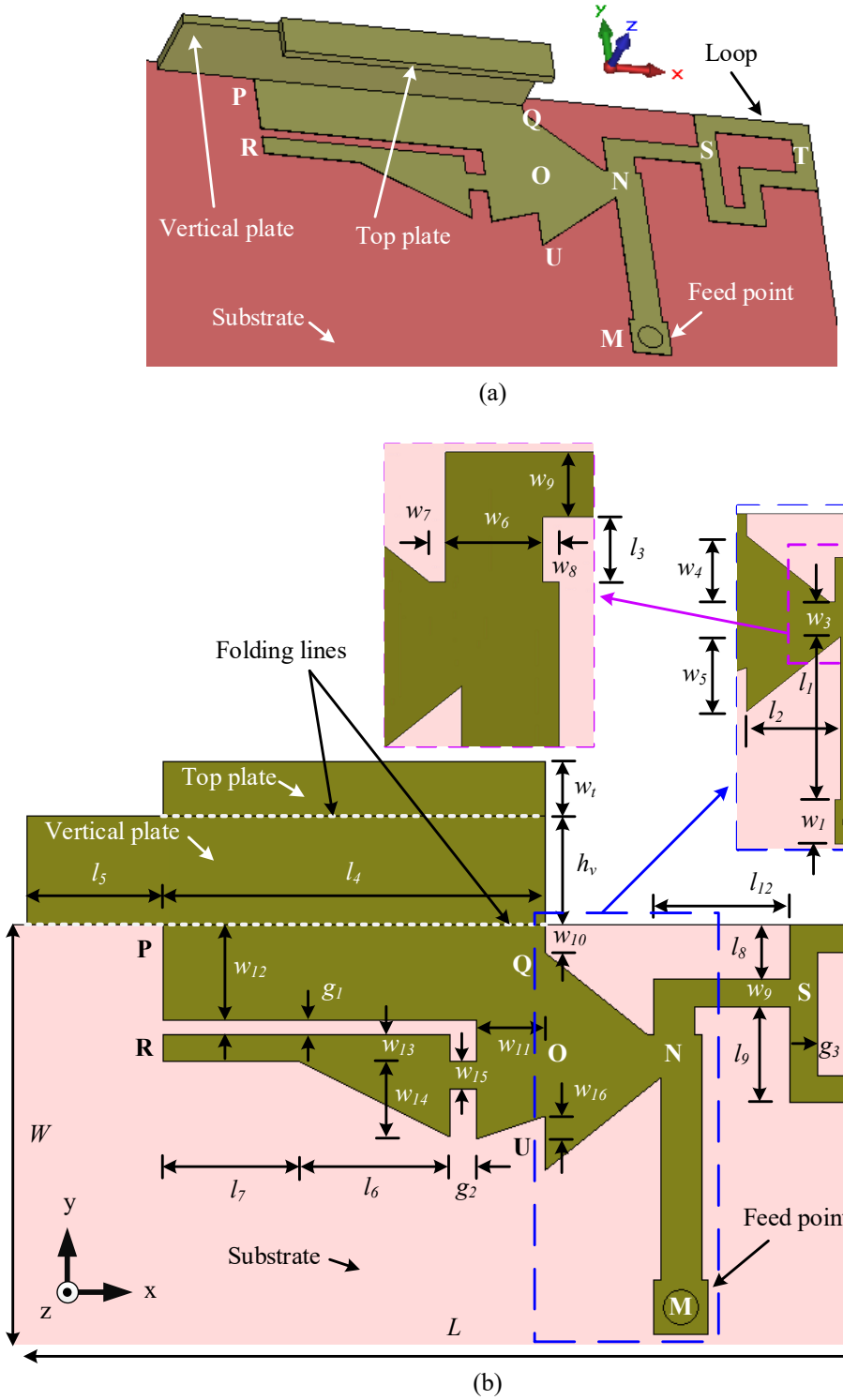

Figure 8.2: Geometry of the proposed wideband antenna (Ant-7) for the mid-LTE and high-LTE bands for LSA and LTE/WWAN hand-held devices: (a) perspective view, and (b) detailed geometry (top view) with vertical plate unfolded along +y-axis.

Table 8.1: Design parameters of the wideband antenna (Ant-7) for mid and high-LTE band operation. All dimensions are in millimeters.

$w_1 = 2$	$w_2 = 1.5$	$w_3 = 1.6$	$w_4 = 3$	$w_5 = 3.4$
$w_6 = 15$	$w_7 = 0.25$	$w_8 = 0.25$	$w_9 = 1$	$w_{10} = 1$
$w_{11} = 2.5$	$w_{12} = 3.5$	$w_{13} = 1$	$w_{14} = 2.75$	$w_{15} = 1$
$w_{16} = 0.75$	$l_1 = 7.4$	$l_2 = 4.25$	$l_3 = 1$	$l_4 = 14$
$l_5 = 5$	$l_6 = 5.5$	$l_7 = 5$	$l_8 = 2$	$l_9 = 3.5$
$l_{10} = 2.5$	$l_{11} = 3$	$l_{12} = 5$	$h_v = 4$	$w_t = 2$
$g_1 = 0.5$	$g_2 = 1$	$g_3 = 1$	$g_4 = 2$	$r = 2$
$L = 34$	$W = 15$			

8.3 Design Procedure and Working Principle

The proposed novel antenna design procedure is divided into the four major steps shown in Fig. 8.3, to describe its working principle. The predicted reflection coefficients of all steps are depicted in Fig. 8.4. The design started with a simple planar antenna such that it can resonate within the mid-LTE band. Secondly, an L-shaped bent plate is loaded to the antenna for tuning its operating bandwidth. Thirdly, another element is added to the antenna to generate a second resonant at the high-LTE band. Fourthly and finally, an L-shaped loop element is added to the antenna to tune the high-LTE band. In addition, the antenna is designed based on the fundamental equations discussed in Section 2.3. To further analyze the working modes of the antenna, the surface current distributions are used at the resonant frequencies.

In this design, the middle element MNO indicated in Fig. 8.3 (Step-1) is the same element used in the antenna design presented in Chapter 7. The effective length of the

element MNO is $l_{ILE} = l_1 + l_2 + (w_1 + w_2 + w_3)/2 = 14.2$ mm. Referring to Fig. 8.3 (Step-1), initially an L-shaped strip UQP is imposed on the middle element MNO. Then a triangular portion is etched off from the lower side of the strip UQ with the base and height of w_{11} and w_{16}, respectively. The antenna as shown in Step-1 (Fig. 8.3) has a -6 dB reflection coefficient bandwidth of 1.5 GHz (1.8-3.3 GHz) with a resonance at 2.66 GHz as revealed in Fig. 8.4 (Step-1 curve). Therefore, the lower frequency limit is about 373 MHz away from the targeted value (1427 MHz). The antenna resonates in the quarter-wavelength mode at 2.66 GHz since the effective length of the antenna is around $l_{ILE} + w_{11}/2 + l_4 + w_{12}/2 + g_1 + w_{13} = 32.7$ mm.

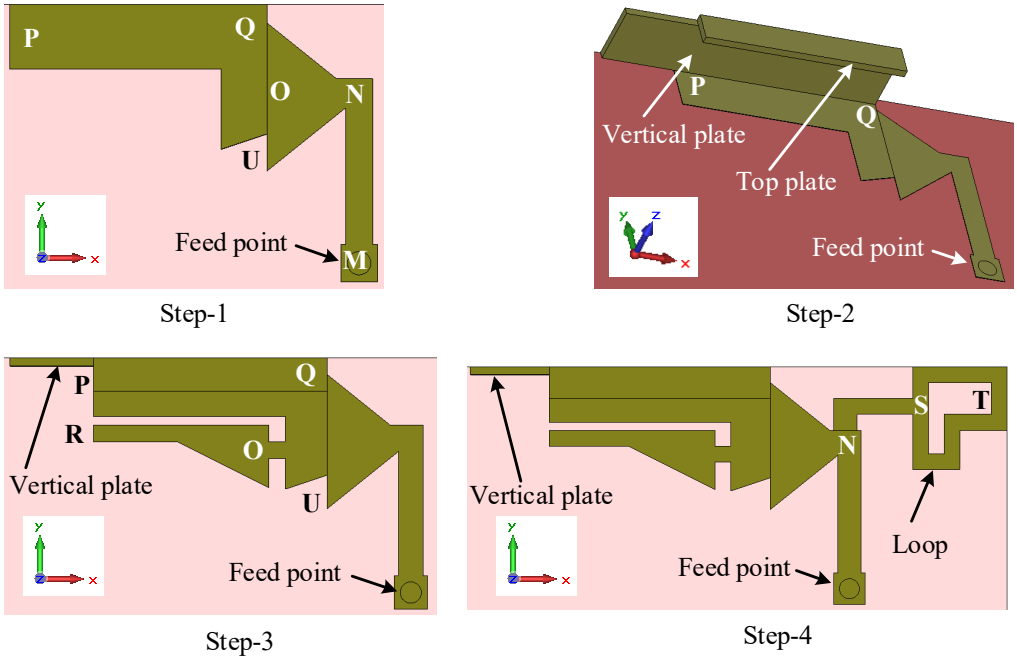

Figure 8.3: Four-steps of evolution of the wideband antenna (Ant-7).

It is necessary to shift the lower frequency limit in order to cover the complete mid-LTE band. In Step-2, a vertical plate with a thickness of 0.4 mm is firstly added to the edge PQ and aligned with the edge point Q as shown in Fig 8.3 (Step-2). This serves to shift the lower frequency limit. The length and height of the vertical plate are $l_4 + l_5$ and

h_v, respectively. Finally, in Step-2, a top plate of size $l_4 \times w_t \times 0.4$ mm^3 is loaded to the top of the vertical plate, and is aligned with the edge point Q shown in Fig. 8.3 (Step-2), resulting in an L-shaped vertical plate loaded to the element UQP. This L-shaped vertical plate is employed to tune the operating band of the antenna and the lower frequency limit. A -6 dB reflection coefficient bandwidth of 1.46 GHz (1.46-2.92 GHz) is achieved as shown in Fig. 8.4 (Step-2 curve). The antenna in Step-2 resonates at 1.82 GHz.

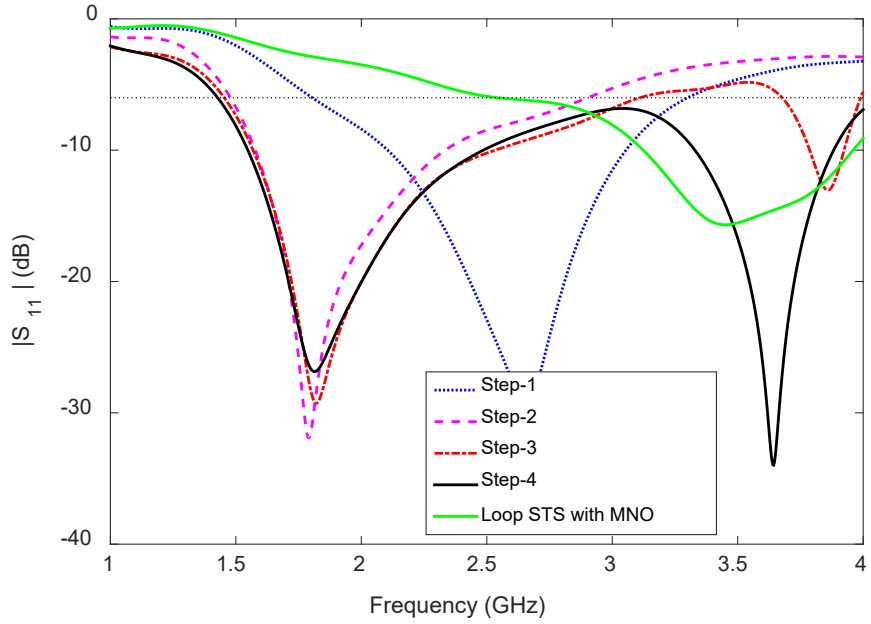

Figure 8.4: Predicted reflection coefficients for the four-steps of evolution of the wideband antenna (Ant-7).

A further shift in the lower frequency limit in the mid-LTE band is now required. Also, a second resonant mode is required to cover the high-LTE band. To do so, in Step-3, an I-shaped patch OR of size $(l_6 + l_7) \times (w_{13} + w_{14})$ is placed close to the L-shaped strip UQP, maintaining the gaps g_1 and g_2 along the y and x directions, respectively. Next, a rectangular portion of dimensions $l_7 \times w_{14}$ (aligned with the edge R) and a triangular portion with a base and height of l_6 and w_{14}, respectively, are etched off from the I-shaped patch (OR). At the end of Step-3, a strip of dimensions $g_2 \times w_{15}$ is employed to connect

the I-shaped strip with the antenna element UQ. The finalized structure of the antenna at this stage is shown in Fig. 8.3 (Step-3). The predicted reflection coefficient (Step-3 curve in Fig. 8.4) confirms that a second resonance occurs at 3.86 GHz with a dip of magnitude -13 dB, and the lower frequency limit shifts from 1.46 to 1.43 GHz. At the second resonant band, the antenna resonates in the half-wavelength mode at 3.86 GHz, as the effective length of the U-slot antenna POR fed by MNO is $l_{ILE}+w_{11}+2(l_6+l_7+g_2) = 39.7$ mm. The -6 dB reflection bandwidths are 1.67 GHz (1.43-3.1 GHz) and 300 MHz (3.68-3.98 GHz) in the first and second operating bands, respectively.

Finally, in Step-4, an L-shaped loop NSTS of strip width w_9 is integrated with the right side of the middle element MNO as shown in Fig 8.3 (Step-4). The purpose is to expand the reflection bandwidth of the antenna at both resonances, especially in the second resonant, in order to cover both bands. The reflection coefficient curve for Step-4 is shown in Fig. 8.4 (Step-4 curve). The lower frequency limit of the mid-LTE band shifts from 1.43 to 1.41 GHz. Also, the upper frequency limit of the mid-LTE band and lower frequency limit of the high-LTE band merge together, resulting in a single wideband antenna with two resonances at: firstly, 1.81 GHz and secondly, 3.64 GHz; a -6 dB reflection bandwidth of the antenna is 2.59 GHz (1.41-4 GHz). The effective length of the loop monopole element MNSTS is around 41 mm which is equal to a half-wavelength at 3.65 GHz.

The predicted reflection coefficient for the L-shaped loop NSTS excited by the middle element MNO (after removing the vertical plate loaded U-shaped patch PQUR from the design) is also shown in Fig. 8.4 (Loop STS with MNO curve). The loop monopole antenna operates close to the half-wavelength mode at the 3.45 GHz. Therefore, the proposed antenna is operating in the quarter- and half-wavelength modes at 1.81 and 3.64 GHz, respectively.

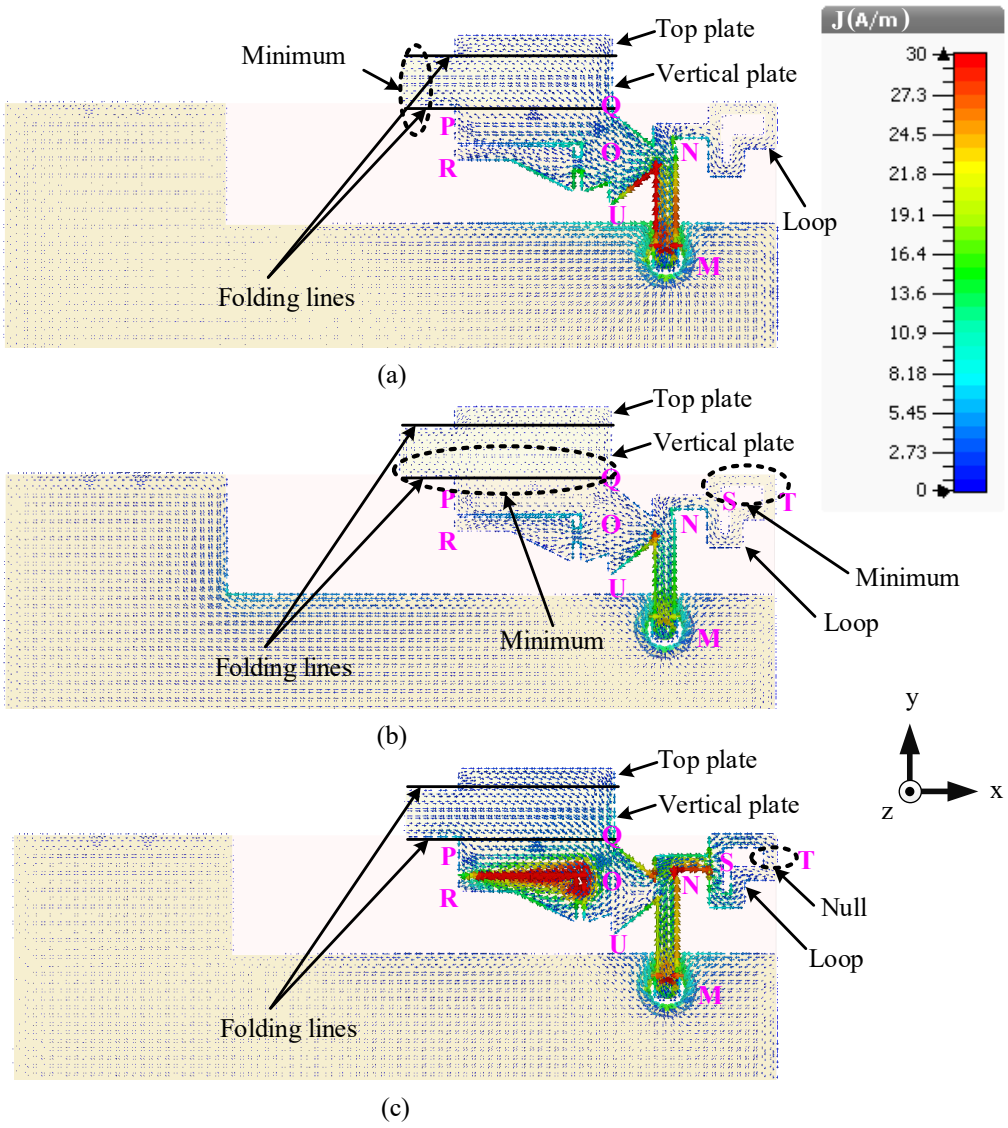

Figure 8.5: Predicted surface current distributions for the wideband antenna (Ant-7) at (a) 1.8, (b) 2.6, and (b) 3.6 GHz.

The predicted current distributions of this antenna at three frequencies - 1.8, 2.6, and 3.6 GHz - are shown in Fig. 8.5. For better presentation the vertical L-shaped load is unfolded along the +y axis. The antenna resonates in the quarter-wavelength mode at 1.8 GHz since only one minimum is observed (in the vertical plate that is close to the edge point P). There are weak currents in the loop NSTS at this resonant mode but no null has

been observed. Two minima are observed (in the vertical plate that is close to the edge QP and in the upper arms of the loop STS), which means that the antenna resonates in the half-wavelength mode at 2.6 GHz as shown in Fig. 8.5 (b). The current distributions in Fig. 8.5 (c) illustrate that the direction of the currents is the same for the upper and lower arms of the loop STS, and a null is present at point T. Hence, the loop monopole antenna resonates in the half-wavelength mode at 3.6 GHz. Also, the left element PQUR has a strong current at 3.6 GHz but no null has been observed.

8.4 Parameter Analysis

The antenna parameter analysis in this section is organized into three steps. Firstly, the antenna parameters that significantly affect the impedance matching and operating bandwidth in the mid-LTE band are discussed. Secondly, the antenna parameters affect the high-LTE band are discussed. Thirdly and finally, the effects of the antenna parameters on both the bands are studied.

Referring to Figs. 8.2, 8.4 and 8.5, the widths w_4 and w_5, and height h_v of the antenna control the impedance matching and impedance bandwidth in the mid operating band. For the high-LTE band, the impedance matching and impedance bandwidth are controlled by the gap widths g_1 and g_2. The length of the vertical plate $l_4 + l_5$ and length of the element PQUR contribute to the matching of both operating bands. When one geometry parameter is analyzed the other parameters of the antenna remain unchanged.

Changes in widths w_4 and w_5 of the antenna element NUQ means the coupling between the feed element MNO and the U-shaped element PQUR is affected. It influences the surface current distributions in the element PQUR in the mid and high bands. However, the effect in the mid-LTE band is significant compared to the high-LTE band, especially in the higher frequency limit of the mid-LTE band as shown in Fig. 8.6. With the change

of the widths w_4 and w_5, the impedance bandwidth in the high-LTE band is unaffected except for the matching at resonance.

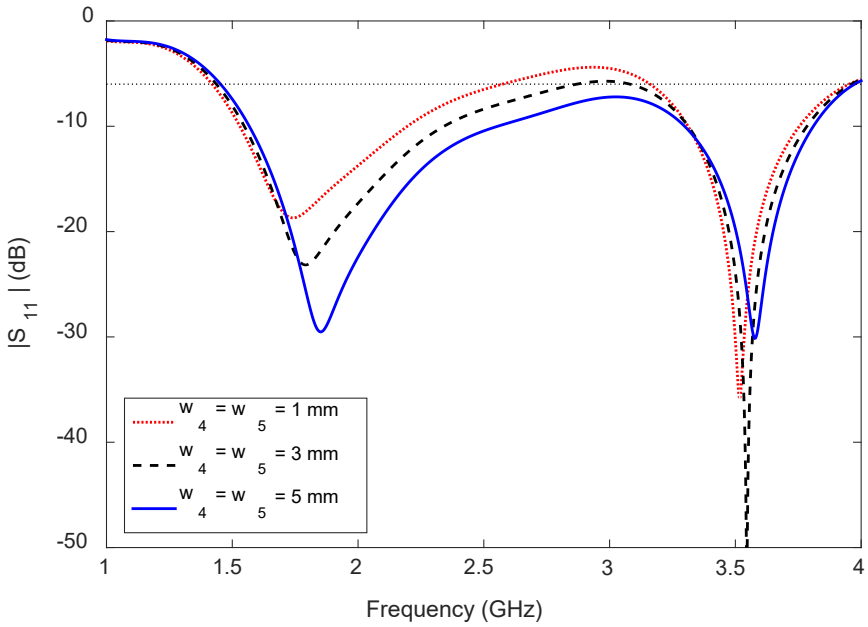

Figure 8.6: Influence of w_4 and w_5 on operating bandwidth and impedance matching at mid-LTE band of the wideband antenna (Ant-7).

Fig. 8.7 depicts the reflection coefficient behavior of the antenna for h_v = 2, 4 and 6 mm. For the lower value of h_v (2 mm), the lower frequency limit in the mid-LTE band shifts towards higher frequency, which means exceeding the targeted value of 1427 MHz. However, impedance matching at the higher frequency limit of the mid-LTE band improves. For h_v = 6 mm, the lower frequency limit moves toward low frequency and the wideband antenna becomes a dual-band antenna while covering the mid and high-LTE bands. Yet the problem is that a higher value of h_v means increasing the height of the mobile device which makes the antenna unsuitable for practical purposes. The values of the widths w_4 and w_5 and height h_v are carefully chosen to be 3 mm, 3.4 mm, and 4 mm, respectively, to cover the mid and high-LTE bands.

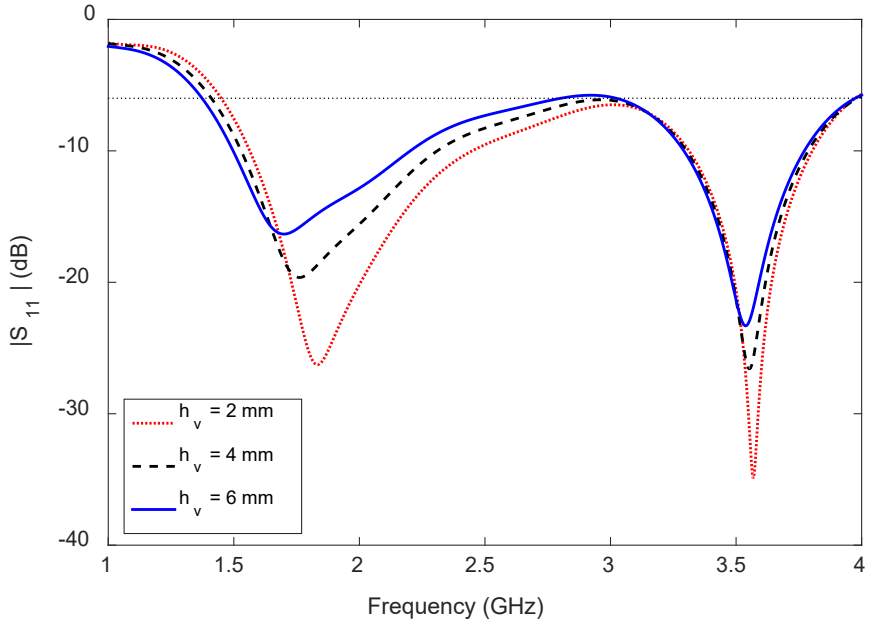

Figure 8.7: Influence of h_v on operating bandwidth and impedance matching at mid-LTE band of the wideband antenna (Ant-7).

The capacitive coupling between the elements PQOU and OR significantly affects the impedance matching and bandwidth on the high-LTE band, while a negligible effect has been observed on the mid-LTE band (see Figs. 8.8 and 8.9). This was illustrated previously using the surface current distribution in Fig. 8.5. With the change of the gap width g_1 the antenna impedance bandwidth in the mid-LTE band changes slightly, but the lower frequency limit in the high-LTE band is unaffected. The higher frequency limit in the high-LTE band is shifted towards low frequency as the gap width g_1 increases, but the frequency of minimum reflection coefficient in the high-LTE band is unaffected with the change of the gap width g_1 from 1 mm to 3 mm.

Changing the gap width g_2 means a change in the coupling capacitance between the elements UQ and OR, which also affects the length of the coupling strip between the elements. Increasing the gap width g_2 means the number of resonant frequencies in the high-LTE band increases along with the change of the antenna impedance matching bandwidth in the same band shown in Fig. 8.9. Changing the gap width g_2 from 1 mm to 3 mm will result in the lower frequency limit of the high-LTE band and lower and upper frequency limit of the mid-LTE band being completely unaffected.

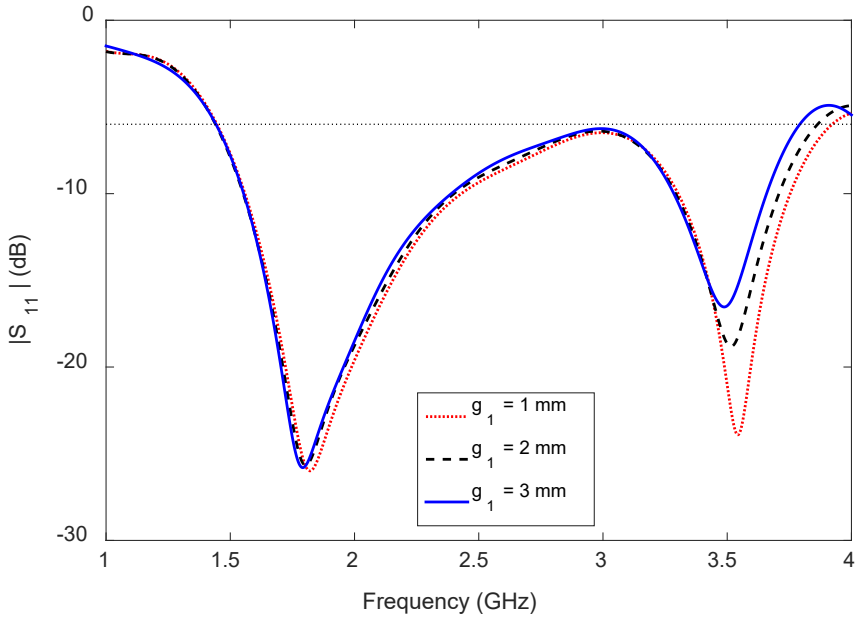

Figure 8.8: Influence of g_1 on operating bandwidth and impedance matching at the high-LTE band of the wideband antenna (Ant-7).

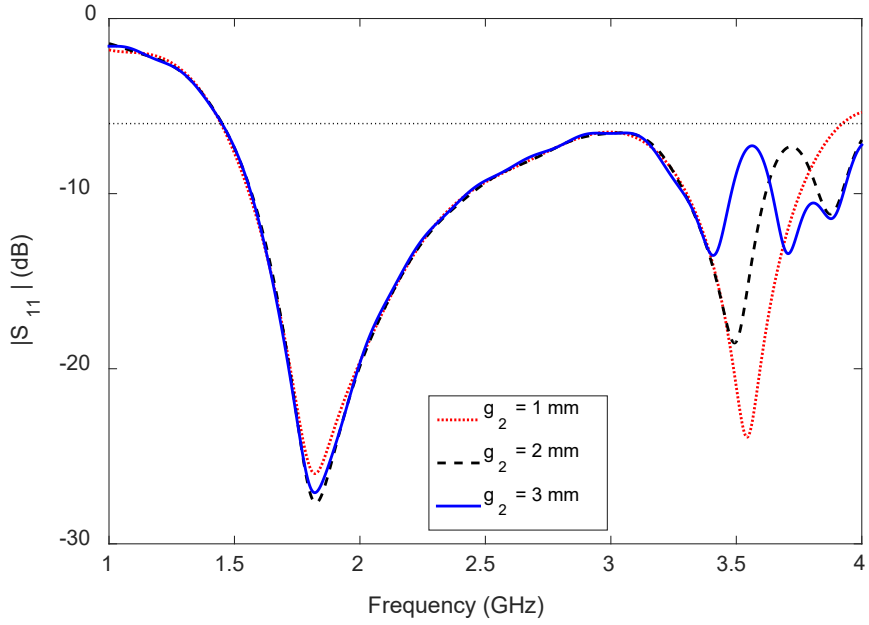

Figure 8.9: Influence of g_2 on operating bandwidth and impedance matching at high-LTE band of the wideband antenna (Ant-7).

Referring to Fig. 8.5, the lengths l_4 and l_5 affect both the mid and high bands. Now, the effect of the lengths of the elements QP (l_4) and OR (l_4) on the reflection coefficient of the antenna is analyzed. Fig. 8.10 shows the antenna reflection coefficient for $l_4 = 11$, 13 and 15 mm. For $l_4 = 11$ mm the lower frequency limit of the antenna exceeds the targeted value of 1427 MHz, meaning that the antenna does not cover the mid-LTE band completely while still covering the high-LTE band with a single resonant. On the other hand, for $l_4 = 15$ mm the wideband antenna becomes a dual band antenna with worse impedance matching than with $l_4 = 11$ mm at the upper frequency limit of the mid-LTE band as shown in Fig. 8.10. Change in the length l_4 means changing the length of the elements PQUR are on the left side of the middle element MNO that affects the lower and upper frequency limit of the mid-LTE band and the lower frequency limit of the high-LTE band. Note that the gap widths g_1, g_2 and the element STS control the upper frequency limit of the high-LTE band.

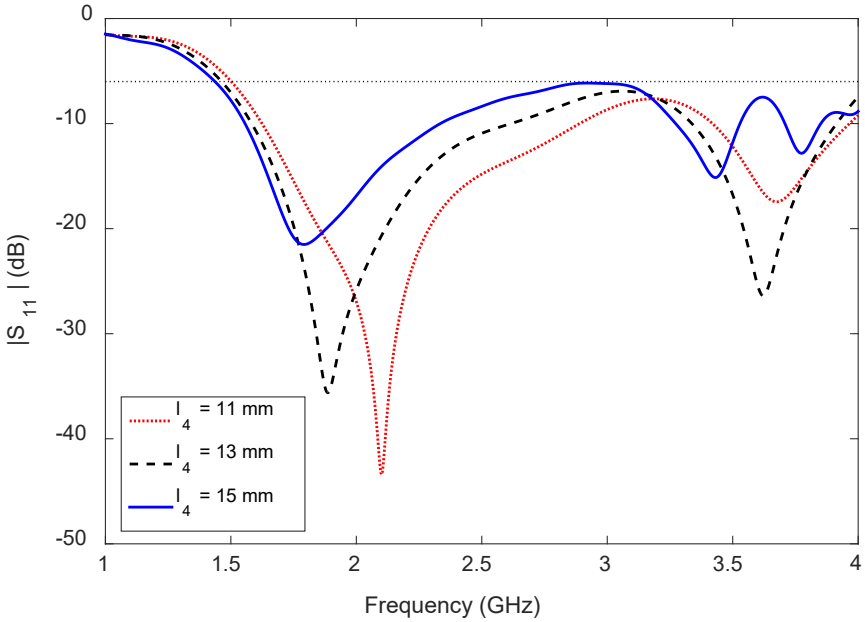

Figure 8.10: Influence of l_4 on operating bandwidth and impedance matching at mid and high bands of the wideband antenna (Ant-7).

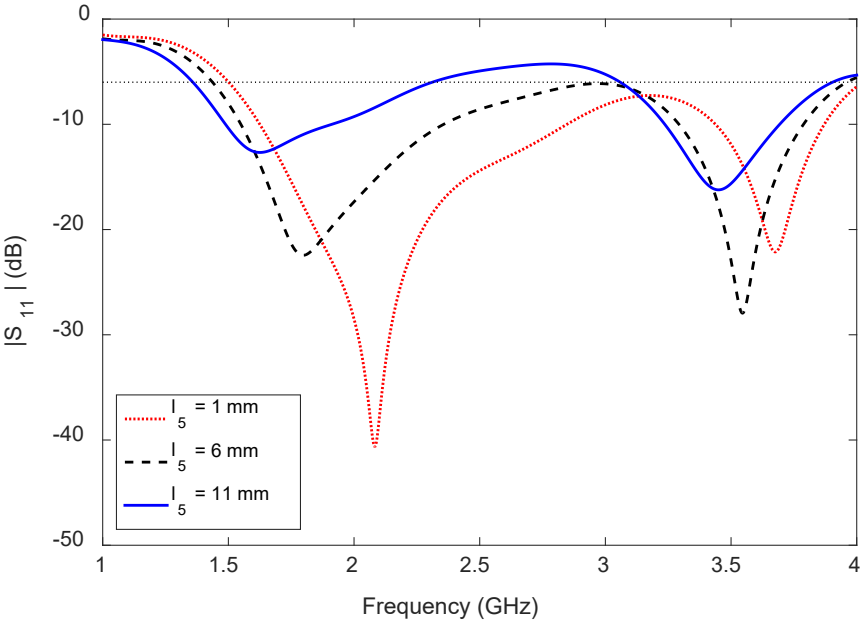

Figure 8.11: Influence of l_4 on operating bandwidth and impedance matching at mid and high bands of the wideband antenna (Ant-7).

Finally, the effect of the extended length of the vertical plate l_5 that in turn affects the impedance matching at both the bands are examined. Fig. 8.11 shows the reflection coefficient of the antenna for l_5 = 1, 6 and 11 mm. Though good impedance matching over the complete operating band of the antenna has been observed for l_5 = 1 mm, the lower frequency limit is away from the targeted value. With the increase of the lengths l_5 from 1 to 11 mm, the lower frequency limit of the mid-LTE band shifts from 1.45 to 1.35 GHz while worsening the antenna impedance matching within the band. Also, the -6 dB reflection coefficient bandwidth in the mid-LTE band decreases when l_5 changes from 1 to 11 mm, but the antenna covers the high-LTE band completely with either value of l_5. Note that the change of length of the vertical plate l_5 has a negligible effect on the upper frequency limit of the high-LTE band.

Therefore, the lengths l_4 and l_5 significantly control the lower and upper frequency limits of the mid-LTE band and the lower frequency limit of the high-LTE band. By controlling these two parameters, the antenna impedance bandwidth can be controlled. It is also possible to convert the antenna from dual band to wideband in order to cover 1.427-3.8 GHz. The values of the lengths l_4 and l_5 are carefully chosen to be 14 and 5 mm, respectively, in order to cover the mid (1.4 - 2.7 GHz) and high (3.3 - 3.8 GHz) bands completely.

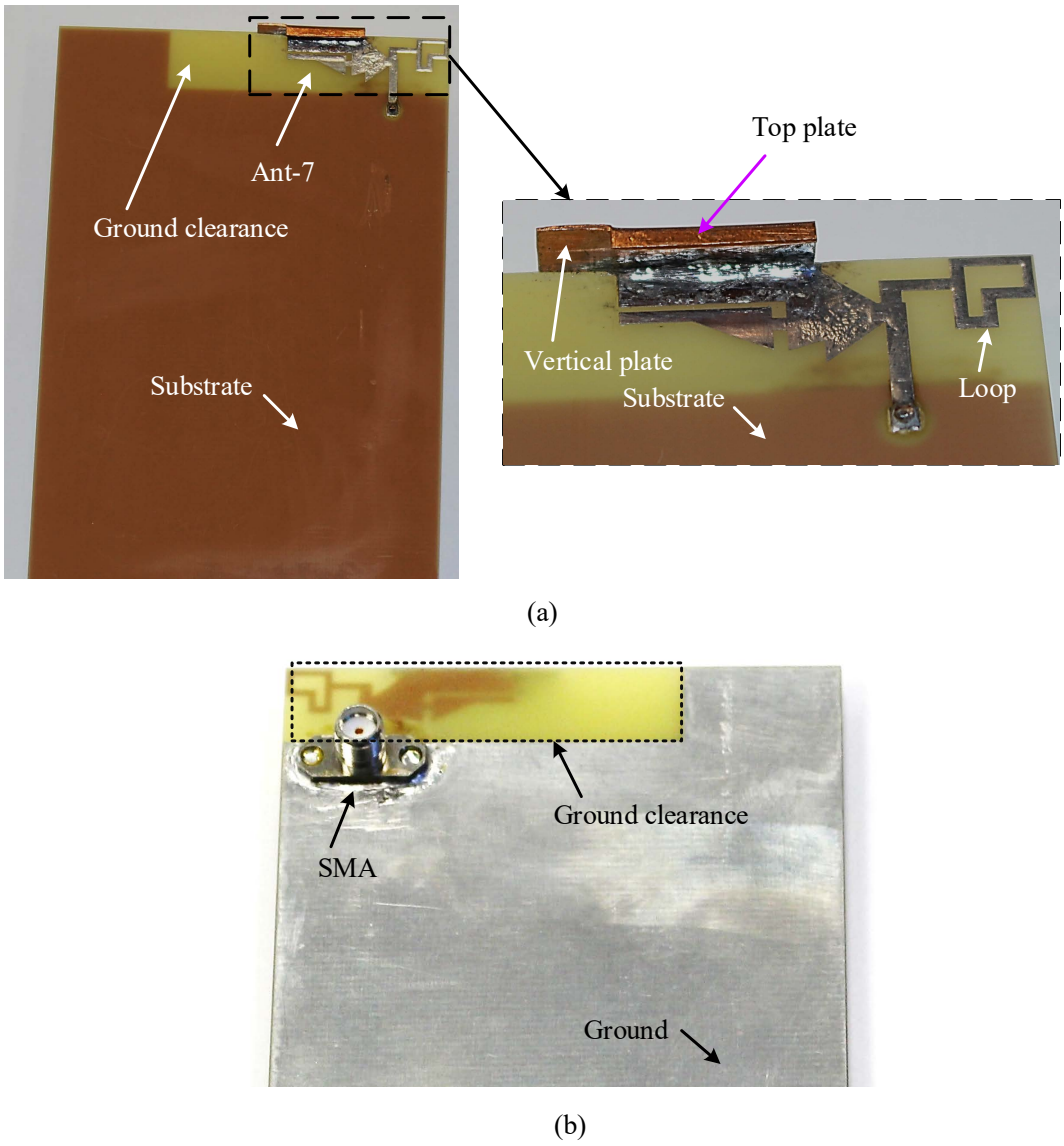

Figure 8.12: Fabricated wideband antenna (Ant-7): (a) top view of the antenna placed in a mobile device substrate (the antenna is shown in the inset), and (b) bottom view.

8.5 Measured and Predicted Results

This section presents the measured reflection coefficient, antenna efficiency, gain, and radiation patterns of the wideband antenna (Ant-7) compared with the predicted results.

The radiation performance of the fabricated antenna was measured using the NSI700S-50 near field range at the Australian Antenna Measurement Facility, CSIRO, Marsfield, Australia. Meanwhile the S-parameters were measured using an Agilent Network Analyzer PNA-X N5242A at Macquarie University, Australia. The top and bottom views of the prototype are shown in Fig. 8.12.

8.5.1 Reflection Coefficient

The measured reflection coefficient of the proposed wideband antenna (Ant-7) is shown in Fig. 8.13 together with the predicted results; an excellent agreement is observed between the measured and the predicted results. The reflection coefficient bandwidth of Ant-7 measured at -6 dB (VSWR < 3) is 2.63 GHz (1.37-4 GHz) which covers the 1.5 and 2.3 GHz LSA, 16 FDD LTE, 11 TDD LTE bands, UMTS, DCS/GSM1800, PCS/GSM1900, 2.4 GHz WLAN, and 3.3 GHz WiMAX bands. A slight change in the impedance matching at the upper frequency limit of the mid-LTE band is observed, which is probably due to the fabrication tolerance effect, especially for the soldering of the L-shaped vertical plate.

8.5.2 Radiation Performance

The measured efficiency together with the predicted results for Ant-7 are shown in Fig. 8.14. The results are presented only within the mid (1.42-2.69 GHz) and high (3.3-3.8 GHz) bands. A good agreement between the measured and predicted results is observed. The maximum antenna efficiency in the mid and high bands is 96% and 94%, respectively, and the minimum antenna efficiency is 66% and 79%, respectively. Therefore, the antenna efficiency is always higher than 66% in both the mid and high bands, which makes the antenna suitable for mobile device applications.

The measured gain together with the predicted results for Ant-7 are illustrated in Fig. 8.15. Similar to the efficiency, the measured and predicted gains are presented only

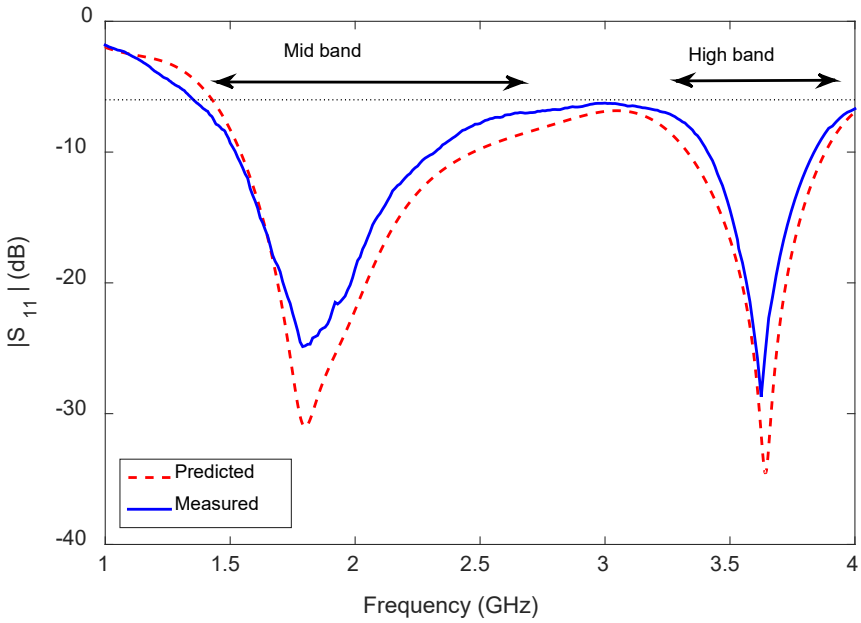

Figure 8.13: Measured and predicted reflection coefficient of the wideband antenna (Ant-7) for hand-held devices.

within the mid (1.42-2.69 GHz) and high (3.3-3.8 GHz) bands. The measured and predicted gains are very close to each other. The measured maximum gains in the mid and high-LTE bands are 2.9 and 5.6 dBi, respectively, while the minimum gains are 1.6 and 4.2 dBi, respectively. Therefore, the gain variations for Ant-7 within the mid and high bands are 1.3 and 1.4 dB, respectively, meaning that the antenna has only a moderate gain variation within the bands.

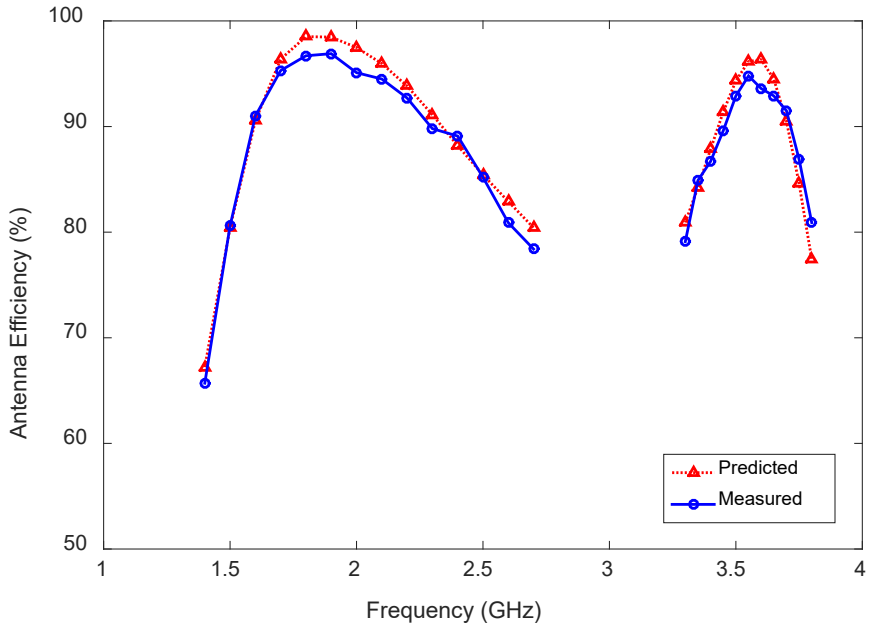

Figure 8.14: Measured and predicted efficiency of the wideband antenna (Ant-7).

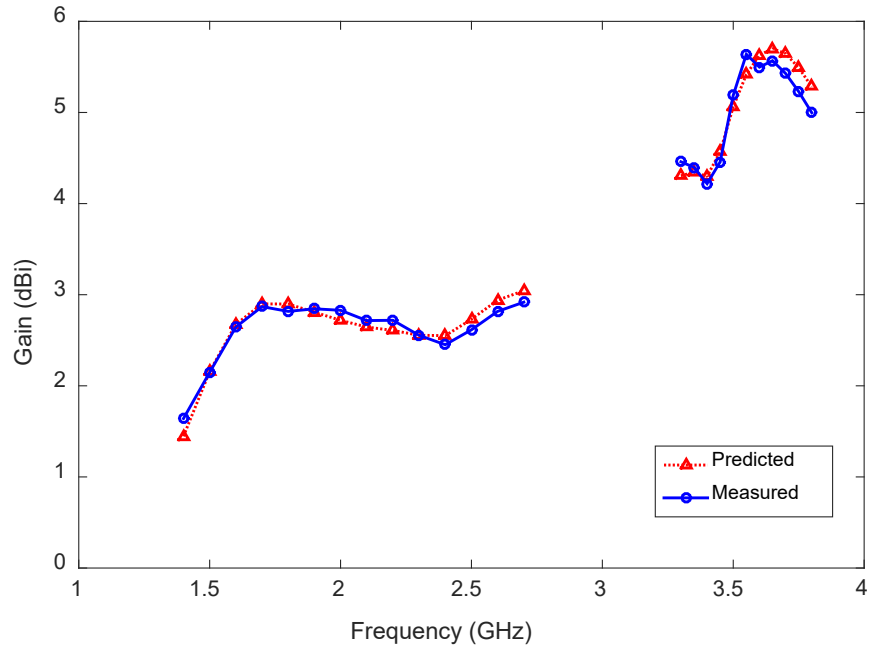

Figure 8.15: Measured and predicted gain of the wideband antenna (Ant-7).

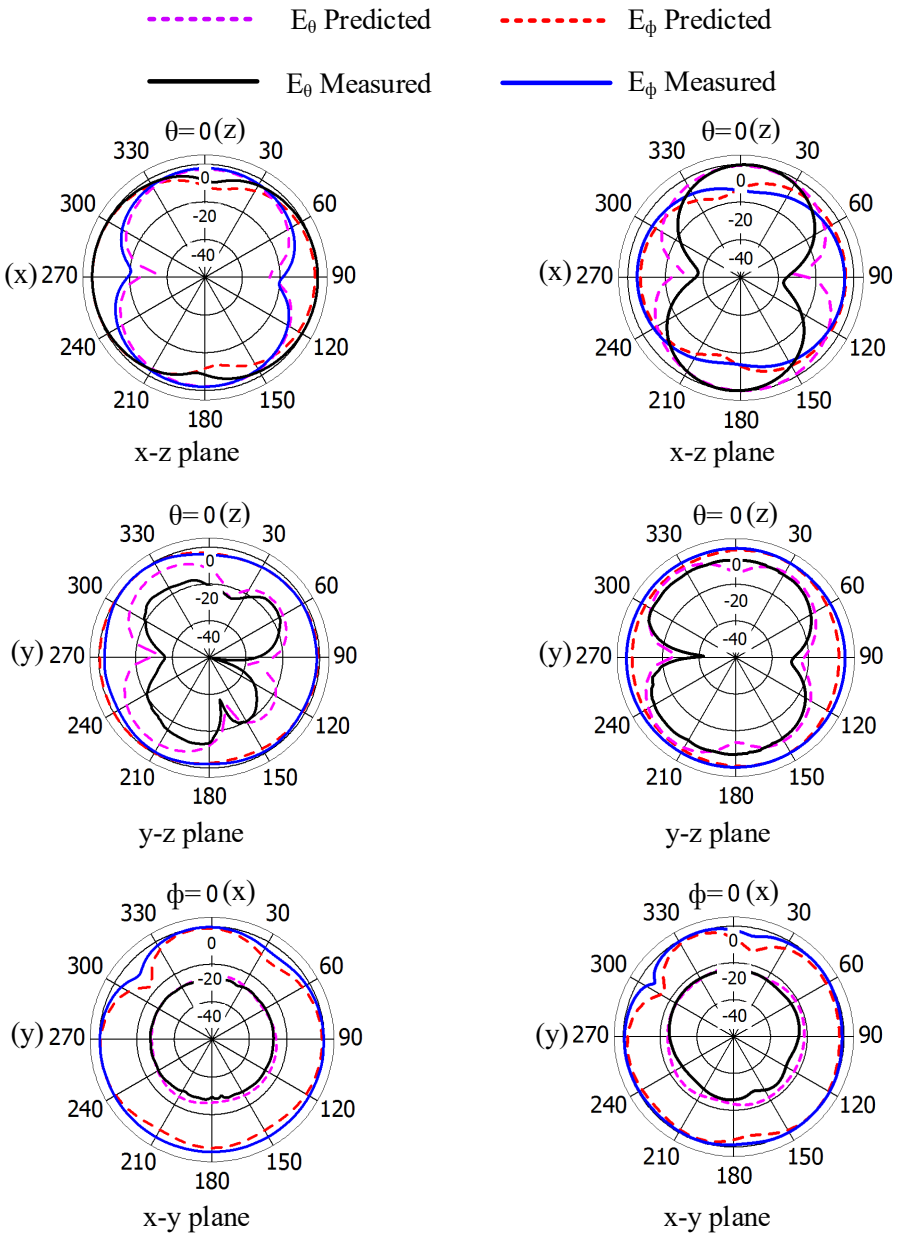

Figure 8.16: Measured and predicted normalized radiation patterns for the proposed antenna (Ant-7) at (a) 1.8, and (b) 2.6 GHz.

The measured E_θ and E_ϕ radiation patterns for the mid-LTE band at 1.8 and 2.6 GHz are shown in Fig. 8.16. Fig. 8.17 portrays the high-LTE band at 3.6 GHz. The predicted

results are compared with the measured results at all presented frequencies. Both results are presented for the three principal planes x-y (parallel to the antenna ground plane), x-z, and y-z. The radiation patterns in each plane are normalized with the maximum value in the corresponding plane. Again there is a good agreement between the predicted and measured results.

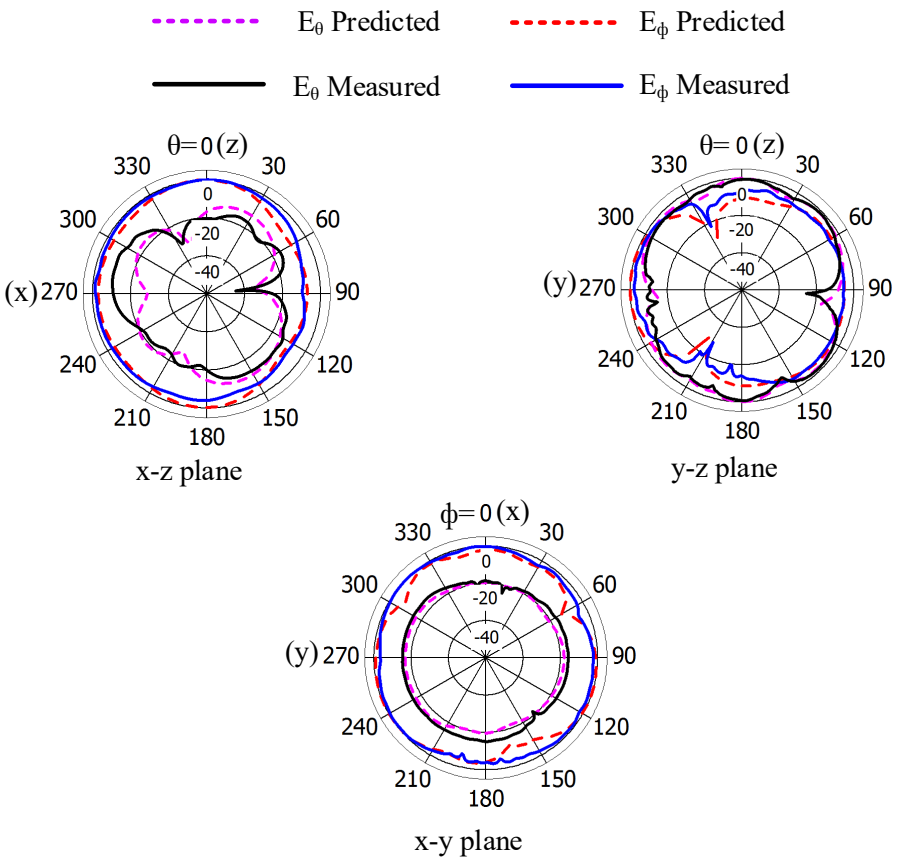

Figure 8.17: Measured and predicted normalized radiation patterns for the proposed antenna (Ant-7) at 3.6 GHz.

The radiation is almost omnidirectional in the x-y and y-z planes and no nulls are observed at the mid-LTE band. In addition, the E_θ and E_ϕ radiation patterns are comparable in the x-z plane at mid-LTE band. Note that comparable radiation pattern is suitable for the complex propagation environment in practical applications [73, 137, 138].

Furthermore, the measured and predicted E_θ radiation patterns are almost omnidirectional in the x-z and x-y planes at the high-LTE band (see Fig. 8.16). In both planes the E_ϕ component is always less than the E_θ component. The E_θ and E_ϕ radiation patterns are comparable in the y-z plane at the high-LTE band. Similar to the mid-LTE band, no null has been observed in the high-LTE band radiation patterns.

8.6 Compatibility with Different-Sized Hand-Held Devices

Like the Ant-6 compatibility analysis presented in Chapter 7, this section presents the simulated reflection coefficients for the wideband antenna (Ant-7) while fitted into different sized mobile phones, and tablet computers. Selected devices with their typical dimensions considered for the proposed antennas compatibility validation are listed in Table 8.2. In each device, Ant-7 is placed at the top-right corner of the selected mobile device substrate. In this study the antenna's parameters are the same as presented in Table 8.1. Also the size of the ground clearance remains the same as previously stated in the design section.

Table 8.2: Substrate dimensions of commonly used hand-held mobile devices and tablet computers for the suitability test of the wideband antenna (Ant-7).

Device Name	Length (mm)	Width (mm)
Smart Phone (SP)	120	70
Smart Phone Plus	160	80
Mini Tablet Computer	200	135
Tablet Computer (TC)	240	170

From the simulated reflection coefficient shown in Fig. 8.18, the higher and lower edge frequencies are slightly affected in the mid-LTE band when the mobile device's size changes. For three types of devices - smart phone plus, mini tablet computer, and tablet computer - the single wideband antenna (Ant-7) becomes a dual-band antenna. The lower frequency limit of the antenna can shift towards a lower frequency by increasing the width w_t of the top plate. The antenna input impedance matching at the frequency of minimum reflection coefficient is affected by the size of the substrate, and very good impedance matching is observed for smart phone plus. As well, a negligible shift in the frequency of minimum reflection coefficient is observed in the mid and high bands for different-sized devices, but the expected -6 dB reflection coefficient bandwidths are always maintained. Nonetheless the upper frequency limit in the high-LTE band is shifted towards the frequency of minimum reflection coefficient with the increase in the substrate size, and the lower frequency limit remains almost unaffected.

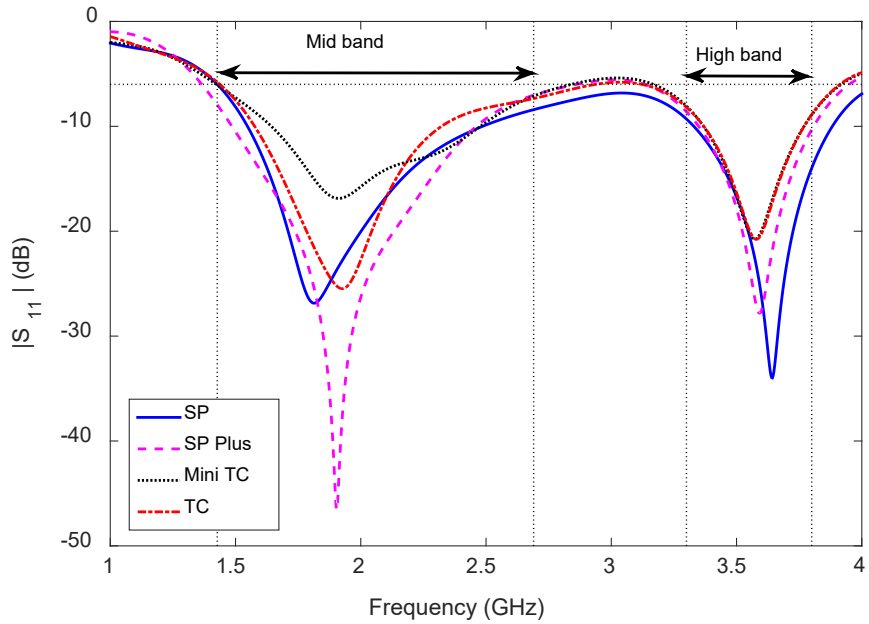

Figure 8.18: Effect of the device sizes on the reflection coefficient of the wideband antenna (Ant-7). Here, SP: smart phone, and TC: tablet computer.

8.7 Comparison between Antennas

The properties of the previously presented dual-band antenna (Chapter 7) and the wideband antenna (Ant-7) presented in this chapter are summarized in Table 8.3. The efficiency of Ant-7 is superior to Ant-6 in both the mid-LTE and high-LTE bands. The gain variation for Ant-7 is 1.3 and 1.4 dB within the mid-LTE and high-LTE bands, respectively, whereas for Ant-6 the variation is 2 and 1.9 dB, respectively. The radiation patterns in the mid-LTE band are omnidirectional for both antennas. In the high-LTE band Ant-7 has omnidirectional radiation patterns but two nulls have been observed of the Ant-6 radiation patterns in the x-y plane.

Table 8.3: Comparing the performance between the proposed dual-band (Ant-6 in Chapter 7) and wideband (Ant-7 in this chapter) antennas.

Parameter	Ant-6	Ant-7
Physical Area (mm^2)	585	510
Bandwidth (GHz)	1.39-2.84, 3.27-3.97	1.37-4
Efficiency (%)	62-90(M), 66-88(H)*	66-96(M), 79-94(H)
Gain (dBi)	1.4-3.4(M), 4.2-6.1(H)	1.6-2.9(M), 4.2-5.6(H)
Nulls in Rad. Pat.	Yes	No

*Here M and H stand for the mid-LTE and high-LTE bands, respectively.

A comparison between the prototyped antenna (Ant-7) and reference antennas is given in Table 8.4 in terms of the null in the radiation patterns and coverage achieved for the LSA and mid-LTE bands. The comparison in Table 8.4 reveals that the proposed antenna covers both the LSA bands and whole mid-LTE band without null in the radiation patterns.

Table 8.4: Comparing the performance of the reference LTE/WWAN mobile device antennas together with the proposed antenna (Ant-7).

Ref.	Cover Both LSA Bands	Cover Mid Frequency Range*	Null Exist in Radiation Patterns
[139]	No	No	Yes
[89]	No	No	Yes
[67]	No	No	Yes
[138]	No	No	Yes
[140]	No	No	Yes
[141]	No	No	Yes
[137]	No	No	Yes
[75]	No	No	Yes
[73]	No	No	Yes
[62]	No	No	Yes
[70]	No	No	Yes
Ant-7	Yes	Yes	No

*Mid frequency range (1427-2690 MHz) covers mid-LTE, GSM1800, GSM1900, DCS, PCS, WLAN (2.4 GHz), UMTS, and WWAN bands.

Area = length × width.

8.8 Summary

This chapter proposed a novel wideband antenna (Ant-7) for mobile devices. The antenna is composed of a planar structure loaded with an L-shaped vertical plate. Ant-7 is 13% smaller than the dual-band antenna (Ant-6 presented in Chapter 7). The working prin-

ciples of the antenna were described using a four-steps evolution and the surface current distributions. The parameters affecting the antenna impedance matching and bandwidth were identified by analyzing the reflection coefficient behavior. The proposed antenna was prototyped and measured. The measured -6 dB reflection coefficient bandwidth of Ant-7 is 2.63 GHz (1.37-4 GHz), which covers both the LSA bands, mid-LTE, high-LTE, GSM1800, GSM1900, UMTS, 2.4 GHz WLAN, and 3.3 GHz WiMAX bands. The gain variation of Ant-7 was found to be moderate within the mid-LTE and high-LTE bands; the variations are 1.3 and 1.4 dB, respectively. The antenna has nearly omnidirectional radiation patterns in the above mentioned bands and no null exist in the antenna's radiation patterns. The antenna's suitability for different-sized mobile devices was verified through an experiment involving simulation. Finally, the proposed antenna was compared with reference antennas in order to justify its suitability for practical application.

The antenna presented in this chapter cover the LSA, mid-LTE and high-LTe bands without null in the radiation patterns. In the next chapter an antenna will be developed for the low-LTE band without null in the radiation patterns.

Chapter 9

Antenna for Low-LTE Band

9.1 Introduction

In this chapter, an inverted-L-feed capacitive-coupled inverted-L antenna with high efficiency is developed without using an input impedance matching circuit. The aim of this design is to cover the low-LTE band (698-960 MHz) and having no null in the radiation patterns. The antenna is suitable for reconfigurable operation and the passive reconfiguration technique is investigated for the antenna structure. The aim here is to select a specific narrow frequency range within the greater low-LTE band, enhancing the antenna's potential for emerging spectrum reallocation or LSA operation in forthcoming 5G systems. The proposed antenna was prototyped and tested experimentally.

This chapter is structured as follows. Section 9.2 presents the configuration of the antenna. Section 9.3 outlines the design procedure and working modes of the antenna. A parametric study is presented in Section 9.4 to understand the working principle of the antenna. Effects of a vertical plate on antenna impedance matching and antenna efficiency are detailed in Section 9.5. The passive reconfiguration technique for the proposed antenna is investigated in Section 9.6. The simulation results are verified through measurements

in Section 9.7 followed by a summary of the main points covered here in Section 9.8.

9.2 Antenna Configuration

Perspective views of the antenna and its detailed geometry are shown in Figs. 9.1 (a) and 9.1 (b), respectively. For better presentation the vertical plate is unfolded along the -y axis. The antenna is placed at the bottom-left corner of a mobile phone substrate of dimensions 120 mm × 70 mm. The placement of the antenna in a mobile phone substrate is shown in Fig. 9.2.

The substrate considered for the antenna design is the FR-4 with relative permittivity ϵ_r of 4.3, loss tangent $\tan\delta$ of 0.025, and a thickness of 0.8 mm. The ground plane's size is equal to that of the substrate. However, a portion of the ground with length and width, measured from the corner point D, are 40 mm and 10 mm, respectively, shown in Fig. 9.2 (b), is removed. The overall size of the antenna is 34 mm × 16.25 mm × 4 mm or $0.08\lambda_0 \times 0.04\lambda_0 \times 0.01\lambda_0$, where λ_0 is the free-space wavelength at the lower operating frequency of 684 MHz. The details concerning the antenna are shown in Fig. 9.1 (b). For better visualization the vertical plate is unfolded along the -y-axis. The optimized design parameters (using parameter analyses in CST) for the antenna are listed in Table 9.1.

Table 9.1: Design parameters of the inverted-L-feed capacitive-coupled inverted-L antenna for spectrum reallocation in the low-LTE band. All dimensions are in millimeters.

$w_1 = 2$	$w_2 = 1.5$	$w_3 = 5$	$w_4 = 2$	$w_5 = 1$
$w_6 = 0.5$	$g_1 = 0.5$	$g_2 = 0.5$	$g_3 = 0.6$	$l_1 = 6.25$
$l_2 = 11.25$	$l_3 = 13$	$l_4 = 5$	$l_5 = 15$	$l_6 = 4.25$
$l_7 = 9.5$	$l_8 = 7.75$	$h = 4$	$L_1 = 34$	$W_1 = 16.25$

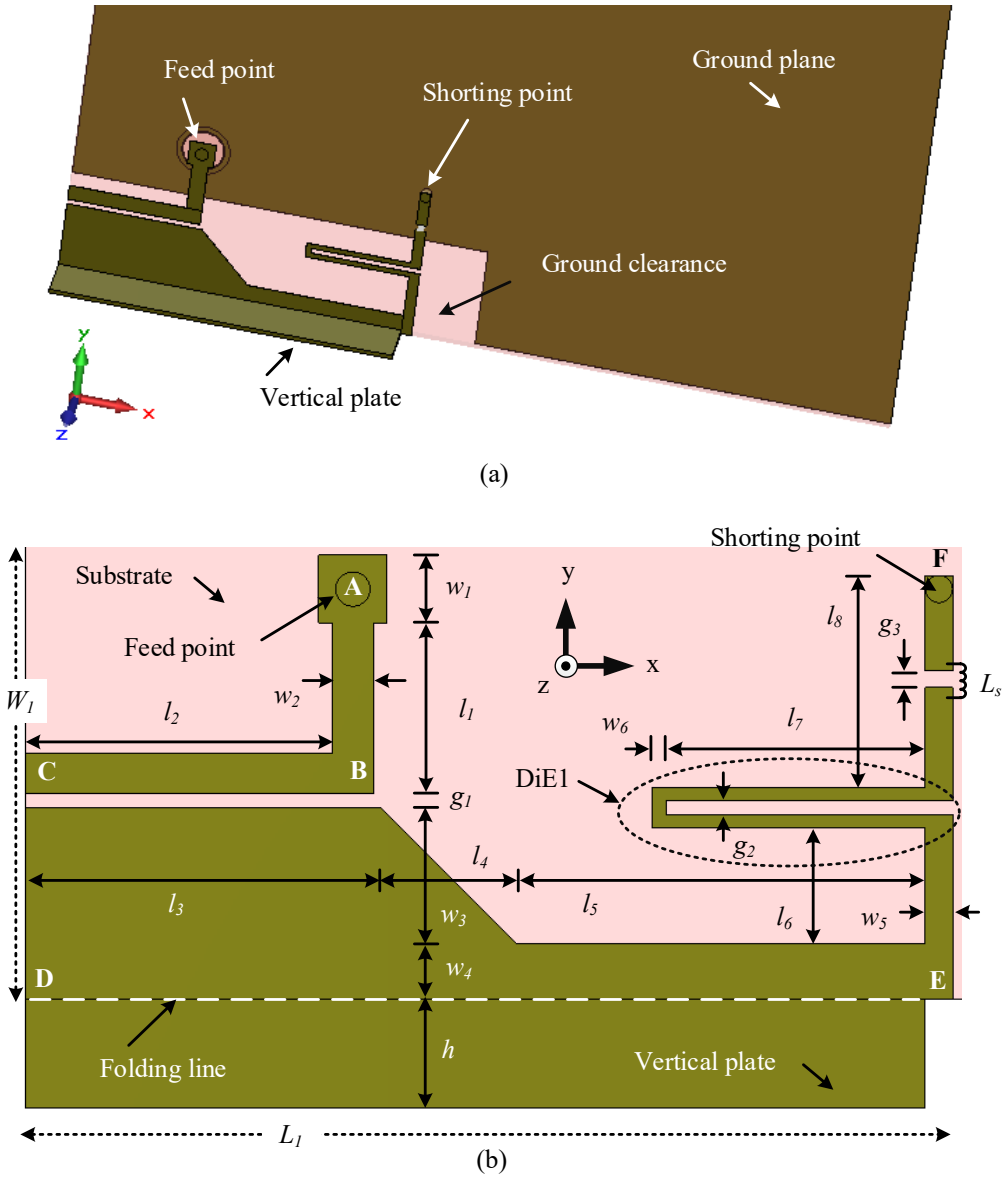

Figure 9.1: Configuration of the inverted-L-feed capacitive-coupled inverted-L antenna: (a) perspective view, and (b) detailed geometry with vertical plate unfolded along -y axis (not to scale).

The proposed antenna is consists of an inverted-L element ABC, and a capacitively-fed inverted-L element DEF, which is connected to the system ground plane with a tuning strip EF, which contains a distributed element ($DiE1$), an operating band selecting induc-

tor (L_s), and a via. In Fig. 9.1 (b), 'A' and 'F' are the feed and via locations, respectively. To increase the antenna's efficiency, a vertically bent plate, perpendicular to the plane of the capacitively coupled inverted-L antenna, is placed at the edge DE as shown in Fig. 9.1. The antenna is fed from the bottom using a SMA connector. A circular area with a radius of 2 mm is etched off from the ground plane to ensure isolation between the center pin and the outer conductor of the SMA connector.

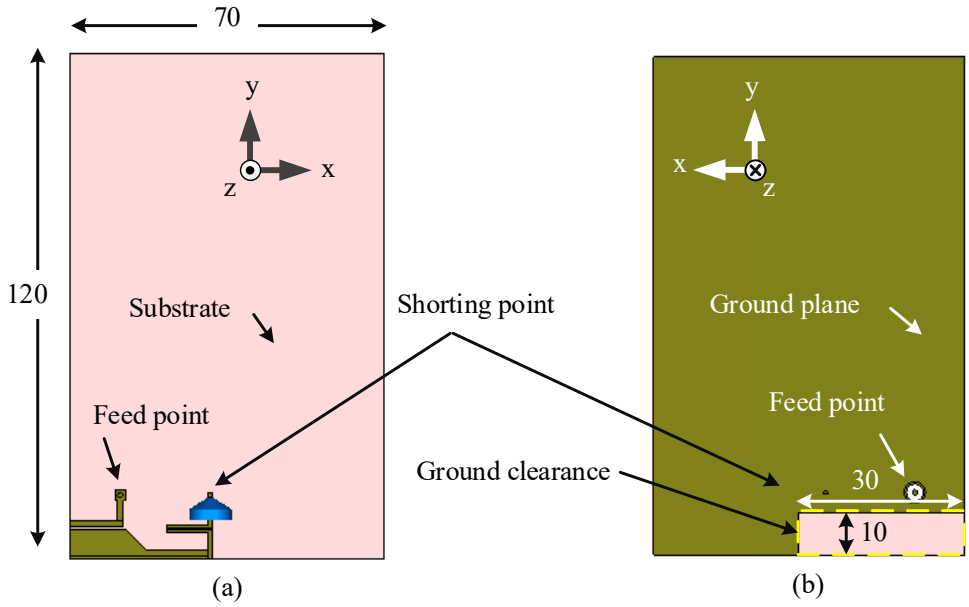

Figure 9.2: Positioning of the inverted-L-feed capacitive-coupled inverted-L antenna in a mobile phone substrate: (a) top view, and (b) bottom view.

9.3 Design Procedure and Working Principle

The design procedure and working principle of the proposed antenna are presented in this section with the help of the antenna geometry shown in Fig. 9.1 and antenna parameters listed in Table 9.1. The antenna is designed based on the fundamental equations discussed in Section 2.3. The proposed antenna geometry evolution in three major steps is shown in Fig. 9.3 and the resulting reflection coefficients are presented in Fig. 9.4.

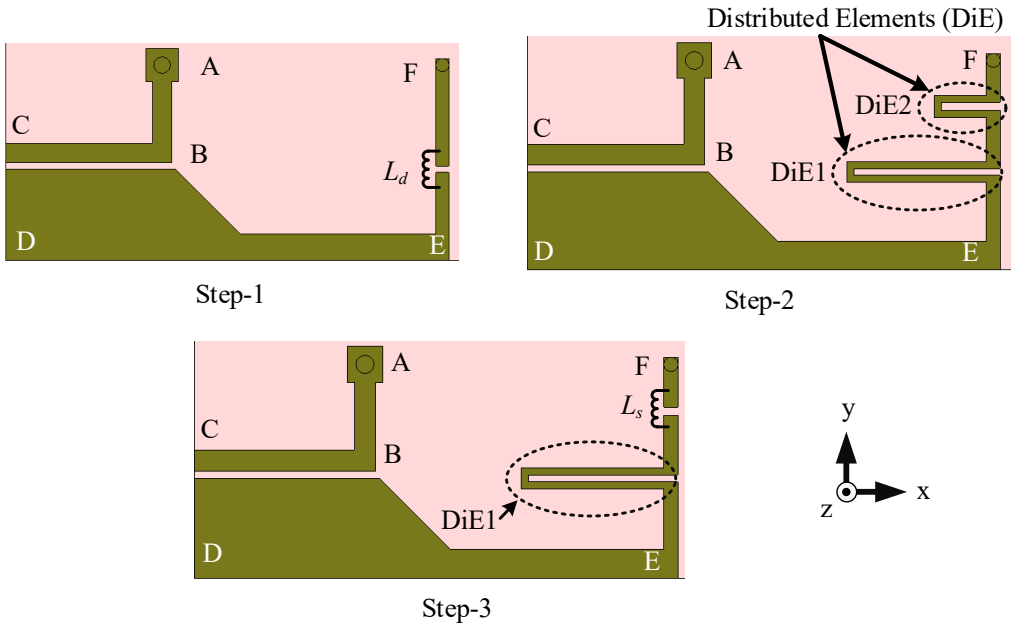

Figure 9.3: The geometrical evolution of the inverted-L-feed capacitive-coupled inverted-L antenna for low-LTE band. Here, $L_d = 6$ nH and $L_s = 1$ nH

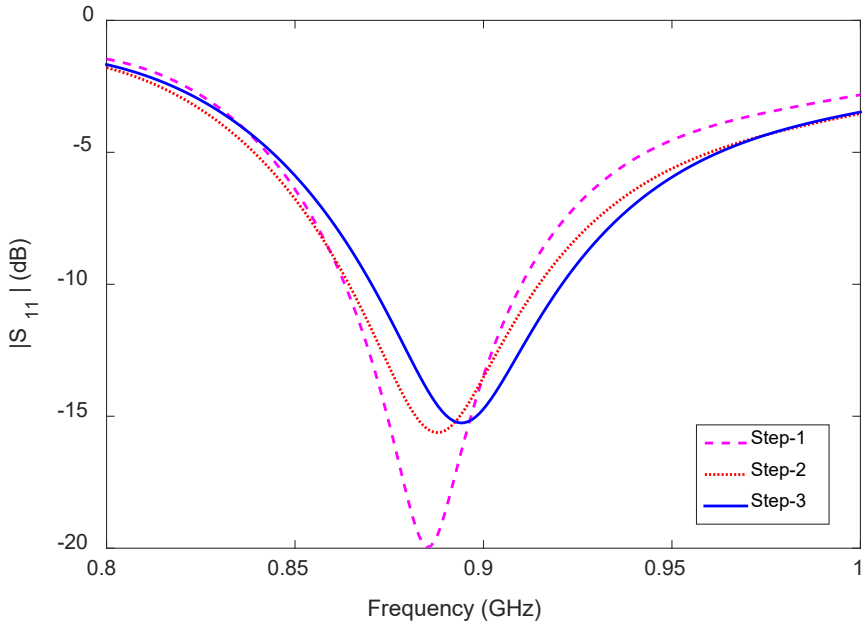

Figure 9.4: Predicted reflection coefficients for the design steps of inverted-L-feed capacitive-coupled inverted-L antenna.

The design started with the planar inverted-L antenna DEF which is capacitively fed by the L-shaped element ABC displayed in Fig. 9.3 (Step-1). Here, the antenna is grounded by a plated-through hole of radius 0.5 mm at point F, and the width of the shorting strip EF is 1 mm. A lumped inductor L_d is employed for tuning the operating band. The antenna resonates at 0.89 GHz with an operating bandwidth of 90 MHz (0.86-0.95 GHz) with respect to the -6 dB reference level, shown in Fig. 9.4(Step-1 curve) for the chip inductor value $L_d = 5$ nH. The overall effective length of the antenna is approximately 84 mm which is equal to the quarter wavelength at 0.89 GHz, indicating that the antenna is operating in the quarter-wavelength mode.

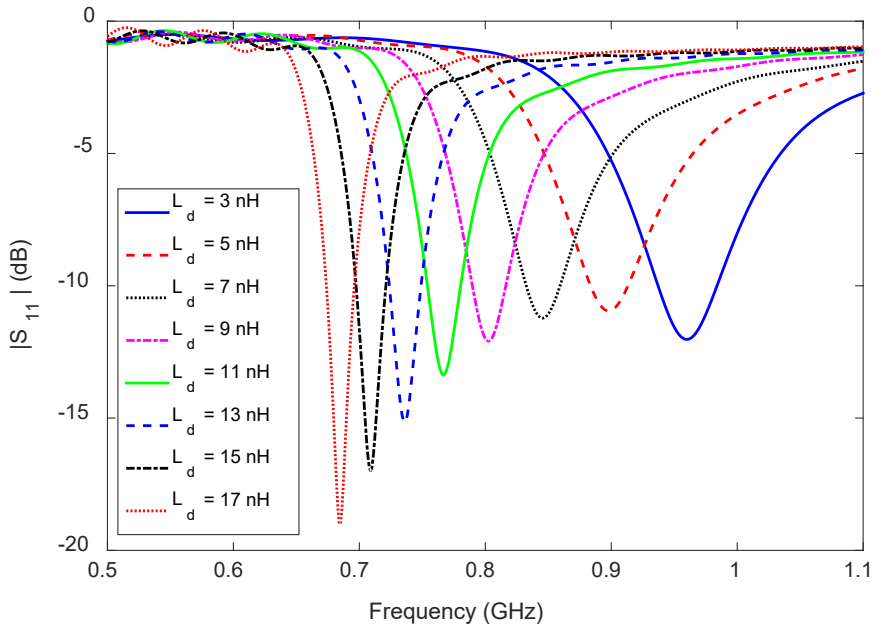

Figure 9.5: Effect of inductor L_d on the frequency of minimum reflection coefficient for the inverted-L-feed capacitive-coupled inverted-L antenna.

To cover the low-LTE band (698-960 MHz), a variable inductor L_d is required instead of a fixed inductor to enable tuning a narrow frequency range within the greater band. The change in the frequency of minimum reflection coefficient with the change of the selected inductor L_d values is shown in Fig. 9.5. The frequency of minimum reflection coefficient

decreases and the operating band becomes narrower with the increase in inductor L_d values. The range of the inductor required to cover the low-LTE band is 14 nH (from 3 nH to 17 nH), which is quite large compared to the chip inductor range required for the low-LTE band coverage shown in [138].

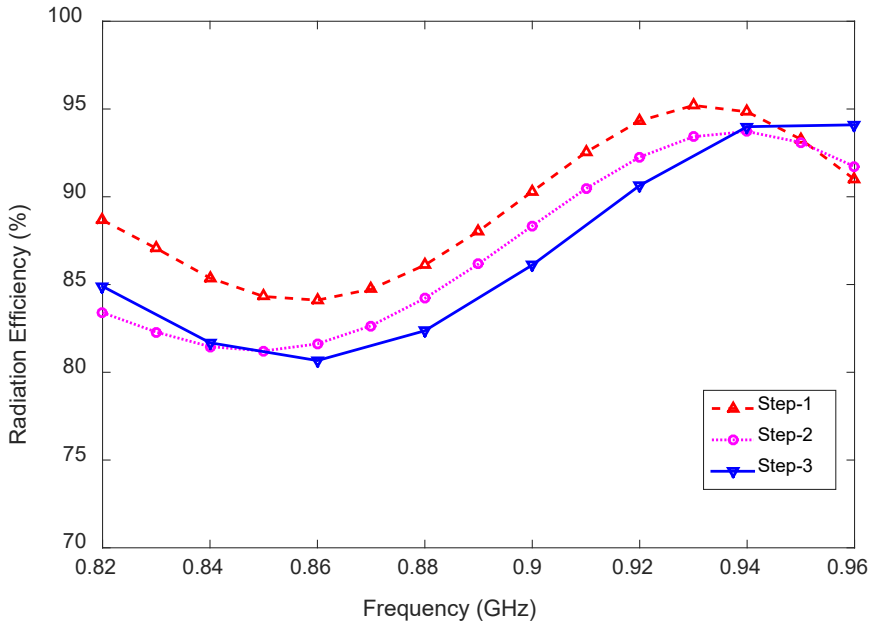

Figure 9.6: Radiation efficiency in the GSM850 and GSM900 bands corresponding to the three-steps of evolution of the inverted-L-feed capacitive-coupled inverted-L antenna.

In order to reduce the range of the values of switching inductor and to widen the reflection coefficient bandwidth of the antenna at the same time, the chip inductor L_d is replaced by the equivalent distributed elements, portrayed in Fig. 9.3 (Step-2). The change in the antenna radiation efficiency within the GSM850 and GSM900 bands when distributed elements replaced L_d is shown in Fig. 9.6. In the case of Step-2, two distributed elements $DiE1$ and $DiE2$ are considered: $DiE1$ for bandwidth enhancement; and $DiE2$ for future switching capabilities.

The geometrical structure of the distributed element is shown in Fig. 9.3 (Step-2). The overall length of the U-shaped distributed elements $DiE1$ and $DiE2$ are 20.5 and

8 mm, respectively. The width of the strip is 0.5 mm and the gap between the two arms of a distributed element is $g_2 = 0.5$ mm. The equivalent inductances of the distributed elements $DiE1$ and $DiE2$ are about 5 and 1 nH, respectively (verified through simulation using lumped elements in CST). After replacing L_d by an equivalent distributed element, the radiation efficiency drops by around 3% within the -6 dB reflection bandwidth but the radiation efficiency drops by approximately 6% at lower frequency limit as shown in Fig. 9.6 (Step-2 curve). However, the -6 dB reflection coefficient bandwidth widened by 15 MHz as indicated in Fig. 9.4 (Step-2 curve).

Finally, the distributed element $DiE2$ is replaced by a lumped inductor $L_s = 1$ nH and slight effect on the antenna reflection coefficient is observed with better antenna input impedance matching as shown in Fig. 9.4 (Step-3 curve). Yet the radiation efficiency drops further by around 3% within the -6 dB reflection coefficient bandwidth and increases by 3% at lower and upper frequency limit as shown in Fig. 9.6 (Step-3 curve).

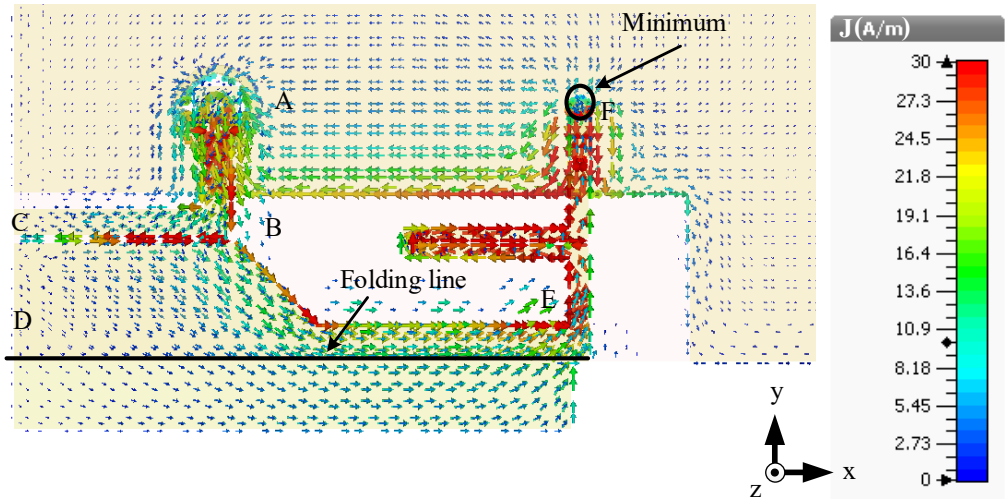

Figure 9.7: Predicted surface current distribution for the inverted-L-feed capacitive-coupled inverted-L antenna at 0.89 GHz.

The surface current distribution for the proposed antenna is studied to understand the working modes of the antenna. Fig. 9.7 shows the surface current distribution at

the frequency of minimum reflection coefficient 0.89 GHz for $L_s = 1$ nH. For better presentation the vertical plate is unfolded along the -y axis. The surface current at its maximum from feed point A to point F, while the minimum is observed at the location of via (F). This means the antenna is operating in quarter-wavelength mode.

9.4 Parameter Analysis

To further clarify the working principles of the antenna, two key parameters are analyzed. Firstly, the effect of the distributed coupling capacitor or gap g_1 on the frequency of minimum reflection coefficient is investigated and the obtained result is depicted in Fig. 9.8. Variation of the gap g_1 means affecting the distributed capacitance value, and this distributed capacitor controls the surface current distribution on the capacitively coupled inverted-L element DEF of the proposed antenna. The resonant frequencies of the antenna are 817 MHz and 937 MHz when the gap g_1 is 0.3 and 0.7 mm, respectively. Also, the frequency of minimum reflection coefficient shifts towards lower frequency as the gap decreases. The antenna's resonant mode is canceled when both antennas are conductively coupled, i.e. without any gap ($g_1 = 0$). In this study, the gap g_1 of the distributed capacitor is selected to be 0.5 mm for better impedance matching.

Secondly, the effects of the distributed inductive element length $2l_7+2w_6+g_2$ (Fig. 9.1) on the frequency of minimum reflection coefficient are studied. The effects of gap g_2 and length l_7 of the distributed element on the frequency of minimum reflection coefficient are shown in Figs. 9.8 and 9.9; here g_2 and l_7 are varied from 0.3 to 0.8, and 3 to 17 mm, respectively. As the gap g_2 or length l_7 increases, the equivalent distributed inductance increases. A higher value of inductance shifts the antenna's resonance to lower frequencies as shown in Fig. 9.9. A similar effect was investigated using a lumped inductor L_d and the results are presented in Fig. 9.5. It is clear that the antenna resonates at 0.89 GHz

when the values of g_1, g_2, and l_7 are 0.5, 0.5, and 10 mm, respectively.

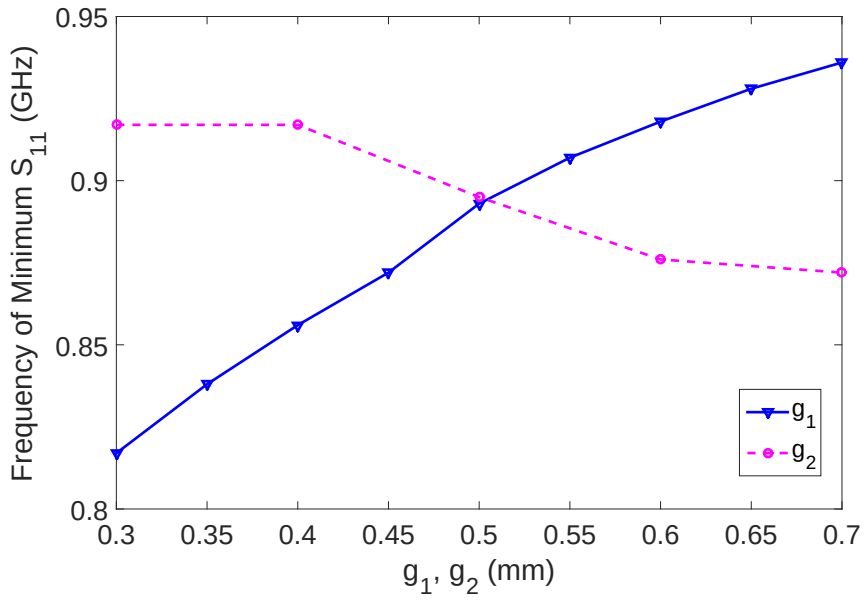

Figure 9.8: Simulated frequency of minimum reflection coefficient as a function of the gap width g_1, g_2 while other geometrical parameters are the same as those in Table 9.1.

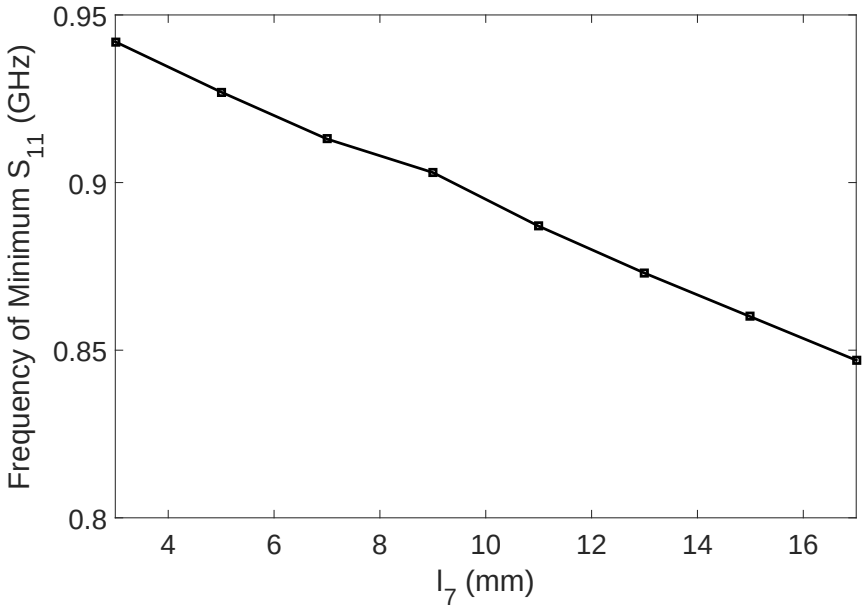

Figure 9.9: Simulated frequency of minimum reflection coefficient as a function of the length l_7 while other geometrical parameters are the same as those in Table 9.1.

9.5 Effects of the Vertical Plate

A vertical plate with dimensions $(l_3 + l_4 + l_5) \times h$ is added to the edge DE in order to improve the antenna performance. The effects of this vertical plate on the antenna reflection coefficient is shown in Fig. 9.10. From the obtained predicted results, 41 MHz reflection coefficient bandwidth improvement is achieved with better antenna input impedance matching. The reflection coefficient bandwidths of the antenna with respect to the -6 dB level with and without the vertical plate, are 142 MHz (from 828-970 MHz), and 101 MHz (from 850-951 MHz), respectively.

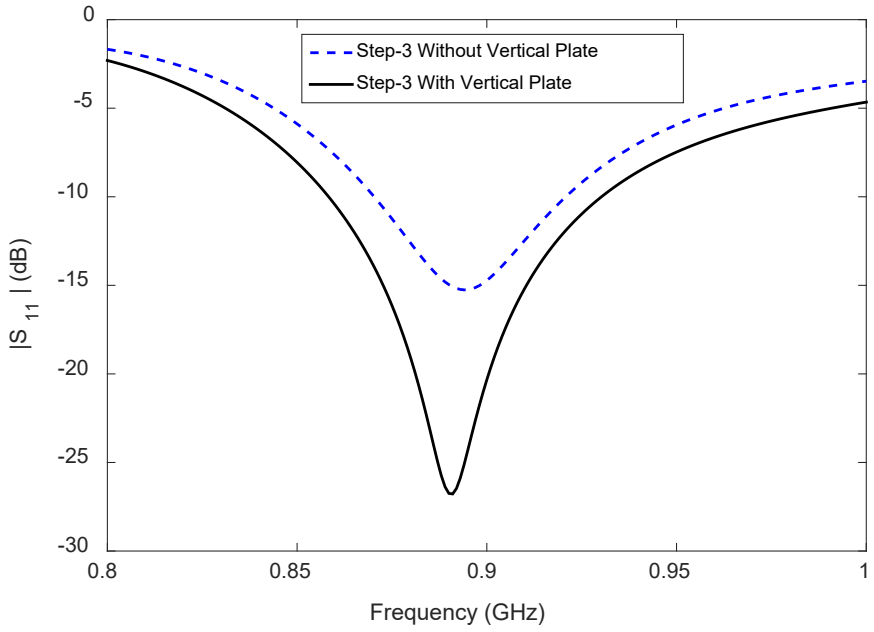

Figure 9.10: Influence of the vertical plate on the antenna reflection coefficient bandwidth and impedance matching.

Effects of the vertical plate on antenna radiation efficiency within the GSM850 and GSM900 bands are shown in Fig. 9.11. Antenna radiation efficiency varies between 80% and 94% within the GSM850 and GSM900 bands when no vertical plate is added to the antenna. The radiation efficiency, however, varies between 86% and 96% within the

GSM850 and GSM900 bands. This means approximately 6% improvement in the radiation efficiency within the -6 dB reflection coefficient bandwidth of the antenna is observed.

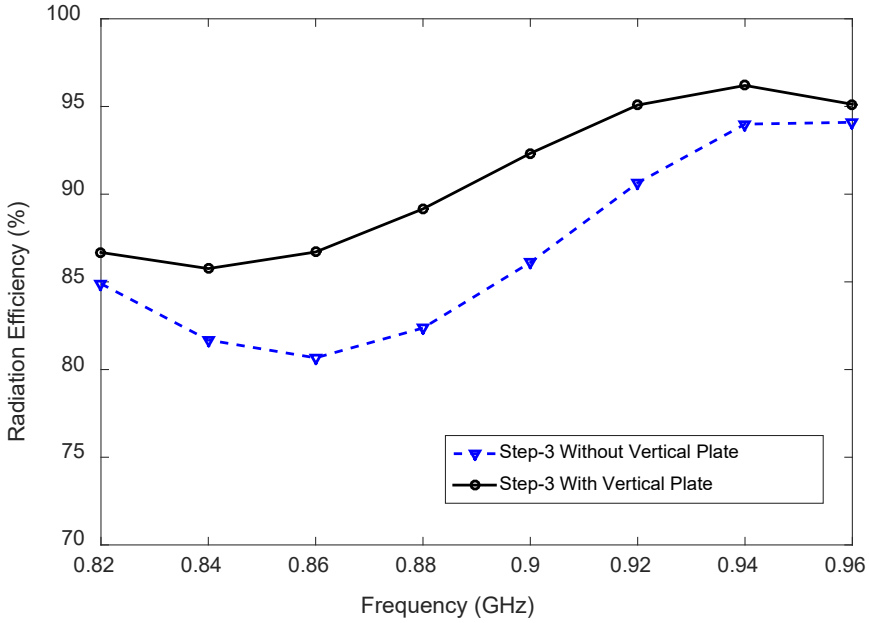

Figure 9.11: Influence of the vertical plate on the radiation efficiency within the GSM850 and GSM900 bands.

9.6 Tuning Bands

It is possible to convert the designed antenna into a passive reconfigurable antenna by replacing the fixed inductor L_s with a variable inductor in order to select a specific sub-operating band within the greater low-LTE band. This can be done by selecting an appropriate inductor value. Using a switchable inductor bank the passive reconfigurable operation to select bands has been investigated in [138, 142]. This section presents the antenna performances for selected values of chip inductor L_s.

9.6.1 Reflection Coefficient

Without distributed element $DiE1$, the range of the switching inductor is required to be 3 to 17 nH to cover the low-LTE band as investigated before, and the results are shown in Fig. 9.5. However, with the presence of distributed element $DiE1$, the range of the switching inductor is significantly reduced to 1-9 nH from 3-17 nH. The predicted reflection coefficients for L_s = 1, 3, 5, 7, and 9 nH are reported in Fig. 9.12. The overall antenna bandwidth with reconfiguration is 275 MHz (695-970 MHz) to cover the greater low-LTE band.

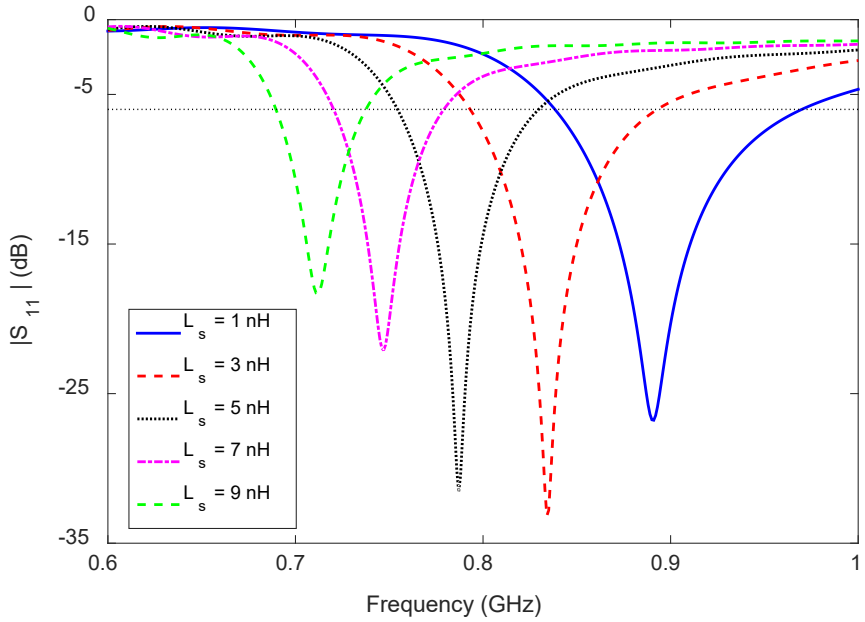

Figure 9.12: Predicted reflection coefficient for the inverted-L-feed capacitive-coupled inverted-L antenna as a function of the inductor L_s for the values 1, 3, 5, 7, and 9 nH.

9.6.2 Radiation Performance

Fig. 9.13 shows the predicted antenna efficiency as a function of L_s for the PILA-based antenna. Here, the simulated antenna efficiencies are presented within the -6 dB reflection coefficient bandwidth for every selected band. The maximum antenna efficiency for the

chip inductor values L_s = 1, 3, 5, 7, and 9 nH is 92%, 89%, 85%, 80%, and 75%, and the minimum efficiency is 52%, 60%, 55%, 52%, and 56%, respectively.

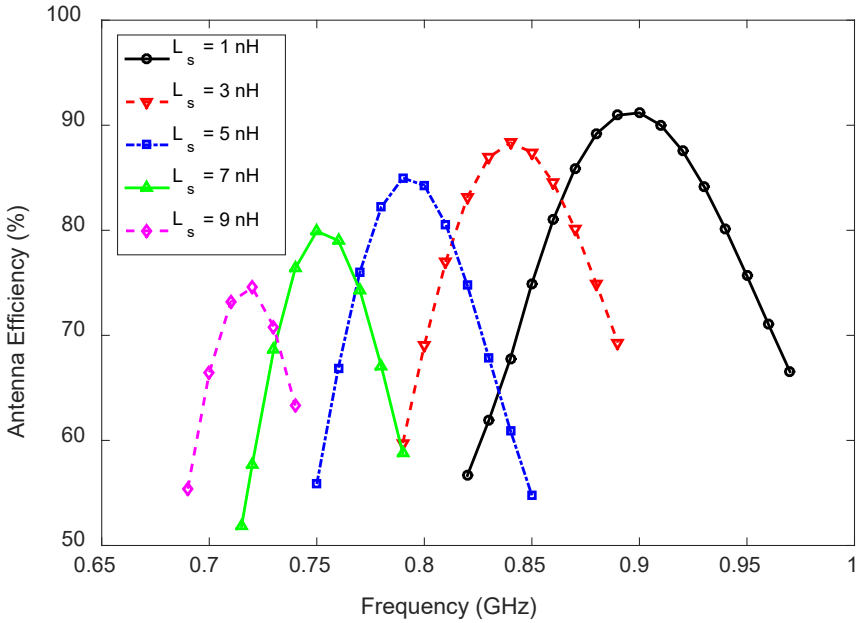

Figure 9.13: Antenna efficiency as a function of L_s (= 1, 3, 5, 7, and 9 nH) of the inverted-L-feed capacitive-coupled inverted-L antenna.

Predicted gain of the passive reconfigurable antenna within the -6 dB reflection coefficient bandwidth for L_s = 1, 3, 5, 7, and 9 nH is shown in Fig. 9.14. The gain variation within the -6 dB reflection coefficient bandwidth for each selected band is around 2 dB. The maximum antenna gain for the chip inductor values L_s = 1, 3, 5, 7, and 9 nH is 2.2, 2, 1.9, 1.7, and 1.6 dBi, and the minimum gain is 0.1, 0.2, 0, 0.2, and 0.2 dBi, respectively.

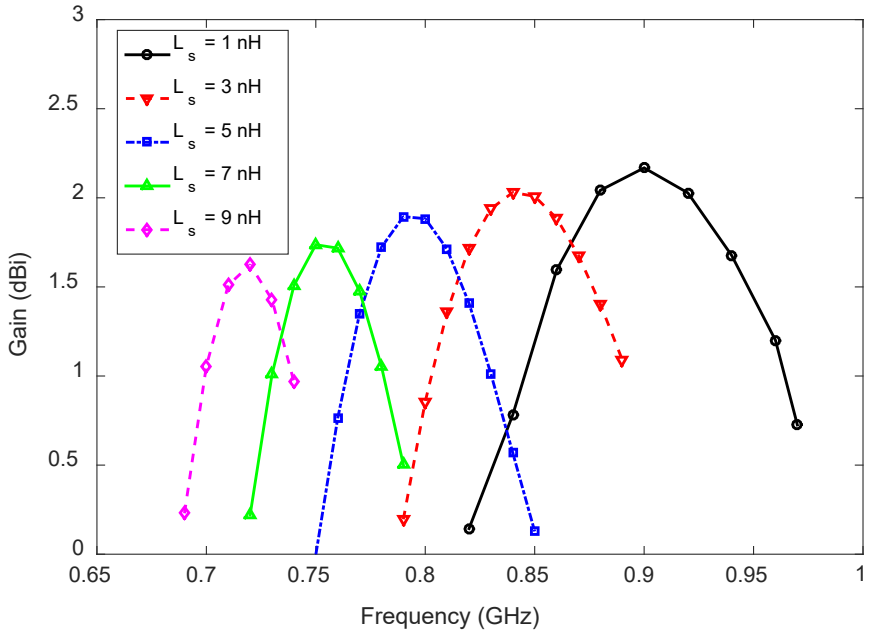

Figure 9.14: The gain of the inverted-L-feed capacitive-coupled inverted-L antenna for L_s = 1, 3, 5, 7, and 9 nH.

Antenna radiation patterns (E_θ and E_ϕ) in three principle planes for L_s = 3, 5, 7, and 9 nH at corresponding frequency of minimum reflection coefficient 0.83, 0.79, 0.75, and 0.71 GHz, respectively, are shown in Figs. 9.15 and 9.16. The radiation patterns at each frequency of minimum reflection coefficient are normalized with the corresponding maximum values of that frequency. The antenna has omnidirectional E_ϕ radiation pattern in the x-z plane at each selected band, and nearly omnidirectional E_ϕ radiation in the x-y plane in each selected band. The E_θ component is always 20 dB below the E_ϕ in the x-z plane and 10 dB below in the x-y planes. However, the E_θ and E_ϕ patterns are comparable in the y-z plane, which is suitable for the complex propagation environment in practical applications [73, 137, 138].

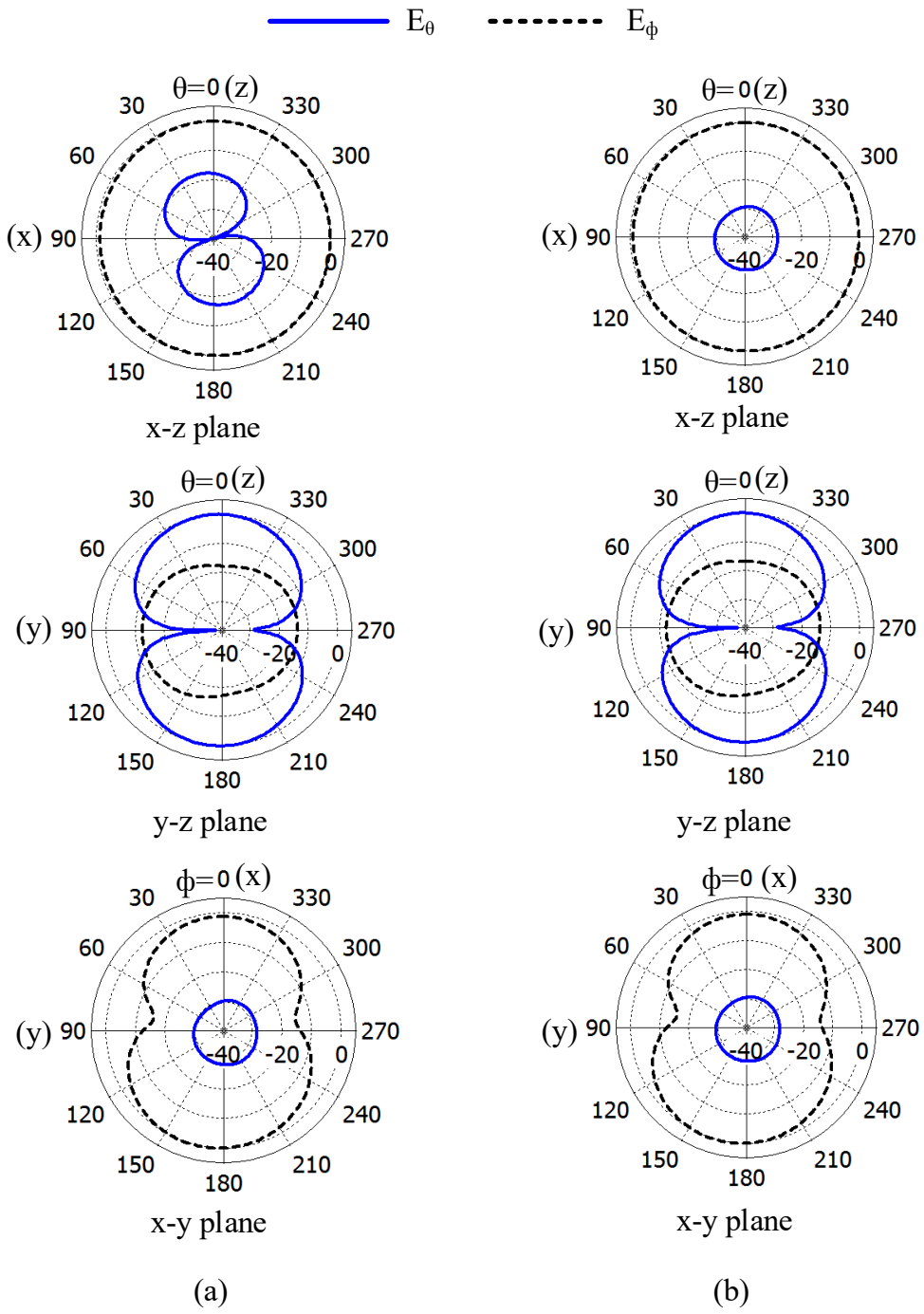

Figure 9.15: E_θ and E_ϕ radiation patterns of the inverted-L-feed capacitive-coupled inverted-L antenna in three principle planes at (a) 830 MHz for $L_s = 3$ nH and (b) 790 MHz for $L_s = 5$ nH.

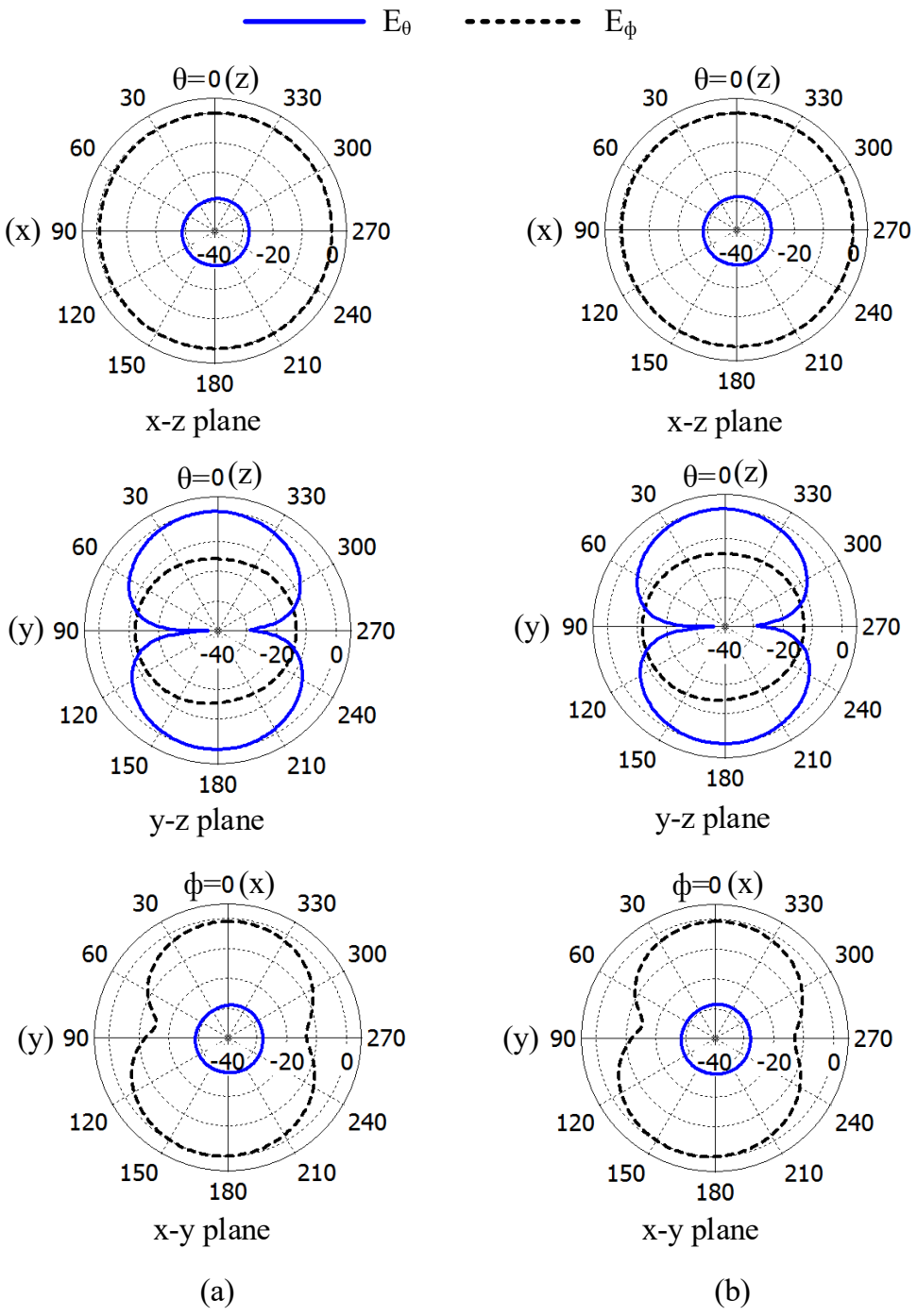

Figure 9.16: E_θ and E_ϕ radiation patterns of the inverted-L-feed capacitive-coupled inverted-L antenna in three principle planes at (a) 750 MHz for $L_s = 7$ nH and (b) 710 MHz for $L_s = 9$ nH.

9.7 Measured and Predicted Results

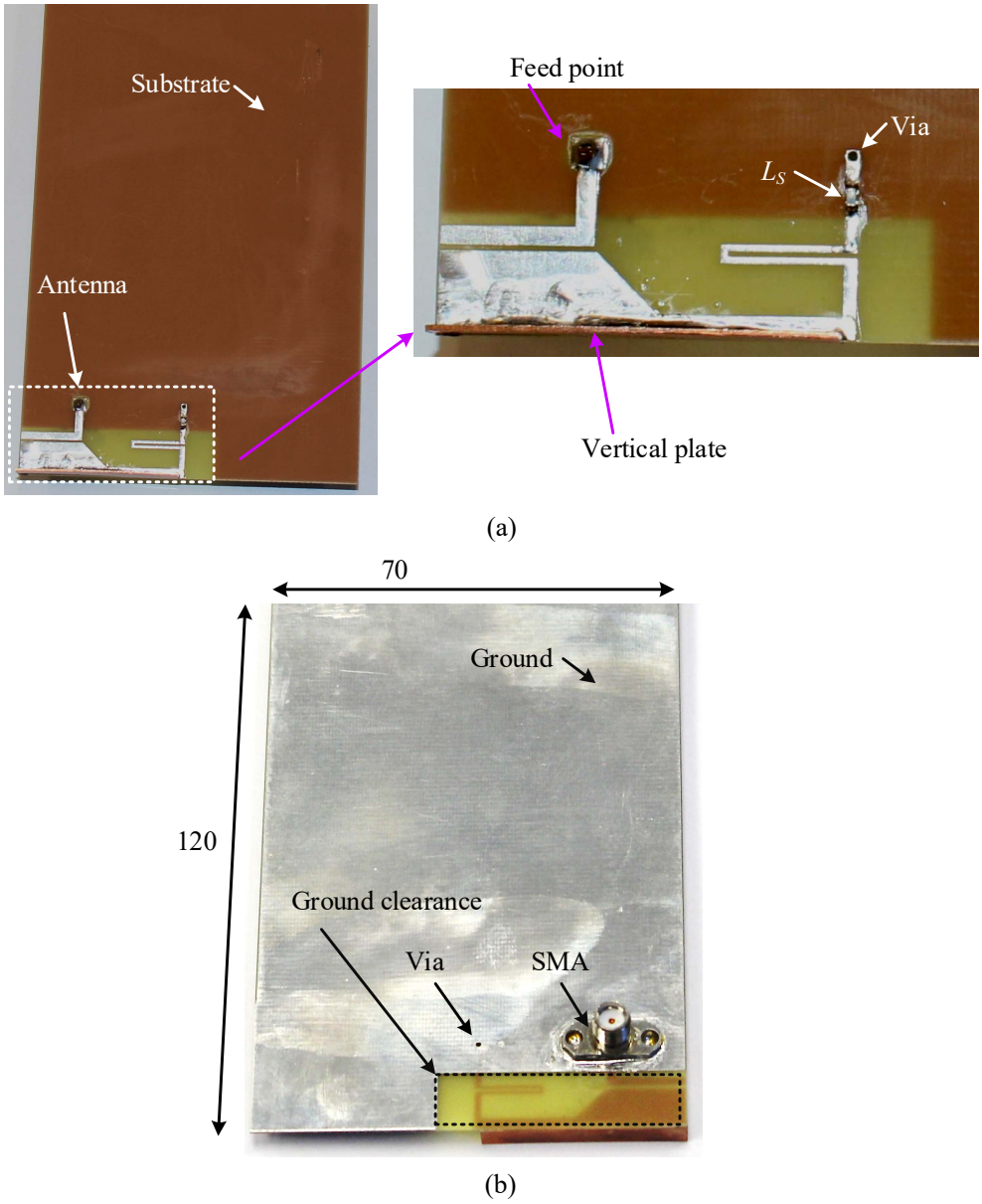

Figure 9.17: Fabricated inverted-L-feed capacitive-coupled inverted-L antenna for low-LTE band: (a) top view, and (b) bottom view. All dimensions are in millimeters.

This section presents the measured and predicted efficiency, gain, and radiation patterns of the new antenna for $L_s = 1$ nH, and predicted and measured reflection coefficients for

L_s = 1, 3, 5, 7, and 9 nH. Fig. 9.17 shows the top and bottom views of the prototype. The radiation performance of the fabricated antenna was measured using the NSI700S-50 near field range at the Australian Antenna Measurement Facility, Australia. Furthermore the reflection coefficient was measured using an Agilent Network Analyzer PNA-X N5242A at Macquarie University, Australia.

9.7.1 Reflection Coefficient

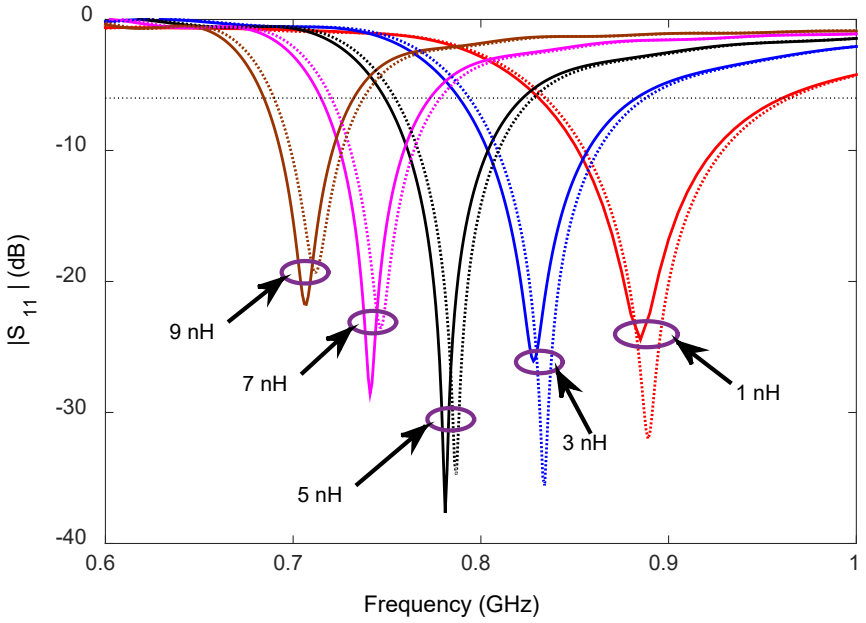

Figure 9.18: Measured and predicted reflection coefficient for the inverted-L-feed capacitive-coupled inverted-L antenna as a function of the inductor L_s for the values 1, 3, 5, 7, and 9 nH. Here, corresponding dotted and solid lines are used to present the predicted and measured results, respectively.

When L_s = 1 nH, the measured reflection coefficient bandwidth of the inverted-L-feed capacitive-coupled inverted-L antenna is 145 MHz (820-965 MHz), which covers the GSM850 and GSM900 bands. The antenna is resonating at 880 MHz; a 10 MHz shift in the frequency of minimum reflection coefficient between the measured and predicted

results. It may be due to fabrication tolerance and effect of soldering. Fig. 9.18 shows the measured reflection coefficient of the inverted-L-feed capacitive-coupled inverted-L antenna for L_s = 1, 3, 5, 7, and 9 nH. A good agreement is observed between the predicted and measured results for all values of L_s. The combined operating bandwidth is 281 MHz (684-965 MHz) measured at -6 dB and the instantaneous bandwidths for L_s = 9, 7, 5, 3, and 1 nH are 684-732, 714-774, 748-823, 788-882, and 820-965 MHz, respectively.

9.7.2 Radiation Performance

For L_s = 1 nH, the measured antenna efficiency together with the predicted results within the -6 dB reflection coefficient bandwidth are shown in Fig. 9.19 and a good agreement is observed.

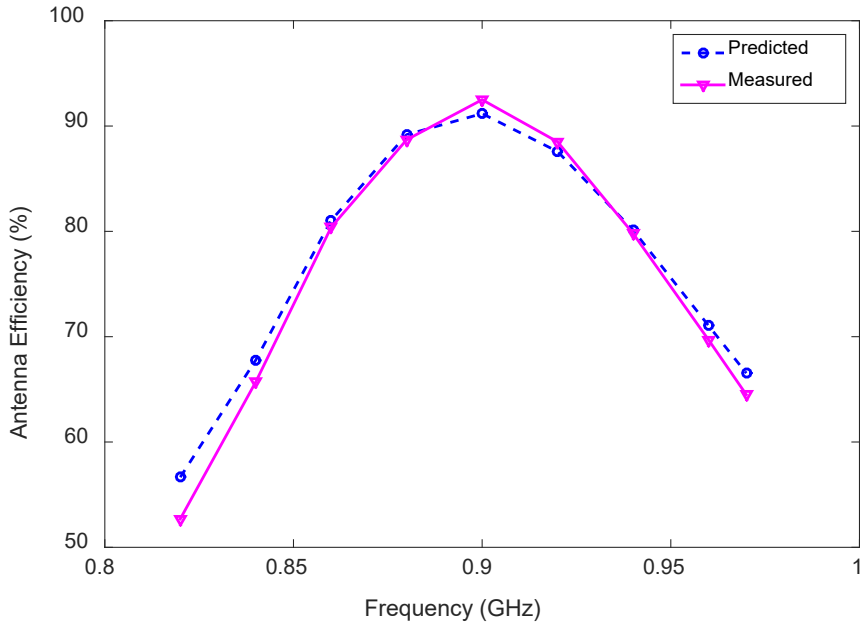

Figure 9.19: Measured and predicted efficiency of the inverted-L-feed capacitive-coupled inverted-L antenna for L_s = 1 nH.

The measured minimum antenna efficiency is 52% at 820 MHz and the maximum is 92% at 900 MHz. The predicted antenna efficiency for the chip inductor values L_s = 1, 3,

5, 7, and 9 nH is shown in Fig. 9.13. The efficiency is always higher than 50% within the low-LTE band (698-960 MHz), which confirms the suitability of the proposed antenna in hand-held mobile device applications.

For $L_s = 1$ nH, the measured and predicted antenna gains within the -6 dB reflection coefficient bandwidth are presented in Fig. 9.20 and a good agreement have been observed. The measured gain is varied between 0.1 and 2.2 dBi. The maximum and minimum antenna gains are observed at 900 and 820 MHz, respectively. In addition, the predicted antenna gains for the chip inductor values $L_s = 1$, 3, 5, 7, and 9 nH are shown in Fig. 9.14.

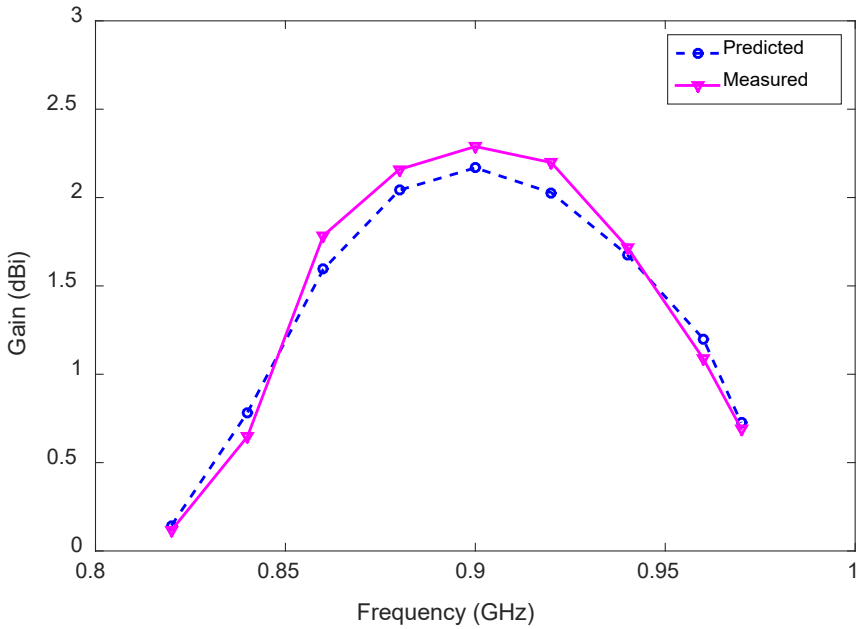

Figure 9.20: Measured and predicted gain of the inverted-L-feed capacitive-coupled inverted-L antenna for $L_s = 1$ nH.

For $L_s = 1$ nH, the measured and predicted E_θ and E_ϕ radiation patterns in three principal planes x-y (parallel to the antenna ground plane), x-z, and y-z at the frequency of minimum reflection coefficient of 0.9 GHz are shown in Fig. 9.21. The radiation patterns in each plane are normalized with the magnitude of that plane. A good agreement between the predicted and measured results has been observed. The radiation pattern is

omnidirectional in the x-z plane and nearly omnidirectional in the x-y plane. No nulls have been observed in the patterns. The comparable E_θ and E_ϕ radiation patterns in the y-z plane are observed.

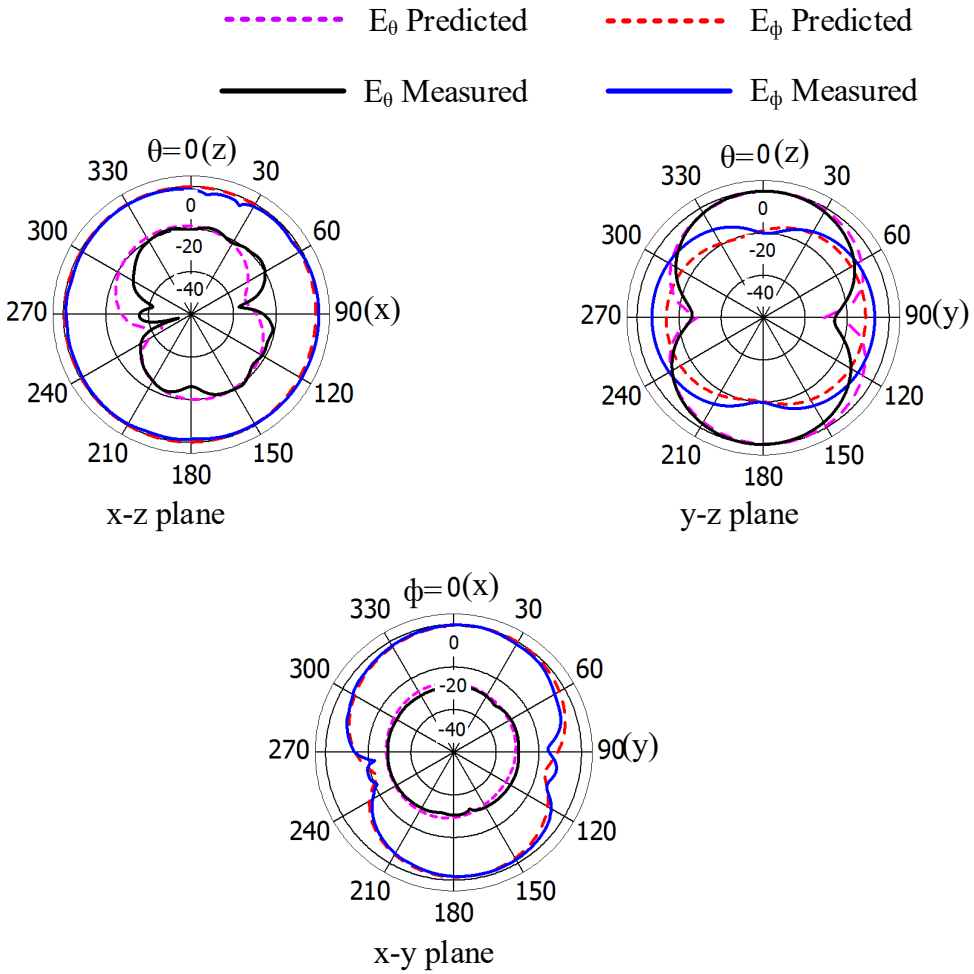

Figure 9.21: Measured and predicted normalized radiation patterns of the inverted-L-feed capacitive-coupled inverted-L antenna at 0.9 GHz with $L_s = 1$ nH.

9.8 Summary

In this chapter an inverted-L antenna-based highly efficient antenna for future LSA or spectrum reallocation within the low-LTE band was developed, prototyped and measured.

The antenna's suitability to realize passive reconfigurable operation was investigated. A 4 mm tall vertical plate was applied to increase antenna efficiency. When variable inductor (L_s) value was 1 nH, a 41 MHz improvement in reflection coefficient bandwidth was achieved, with better antenna input impedance matching. The combined antenna operating band was 684-990 MHz, and this was achieved by selecting appropriate inductor L_s values ranging from 1 to 9 nH. The antenna gain variation below 2 dB and efficiency above 50% was observed at each selected frequency range. Finally, the antenna exuded good omnidirectional radiation without null at every selected frequency range within the greater low-LTE band.

Chapter 10

Conclusions and Future Work

10.1 Conclusions

The development of a 5G mobile communication system has begun as a consequence of increasing demand from various kinds of users of mobile devices. Two technologies, millimeter-wave and cognitive radio, from the five disruptive technologies, device-centric architecture, millimeter-wave, cognitive radio, smart device, and native support for machine to machine (M2M) communications, are in the priority list for the future 5G mobile communication system. Although the standards for the 5G mobile communication system are not yet finalized, according to the literature there are proposals that are in the development stages but high data rate would be one of the key features of upcoming 5G technology. The data rate of a mobile communication system is related to the bandwidth efficiency which is dependent on modulation technique. Therefore, antenna with wide reflection coefficient bandwidth is required such that it can cover the whole millimeter-wave band for future mobile devices. In this thesis, four planar antennas with a directive boresight beam for 28 GHz millimeter-wave 5G mobile devices were developed. Also, antennas for the 1-D and 2-D beam switching were developed and verified through exper-

iment suitable for forthcoming 5G mobile devices. Another promising technology named licensed shared access (LSA) is a new technology of cognitive radio tested practically for future 5G mobile communications.

In this thesis four planar antennas were developed, for the first time, to cover all the LSA bands allocated in Europe for the 5G together with the coverage for mid-long term evolution (LTE) band. All the reported antennas for LTE/wireless wide area network (WWAN) mobile devices suffer from nulls in the radiation patterns, especially at the frequency close to the upper frequency limit of the mid-LTE band as well as in the entire high-LTE band. These limitations were found for most of the antenna designs regardless if the antenna uses an input impedance matching circuit or multiple feed points. This thesis developed two planar antennas to cover all the LTE/WWAN bands: one was developed to cover all the LSA bands and mid and high-LTE bands; and the other to cover the low-LTE bands without null in the radiation patterns. Both antennas were prototyped and tested to validate the concept experimentally. Furthermore the antenna was developed to ensure the low-LTE band is suitable for frequency reconfigurable operation. This makes it a promising candidate for future spectrum reallocation/LSA operation.

Three antennas radiating at the boresight direction were developed for 28 GHz millimeter wave 5G mobile devices. A superstrate that acts as a dielectric load was applied to enhance the performance of the antennas and especially their efficiency. To make the antenna structure simpler, the superstructure was made out of a substrate maintaining the same thickness as that used for antenna substrate. Firstly, a narrow-band PIFA was developed on a Rogers 5870 substrate. A Teflon superstrate serving as a dielectric load was applied to enhance the efficiency, gain and directivity of the antenna. The antenna efficiency was improved by 66% when the superstrate was applied on top of the antenna. Secondly, a leaky-wave antenna (LWA) array radiating at the boresight direction was developed with a reduced number of different dielectrics, i.e. using the same material for the

superstrate and the antenna substrate. Thirdly, the narrow-band PIFA was studied to achieve wide operating band and hence a wideband PIFA with superstrate was developed.

Following the investigation conducted for the LWA array design, a basic LWA with radiating microstrip of length $\approx 5\lambda_0$ (calculated at the center frequency, 28 GHz, of the 5G millimeter-wave band) was designed and investigated for 28 GHz millimeter-wave band. Then a half-width microstrip LWA (HW-MLWA) of length $1.8\lambda_0$ was developed for 28 GHz millimeter-wave 5G mobile devices. Both antennas radiate in the forward (region between the +z and +x-axes) direction. The developed LWA is able to scan beam in the x-z-plane from $\theta = 36°$ to $\theta = 62°$ when frequency varies from 27 GHz to 30 GHz. Following that, a single element LWA was investigated by feeding the antenna at the center using a probe to achieve boresight radiation. Two beams from two sections of the LWA combined to produce a boresight beam. However, at high frequency the beam starts splitting because of the inherent beam scanning properties of LWA. The frequency beyond which the single-beam antenna becomes a dual-beam antenna with a null at boresight direction was examined. Using the off-boresight and boresight radiating LWA, a novel single element LWA with 3 ports was developed to achieve 1-D beam switching. The proposed 1-D beam switching antenna was prototyped and tested to prove the concept. Using the three feeds the beam can be pointed at θ = -37° (off-bore-left), θ = -37° (boresight), and θ = +37° (off-bore-right) in the x-z-plane with a combined 3-dB coverage of 128° (θ = -64° to θ = +64°) within the frequency range 27-30 GHz. To achieve 2-D beam switching two 1-D beam switching antennas are placed at right angles next to each other. The 2-D beam switching antenna was prototyped and tested. The 3-dB coverage is 167° (from θ = +78° to θ = -89°) in the x-z plane ($\phi = 0°$) and 154° (from θ = +82° to θ = -72°) in the y-z plane ($\phi = 90°$).

Two bands below 6 GHz were allocated for the LSA/spectrum reallocation in 5G mobile communication and more bands will be allocated in the future. Two planar antennas

for both LSA bands were designed, developed, and investigated. These antennas cover the mid-LTE, WWAN, and WLAN (2.4 GHz), global system for mobile communications (GSM)1800, GSM1900, digital cellular systems (DCS), personal communications service (PCS), and a few universal mobile telecommunications service (UMTS) bands. One of the planar antennas has two nulls in the radiation patterns over the operating band and the other has one null. Then a dual-band antenna loaded with an I-shaped vertical plate was developed, based on the investigation conducted on two planar antennas, aiming to increase the operating band and reduce nulls from the radiation patterns. The dual-band antenna is more compact than the other two planar antennas. The dual-band antenna covers lower LSA, GSM1800, GSM1900, DCS, and PCS bands without any null in the radiation pattern. It also covers higher LSA, mid-LTE, UMTS, WWAN, and 2.4 GHz WLAN bands with a null, and high-LTE, and 3.3 GHz WiMAX bands with two nulls in the radiation patterns. The dual-band antenna has -6 dB reflection coefficient bandwidths of 1450 MHz (1.39-2.84 GHz) and 700 MHz (3.27-3.97 GHz).

Based on the study on planar and dual-band antennas, a novel wideband antenna loaded with an L-shaped vertical plate was developed, prototyped, and tested. The measured -6 dB reflection coefficient bandwidth of the wideband antenna is 2.63 GHz (1.37-4 GHz). It covers the LSA bands, mid-LTE, high-LTE, GSM1800, GSM1900, WWAN, 2.4 GHz WLAN, and 3.3 GHz WiMAX, DCS, PCS, and UMTS bands. The antenna has nearly omnidirectional radiation patterns in the above-mentioned bands and no null exists in the radiation patterns over the operating band. The suitability of the dual-band and wideband antennas for different-sized mobile devices (e.g. smart phones, tablet computers, etc.) were verified through simulation.

An inverted-L antenna-based highly efficient antenna for future LSA or spectrum reallocation within the low-LTE band was designed, prototyped and measured. The antenna's suitability to realize passive reconfigurable operation was investigated. The overall an-

tenna operating band of 684-990 MHz is achieved by changing an inductor value from 1 nH to 9 nH. The proposed antenna has an omnidirectional radiation pattern without any null at each selected band. All antennas proposed for the 5G and 4G mobile devices were developed without an active or passive lumped component-based input impedance matching circuit to improve the antenna's efficiency.

10.2 Recommendations for Future Research

In this thesis, antennas radiating at boresight direction with single-beam, 1-D, and 2-D patterns configurable operation were proposed for forthcoming 28 GHz millimeter-wave 5G mobile devices. Antennas without any null in the radiation patterns were proposed for LSA/5G, and 4G/LTE mobile devices. Although the results are promising, several problems can be addressed in future research as follows:

- The frequency band selection from the inverted-L-feed capacitive-coupled inverted-L antenna was tested and verified using different inductor values. To achieve seamless control of the frequency bands for the forthcoming LSA/spectrum reallocation in 5G mobile communications, a switchable inductor bank can be used to control the frequency bands electronically.

- A low-powered, low-loss, and switchable 3 ports and 6 ports power divider can be developed to integrate with the 1-D and 2-D pattern reconfigurable antennas, proposed in this thesis, for smooth electronic control.

- In this thesis different antennas are developed for 28 GHz millimeter-wave 5G mobile devices. The proposed 1-D beam switching antenna can be extended to multiple-input and multiple-output (MIMO) application by applying an appropriate isolation method between antennas.

- It would be interesting and useful to develop a 3-D pattern reconfigurable antenna using the proposed 1-D and 2-D pattern reconfigurable antennas for forthcoming 5G mobile devices.

Bibliography

[1] T. S. Rappaport, S. Sun, R. Mayzus, H. Zhao, Y. Azar, K. Wang, G. N. Wong, J. K. Schulz, M. Samimi, and F. Gutierrez, "Millimeter wave mobile communications for 5G cellular: It will work!" *IEEE Access*, vol. 1, pp. 335–349, May 2013.

[2] J. G. Andrews, S. Buzzi, W. Choi, S. V. Hanly, A. Lozano, A. C. K. Soong, and J. C. Zhang, "What will 5G be?" *IEEE J. Sel. Areas Commun.*, vol. 32, no. 6, pp. 1065–1082, Jun. 2014.

[3] ETSI, "LTE; evolved universal terrestrial radio access (E-UTRA); user equipment (UE) radio transmission and reception (release 14)," 3GPP TS 36.101 V14.3.0 Release 14, Apr. 2017.

[4] ——, "Technical specification digital cellular telecommunications system (phase 2+); radio transmission and reception (release 10)," 3GPP TS 45.005 V10.0.0, Release 10, Apr. 2011.

[5] A. Technologies and M. Rumney, *LTE and the Evolution to 4G Wireless: Design and Measurement Challenges*. Wiley Telecom, 2013.

[6] ITU-R, "Requirements related to technical performance for IMT-advanced radio interface(s)," Report M.2134-0, Nov. 2008. [Online]. Available: http://www.itu.int/

[7] 3GPP. (accessed Oct. 2017) LTE. [Online]. Available: http://www.3gpp.org/technologies/keywords-acronyms/98-lte

[8] ——. (accessed Oct. 2017) LTE advanced. [Online]. Available: http://www.3gpp.org/technologies/ keywords-acronyms/97-lte-advanced

[9] S. Parkvall, E. Dahlman, A. Furuskar, Y. Jading, M. Olsson, S. Wanstedt, and K. Zangi, "LTE-advanced - evolving LTE towards IMT-advanced," in *IEEE 68th Vehicular Technology Conference (VTC 2008-Fall)*, Sep. 2008, pp. 1–5.

[10] C. X. Wang, F. Haider, X. Gao, X. H. You, Y. Yang, D. Yuan, H. M. Aggoune, H. Haas, S. Fletcher, and E. Hepsaydir, "Cellular architecture and key technologies for 5G wireless communication networks," *IEEE Commun. Mag.*, vol. 52, no. 2, pp. 122–130, Feb. 2014.

[11] F. Boccardi, R. W. Heath, A. Lozano, T. L. Marzetta, and P. Popovski, "Five disruptive technology directions for 5G," *IEEE Commun. Mag.*, vol. 52, no. 2, pp. 74–80, Feb. 2014.

[12] N. Bhushan, J. Li, D. Malladi, R. Gilmore, D. Brenner, A. Damnjanovic, R. T. Sukhavasi, C. Patel, and S. Geirhofer, "Network densification: the dominant theme for wireless evolution into 5G," *IEEE Commun. Mag.*, vol. 52, no. 2, pp. 82–89, Feb. 2014.

[13] Y. Li, E. Pateromichelakis, N. Vucic, J. Luo, W. Xu, and G. Caire, "Radio resource management considerations for 5G millimeter wave backhaul and access networks," *IEEE Commun. Mag.*, vol. 55, no. 6, pp. 86–92, Jun. 2017.

[14] P. K. Agyapong, M. Iwamura, D. Staehle, W. Kiess, and A. Benjebbour, "Design considerations for a 5G network architecture," *IEEE Commun. Mag.*, vol. 52, no. 11, pp. 65–75, Nov. 2014.

[15] W. Hong, K. H. Baek, Y. Lee, Y. Kim, and S. T. Ko, "Study and prototyping of practically large-scale mmWave antenna systems for 5G cellular devices," *IEEE Communications Magazine*, vol. 52, no. 9, pp. 63–69, Sep. 2014.

[16] T. S. Rappaport, G. R. MacCartney, S. Sun, H. Yan, and S. Deng, "Small-scale, local area, and transitional millimeter wave propagation for 5G communications," *IEEE Trans. Antennas Propag.*, vol. PP, no. 99, pp. 1–1, 2017.

[17] S. F. Jilani and A. Alomainy, "A multiband millimeter-wave two-dimensional array based on enhanced Franklin antenna for 5G wireless systems," *IEEE Antennas Wireless Propag. Lett.*, vol. PP, no. 99, pp. 1–1, 2017.

[18] W. Hong, K. h. Baek, and S. Ko, "Millimeter-wave 5G antennas for smartphones: Overview and experimental demonstration," *IEEE Trans. Antennas Propag.*, vol. PP, no. 99, pp. 1–1, 2017.

[19] O. Jo, J. J. Kim, J. Yoon, D. Choi, and W. Hong, "Exploitation of dual-polarization diversity for 5G millimeter-wave MIMO beamforming systems," *IEEE Trans. Antennas Propag.*, vol. PP, no. 99, pp. 1–1, 2017.

[20] M. Sung, S. H. Cho, J. Kim, J. K. Lee, J. H. Lee, and H. S. Chung, "Demonstration of IFoF based mobile fronthaul in 5G prototype with 28 GHz millimeter-wave," *J. Lightw. Technol.*, vol. PP, no. 99, pp. 1–1, 2017.

[21] J. Zhang, X. Ge, Q. Li, M. Guizani, and Y. Zhang, "5G millimeter-wave antenna array: Design and challenges," *IEEE Wireless Commun.*, vol. 24, no. 2, pp. 106–112, Apr. 2017.

[22] M. Mustonen, M. Matinmikko, M. Palola, S. Yrjl, and K. Horneman, "An evolution toward cognitive cellular systems: licensed shared access for network optimization," *IEEE Commun. Mag.*, vol. 53, no. 5, pp. 68–74, May 2015.

[23] M. Matinmikko, M. Palola, H. Saarnisaari, M. Heikkil, J. Prokkola, T. Kippola, T. Hnninen, M. Jokinen, and S. Yrjl, "Cognitive radio trial environment: First live authorized shared access-based spectrum-sharing demonstration," *IEEE Veh. Technol. Mag.*, vol. 8, no. 3, pp. 30–37, Sep. 2013.

[24] N. U. Hasan, W. Ejaz, N. Ejaz, H. S. Kim, A. Anpalagan, and M. Jo, "Network selection and channel allocation for spectrum sharing in 5G heterogeneous networks," *IEEE Access*, vol. 4, pp. 980–992, Feb. 2016.

[25] N. S. Policy, "Licensed shared access: A managed approach to dynamic spectrum access," 2015. [Online]. Available: www.lstelcom.com

[26] H. Chung, J. Kim, G. Noh, B. Hui, I. Kim, Y. Choi, C. Choi, M. Lee, and D. K. Kim, "From architecture to field trial: A millimeter wave based MHN system for HST communications toward 5G," in *European Conference on Networks and Communications (EuCNC)*, Jun. 2017, pp. 1–5.

[27] Y. Inoue, S. Yoshioka, Y. Kishiyama, J. Kepler, M. Cudak, S. Suyama, and Y. Okumura, "Field experimental trials for 5G mobile communication system using 70 GHz-band," in *IEEE Wireless Communications and Networking Conference Workshops (WCNCW)*, Mar. 2017, pp. 1–6.

[28] DigitalEurope, "Releasing new radio spectrum bands for mobile broadband in Europe," Brussels, Oct. 2014. [Online]. Available: www.digitaleurope.org

[29] ETSI, "Mobile broadband services in the 2300-2400 MHz frequency band under licensed shared access regime," ETSI RRS System Reference Document, TR 103 113, V. 1.1.1., Jul. 2013.

[30] ITU, "Final acts wrc-15," *World Radiocommunication Conference*, Geneva 2015.

[31] GSMA, "5G spectrum - public policy position," Nov. 2016.

[32] HUAWEI, "5G spectrum - public policy position," 2017.

[33] FCC. (accessed Oct. 2017) Forging our 5G future. [Online]. Available: https://www.fcc.gov/5G

[34] Y. Azar, G. N. Wong, K. Wang, R. Mayzus, J. K. Schulz, H. Zhao, F. Gutierrez, D. Hwang, and T. S. Rappaport, "28 GHz propagation measurements for outdoor cellular communications using steerable beam antennas in New York city," in *IEEE International Conference on Communications (ICC)*, Jun. 2013, pp. 5143–5147.

[35] Z. Qingling and J. Li, "Rain attenuation in millimeter wave ranges," in *International Symposium on Antennas, Propagation EM Theory (ISAPE)*, Guilin, Guangxi, China, Oct. 2006, pp. 1–4.

[36] A. I. Sulyman, A. T. Nassar, M. K. Samimi, G. R. Maccartney, T. S. Rappaport, and A. Alsanie, "Radio propagation path loss models for 5G cellular networks in the 28 GHz and 38 GHz millimeter-wave bands," *IEEE Commun. Mag.*, vol. 52, no. 9, pp. 78–86, Sep. 2014.

[37] ETSI, "Technical specification LTE; evolved universal terrestrial radio access (E-UTRA); radio frequency (RF) system scenarios (release 9)," 3GPP TR 36.942 version 9.0.1, Release 9, Apr. 2010.

[38] ——, "Technical specication lte; evolved universal terrestrial radio access (E-UTRA); user equipment (UE) radio transmission and reception (release 12)," 3GPP TS 36.101 version 12.7.0, Release 12, May 2015.

[39] (accessed Oct. 2017) Telecommunications bureau of the ministry of internal affairs and communications. [Online]. Available: http://www.tele.soumu.go.jp/e/

[40] (accessed Oct. 2017) National telecommunications and information administration. [Online]. Available: https://www.ntia.doc.gov

[41] S. K. Goudos, A. Tsiflikiotis, D. Babas, K. Siakavara, C. Kalialakis, and G. K. Karagiannidis, "Evolutionary design of a dual band E-shaped patch antenna for 5G mobile communications," in *International Conference on Modern Circuits and Systems Technologies (MOCAST)*, May 2017, pp. 1–4.

[42] O. M. Haraz, M. M. M. Ali, S. Alshebeili, and A. R. Sebak, "Design of a 28/38 GHz dual-band printed slot antenna for the future 5G mobile communication networks," in *IEEE International Symposium on Antennas and Propagation USNC/URSI National Radio Science Meeting*, Jul. 2015, pp. 1532–1533.

[43] A. T. Alreshaid, O. Hammi, M. S. Sharawi, and K. Sarabandi, "A compact millimeter-wave slot antenna array for 5G standards," in *IEEE 4th Asia-Pacific Conference on Antennas and Propagation (APCAP)*, Jul. 2015, pp. 84–85.

[44] O. M. Haraz, M. M. M. Ali, A. Elboushi, and A. R. Sebak, "Four-element dual-band printed slot antenna array for the future 5G mobile communication networks," in *IEEE International Symposium on Antennas and Propagation USNC/URSI National Radio Science Meeting*, Jul. 2015, pp. 1–2.

[45] A. Elboushi and A. Sebak, "High gain 4-element antenna array for millimeter-wave applications," in *IEEE International Conference on Communication, Networks and Satellite (COMNETSAT)*, Nov. 2014, pp. 17–20.

[46] M. C. Tang, T. Shi, and R. W. Ziolkowski, "A study of 28 GHz, planar, multi-layered, electrically small, broadside radiating, huygens source antennas," *IEEE Trans. Antennas Propag.*, vol. PP, no. 99, pp. 1–1, 2017.

[47] Z. Chen and Y. P. Zhang, "FR4 PCB grid array antenna for millimeter-wave 5G mobile communications," in *IEEE MTT-S International Microwave Workshop Series on RF and Wireless Technologies for Biomedical and Healthcare Applications (IMWS-BIO)*, Dec. 2013, pp. 1–3.

[48] H. Chu, J. X. Chen, S. Luo, and Y. X. Guo, "A millimeter-wave filtering monopulse antenna array based on substrate integrated waveguide technology," *IEEE Trans. Antennas Propag.*, vol. 64, no. 1, pp. 316–321, Jan. 2016.

[49] W. Han, F. Yang, J. Ouyang, and P. Yang, "Low-cost wideband and high-gain slotted cavity antenna using high-order modes for millimeter-wave application," *IEEE Trans. Antennas Propag.*, vol. 63, no. 11, pp. 4624–4631, Nov. 2015.

[50] T. Y. Yang, W. Hong, and Y. Zhang, "Wideband millimeter-wave substrate integrated waveguide cavity-backed rectangular patch antenna," *IEEE Antennas Wireless Propag. Lett.*, vol. 13, pp. 205–208, Jan. 2014.

[51] S. J. Park, D. H. Shin, and S. O. Park, "Low side-lobe substrate-integrated-waveguide antenna array using broadband unequal feeding network for millimeter-wave handset device," *IEEE Trans. Antennas Propag.*, vol. 64, no. 3, pp. 923–932, Mar. 2016.

[52] Q. L. Yang, Y. L. Ban, S. R. Yang, and M. Y. Li, "Omnidirectional slot arrays fed by stacked butler matrix for 5G handset devices," in *IEEE 9th UK-Europe-China Workshop on Millimetre Waves and Terahertz Technologies (UCMMT)*, Sep. 2016, pp. 245–247.

[53] W. S. Chang, C. F. Yang, C. K. Chang, W. J. Liao, L. Cho, and W. S. Chen, "Pattern reconfigurable millimeter-wave antenna design for 5G handset applications," in *European Conference on Antennas and Propagation (EuCAP)*, Apr. 2016, pp. 1–3.

[54] H. Zhou, "Phased array for millimeter-wave mobile handset," in *IEEE Antennas and Propagation Society International Symposium (APSURSI)*, Jul. 2014, pp. 933–934.

[55] N. Ojaroudiparchin, M. Shen, and G. F. Pedersen, "Design of Vivaldi antenna array with end-fire beam steering function for 5G mobile terminals," in *Telecommunications Forum Telfor (TELFOR)*, Nov. 2015, pp. 587–590.

[56] ——, "A 28 GHz FR-4 compatible phased array antenna for 5G mobile phone applications," in *International Symposium on Antennas and Propagation (ISAP)*, Nov. 2015, pp. 1–4.

[57] H. Xia, J. Lei, L. Meng, and G. Yang, "Design and analysis of a compact reconfigurable phased antenna array with 3D coverage for 5G applications in portable devices," in *Progress in Electromagnetic Research Symposium (PIERS)*, Aug. 2016, pp. 2459–2463.

[58] A. T. Alreshaid, O. Hammi, M. S. Sharawi, and K. Sarabandi, "A millimeter wave switched beam planar antenna array," in *IEEE International Symposium on Antennas and Propagation USNC/URSI National Radio Science Meeting*, Jul. 2015, pp. 2117–2118.

[59] A. Carroll and G. Heiser, "An analysis of power consumption in a smartphone," in *USENIX Annual Technical Conference (USENIXATC'10)*, Jun. 2010.

[60] Pasternack. (accessed Oct. 2017) 8 bit programmable phase shifter, 32 GHz to 37 GHz, 360 deg phase shift, 256 steps and SMA. [Online]. Available: http://www.pasternack.com/

[61] D. Wu, S. W. Cheung, and T. I. Yuk, "A compact and low-profile loop antenna with multiband operation for ultra-thin smartphones," *IEEE Trans. Antennas Propag.*, vol. 63, no. 6, pp. 2745–2750, Jun. 2015.

[62] J. Lee, Y. Liu, and H. Kim, "Mobile antenna using multi-resonance feed structure for wideband operation," *IEEE Trans. Antennas Propag.*, vol. 62, no. 11, pp. 5851–5855, Nov. 2014.

[63] K. L. Wong and C. Y. Tsai, "Small-size stacked inverted-F antenna with two hybrid shorting strips for the LTE/WWAN tablet device," *IEEE Trans. Antennas Propag.*, vol. 62, no. 8, pp. 3962–3969, Aug. 2014.

[64] J. H. Lu and J. L. Guo, "Small-size octaband monopole antenna in an LTE/WWAN mobile phone," *IEEE Antennas Wireless Propag. Lett.*, vol. 13, pp. 548–551, Apr. 2014.

[65] J. H. Lu and Y. S. Wang, "Planar small-size eight-band LTE/WWAN monopole antenna for tablet computers," *IEEE Trans. Antennas Propag.*, vol. 62, no. 8, pp. 4372–4377, Aug. 2014.

[66] Y. L. Ban, C. L. Liu, Z. Chen, J. L. W. Li, and K. Kang, "Small-size multiresonant octaband antenna for LTE/WWAN smartphone applications," *IEEE Antennas Wireless Propag. Lett.*, vol. 13, pp. 619–622, Mar. 2014.

[67] Y. Wang and Z. Du, "Wideband monopole antenna with less nonground portion for octa-band WWAN/LTE mobile phones," *IEEE Trans. Antennas Propag.*, vol. 64, no. 1, pp. 383–388, Jan. 2016.

[68] T. Zhang, R. Li, G. Jin, G. Wei, and M. M. Tentzeris, "A novel multiband planar antenna for GSM/UMTS/LTE/Zigbee/RFID mobile devices," *IEEE Trans. AntennasPropag.*, vol. 59, no. 11, pp. 4209–4214, Nov. 2011.

[69] K. L. Wong and P. R. Wu, "Dual-wideband linear open slot antenna with two open ends for the LTE/WWAN smartphone," *Microwave Opt. Technol. Lett.*, vol. 57, no. 6, pp. 1269–1274, Jun. 2015.

[70] B. Y. Park, M. H. Jeong, and S. O. Park, "A magneto-dielectric handset antenna for LTE/WWAN/GPS applications," *IEEE Antennas Wireless Propag. Lett.*, vol. 13, pp. 1482–1485, Aug. 2014.

[71] K. L. Wong and L. Y. Chen, "Small-size LTE/WWAN tablet device antenna with two hybrid feeds," *IEEE Trans. Antennas Propag.*, vol. 62, no. 6, pp. 2926–2934, Jun. 2014.

[72] J. Ilvonen, R. Valkonen, J. Holopainen, and V. Viikari, "Design strategy for 4G handset antennas and a multiband hybrid antenna," *IEEE Trans. Antennas Propag.*, vol. 62, no. 4, pp. 1918–1927, Apr. 2014.

[73] K. L. Wong and Z. G. Liao, "Passive reconfigurable triple-wideband antenna for LTE tablet computer," *IEEE Trans. Antennas Propag.*, vol. 63, no. 3, pp. 901–908, Mar. 2015.

[74] H. Liu, R. Li, Y. Pan, X. Quan, L. Yang, and L. Zheng, "A multi-broadband planar antenna for GSM/UMTS/LTE and WLAN/WiMAX handsets," *IEEE Trans. Antennas Propag.*, vol. 62, no. 5, pp. 2856–2860, May 2014.

[75] H. Xu, H. Wang, S. Gao, H. Zhou, Y. Huang, Q. Xu, and Y. Cheng, "A compact and low-profile loop antenna with six resonant modes for LTE smartphone," *IEEE Trans. Antennas Propag.*, vol. 64, no. 9, pp. 3743–3751, Sep. 2016.

[76] 3GPP, "3rd generation partnership project; technical specification group GSM/EDGE radio access network; radio transmission and reception (release 8)," 3GPP TS 45.005 V8.8.0, Release 08, Mar. 2010.

[77] Z. Zhang, *Antenna Design for Mobile Devices*, 1st ed. John Wiley & Sons (Asia) Pte Ltd, Feb. 2011.

[78] R. Electronics. (accessed Oct. 2017) GSM frequencies and frequency bands. [Online]. Available: http://www.radio-electronics.com/info/cellulartelecomms/

[79] R. Cafe. (accessed Oct. 2017) GSM timeslot & frequency specifications. [Online]. Available: http://www.rfcafe.com/references/electrical/gsm-specs/

[80] 3GPP, "Technical specification ground radio access network; user equipment (UE) radio transmission and reception (FDD/TDD) (release 9)," 3GPP TS 25.101/102/104/105 V9.5.0, Release 09, Sep. 2010.

[81] 3Gpp. (accessed Oct. 2017) Universal mobile telecommunications system. [Online]. Available: http://www.3gpp.org/technologies/keywords-acronyms/103-umts

[82] R. Electronics. (accessed Oct. 2017) 3G UMTS WCDMA frequency bands & UARFCN. [Online]. Available: http://www.radio-electronics.com/info/cellulartelecomms/

[83] ETSI. (accessed Oct. 2017) ETSI releases specifications for licensed shared access. [Online]. Available: www.etsi.org

[84] S. Mattisson, "Overview of 5G requirements and future wireless networks," in *43rd IEEE European Solid State Circuits Conference (ESSCIRC)*, Sep. 2017, pp. 1–6.

[85] ITU, "Minimum requirements related to technical performance for IMT-2020 radio interface(s)," in *43rd IEEE European Solid State Circuits Conference (ESSCIRC)*, Feb. 2017.

[86] Y. Li, Z. Zhang, J. Zheng, Z. Feng, and M. F. Iskander, "A compact hepta-band loop-inverted F reconfigurable antenna for mobile phone," *IEEE Trans. Antennas Propag.*, vol. 60, no. 1, pp. 389–392, Jan. 2012.

[87] H. D. Chen, H. W. Yang, and C. Y. D. Sim, "Single open-slot antenna for LTE/WWAN smartphone application," *IEEE Trans. Antennas Propag.*, vol. 65, no. 8, pp. 4278–4282, Aug. 2017.

[88] M. Stanley, Y. Huang, H. Wang, H. Zhou, Z. Tian, and Q. Xu, "A novel reconfigurable metal rim integrated open slot antenna for octa-band smartphone applications," *IEEE Trans. Antennas Propag.*, vol. 65, no. 7, pp. 3352–3363, Jul. 2017.

[89] R. Tang and Z. Du, "Wideband monopole without lumped elements for octa-band narrow-frame LTE smart phone," *IEEE Antennas Wireless Propag. Lett.*, no. 99, Aug. 2016.

[90] C. Rowell and E. Y. Lam, "Mobile-phone antenna design," *IEEE Antennas Propag. Magn.*, vol. 54, no. 4, pp. 14–34, Aug. 2012.

[91] K. L. Wong, *Compact and Broadband Microstrip Antennas*, 1st ed. John Wiley & Sons, Inc., Jan. 2002.

[92] H. T. Chattha, Y. Huang, X. Zhu, and Y. Lu, "An empirical equation for predicting the resonant frequency of planar inverted-F antennas," *IEEE Antennas Wireless Propag. Lett.*, vol. 8, pp. 856–860, Jul. 2009.

[93] (accessed Apr. 2018) Planar inverted-F antenna. [Online]. Available: www.antenna-theory.com

[94] C. H. See, H. I. Hraga, R. A. Abd-Alhameed, N. J. McEwan, J. M. Noras, and P. S. Excell, "A low-profile ultra-wideband modified planar inverted-F antenna," *IEEE Trans. Antennas Propag.*, vol. 61, no. 1, pp. 100–108, Jan. 2013.

[95] K. R. Boyle and P. G. Steeneken, "A five-band reconfigurable PIFA for mobile phones," *IEEE Trans. Antennas Propag.*, vol. 55, no. 11, pp. 3300–3309, Nov. 2007.

[96] M. Z. Azad and M. Ali, "A miniaturized Hilbert PIFA for dual-band mobile wireless applications," *IEEE Antennas Wireless Propag. Lett.*, vol. 4, no. 1, pp. 59–62, Jan. 2005.

[97] C. H. Chang and K. L. Wong, "Printed $\lambda/8$-PIFA for penta-band WWAN operation in the mobile phone," *IEEE Trans. Antennas Propag.*, vol. 57, no. 5, pp. 1373–1381, May 2009.

[98] J. Lee and Y. Sung, "Heptaband inverted-F antenna with independent resonance control for mobile handset applications," *IEEE Antennas Wireless Propag. Lett.*, vol. 13, pp. 1267–1270, Jun. 2014.

[99] C. Hung and T. Chiu, "Dual-band reconfigurable antenna design using slot-line with branch edge," *IEEE Trans. Antennas Propag.*, vol. 63, no. 2, pp. 508–516, Feb. 2015.

[100] G. H. Kim and T. Y. Yun, "Small wideband monopole antenna with a distributed inductive strip for LTE/GSM/UMTS," *IEEE Antennas Wireless Propag. Lett.*, vol. 14, pp. 1677–1680, Mar. 2015.

[101] C. S. Liu, C. N. Chiu, and S. M. Deng, "A compact disc-slit monopole antenna for mobile devices," *IEEE Antennas Wireless Propag. Lett.*, vol. 7, pp. 251–254, Mar. 2008.

[102] C. K. Hsu and S. J. Chung, "Compact antenna with U-shaped open-end slot structure for multi-band handset applications," *IEEE Trans. Antennas Propag.*, vol. 62, no. 2, pp. 929–932, Feb. 2014.

[103] Y. L. Ban, Z. X. Chen, Z. Chen, K. Kang, and J. L. W. Li, "Reconfigurable narrow-frame antenna for heptaband WWAN/LTE smartphone applications," *IEEE Antennas Wireless Propag. Lett.*, vol. 13, pp. 1365–1368, Apr. 2014.

[104] Y. F. Lin, H. M. Chen, C. Y. Lin, and S. C. Pan, "Planar inverted-L antenna with a dielectric resonator feed in a mobile device," *IEEE Trans. Antennas Propag.*, vol. 57, no. 10, pp. 3342–3346, Oct. 2009.

[105] Y. L. Ban, S. C. Sun, P. P. Li, J. L. W. Li, and K. Kang, "Compact eight-band frequency reconfigurable antenna for LTE/WWAN tablet computer applications," *IEEE Trans. Antennas Propag.*, vol. 62, no. 1, pp. 471–475, Jan. 2014.

[106] J. T. Yeh, W. J. Liao, and S. H. Chang, "Compact internal antenna for handheld devices with comprehensive DTV band coverage," *IEEE Trans. Antennas Propag.*, vol. 62, no. 8, pp. 3998–4007, Aug. 2014.

[107] S. C. del Barrio, E. Foroozanfard, A. Morris, and G. F. Pedersen, "Tunable handset antenna: Enhancing efficiency on TV white spaces," *IEEE Trans. Antennas Propag.*, vol. 65, no. 4, pp. 2106–2111, Apr. 2017.

[108] M. C. Tang, T. Shi, and R. W. Ziolkowski, "A study of 28 GHz, planar, multi-layered, electrically small, broadside radiating, Huygens source antennas," *IEEE Trans. Antennas Propag.*, vol. PP, no. 99, pp. 1–1, May. 2017.

[109] A. Bhattacharyya, "Effects of dielectric superstrate on patch antennas," *Electron. Lett.*, vol. 24, no. 6, pp. 356–358, Mar. 1988.

[110] R. Afzalzadeh and R. N. Karekar, "Effect of dielectric protecting superstrate on radiation pattern of microstrip patch antenna," *Electron. Lett.*, vol. 27, no. 13, pp. 1218–1219, Jun. 1991.

[111] O. M. Haraz, A. Elboushi, S. A. Alshebeili, and A. R. Sebak, "Dense dielectric patch array antenna with improved radiation characteristics using EBG ground structure and dielectric superstrate for future 5G cellular networks," *IEEE Access*, vol. 2, pp. 909–913, Aug. 2014.

[112] J. L. Gomez-Tornero, F. Quesada-Pereira, and A. Alvarez-Melcon, "Application of the high-gain substrate-superstrate configuration to dielectric leaky-wave antennas," *IEEE Microwave Wireless Components Lett.*, vol. 15, no. 4, pp. 250–252, Apr. 2005.

[113] B. A. Zeb, R. M. Hashmi, and K. P. Esselle, "Wideband gain enhancement of slot antenna using one unprinted dielectric superstrate," *Electron. Lett.*, vol. 51, no. 15, pp. 1146–1148, Jul. 2015.

[114] M. Akbari, S. Gupta, M. Farahani, A. R. Sebak, and T. A. Denidni, "Gain enhancement of circularly polarized dielectric resonator antenna based on FSS superstrate for MMW applications," *IEEE Trans. Antennas Propag.*, vol. 64, no. 12, pp. 5542–5546, Dec. 2016.

[115] M. Asaadi and A. Sebak, "Gain and bandwidth enhancement of 2 x 2 square dense dielectric patch antenna array using a holey superstrate," *IEEE Antennas Wireless Propag. Lett.*, vol. 16, pp. 1808–1811, Mar. 2017.

[116] S. X. Ta and T. K. Nguyen, "AR bandwidth and gain enhancements of patch antenna using single dielectric superstrate," *Electron. Lett.*, vol. 53, no. 15, pp. 1015–1017, Jul. 2017.

[117] D. K. Karmokar, K. P. Esselle, and T. S. Bird, "An array of half-width microstrip leaky-wave antennas radiating on boresight," *IEEE Antennas Wireless Propag. Lett.*, vol. 14, pp. 112–114, Sep. 2015.

[118] Q. Lai, C. Fumeaux, and W. Hong, "Periodic leaky-wave antennas fed by a modified half-mode substrate integrated waveguide," *IET Microw. Antennas Propag.*, vol. 6, no. 5, pp. 594–601, Apr. 2012.

[119] S. K. Podilchak, A. P. Freundorfer, and Y. M. M. Antar, "Broadside radiation from a planar 2-D leaky-wave antenna by practical surface-wave launching," *IEEE Antennas Wireless Propag. Lett.*, vol. 7, pp. 517–520, Oct. 2008.

[120] Y. Li, Q. Xue, E. K. N. Yung, and Y. Long, "The periodic half-width microstrip leaky-wave antenna with a backward to forward scanning capability," *IEEE Trans. Antennas Propag.*, vol. 58, no. 3, pp. 963–966, Mar. 2010.

[121] D. R. Jackson, C. Caloz, and T. Itoh, "Leaky-wave antennas," *Proceedings of the IEEE*, vol. 100, no. 7, pp. 2194–2206, Jul. 2012.

[122] D. R. Jackson and A. A. Oliner, "Leaky-wave antennas," in *Modern Antenna Handbook*, C. A. Balanis, Ed. John Wiley & Sons, Inc., 2007, ch. 07, pp. 325–367.

[123] G. M. Zelinski, G. A. Thiele, M. L. Hastriter, M. J. Havrilla, and A. J. Terzuoli, "Half width leaky wave antennas," *IET Microw. Antennas Propag.*, vol. 1, no. 2, pp. 341–348, Apr. 2007.

[124] D. K. Karmokar, K. P. Esselle, and T. S. Bird, "Wideband microstrip leaky-wave antennas with two symmetrical side beams for simultaneous dual-beam scanning," *IEEE Trans. Antennas Propag.*, vol. 64, no. 4, pp. 1262–1269, Apr. 2016.

[125] A. A. Oliner, "Leakage from higher modes on microstrip line with application to antennas," *Radio Science*, vol. 22, no. 6, pp. 907–912, Nov. 1987.

[126] J. S. Bagby, C. H. Lee, D. P. Nyquist, and Y. Yuan, "Identification of propagation regimes on integrated microstrip transmission lines," *IEEE Trans. Microw. Theory Tech.*, vol. 41, no. 11, pp. 1887–1894, Nov. 1993.

[127] A. A. Oliner and D. R. Jackson, "Leaky-wave antennas," in *Antenna Engineering Handbook*, 4th ed., J. Volakis, Ed. McGraw-Hill Professional, 2007, ch. 11, pp. 11.1–11.56.

[128] J. Xu, W. Hong, H. Tang, Z. Kuai, and K. Wu, "Half-mode substrate integrated waveguide (HMSIW) leaky-wave antenna for millimeter-wave applications," *IEEE Antennas Wireless Propag. Lett.*, vol. 7, pp. 85–88, Apr. 2008.

[129] M. Archbold, E. J. Rothwell, L. C. Kempel, and S. W. Schneider, "Beam steering of a half-width microstrip leaky-wave antenna using edge loading," *IEEE Antennas Wireless Propag. Lett.*, vol. 9, pp. 203–206, Mar. 2010.

[130] D. K. Karmokar and K. P. Esselle, "Periodic U-slot-loaded dual-band half-width microstrip leaky-wave antennas for forward and backward beam scanning," *IEEE Trans. Antennas Propag.*, vol. 63, no. 12, pp. 5372–5381, Dec. 2015.

[131] Y. Li, Q. Xue, H. Z. Tan, and Y. Long, "The half-width microstrip leaky wave antenna with the periodic short circuits," *IEEE Trans. Antennas Propag.*, vol. 59, no. 9, pp. 3421–3423, Sep. 2011.

[132] Y. Li, Q. Xue, E. K. N. Yung, and Y. Long, "Quasi microstrip leaky-wave antenna with a two-dimensional beam-scanning capability," *IEEE Trans. Antennas Propag.*, vol. 57, no. 2, pp. 347–354, Feb. 2009.

[133] R. O. Ouedraogo, E. J. Rothwell, and B. J. Greetis, "A reconfigurable microstrip leaky-wave antenna with a broadly steerable beam," *IEEE Trans. Antennas Propag.*, vol. 59, no. 8, pp. 3080–3083, Aug. 2011.

[134] D. K. Karmokar, K. M. Morshed, S. Hossain, and N. Mollah, "A high-gain slot-loaded microstrip patch antenna fed by a half-width microstrip line for 5.5 and

5.8 GHz Wi-Fi/WiMAX applications," in *2015 2nd International Conference on Electrical Information and Communication Technologies (EICT)*, Dec. 2015, pp. 359–363.

[135] L. J. Xu, Y. X. Guo, and W. Wu, "Miniaturized circularly polarized loop antenna for biomedical applications," *IEEE Trans. Antennas Propag.*, vol. 63, no. 3, pp. 922–930, Mar. 2015.

[136] S. F. Jilani and A. Alomainy, "A multiband millimeter-wave two-dimensional array based on enhanced Franklin antenna for 5G wireless systems," *IEEE Antennas Wireless Propag. Lett.*, vol. PP, no. 99, pp. 1–1, Sep. 2017.

[137] K. L. Wong and Y. C. Chen, "Small-size hybrid loop/open-slot antenna for the LTE smartphone," *IEEE Trans. Antennas Propag.*, vol. 63, no. 12, pp. 5837–5841, Dec. 2015.

[138] K. L. Wong and C. Y. Tsai, "IFA-based metal-frame antenna without ground clearance for the LTE/WWAN operation in the metal-casing tablet computer," *IEEE Trans. Antennas Propag.*, vol. 64, no. 1, pp. 53–60, Jan. 2016.

[139] H. Chen and A. Zhao, "LTE antenna design for mobile phone with metal frame," *IEEE Antennas Wireless Propag. Lett.*, vol. 15, pp. 1462–1465, Dec. 2016.

[140] S. Wang and Z. Du, "A dual-antenna system for LTE/WWAN/WLAN/WiMAX smartphone applications," *IEEE Antennas Wireless Propag. Lett.*, vol. 14, pp. 1443–1446, Jul. 2015.

[141] K. L. Wong and C. Y. Huang, "Triple-wideband open-slot antenna for the LTE metal-framed tablet device," *IEEE Trans. Antennas Propag.*, vol. 63, no. 12, pp. 5966–5971, Dec. 2015.

[142] D. Darnell *et al.*, "Tunable antenna system with multiple feeds," Aug. 5 2014, uS Patent 8,798,554. [Online]. Available: http://www.google.com/patents/US8798554